Geological characteristics, genesis and ore controlling factors of the Tick Hill Au deposit, Dajarra District, NW Queensland, Australia

Thesis submitted by

Truong Xuan Le

M.Ec. Geology, University of Tasmania, 2014

B.Sc. Geological Sciences, Hanoi University of Mining and Geology, 2001

For the Degree of Doctor of Philosophy

College of Science and Engineering

James Cook University

(Townsville)

July 2021

Statement of Access

I, the undersigned author of this thesis, understand that James Cook University will make this thesis available for use within the university library and allow access in other approved libraries after its submission. All users consulting this thesis will have to sign the following statement:

In consulting this thesis, I agree not to copy or closely paraphrase it in whole or in part without the written consent of the author, and to make proper public written acknowledgement for any assistance that I have obtained from it.

Beyond this, I do not wish to place any restrictions on access to this thesis.

Truong Xuan Le

July 2021

Declaration

I declare that this thesis is my own work and has not been submitted in any form for another degree or diploma at any university or other institute of tertiary education. Information derived from the published or unpublished work of others has been acknowledged in the text and a list of reference is given.

Truong Xuan Le

July 2021

Acknowledgements

Statement of contribution of others

Name and affiliation of contributors	Contribution	Nature of Assistance
Prof. Paul Dirks, JCU	Primary supervision	Intellectual support
Dr. Ioan Sanislav, JCU	Supervision	
Dr. Jan Huizenga, JCU	Supervision	
Dr. Yi Hu, JCU/AAC Dr. Huiqing (Jeffrey) Huang, JCU Dr. Kevin Blake, JCU/AAC Dr. Shane Ankew, JCU/AAC Pof. Chris Harris, UCT, S. Africa	Assistance with data analysis	
Geological Survey of Queensland	Research funding, conferences	Financial support
AAS, Department of Foreign Affairs and Trade	Tuition Fees, stipend, travelling	
JCU, Graduate Research School	Tuition Fees, student services and amenities fees (SSA fees)	

Abstract

The high grade, gold-only and single-ore body, Tick Hill deposit occurs in the southern Mary Kathleen Domain in the Mt Isa Inlier (northeast Queensland, Australia). The deposit is hosted in a sequence comprising calc-silicate gneiss, amphibolite, biotite schist, quartzite and quartz-feldspar mylonite. This sequence was affected by D_1 shearing and D_2 upright folding at high-grade metamorphic conditions, followed by D_3 normal faulting accompanied with widespread quartz-feldspar alteration, and D_4 strike-slip faulting. Peak metamorphic conditions at Tick Hill were determined to be 6.0-7.6 kbar and 720-760°C. The Tick Hill ore body parallels a D_1 foliation truncation plane that coincides with the intersection between two sets of D_3 faults. Gold mineralization formed during two discrete events. Early gold grains and inclusions intergrown with syn-D_{1-2}, peak-metamorphic minerals (i.e. diopside, scapolite and hornblende) indicate an early mineralization episode predating or concomitant with D_1 events. Late gold is hosted within quartz-feldspar mylonite and intensely silicified units, which were affected by D_3 fracturing and associated alteration.

Alteration during early stage mineralization (syn-D_1) involved silicification and the formation of magnetite, concentrated in the hanging wall of the orebody. Late-stage (syn-D_3) mineralization events at Tick Hill are characterized by gold-bismuth selenide assemblages and a paucity of sulphides. Syn-D_3 alteration involved: (1) the destruction of magnetite, (2) the emplacement of abundant laminar quartz veins resulting from the quartz-feldspar alteration overprinting the D_{1-2} mylonitic rocks, and (3) the deposition of proximal albite, hematite, chlorite, amphibole, epidote overprinted by later K-feldspar, sericite, clay minerals and minor calcite. The ore zone is bounded by a strongly silicified zone and surrounded by a chlorite-epidote shell, but late-stage chlorite-epidote alteration also occurs in the proximal zone. D_3 gold events involved a strongly oxidized, S-undersaturated, acidic, saline and hydrous fluid. Chlorite thermometry estimates indicate that the gold was mobilized during D_3 over a wide range of temperatures (380-130°C). The presence of selenides in the ore assemblage suggests that this happened at low pressures (<1 kbar)

In terms of mineralization style, the Tick Hill deposit shares some similarities in alteration characteristics with IOCG deposits in the region. However, its high-grade, gold-only nature, the paucity of copper sulphides, and the presence of Bi-selenides make Tick Hill a unique deposit in the Mt Isa Inlier. Textural evidence suggests that early gold enrichment existed in the area, and that later metasomatic fluids may have mobilized this gold into suitable structural traps during D_3, with a possibility of further gold enrichment.

The stratigraphic sequence at Tick Hill was strongly deformed and intruded by pre-D_1 to syn-D_3 igneous rocks. The igneous rocks and quartzite from the Tick Hill region were dated to constrain the age of the stratigraphy, deformation events, and gold mineralization. LA-ICP-MS, U-Pb zircon ages

combined with field relationships confirm the presence of: (1) 1850-1855 Ma (pre-D_1) granite belonging to the Kalkadoon Supersuite at 4-10 km west of Tick Hill; (2) 1770-1790 Ma (syn D_{1-2}) granite, leucogranite, and quartz-feldspar mylonite in the vicinity of Tick Hill and the surrounding area; and (3) 1520-1525 Ma (syn-D_3) pegmatite and associated hydrothermal activity in the Tick Hill area that resulted in the remobilization of gold. The youngest detrital zircon population from a quartzite unit in the footwall of the deposit yields an age of 1841±15 Ma. The field evidence suggests that the 1770-1790 Ma granites intruded into the sedimentary sequence that hosts gold mineralisation, indicating that the supracustal rocks were formed sometime between ca. 1790-1841 Ma and should not be grouped as Corella Formation, but a new unnamed formation.

At Tick Hill, the Au-rich quartz-feldspar mylonite has $\delta^{18}O_{quartz}$ values of 11.3-13.6‰ that are similar to the $\delta^{18}O_{quartz}$ values of 10.5-13.7‰ from the surrounding lithologies. This similarity implies that $\delta^{18}O_{quartz}$ cannot be used as an exploration tool. The relative narrow range of $\delta^{18}O_{quartz}$ values from different rock units formed during D_{1-3} events in the Tick Hill area most likely reflects the regional fluid conditions at 1520-1525 Ma during the late Isan hydrothermal overprint. The $\delta^{18}O_{quartz}$ values overlap with reported $\delta^{18}O$ values for both metamorphic and igneous fluids. A temperature range of 350-550°C was calculated for the $\delta^{18}O_{quartz}$ and $\delta^{18}O_{calcite}$ results available from the literature, which is consistent with observed alteration assemblages that were associated with the mineralization, and T estimates obtained from alteration chlorite.

The main issue with the Tick Hill deposit is that it is unclear when it originally formed. There is clear evidence that coarse-grained gold mineralisation must have formed relatively early (pre- to syn-D_1) and that the gold was mobile during several of stages of D_3. Earlier studies have interpreted Tick Hill as a gold-rich end-member IOCG deposit, but a wide range of characteristics typical for IOCG deposits do not fit the Tick Hill mineralisation style. Instead, the Tick Hill deposit shares significant similarities with the Au-Bi-Se end-member type for the Au-Cu-Bi deposits hosted in ca. 1850 Ma ironstone in the Tennant Creek Gold field.

Table of Contents

List of Tables

List of Figures

(Se-Po). (c) Zoned coronal reaction rim of stage 3 green chlorite (ch_2), albite and quartz around an early coarse-grained pyrite (py_1). The matrix assemblage preserves earlier, stage 2 chlorite$_1$ (ch_1); the red box shows the area shown in (d). (d) SEM image showing more details of the reaction textures in (c) with early stage 3 albite inter-grown with chlorite$_2$ being replaced by later stage 3 K-feldspar. (e) Inclusion of fine-grained gold inside stage 3, chlorite$_2$ (ch_2). (f) Stage 3, chlorite$_2$ (ch_2) intergrown with epidote (epi). (g) Reflected light image of gold (Au) associated with stage 2 and 3 hematite (ht) after stage 1 magnetite (mt). (h) Stage 4 gold (Au), chalcopyrite (cpy) and bismuth selenide (bse) intergrown with calcite (cal; reflected light). 43

Chapter 1: Introduction

1.1. Context of the Tick Hill gold deposit

The Tick Hill Gold Deposit is situated at 21º38'N - 139º55'E, in the Mary Kathleen Domain in the Mount Isa Inlier (Fig. 1.1), which is a highly mineralized geological terrain with world-class lead, zinc and copper deposits (Withnall and Hutton, 2013). Most major Pb-Zn deposits have been discovered in the western part of the inlier, whilst the bulk of IOCG-style Cu-Au mineralization is concentrated in the eastern part of the inlier. In the central areas of the Mt Isa Inlier (i.e., the Kalkadoon-Leichhardt Belt and Mary Kathleen Domain), where the Tick Hill deposit is located, mineralization appears to be less abundant.
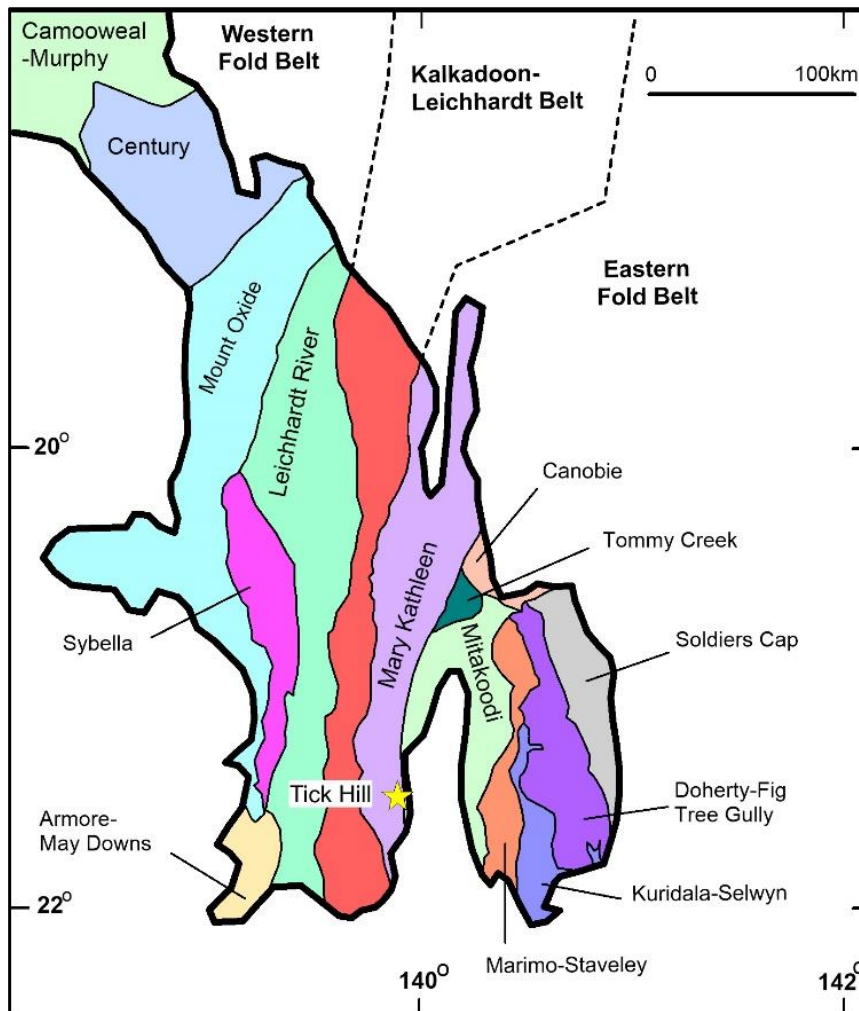
Figure 1.1. Tectonic subdivisions of the Mt Isa Inlier as defined by Withnall and Hutton (2013) showing different domains and the boundaries of the Eastern Fold Belt and Western Fold Belt on either side of the Kalkadoon-Leichhardt Belt.

The Tick Hill gold deposit is a single ore lens deposit that is 140 m long, 1 to 30 m wide, and

extends 320 m down dip (to ~240 m below surface). The high-grade of the deposit, the lack of sulphides and the presence of almost exclusively free gold within upper-amphibolite facies, quartz-feldspar mylonite units, makes Tick Hill a unique gold deposit in the Mount Isa Inlier.

1.2. Exploration and mining history of Tick Hill

The Tick Hill deposit was discovered by Mount Isa Mines Ltd (MIM, formerly Xstrata, now part of the Glencore Group) in October 1989 after follow up of a Bulk Leach Extractable Gold anomaly in a stream sediment sample. Following resource definition, mining commenced in August 1991 and the first gold was poured in December 1991. Open pit and underground mining was done by Carpentaria Gold Pty Ltd and ceased in April 1995. The deposit produced a total of 511,000 ounces of gold from 706,000 tonnes of ore at an average grade of 22.52g/t Au. Metallurgical recovery averaged 97% and production costs were low. In 1998-1999, Cullen in joint venture with MIM re-evaluated the deposit and did extensive exploration in the area without any success. In August 2004, Diatreme Resources Limited (DRX) acquired the right to explore for gold in the Tick Hill area. Further drilling around the deposit was unsuccessful, but a limited gold resource was defined in the waste rock piles around the open pit. In March 2019, the mine was obtained by Carnaby Resources, who commenced renewed exploration in the area in June 2019. Following the acquisition of Tick Hill, Carnaby Resources expanded the Tick Hill Mineral Resource, adding 215,000 tonnes of ore at a grade of 6.52 g/t (equal to 45,100 ounces). Recently, 838,000 tonnes of ore at a grade of 2.41 g/t (equal to 65,000 ounces and) have been added (Carnaby Resources, 2021).

1.3. Historical studies and significance of the Tick Hill deposit

Public information on the Tick Hill deposit is limited to several Honours and MSc theses from the early 1990's, several company reports and a few core logs available on-line (e.g. Tedman-Jones, 1993; Watkins, 1993; Choy, 1994; Rutherford, 1999; Rutherford, 2000; Geological Survey of Queensland, 2015). There is, however, a significant amount of information contained in mostly confidential exploration reports held by MIM and Carnaby Resources, the principle conclusions of which are reviewed below. The most comprehensive and detailed re-evaluation of the deposit was provided by Tedman-Jones (2001).

The Tick Hill ore body is hosted in fractured and silica-hematite-altered gneiss (Tedman-Jones, 2001). The principle host rock to mineralization is a metasomatised quartzo-feldspathic mylonite that was labelled "galahstone" to denote its laminated pink and grey appearance. It was derived from sheared quartz-feldspar porphyry, pegmatite and/or calc-silicate metasediments (e.g., Laing, 1992; Tedman-Jones, 2001). To emphasise the metasomatic overprint of the mylonite and the presence of thin quartz-feldspar alteration selvedges along the mylonitic fabric, Laing (1992) proposed the term "quartz-feldspar

laminite". In a later review of drill core, Tedman-Jones (2001) described the pervasive occurrence of dilation fractures and thin sheeted partings along S_1 mylonite planes, and linked it to the introduction of K-Na feldspar metasomatism and gold.

Tedman-Jones (2001) noted that the high-grade ore zone is associated with the formation of north-northeast- to east-trending fractures, and the ore zone stopped abruptly at the northern end of the open pit where the "galahstone" terminated against an east-trending structure. The mineralization also pinches out at depth as the main foliation, which dips 55° to the west in the upper drives, switches to a northerly dip observed on the two lowest mine levels (130 and 117 mRL). On these levels, coarse-grained gold was mined from fault hosted chlorite-hematite-carbonate breccia veins that formed the keel of the ore zone, and the breccia veins possibly acted as feeder structures (Tedman-Jones, 2001). Laing (1992) and Tedman-Jones (2001) further noted that east (085°)-trending zones of more extensive dilation appear to occur at 10 m intervals across the deposit, and that these fractures are characterized by pervasive pink and red feldspar fill and associated alteration.

Following the discovery of the Tick Hill deposit in 1989, extensive exploration led by MIM failed to locate an economic resource beyond the original discovery. Most exploration for Tick Hill-style mineralization was premised on the assumption that gold mineralization related to early, ductile (D_1 or D_2) deformation events (Tedman-Jones, 2001). Because gold was described as being associated with the peak metamorphic assemblage (e.g. Choy, 1994; Oliver, 1998), it was suggested that the main stage of mineralization was early (1750-1740 Ma), and possibly followed by later remobilization (e.g. England, 1993; Choy, 1994; England, 1995; Oliver, 1995). In developing an exploration strategy, it was proposed that gold mineralization was deposited from saline oxidized fluids into a dilatant brittle-ductile ramp structure within a flat lying extensional decollement of D_1 origin (e.g. Oliver, 1998). In the Tick Hill area, it was assumed that the hanging wall and footwall quartzite units were the metasomatic expressions of the decollement, and thus the controlling structures (Tedman- Jones, 2001). This approach did not lead to further gold discoveries.

The possibility that gold mineralization was related to later deformation events (D_3 or D_4) was also suggested (e.g. Laing, 1992; Tedman-Jones, 2001). In 1998-1999, Cullen in joint venture with MIM investigated late stage mineralization concepts, and focused on a possible association between gold, porphyry systems and red rock alteration associated with brittle structures (Tedman-Jones, 2001), but again this work did not lead to further discoveries.

The MIM exploration efforts were reviewed by Tedman-Jones (2001) and Johnson (2002) who concluded that gold mineralization was introduced by late, relatively low temperature, oxidized hydrothermal brines. Tedman-Jones (2001) linked the mineralizing fluids to a granite intrusion at depth, immediately southwest of the Tick Hill deposit. Evidence for an intrusive source comes from

geophysical interpretations (Nano, 1999) supported by oxygen isotope studies (Hannan, 1994). Aeromagnetic data obtained by MIM in the late 1990s showed that the Tick Hill orebody is located at the northeastern margin of a 3 × 2 km oval shaped zone of magnetic depletion interpreted to be the expression of a concealed intrusion (Nano, 1999). Hannan (1994) reported a narrow range of $\delta^{18}O_{VSMOW}$ values (+10.2 to +12.9‰) for quartz separates from Tick Hill mine (ore zone and altered surrounding rocks) and suggested that gold formed from a single fluid over a narrow temperature range close to ~450°C. A similar range of quartz $\delta^{18}O$ values from the ore zone was reported by Choy (1994), who also suggested a granitic source for the fluids.

Available research data and the interpretations derived from that are at times contradictory, which suggests that the Tick Hill deposit could be more complex and the result of more than one control. At this point, there is too little information on the deposit available in the public domain. Hence, this study has been conducted with the aims to understand the geological characteristics and the mineralization style of the deposit as following.

1.4. Rationale and thesis objectives

This PhD project aims to (1) characterizes the geological-structural setting of the Tick Hill deposit; (2) clarify the mineralization style for the deposit; and (3) constrain the timing of mineralization. To achieve these goals, I have set objectives and methods as summarized in Table 1.1.

Table 1.1. Objectives and study methodologies applied for the Tick Hill project

Objective	Methodology
1. Establish the structural - geological framework of the deposit involving: • geology of the deposit and its immediate surroundings • deformation-intrusive scheme relative to mineralization • structures, intrusive phases and the relative timing of the geological events	A. Literature review B. Mapping the pit walls where possible C. Mapping the geology and structures surrounding the deposit D. Structural-lithological-alteration logging of oriented cores if available
2. Characterize the mineralization style including alteration and mineralization mineralogy, ore texture and paragenesis	A. Pit mapping and core logging B. Petrography using microscopy C. Mineral geochemistry investigation using SEM and EPMA
3. Geochemically study the ore and alteration minerals and calculate the P-T conditions	A. Petrography using microscopy B. Geothermobarometry using mineral geochemistry data
4. Defining the sources of ore-bearing fluids	A. Quartz oxygen isotope analyses focusing on Au-rich samples, alteration rock and intrusive units
5. Dating and characterization of selected samples to establish the timing of deformation, as well as intrusive and mineralization events	A. Dating intrusive and deformation phases using LA-ICP-MS U-Pb zircon technique B. Laser ablation ICP-MS (LA-ICP-MS) zircon trace element analysis C. Major and trace element study on selected rock types

1.5. Thesis structures and authorship

This thesis is organized following the standard criteria advised by the Graduate Research School of James Cook University. At the time of thesis submission, Chapters 2 has been published in the Ore Geology Reviews journal while Chapter 3 are under review in Precambrian Research journal. Chapter 5 and 6 are under review in the Australian Journal of Earth Sciences. These four manuscripts have been reformatted to comply with the thesis format. The thesis has been divided into seven chapters, with the structure as following:

1.5.1. Chapter 1

The introductory Chapter 1 provides a general background to the Tick Hill deposit including the context of the deposit, the historical exploration activities and studies, the aims and methods used in this study and the structure of the thesis.

The original idea for this thesis was proposed by Rick Valenta and the Geological Survey of Queensland to record the history and nature of the Tick Hill deposit in the formal literature.

1.5.2. Chapter 2

Chapter 2 entitled "*Geological setting and mineralization characteristics of the Tick Hill Gold Deposit*" presents the geological and structural-metamorphic setting in relation to the orebody geometry. The chapter also presents the mineralization-alteration characteristics of the Tick Hill deposit.

This chapter has been published in the Ore Geology Reviews as "Le, T.X., Dirks, P.H.G.M., Sanislav, I.V., Huizenga, J.M., Cocker, H., Manestar, G.N., 2021. *Geological setting and mineralization characteristics of the Tick Hill Gold Deposit, Mt Isa Inlier, Queensland, Australia*. Ore Geology Reviews. 137:104288.

The work presented in this chapter is based on fieldwork, core logging and petrography commenced in late 2017. Fieldwork was done by Truong Le, with assistance from Paul Dirks and Ioan Sanislav. Core logging, rock and thin section descriptions were performed by Truong Le with assistance from Paul Dirks and other co-authors including Ioan Sanislav, Jan Huizenga, Helen Cocker and Grace Manestar. Paul Dirks assisted with the development of the approach, interpretation of results and editing. Early versions of this chapter were edited by Kaylene Kamuti whilst later versions were edited by Paul Dirks. Peter Rea, Alex Brown, Paul Tan, Brett Davis and Rob Watkins provided support for fieldwork and access to drill cores and data sets. Nick Oliver and Peter Rea donated Tick Hill samples for this study. Kevin Blake and Shane Ankew provided assistance in SEM and EPMA analyses.

1.5.3. Chapter 3

The Chapter 3, entitled "*Geochronological constraints on the geological history and gold mineralization in the Tick Hill region, Mt Isa Inlier*", presents U-Pb zircon ages and whole-rock geochemistry for a range of igneous rocks in the Tick Hill area. These new ages constrain: (1) the timing of igneous events in the area; (2) the age of sequences in the area including rock units that host the Tick Hill deposit; and (3) the timing of deformation and mineralization events in the area.

The chapter has been submitted to Precambrian Research as "Le, T.X., Dirks, P.H.G.M., Sanislav, I.V., Huizenga, J.M., Cocker, H., Manestar, G.N., 2021. *Geochronological constraints on the geological history and gold mineralization in the Tick Hill region, Mt Isa Inlier"*. The manuscript is currently under review, and review comments have been incorporated in the thesis.

Fieldwork was done by Truong Le, with assistance from Paul Dirks and Ioan Sanislav. Core logging, rock and thin section descriptions and geochronological analysis were performed by Truong Le with assistance from co-authors including Paul Dirks, Ioan Sanislav Jan Huizenga. Paul Dirks assisted with the development of the approach, interpretation of results and editing. In addition, Peter Rea, Paul Tan, Brett Davis, and Rob Watkins assisted in fieldwork, access to drill core and data sets. Nick Oliver donated Tick Hill samples for this study. Yi Hu, Huang Huiqing, Ioan Sanislav, Helen Cocker and Grace Manestar helped with LA-ICP-MS zircon dating. Kaylene Camuti edited early versions of the manuscript.

1.5.4. Chapter 4

Chapter 4 is entitled "*Trace element geochemistry for zircon used in geochronology*". This chapter explores the geochemistry of the (1) zircon aged ca. 1780-1770 Ma from igneous and intensely silicified units and (2) zircon aged ca. 1600-1520 Ma from pegmatite veins, with the aim to discriminate the zircon populations and constrain the zircon sources.

The work was done by Truong Le with assistance from Paul Dirks in interpretation of results and editing. Ioan Sanislav, Yi Hu, and Huang Huiqing helped with LA-ICP-MS analysis and data processing.

1.5.5. Chapter 5

Chapter 5 is titled "*Mineral chemistry and P-T conditions*". This chapter presents the results of mineral geochemistry obtained by SEM and EPMA to determine the compositions of the various mineral assemblages formed during metamorphic and mineralization events. The chapter also provides the P-T conditions for metamorphism and hydrothermal alteration using various geothermobarometers.

This chapter has been submitted to the Australian Journal of Earth Sciences as "Le, T.X., Dirks, P.H.G.M., Sanislav, I.V., Huizenga, J.M., Cocker, H., Manestar, G.N., 2021. *Mineral geochemistry and geobarothermometry at Tick Hill Gold Deposit, Mt Isa, Queensland, Australia*" that is currently under review.

The supervisory team assisted in the development of concepts and ideas presented in this chapter. The work was done by Truong Le with assistance from Paul Dirks in analyses, interpretation of results and editing. Kevin Blake and Shane Ankew provide assistance in SEM and EPMA analyses.

1.5.6. Chapter 6

Chapter 6 is entitled "*Oxygen isotope data for quartz from Tick Hill and surrounding rocks*". The chapter presents the $\delta^{18}O_{quartz}$ composition from various rock types in the Tick Hill area, focusing on Au-rich quartz-feldspar mylonite units, with the aim of determining the $\delta^{18}O_{quartz}$ signatures of Au-rich units in comparison with the host rocks and igneous units.

This chapter has been submitted to the Australian Journal of Earth Sciences as "Le, T.X., Dirks, P.H.G.M., Sanislav, I.V., Harris, C., Huizenga, J.M., Cocker, H., Manestar, G.N., 2021c. *Quartz oxygen isotopes from Tick Hill Area in Mt Isa Inlier - indication of a regional fluid overprint*" that is currently under review.

Truong Le developed the concept with consultation from the supervisor team. Chris Harris assisted in sample analysis, whilst Paul Dirks assisted in interpretation of results and editing.

1.5.7. Chapter 7

Chapter 7 is the "*Summary and conclusions*" chapter that presents a summary of the key findings and conclusive discussions for the Tick Hill project, including the geological setting, structural-metamorphic setting and its constrains on mineralization, and the timing of mineralization. The chapter also summarizes and discusses the mineralization-alteration characteristics (i.e. ore and alteration mineralogy, ore forming conditions and mineralization styles) and the exploration implications for similar deposits in the area.

1.5.8. Appendices

Appendices 1-10 contain supplementary materials in support of this thesis. The following table provides a summary on the materials attached as appendices to this thesis.

Table 1.2. List of appendices

Oder	*Appendix title*	*Linked chapter*
Appendix1	*Data for TH007: core photos, hyperspectral (Hy-logger) and assay data* presents hyperspectral data in combination with core photos and assay data to show any possible linkage with mineralization	*Chapter 2*
Appendix 2	*Data base of historical geochronology in the Mary Kathleen Domain* shows geochronological results that have been published in journals or uploaded in QDEX or Australian GeoScience, between 1978 and 2019.	*Chapter 3*
Appendix 3	*LA-ICP-MS data for zircon geochronology* present LA-ICP-MS data from 1198 analyses for 16 samples (listed in Table 3.2, Chapter 3), and 566 analyses for standard samples.	*Chapter 3*
Appendix 4	*Cathodoluminescence images for zircon* from 16 samples that have been shown in this appendix. The (near-) concordant analyses for the youngest zircon population (listed in Table 3.2, Chapter 3) are marked by analysis location and spot number.	*Chapter 3*
Appendix 5	*Trace element geochemistry for zircon* showing the LA-ICP-MS trace element compositions of zircon from of four main groups that has been dated in Part 3, including: Group 1 hydrothermal zircon from syn-D_3 pegmatite aged 1520-1525 Ma (n = 51); Group 2 inherited zircon aged 1550-1600 Ma from syn-D_3 pegmatite (n = 15); Group 3 magmatic zircon aged 1770-1780 Ma obtained from syn-D_{1-2} intrusive granites (n = 55); and Group 4 zircon from the hanging wall quartzite aged ca. 1780 Ma (n = 14).	*Chapter 4*
Appendix 6A	*Data of SEM and EPMA mineral analyses* presents the composition of minerals from 6 samples. A list of tables for compositions of different minerals have been included.	*Chapter 5*
Appendix 6B	*Images of SEM and EPMA mineral analyses* show the microscope and SEM images of minerals from 6 samples selected for SEM and EPMA analyses. The details for spot analysis numbers and its locations are shown in each image.	*Chapter 5*
Appendix 7	*Sample list* with information for 176 samples that were selected for different types of analyses, including petrological microscope (thin section), geochronology, geochemistry and oxygen isotope. A map of sample locations is included.	*General database*
Appendix 8	*Sample images* for 176 samples that have been selected for different types of analyses, with close-ups for Au-rich locations and geological features of interest.	
Appendix 9	*Drill logs* present the logs for 27 drill holes that were completed during 2018-2019 field campaigns. A list and a map of drill holes that were logged have been included.	
Appendix 10	*Bibliography of exploration reports and data*. This appendix provides a list of reports and data collected for this study.	

Chapter 2: Geological setting and mineralization characteristics of the Tick Hill Gold Deposit, Mount Isa Inlier, Queensland, Australia

Abstract

The high grade (~22.5 g/t), gold-only Tick Hill deposit presents a unique mineralization style in the Mt Isa Inlier. The deposit was mined in the early 1990s, and is hosted in biotite schist, calc-silicate gneiss, quartzite and quartzo-feldspar mylonite. These rocks were affected by D_1 shearing and D_2 upright folding at high-grade metamorphic conditions, followed by D_3 normal faulting with widespread quartz-feldspar alteration and D_4 strike-slip faulting. The Tick Hill ore body is linear in shape and paralleled the D_1 mineral elongation lineation, and the intersection lineation between sets of D_3 faults. Gold is dominantly hosted within intensely silicified units affected by D_3 fracturing and associated alteration. Some gold grains are contained within syn-D_1, peak-metamorphic minerals indicating that mineralization involved two separate events; an early event predating or concomitant with D_1 when gold was first introduced and concentrated, and a second event during D_3 when gold was remobilized and/or further enriched to be deposited in its final configuration. Mineralization at Tick Hill is characterized by coarse grained gold associated with Bi-selenides, minor sulfides, and a general paucity of other metals except for a slight enrichment of Cu in the footwall to the ore zone. Alteration is characterized by early silicification and magnetite alteration that formed during the initial D_{1-2} events and may have coincided with the first stage of gold enrichment. During syn-D_3 mobilization of gold, alteration involved the destruction of magnetite, the emplacement of abundant laminar quartz veins, and the deposition of proximal albite, hematite, chlorite, amphibole, epidote overprinted by later K-feldspar, sericite, clay minerals and minor calcite. The ore zone is bounded by a strongly silicified zone and surrounded by a chlorite-epidote shell. The low pressure (< 1 kbar) D_3 gold mobilization event involved an oxidized, S-under-saturated, acidic, saline aqueous fluid. In terms of alteration characteristics, the Tick Hill deposit shares similarities with IOCG deposits in the area. However, its high-grade gold-only nature, lack of Cu, and the presence of Bi-selenides makes it a unique deposit in the Mt Isa Block. Textural evidence suggests that early gold enrichment existed in the area, and that later metasomatic fluids may have mobilized this gold into suitable structural traps during D_3.

2.1. Introduction

The Mesoproterozoic (1900-1500 Ma) Mt Isa block is one of Australia's foremost mineral provinces and is famous for its world-class SEDEX-type, Cu-Pb-Zn-Ag (e.g. Mt Isa mine; Huston et al., 2006), structurally modified and metamorphosed SEDEX (e.g. Dugald River, Cannington; Xu, 1996; Walters and Bailey, 1998) and Cu-Au IOCG deposits (e.g. Ernest Henry; Mark et al., 2006). In addition to these, there are many other large deposit including Mo (e.g. Merlin; Babo et al., 2017), Co (Walford

Creek; Aeon Metal Limited, 2017), REE/U (Mary Kathleen; Oliver et al., 1999) and gold-rich IOCG's deposits (e.g. Starra; Duncan et al., 2014).

The Mt Isa block also represents one of the most extensively altered terrains on Earth exemplified by widespread albite-hematite-scapolite-epidote alteration, which is linked to the remobilization of evaporite deposits during various deformational and intrusive events (e.g. Oliver et al., 1994; Oliver, 1995; De Jong and Williams, 1995; Withnall and Hutton, 2013). This alteration is accompanied by widespread brecciation, and the syn- to post-tectonic emplacement of both felsic and mafic intrusions (e.g. Oliver, 1995; Oliver et al., 2008). The alteration and brecciation are characteristic features of the IOCG deposits in the Mt Isa Block (Williams et al., 2005) and are hallmarks for many of the other deposit types as well.

Whilst Cu-Au deposits are common in the Mt Isa block, especially in the higher grade and more strongly deformed Eastern Fold Belt (Fig. 1.1, Chapter 1), gold grades in such deposits rarely exceed 1-2 g/t, and gold-rich deposits are rare (e.g. Duncan et al., 2011; Denaro et al., 2013). One notable exception to this is the Tick Hill gold deposit in the southern part of the Mary Kathleen Domain (MKD; Fig. 1.1, Chapter 1). Although the Tick Hill deposit presents a mineralization style of great interest to exploration companies, little is known about the deposit other than that it is a gold-rich, shear-hosted hydrothermal deposit (Denaro et al., 2013) that has been interpreted as a possible end-member IOCG deposit (e.g. Groves et al., 2010). Tick Hill was discovered in 1989, and was mined over a short period of time (1991-1994). Apart from several student theses (Tedman-Jones, 1993; Watkins 1993; Choy, 1994) no detailed studies have been published on the deposit or its style of mineralization.

The high-grade Tick Hill deposit is situated in high-grade metamorphic rocks and characterized by the occurrence of free gold with little to no silver and a paucity of sulphides and associated metals (e.g. Cu, Co). As such, Tick Hill is a unique gold-rich deposit in the Mount Isa Inlier, which was highly profitable when mined. This study provides an overview of the geological setting and mineralization style of the Tick Hill deposit based on mapping, core logging and petrography. It aims to present details on the orebody geometry in relation to lithological and structural-metamorphic controls, together with a characterization of the gold mineralization and associated alteration.

2.2. Geological setting

2.2.1. Regional geological setting

The Mount Isa Inlier in northwest Queensland exposes complexly deformed, strongly altered and extensively mineralized, mid-Proterozoic rocks that comprise at least three separate basinal sequences (originally referred to as Cover Sequences 1 to 3; Blake, 1987) deformed by two orogenic cycles

(Etheridge et al., 1987; Foster and Austin, 2008). The inlier was originally sub-divided into three, north-trending tectonic units including the Western Fold Belt, the central Kalkadoon-Leichhardt Belt and the Eastern Fold Belt (Day et al., 1983), to delineate large-scale subdivisions with broadly similar tectono-stratigraphic histories. These subdivisions were further split into a series of geological domains based on stratigraphic, structural and geochronological similarities (Fig. 1.1, Chapter 1; Withnall and Hutton, 2013). Thus, the Eastern Fold Belt, which occurs east of the Kalkadoon-Leichardt Domain, comprises eight domains including the MKD that hosts the Tick Hill deposit (Fig. 1.1, Chapter 1). To the west, the metasedimentary rocks of the MKD uncomfortably overlie rocks of the Kalkadoon-Leichhardt Domain (Withnall and Hutton, 2013). To the east, the MKD is separated from the rest of the Eastern Fold Belt by the Pilgrim fault in the south and the Rose Bee fault in the north (Withnall and Hutton, 2013).

The Tick Hill deposit is situated in the southern part of the MKD. This part of the MKD is relatively poorly studied and stratigraphic and tectonic interpretations for rocks around Tick Hill largely rely on lateral correlations with better studied rocks further north (e.g. Passchier, 1986, 1992; Passchier and Williams, 1989; Holcombe et al., 1991; Neumann et al., 2009; Carson et al., 2011; Withnall and Hutton, 2013; Kositcin et. al., 2019). In the central part of the MKD, gneiss of the Kalkadoon-Leichhardt complex, and overlying mafic and felsic volcanics of the Magna Lynn metabasalt unit, and the 1770-1780 Ma Argylla Formation (e.g. Page, 1978; Foster and Austine, 2008, Neumann et al., 2009; Fig. 2.1), form basement to unconformably overlying shallow water sediments (e.g. Witnall and Hutton, 2013). These consist of the ca. 1755 Ma Ballara Quartzite and extensive deposits of the 1738-1750 Ma Corella Formation (Blake et al., 1982; Foster and Austin, 2008; Neumann et al., 2009; Withnall and Hutton, 2013; Kositcin et. al., 2019; Fig. 2.1). In the central MKD, the Corella Formation is composed of shallow marine sediments, including scapolitic-bearing calc-silicate, para-amphibolite, calcite marble, metapelite, quartzite and other metasedimentary units with minor felsic and mafic metavolcanics (Blake, 1987; Foster and Austin, 2008). The correlative stratigraphic unit of the Corella Formation in the area around Tick Hill has not been dated directly and its age has been interpreted (e.g. Wyborn 1997; Foster and Austin, 2008). Intrusions in the southern MKD have been grouped into granites assigned to the ca. 1740 Ma Burstall-Wonga suite (e.g. Monument syenite, Saint Mungo granite, Birds Well granite and Tick Hill granite; Fig. 2.2) and Kalkadoon batholith, which mostly occurs to the W of Tick Hill (e.g. Blake et al., 1982; Wyborn, 1997; Withnall and Hutton 2013).

The metamorphic and deformational history of the MKD involved four major deformational events (D_1 to D_4; e.g. Passchier and Williams, 1989; Holcombe et al., 1991; Oliver, 1995). The early D_1 event (1750-1730 Ma) is thought to be extensional in nature and has been linked to an early gneissic fabric exposed in high strain zones along the central part of the MKD termed the Wonga-Shinfield zone (Passchier and Williams, 1989; Holcombe et al., 1991). Upright folding occurred during D_2 and was originally interpreted to relate to the main stage of the Isan Orogeny around 1590-1550 Ma, when peak

metamorphic conditions were attained (e.g. Page, 1983; Passchier and Williams, 1989; Holcombe et al., 1991; Oliver, 1995). More recently, however, Spence et al. (2020) have shown that D_2 upright folding in the central MKD took place before 1710 Ma. The D_2 deformation resulted in the development of upright, tight, north-trending folds with an axial planar cleavage, a penetrative S_2 fabric, and steep east-dipping reverse faults parallel to F_2 fold axial planes (e.g. Holcombe et al., 1991; MacCready et al., 1998). D_3 events marked a change from ductile to brittle deformation and led to the formation of a fault network (O'Dea et al., 1997; Betts et al., 2006). In the southern MKD, the Wonga-Shinfield zone was offset by a series of northeast and northwest striking D_3 faults in response to east-west compression (Forrestal et al., 1998). D_3 events were coeval with the regional emplacement of the Wimberu/Williams granite plutons (1530-1500 Ma; Foster and Austin, 2008) to the east and related regional albite-hematite-alteration (Wyborn et al., 1988). D_4 events involved brittle reactivation of older fault zones at shallow crustal levels, at temperatures less than 350-400ºC, with the age of deformation ranging from 1500 Ma to 1100 Ma (e.g. Oliver, 1995).
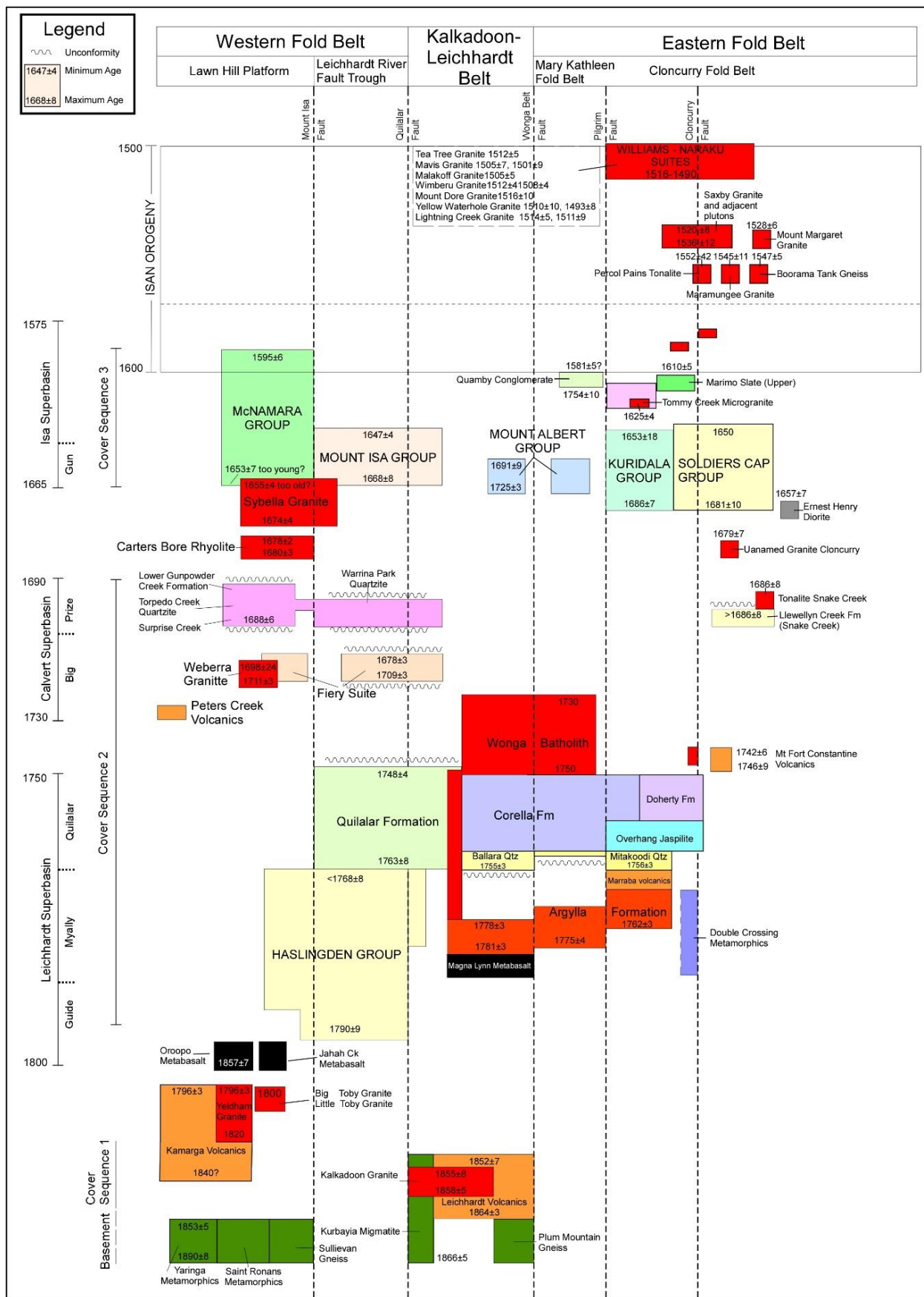
Figure 2.1. Chronostratigraphic time-space plot for the Mt Isa Inlier (after Foster and Austin, 2008; Withall and Hutton, 2013).
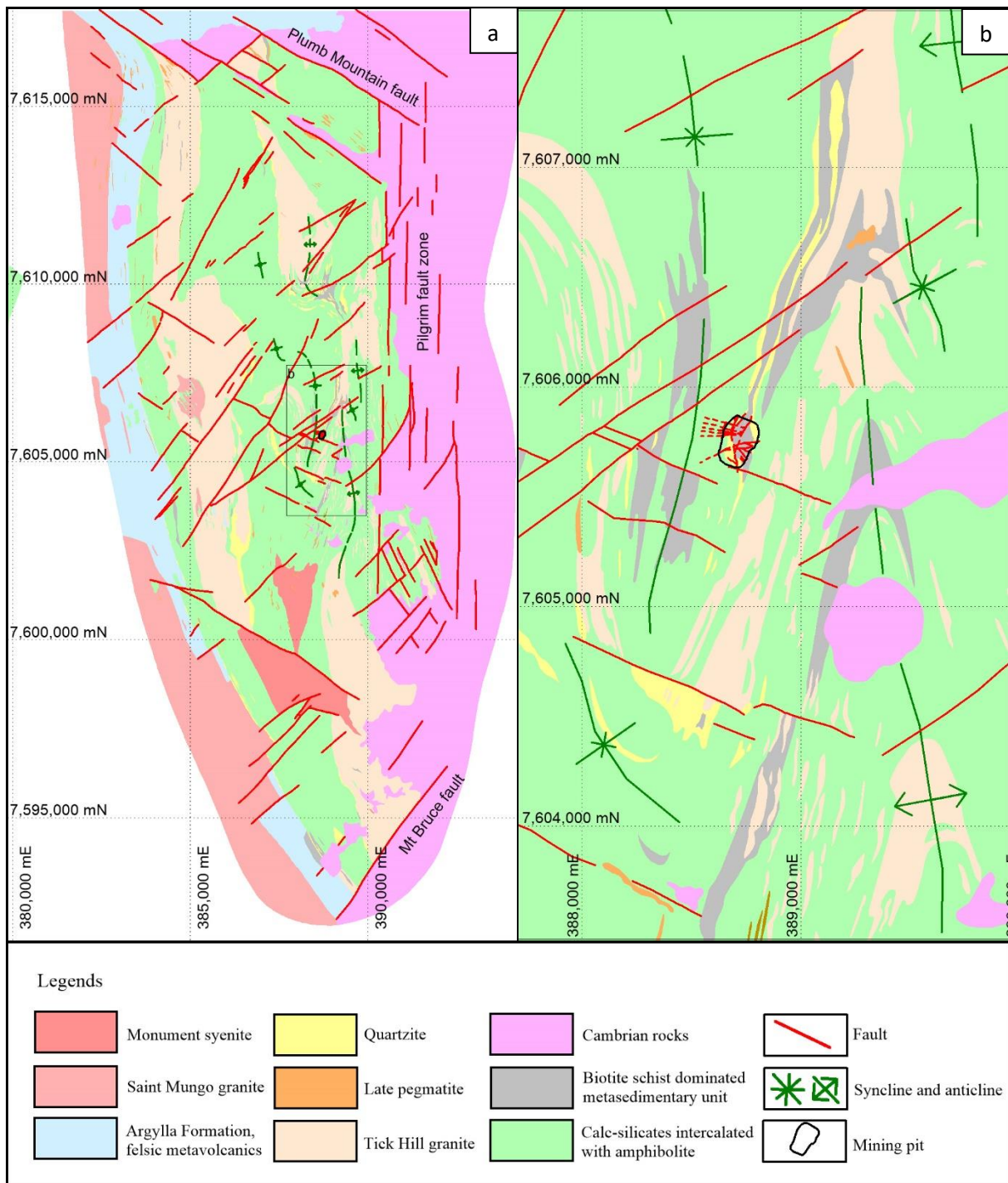
Figure 2.2. (a) Geological map of Tick Hill Area with (b) a close-up of the Tick Hill Syncline. Note that the calcsilicate, amphibolite, biotite schist and quartzite units were interpreted as the Corella Formation while the felsic metavolcanics were assigned to the Argylla Formation (adapted from Wyborn, 1997; Rutherford, 2000).

2.2.2. Geological setting of the Tick Hill Area

The Tick Hill area is underlain by rocks mapped as Corella Formation bounded in the east by the Pilgrim fault and in the west by granitic gneiss of the Saint Mungo granite overlain by Argylla Formation (Coughlin, 1993; Wyborn, 1997). To the north, the area is bounded by the northwest-trending Plumb

Mountain fault and to the south by the northeast-trending Mt Bruce fault (Forrestal et al., 1998; Fig. 2.2a). The rocks of the Corella Formation were intruded by syn- to post-tectonic granite plutons and pegmatites of the Tick Hill Complex (Wyborn, 1997) and Monument Syenite (Fig. 2.2a, Rutherford, 2000). Cambrian rocks outcrop to the east of the Pilgrim fault and are locally preserved as erosion remnants overlying the Corella Formation to the east of the Tick Hill pit (Fig. 2.2a).

Detailed mapping of the Tick Hill Area and the surrounding geology during exploration by MIM (Fig. 2.2; Coughlin, 1993; Rutherford, 2000) led to the development of a D_1 to D_4 deformation sequence that was linked to the regional tectonic framework further north. Around Tick Hill, D_1 refers to the development of the mylonitic gneissic fabric that hosts the Tick Hill deposit. The mylonite formed along a north-trending belt, west of the Pilgrim fault, and is characterized by a prominent S_1 foliation with a westerly dip (around 280/60; all orientation measurements for planes are presented as dip direction/dip) and a well-developed steeply southwest pitching mineral lineation and/or rodding lineation (L_{1x}). The fabric is defined by oriented hornblende-plagioclase-clinopyroxene assemblages in metabasalt and silimanite-biotite-scapolite in meta-sediments. Numerous quartzo-feldspathic horizons and sheared leucogranite layers suggest the presence of abundant granite melt pockets, either formed as the result of local migmatisation, granite intrusions or both (Fig. 2.2). Intrafolial folds and sheath folds in the mylonitic fabric can be observed on centimeter to meter scale, and in places several overprinting generations of intrafolial folds have been described (e.g. Choy, 1994; Oliver, 1998). F_1 fold axes associated with the intrafolial folds are commonly parallel to the mineral lineation. The D_1 high strain fabric has been linked to the Shinfield-Wonga belt north of Tick Hill (Oliver, 1998). By inference, this fabric was interpreted as an expression of the ca. 1740 Ma, mid-crustal extensional shear zone (e.g. Oliver, 1998). The D_1 mylonites were folded during D_2 in a series of km-scale, tight, asymmetric upright folds. The Tick Hill deposit is situated in the eastern limb of one such large D_2 syncline (the Tick Hill syncline; Fig. 2.2b), which has an axial planar trace that largely parallels the D_1 gneissic fabric (Choy, 1994). The D_2 folds tighten and intensify west of the Tick Hill pit, where they become transposed in a north-trending high strain zone that parallels the S_1 fabric, suggesting that D_1 and D_2 events may be expressions of a single, progressive shearing event (Laing, 1993). D_2 folds open up towards the Pilgrim fault to the east. Later deformation events (D_3 and D_4) were described as northwest- and northeast-trending normal fault sets with associated red rock alteration (Tedman-Jones, 2001). The main D_3 structures bound the Tick Hill Area to the north and south (Fig. 2.2). Within the deposit, D_3 is manifested as an interconnected network of fractures and veins with associated quartz-feldspar alteration and gold mineralization (Tedman-Jones, 2001). D_4 deformation includes a series of strike-slip faults that trend northeast, and offset the D_1 Tick Hill gneiss fabric and D_2 fold axes (Coughlin, 1993), and overprinted the D_3 red rock alteration (Tedman-Jones, 2001).

2.3. Geological framework for the Tick Hill Deposit

The deformation scheme and lithological descriptions presented here are based on mapping of the Tick Hill pit in November 2017, together with drill core logging of a limited number of available cores, and petrological studies. This is augmented with regional maps compiled by MIM in the 1990's (Fig. 2.2; Coughlin, 1993; Rutherford, 2000).

2.3.1. Lithological units in Tick Hill Pit

The host rocks to the Tick Hill deposit as exposed in the pit and its immediate surroundings, consist of gneissic and schistose units that have been interpreted as part of the Corella Formation (e.g. Coughlin, 1993; Choy, 1994; Wyborn 1997, Figs. 2.2, 2.3). They include from west to east (i.e. from hanging wall to footwall): (1) a hanging wall calc-silicate unit interlayered with amphibolite gneiss, (2) hanging wall quartzite, (3) a central metasedimentary unit dominated by biotite schist, (4) footwall quartzite, and (5) footwall calc-silicate interlayered with amphibolite gneiss. The ore zone is largely contained within the central biotite schist unit, where it is interlayered with quartzo-feldspathic gneiss that is similar in composition as the nearby Tick Hill Granite Complex (Chapter 3) and probably of intrusive origin. The origin of the quartzite ridges is uncertain, and most exploration reports refer to them as metasomatic alteration zones, rather than sedimentary units, citing their cross-cutting, discontinuous nature (e.g. Laing, 1993; Coughlin, 1993; Oliver, 1998). All units are truncated by weakly deformed quartz and pegmatite veins. The distribution of the various lithologies in the pit is presented in Fig. 2.3 and the peak-metamorphic mineral assemblages in each rock unit are listed in Table 2.1.

Hanging wall calc-silicate interlayered with amphibolite gneiss

This unit is well-exposed in the west wall of the pit, and in many drill cores. The unit comprises banded or laminated gneissic calc-silicate and amphibolite, interbedded with lesser biotite schist, and can be sub-divided into amphibolite, amphibole-rich calc-silicate, calc-silicate, and magnetite-rich calc-silicate sub-units (Fig. 2.4).

The gneissic amphibolite sub-unit is best exposed along the top benches of the open pit where it overlies calc-silicate (Fig. 2.3a). The amphibolite is strongly foliated, with the foliation defined by oriented hornblende, which comprises ~50-80% of the rock (Figs. 2.4a, 2.5a). Other minerals include plagioclase, scapolite, quartz, magnetite, actinolite, garnet and accessory minerals including zircon and apatite (enclosed in quartz). Locally, the amphibolite sub-unit displays variations in composition on m-scales, with quartz-rich (>10% quartz) amphibolite horizons alternating with plagioclase-rich or calc-silicate-rich horizons.
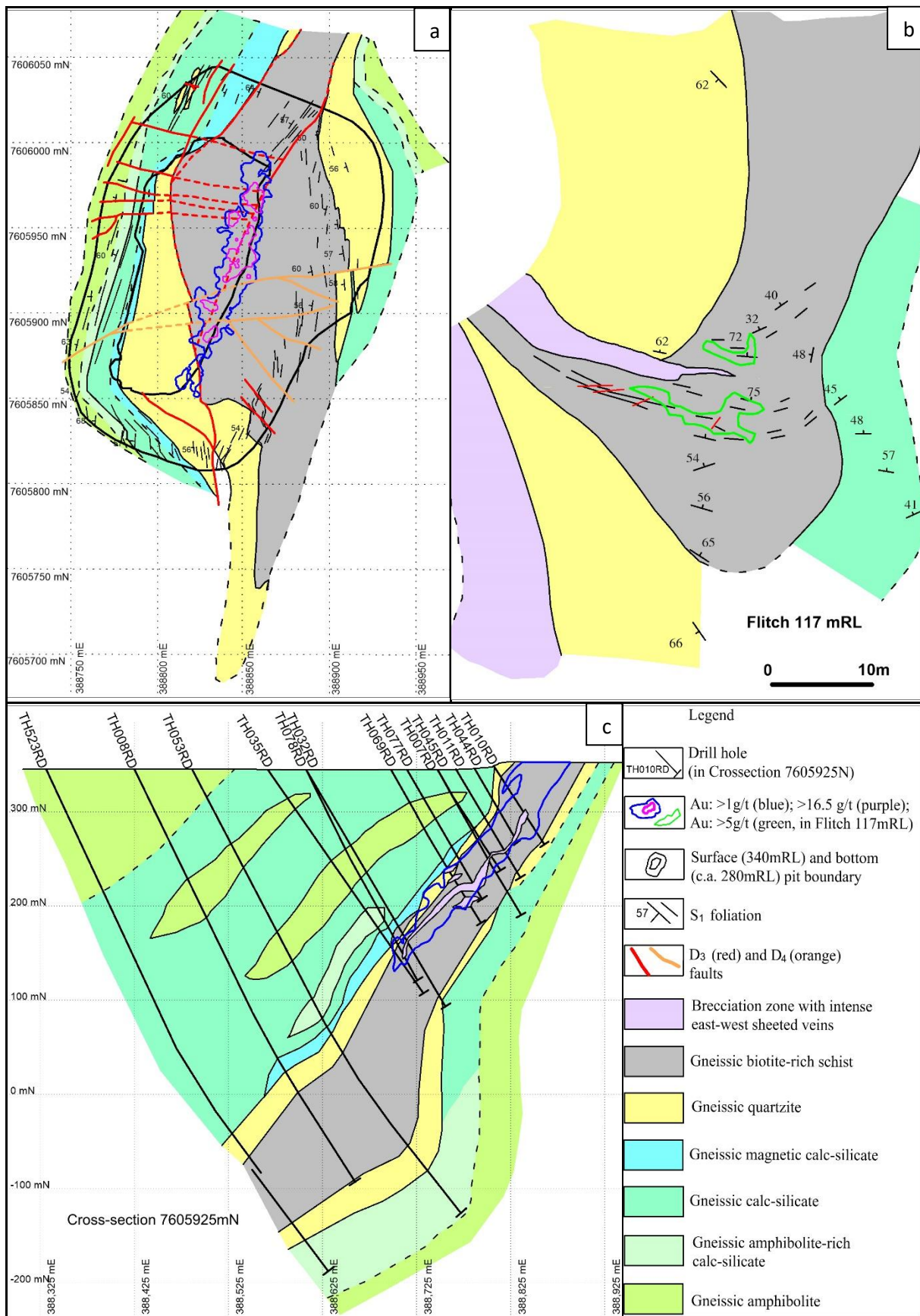
Figure 2.3. Geology of the Tick Hill deposit. (a) Geological map of Tick Hill Pit as exposed in November 2017. The surface elevation responds to mine level 340 mRL; (b) Underground geological map of level 117 mRL towards the base of the mine, showing folded layering and a shift of the ore zone from a north-

northeast trend at surface to an east-trend (adapted from MIM, 1993); (c) Cross-section 7605925 mN showing the lithological host rocks in spatial relationship with the 1g/t ore envelope and brecciation zones. Drill holes are projected onto the section from 20m north and south (adapted from Downs, 2000). The 1g/t ore envelope is hosted in biotite schist and hanging wall quartzite. Brecciation with emplacement of east-west sheeted veins coincided with the ore envelope.

The gneissic calc-silicate sub-unit (Fig. 2.4b) constitutes the bulk of the rock in the sequence above the hanging wall quartzite, and is well-exposed in the west wall of the pit (Fig. 2.3a). The general composition of the calc-silicate is feldspar (40-60%), scapolite (20-35%), quartz (10-15%), magnetite (<3-4%) and variable amounts of hornblende, actinolite and chlorite (e.g. Fig. 2.5b). The scapolite content is highly variable from one layer to the next. Where scapolite is most abundant it preserves a spotty texture, with individual grains aligned within the foliation. Hornblende occurs in discontinuous patches along the mylonitic foliation and locally defines the mineral lineation (Fig. 2.4b). Amphibole-rich layers consisting of quartz-feldspar-amphibole (± scapolite, biotite, and magnetite) occur as intervals in the more massive calc-silicate sequence. The calc-silicate sub-unit is generally altered and overprinted by sericite and clay after feldspar, and chlorite-hematite-goethite after amphibole-biotite-magnetite. Layers of biotite-schist are locally intercalated with the calc-silicate, but they are too thin and laterally too discontinuous to be mapped as separate units.

The magnetite-rich calc-silicate sub-unit occurs directly above the hanging wall quartzite unit and locally reaches a thickness of 30m. This sub-unit is similar in composition to calc-silicate except that the magnetite content is much higher. In drill core (e.g. Geological Survey of Queensland, 2015), the magnetite concentration increases toward the contact with the hangingwall quartzite, to form a 4-6 m wide contact zone consisting of discontinuous, semi-massive to massive granular magnetite lenses (Fig. 2.4c). The magnetite-rich calc-silicate is locally intercalated with thin bands of magnetite-bearing amphibolite. Magnetite is aligned in the gneissic fabric and appears to have formed as an early alteration product overprinting and replacing the dominant rock forming minerals, as shown by the presence of abundant aligned magnetite replacing biotite along the S_1 fabric.

Hanging wall quartzite

The hanging wall quartzite unit is best exposed in the southern wall of the pit, and in drill cores. The hanging wall quartzite has been intensely deformed and in the immediate hanging wall to mineralization it has been affected by quartz-feldspar alteration. The unit is gray-white in colour and dominated by quartz, but it varies in the composition of secondary minerals that occur as inclusions in quartz. As a result, the quartzite can be locally enriched in biotite, or hornblende-chlorite-epidote or feldspar, with inclusion phases aligned in the gneissic layering and partly overgrown by quartz (Fig. 2.4d). The quartzite is magnetite-bearing along the contact with the overlying calc-silicate unit, but the magnetite content of the rock decreases away from the contact, to form a weakly magnetic middle

interval of glassy quartzite. This middle interval is discontinuous along strike, and the magnetite-rich quartzite locally occurs directly above the mineralized zone, especially in amphibolite-rich areas. Intercalations of silicified biotite schist are locally common. The hanging wall quartzite displays an annealed granoblastic texture, in which the dominant foliation is only weakly preserved. It can be intensely brecciated and pervasively altered resulting in a spotty texture. The effects of this alteration are well exposed in the upper benches in the southeast corner of the pit (Fig. 2.3a). Where alteration is prevalent, chlorite and hematite appears, and feldspar has been altered to sericite and clay minerals.

Biotite schist

The biotite schist unit is well exposed in the north wall of the pit, and is a major host rock to mineralization. However, the strongly altered and mineralized varieties of this unit (including the high-grade ore zones or "galahstone") can only be seen in drill cores. The biotite schist unit is located between the hanging wall and footwall quartzite units (Fig. 2.3a), and comprises three sub-units: (1) quartz-feldspar-biotite-amphibole schist (i.e. meta-psammite); (2) biotite-schist that locally contains sillimanite (i.e. meta-pelite), and (3) quartz-feldspar mylonite, which is probably of intrusive origin and commonly gold-rich (see Chapter 3). Other minor intercalations include amphibolite gneiss and quartzite.

The quartz-feldspar-biotite-amphibole schist sub-unit occurs along the base of the hanging wall quartzite, between the quartzite and the ore zone. The transition from the hanging wall quartzite to biotite schist is gradational and the exact contact is masked by silicification. The least altered parts of this sub-unit contain a fine-grained, light-tan, massive to weakly foliated arkose siltstone or arenite (Fig. 2.4e). The composition varies laterally and includes quartz (35-60%, including secondary quartz due to silicification), feldspar (15-20%), biotite (5-20%), amphibole (10-20%) and magnetite (± ilmenite, 2-3%). Oriented biotite, amphibole and quartz define a strong schistose fabric.

Biotite schist commonly occurs below the quartz-feldspar-biotite-amphibole schist, close to or coinciding with the high-grade ore zone, and it extends into the footwall of the ore zone. Biotite-rich varieties occur along layers, and sillimanite is locally abundant, especially in footwall zones to the ore body (Fig. 2.4f), although much of the sillimanite has been replaced by muscovite. Within the ore zone, the biotite schist has been intensely silicified, and chlorite-hematite altered (TH76) and the older mylonitic texture was strongly recrystallized into an interlocking texture of granoblastic quartz grains. The biotite sub-unit generally consists of fine- to coarse-grained biotite and/or biotite-amphibole (30-80%), with quartz (<30%) and feldspar (K-feldspar and plagioclase, <50%) that was partially altered to sericite and clay minerals; Fig. 2.5d).

The quartz-feldspar mylonite sub-unit is the principle host to gold mineralization in the sequence and occurs as layers within biotite schist. It consists of equal amounts of quartz and feldspar (albite and oligoclase) that occur as discontinuous ribbon grains interlaminated with thin quartz bands (Figs. 2.4i, 2.5e). Individual quartz and feldspar lamellae generally do not exceed 3 mm in width, and they are mostly thinner than that, but in places quartz-rich or feldspar-rich bands (or veins) can be up to 10 cm thick. Feldspar consists of albite with minor K-feldspar and Na-rich oligoclase. The quartz-feldspar mylonite is characterized by a sugary, granoblastic texture reflecting post-deformational annealing and recovery (Fig. 2.5f). In places, the recrystallized fine-grained quartz-feldspar mylonite is truncated by, or overprinted by laminated thin (< 2 mm) partings of grey quartz, which formed parallel or at low angles to the original mylonitic foliation (i.e. the "laminate" of Laing, 1992). The composition of the quartz-feldspar mylonite suggests that it originated as intrusive granite sheets or granitic migmatite (Chapter 3).

Footwall quartzite

This unit is best exposed in the northeast corner of the pit. Most drill cores do not penetrate this unit, limiting descriptions to field observations. The thickness of the footwall quartzite varies along strike and with depth and it pinches out towards the south end of the pit (Fig. 2.3a). The unit is thickly bedded (>30cm), and consists of grey-white translucent orthoquartzite (Fig. 2.4k) with traces of biotite, magnetite and heavy minerals including zircon and apatite. The unit has a granoblastic texture with a common grain size of 150-350 µm, and has been strongly deformed, but it lacks the spotty texture resulting from abundant inclusions of feldspar, magnetite, hornblende or biotite, and alteration, which characterizes the hanging wall quartzite.

Footwall calc-silicate interlayered with amphibolite gneiss

This unit is not exposed in the pit, and few drill cores penetrate it. The unit is similar in appearance to the various calc-silicate and amphibolite lithologies described above. In the immediate footwall to the footwall quartzite unit, calc-silicate lithologies dominate, whilst away from the quartzite the unit is transitional into amphibolite (Fig. 2.3a).
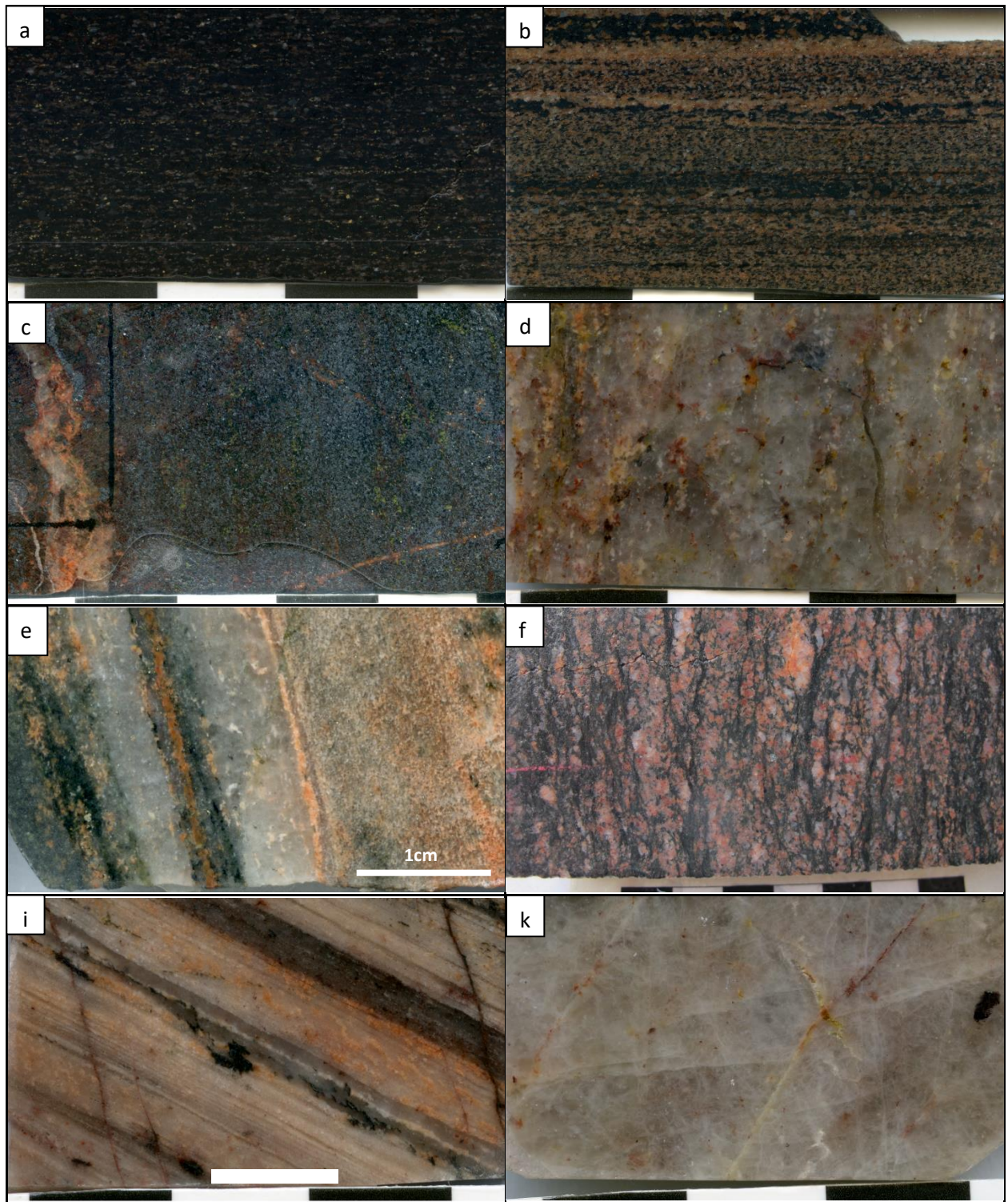
Figure 2.4. Rock units from Tick Hill. (a) Gneissic amphibolite composed of amphibole and plagioclase defining S₁; (b) Gneissic calc-silicate composed of amphibole, scapolite, plagioclase defining S₁; (c) Amphibole-rich calc-silicate consisting of amphibole-rich bands interlayered with calc-silicate bands that consist of amphibole-quartz-plagioclase-scapolite-magnetite; (d) Hanging wall quartzite showing distributed feldspar grains affected by quartz alteration; (e) Quartz-feldspar-biotite-amphibole schist sub-unit within the biotite schist; (f) Biotite schist in the pit wall composed by biotite, feldspar, sillimanite and amphibole, overprinted by red-rock alteration; (i) Typical quartz-feldspar mylonite, with feldspar-quartz laminae intercalated with thin quartz vein that have the appearance of ribbon grains. (k) Foot wall quartzite composed of strongly recrystallized granoblastic quartz.
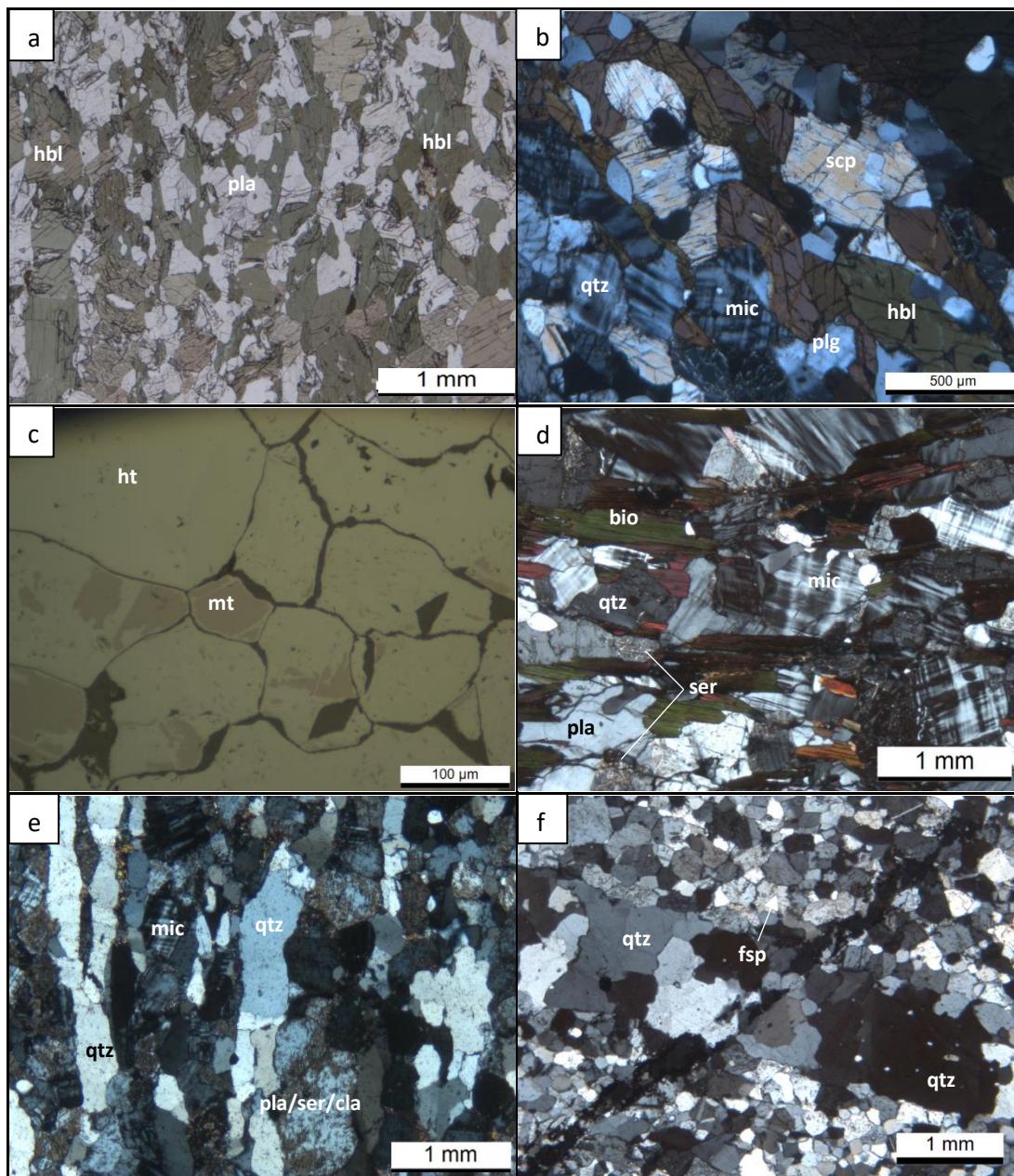
Figure. 2.5. Photos of thin sections for rock units from Tick Hill. (a) Foliated (S₁) amphibolite composed of hornblende (hbl) and plagioclase (pla) (plain-polarized light); (b) Foliated (S₁) amphibole-rich calc-silicate with scapolite (scp), hornblende (hbl), plagioclase (pla), microcline (mic) and quartz (qtz) (crossed-polarized light); (c) Hematite (ht)replacing magnetite (mt) in the magnetic calc-silicate sub-unit (reflected light); (d) Foliated (S₁) biotite schist composed of quartz, biotite, microcline and plagioclase (crossed-polarized light). The fabric displays annealing textures in which quartz-feldspar grain growth was restricted by biotite grains. Feldspar is partially altered to sericite (ser); (e) Quartz-feldspar mylonite composed of ribbon grains of quartz (qtz), microcline (mic) and plagioclase (pla) that was altered to sericite and clay minerals (crossed-polarized light); (f) Quartz-feldspar mylonite cut by a thin quartz vein (running left to right) that parallels the main mylonitic fabric, and a later fracture filled with opaques (bottom left to upper-right). The quartz displays a granoblastic textures reflecting post-deformational annealing and recovery (crossed-polarized light).

Late pegmatite veins

The gneiss units in the Tick Hill pit were intruded by late-tectonic pegmatite dykes, and the gneissic layering is locally overprinted by pegmatite-like metasomatic alteration zones which developed as rims along late fractures. Although somewhat deformed and locally boudinaged, the pegmatite veins exhibit no penetrative, mylonitic deformation fabrics and they transect the pervasive gneissic layering that characterizes the host rocks.

Late pegmatite veins occur as thin (<0.6 m) dyke-like bodies and preserve a fine- to medium-grained texture of intergrown feldspar-plagioclase and quartz near the margins of the dykes with a core dominated by plagioclase (85-95%) with variable amounts of quartz (<10%), K- feldspar (<5%) and biotite (0-10%). In drill core pegmatite-like veins appear in the footwall of the ore body and are associated with metasomatised zones with a granular texture and diffuse boundaries in which feldspar (~30-40%), quartz (20-30%) and minor biotite (<5%), overprint and replace the underlying metamorphic fabrics. The late-tectonic pegmatite intrusions were strongly affected by later hydrothermal alteration, in which feldspar was replaced by an albite-sericite assemblage.

2.3.2. Deformation sequence in the Tick Hill deposit

Rocks hosting the Tick Hill deposit were affected by four distinct deformation and metamorphic events: (1) D_1 shearing at upper amphibolite to granulite facies metamorphic conditions, (2) D_2 upright folding at upper amphibolite facies metamorphic conditions, (3) D_3 normal faulting with extensional veining and widespread quartz-feldspar alteration at lower amphibolite to upper greenschist facies, and (4) D_4 strike-slip faulting with cataclasite formation along fault planes. Each of the events as seen in the pit and its immediate surroundings, and in drill cores has been described in more detail below.

D_1 events

The dominant structural element in Tick Hill pit and its immediate surroundings is a well-developed, moderately west-dipping schistose or gneissic layering and associated mineral lineation, which formed during the earliest stages of deformation referred to as D_1. This layering consists of an annealed mylonitic fabric with sugary, granoblastic characteristics in quartz-feldspar-rich lithologies (i.e. blasto-mylonites), and has an orientation within the pit that varies from 305/65 (dip direction/dip) to 250/50 (Fig. 2.6a). The layering is a composite tectonic fabric and locally contains isoclinal intrafolial folds, which are best preserved within the calc-silicate unit. Around the hinge zones of the intrafolial folds (F_1) an earlier phase of the mylonitic fabric (S_{1a}) was folded before being transposed in the dominant fabric (S_{1b}). Thus, the main foliation is a composite fabric herein called $S_{1a,b}$ or S_1 for short (Fig. 2.7a). S_1 contains a well-developed mineral lineation or rodding lineation, L_{1x}, which

typically pitches steeply to the southwest (251/55, azimuth/plunge, Figs. 2.6a,b). L_{1x} is defined by the oriented growth of plagioclase aggregates, hornblende and scapolite in calc-silicate and amphibolite units, by biotite and sillimanite in biotite schist, and by quartz-feldspar-rodding in more felsic units and quartzite. F_1 intrafolial folds have fold axes that are close to parallel to L_{1x}, and sheath-folds have been observed outside the pit.
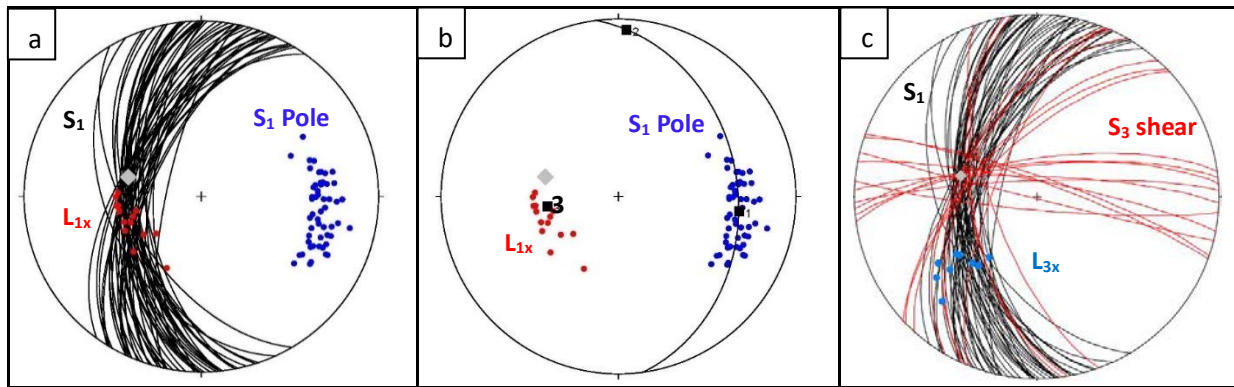
Figure. 2.6. Lower-hemisphere stereonet of structural elements visible in the pit at Tick Hill. (a) Great circles = S_1; blue dots = poles to S_1; red dots = L_{1x}; grey diamond = long axis of 16.5g/t Au ore envelope. Note that the ore envelope is not parallel to L_{1x}. (b) As above. Shown is the best fit great circle through the poles to S_1. Note this great circle has a pole (3) that coincides with L_{1x}, i.e. the foliation truncation plane responsible for the variations in S_1 directions probably formed during D_1. (c) Black great circles = S_1; red great circles = S_3 shear zones and normal faults; blue dots = L_{3x}; grey diamond = long axis of 16.5g/t Au ore envelope. Note that the ore envelope is parallel to the intersection lineation between S_1 and S_3.

In more quartzo-feldspathic units in the main ore zone, the S_1 foliation intensifies to a mm-scale lenticular to laminar fabric characteristic of mylonite (Fig. 2.4i). This fabric has been largely annealed resulting in a granular texture in thin section, characterized by alternating ribbon grains of quartz and plagioclase (Fig. 2.5e). Within the present geometry, trails of rotated boudin blocks of coarse-grained black quartzite layers within calc-silicate, exposed in the north wall of the pit, are consistent with a normal west-down shear sense, but otherwise shear sense indicators (asymmetric clasts, S-C fabrics, shear bands etc.) are lacking.

Across the pit the orientation of S_1 varies around two principal groupings: 300/60 and 260/55 (Fig. 2.6). In the western half of the pit, S_1 dips to the west-northwest (300/60), whilst in the eastern half of the pit, S_1 dips due to the west or south-southwest with S_1 steepening from 55 to 70° in the southeast corner of the pit (Fig. 2.3a). L_{1x} does not vary greatly in orientation in either of the two domains and remains more or less constant around 250/55, which is parallel to the intersection line between the various S_1 orientations (Fig. 2.6b). An abrupt change in orientation of the S_1 foliation occurs in the center of the pit where it can be mapped as a foliation truncation plane, characterized by an intensely foliated biotite-chlorite-schist zone. The foliation truncation plane originated during D_1, but was reactivated as a brittle-ductile shear zone during D_3 as discussed below. The north to north-

northeast trending foliation truncation plane dips ~55° to the west and connects the hanging wall quartzite in the southern wall of the pit to the footwall quartzite in the north (Fig. 2.3a). It more-or-less coincides with the ore zone (Fig. 2.6). Within the open pit, S_1 orientations also vary around quartzite boudins and along 10 m scale northwest-trending shear-band-like high strain zones that locally cross the main foliation (e.g. in the upper benches in the southeast corner of the pit).

Peak-metamorphic conditions in Tick Hill pit were reached during D_1 shearing and folding (e.g. Choy, 1994). The grade of metamorphism during D_1 reached upper-amphibolite to granulite facies as indicated by the ductile behavior of K-feldspar and plagioclase in sheared quartzo-feldspathic mylonite, intense ductile folding (including sheath folding) in amphibolite, the presence of coarse-grained metamorphic pyroxene in leucocratic segregations within amphibolite, and hornblende-pyroxene and sillimanite assemblages defining the S_1-L_1 fabrics. In addition, garnet-hornblende-pyroxene-plagioclase-quartz assemblages in amphibolite gneiss were encountered in drill core 800 m north of the pit. The D_1 deformation features in Tick Hill correlate with regional D_1 deformation events described in the southern MKD (e.g. Blake and Steward 1992; Passchier, 1992; Rutherford, 2000).

Within the pit and surrounding areas numerous quartzo-feldspathic granitic bodies occur that are variably deformed. Many are strongly mylonitic and fine-grained throughout, whereas others preserve less deformed cores with mylonitic rims. The quartzo-feldspathic units were described as the intrusive Tick Hill Complex (Wyborn, 1997) and have been interpreted as granite intrusions that were emplaced syn-tectonically at various times during the development of S_1.

D_2 events

Regional mapping shows that the Tick Hill deposit is situated in the eastern limb of a large (km-scale) synformal, D_2 structure (the Tick Hill syncline; Fig. 2.2b) that folds S_1 around an upright fold with an axial planar trace that parallels the regional trend of S_1. Within the pit no clear D_2 structures are visible with the exception of rare open, near-cylindrical similar folds that occur on a 0.1-1 m scale (Fig. 2.7b). Such F_2 folds are invariably east-verging with near-horizontal north-trending (020) fold axes, and they contain no clear axial planar fabrics. Metamorphic conditions during D_2 are poorly constrained due to the absence of clear S_2 fabrics or mineral assemblages, but the highly ductile nature of regional D_2 folds, their transposition into the main fabric further west (Laing, 1993) and continued stability of peak assemblages within D_2 fold hinge zones suggests that conditions remained high.
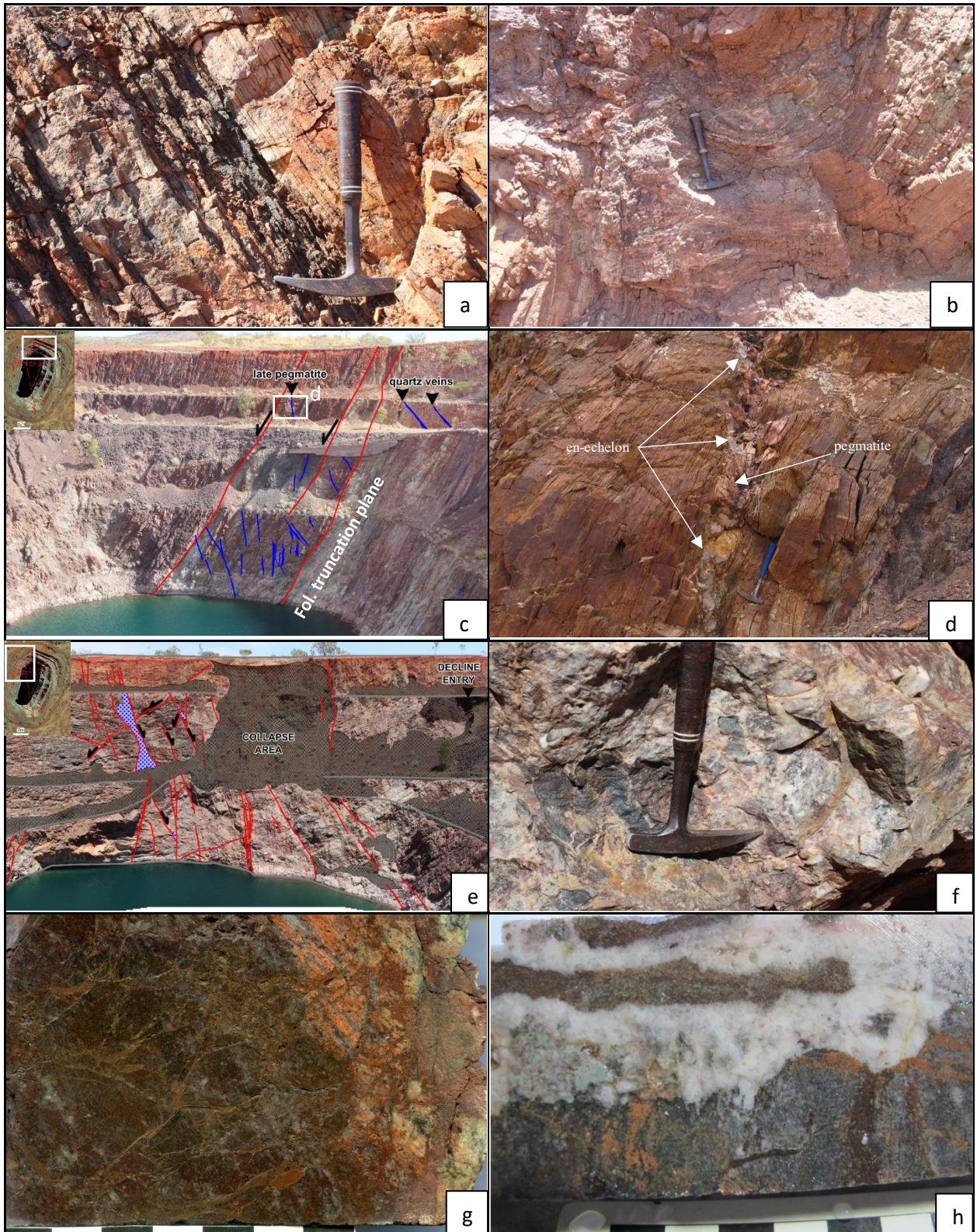
Figure 2.7. Representative D₁₋₄ structures and alteration textures. (a) S₁ fabric in gneissic calc-silicate intercalated with biotite schist bands in the north wall of the pit; (b) D₂ up-right folds in the north wall of the pit; (c) North pit wall, showing the D₁ foliation plane reactivated as a D₃ shear zone (red). En echelon D₃ pegmatite and quartz veins (blue) are indicative of sinistral-normal movement on the shear zone during D₃; (d) Close-up of syn-D₃ pegmatite containing en-echelon quartz veins in (c) that indicate a normal shear sense; (e) East-trending, D₃ normal faults (red), some with breccia (blue) in the northwest corner of the pit; (f) D₃ brecciated and altered calcsilicate gneiss with trace sulphides derived

26

from underground workings; (g) High-grade calc-silicate breccia in the ore zone, which is associated with D₃ sheeted veins and quartz-feldspar-chlorite-hematite alteration; (h) D₄ veins with calc-silicate breccia fragments consisting of quartz, carbonate and green clay minerals that over print the late D₃ red rock alteration.

D₃ events

D₃ in the Tick Hill pit is characterized by a network of fault zones and associated fractures and veins that accommodated normal movements and facilitated retrograde alteration (Figs. 2.7c-e). The S_1 foliation is locally reactivated as, or truncated by D₃ fault zones, that are characterized by a micaceous foliation and the alignment of fine-grained chlorite (after biotite) to define L_{3x} (most clearly observed in the northern wall of the pit). This lineation pitches shallowly to moderately south-southwest (~230/40, Fig. 2.6c), and is locally paralleled by quartz striations. D₃ fault planes are associated with damage zones including breccia zones and quartz veins, some of which are arranged in an en-echelon fashion (Figs. 2.7c,d) consistent with a sinistral-normal sense of movement. The most conspicuous D₃ shear is exposed in the northern wall of the pit as a biotite-chlorite schist zone that parallels the D_1 foliation truncation plane passing through the center of the pit. This fault zone coincides with the ore zone. D₃ fault zones also developed along the margins of the quartzite units and a major fault truncates the hanging wall quartzite in the southern wall of the pit (Fig. 2.3a).

A series of parallel, east-trending, steeply (mostly north) dipping, normal faults (Figs. 2.3a, 2.6c, 2.7e) are prominently developed in the northwest corner of the pit. These faults mostly do not cross the pit but appear to merge with the north-northeast-trending D₃ faults in the center of the pit, including the main D₃ fault that parallels the D_1 foliation truncation plane (Fig. 2.3a). The east-trending faults display dm- to m-wide, quartz-feldspar alteration haloes or rims developed on either side of individual faults, and associated albite-epidote-hematite veins.

D₃ faulting involved widespread fracturing, veining, breccia formation and quartz-feldspar alteration visible in outcrop and in drill core. These features are concentrated in the strongly silicified core of the deposit, and the D₃ fracturing, at least in part overprints earlier silicification. Fracture sets include thin (< 2 mm wide) grey quartz veins that trend between 80-100° and that occur as bundles of partings along the S_1 mylonite fabric, especially in the quartz-feldspar mylonite, and drill intersections suggest that breccia is commonly associated with the sheeted veins in the lower levels of the high-grade ore zone (Figs. 2.3b; 2.7f,g).

Fracture sets also include northeast trending faults (~030) that display sinistral displacements in drill core and are associated with albite-hematite altered quartz veins, and north- and east-trending cataclastic shatter zones best developed in silicified quartzite and schist. D₃ fractures are commonly highlighted by pink and red feldspar alteration, which also forms the matrix to shatter zones along

fractures. In the ore zone (the "galahstone"), these fracture sets merge into a continuous network and many of the fractures and associated quartz veins contain visible gold. Steep east-trending fracture zones are present in all drill cores through the ore zone, and they are particularly common in gold-bearing zones. In some drill cores the fracture zones widen to several 10s of cm where they are characterized by chaotic fabrics (poor core recovery) and breccia. D_3 fracture zones coincide with widespread quartz-feldspar-chlorite-hematite alteration as well as locally developed carbonate alteration.

Several drill cores preserve late-stage, coarse-grained quartz-feldspar veins, which resemble the metasomatic alteration rims that decorate D_3 fractures and veins. These late tectonic quartz-feldspar zones have been interpreted as syn-D_3 metasomatic overgrowths.

D_4 events

D_4 structures represent the latest phase of deformation recorded in the Tick Hill pit. On the scale of the pit, D_4 involved the formation of brittle east-northeast-trending and steeply north-dipping faults (Fig. 2.3a) that formed in combination with steep northwest-trending secondary faults. The main east-northeast-trending fault has an apparent dextral displacement. D_4 faults displace the quartzite units and are associated with cataclasite formation and chlorite-hematite-goethite alteration along slicken-sided fracture zones as well as open-space carbonate fill. In drill core, D_4 structures include late-stage fractures and cataclasite zones with quartz-carbonate-clay fill and associated clay alteration haloes, which overprint D_3 fractures and veins (Fig. 2.7h).

2.4. Gold mineralization and alteration at Tick Hill deposit

As mentioned in the introduction earlier workers at Tick Hill noted the problem that gold seemed to have a relationship to both old (D_1) and young (D_3) structures (e.g. Choy, 1994; Tedman-Jones, 2001). Gold inclusions in peak-metamorphic minerals, an alignment of gold with the S_1 fabric and a spatial association with syn-D_1 silicified deformation zones were cited as evidence for early gold (e.g. Choy, 1994). A spatial association with late-tectonic laminar quartz veins and associated chlorite-albite-hematite alteration, and the presence of gold along D_3 fractures and breccia zones were cited as evidence for a D_3 origin (e.g. Tedman-Jones, 2001). What follows is a description of gold distribution patterns and associated mineral assemblages in relation to the earlier and later structures. An in depth discussion of the potential genesis of the ore body is provided in the discussion.

2.4.1. Ore body geometry and associated metal distribution

The ore body geometry as defined by the 1 g/t ore envelope for the Tick Hill deposit is carrot-shaped and tapers down to a vertical depth of 240 m (MIM 1993, 2000; Tedman-Jones, 2001). The ore

body dips ~55º to the west, i.e. parallel to S_1, and has a linear high-grade (i.e. 16.5 g/t) core that plunges 55° to 285 (Fig. 2.6). With increased depth, the strike extent of the ore zone decreases and in the two lowest mine levels (130 mRL and 117 mRL; e.g., Fig. 2.3b), the ore trend switches abruptly from north-northeast (Fig. 2.3a) to east and the ore zone narrows to several meter-wide chlorite-hematite-carbonate breccia veins (Fig. 2.3b, Tedman-Jones, 2001).

The geochemical surface expression of the Tick Hill gold anomaly (> 0.1ppm) was about 160 × 30 m and coincided with a pre-mining, north-northeast-trending, 210 × 50m magnetic low (Nano et al., 2000, Fig. 2.8). The location of the gold anomaly that runs across the pit overlaps with a strongly D_3 fractured and hematite-altered zone in the immediate hanging wall of the D_1 foliation truncation plane that was reactivated as a D_3 shear zone (Figs. 2.3a, 2.6b). The plunge of the high-grade core of the ore body coincides with the intersection lineation between the north-northeast- and east-trending D_3 faults and the intersection lineation between the D_3 faults and the S_1 foliation planes as measured in the pit. The plunge of the high-grade core is also close in orientation to the measured L_{1x} mineral lineation, which is somewhat variable in orientation (Figs. 2.3a, 2.6c). The low grade (i.e. 0.1 g/t) ore envelope coincides with areas where east-trending D_3 fractures and breccia zones are most prominent, and extends outside the pit along some of the more prominent east-trending D_3 fracture zones.

Gold mineralization is largely confined to the strongly altered quartz-feldspar mylonite sub-unit and adjacent biotite schist, calcsilicate, and hanging wall quartzite (Fig. 2.3). The historical assay data shows that the boundaries to the mineralization are sharp as grades drop abruptly away from the D_{1-2} silicied and D_3 altered fracture zones. Gold occurs almost exclusively as disseminated grains of free gold up to 0.5 mm in size with Au/Ag ratios of >100.

In drill cores and thin sections, gold can be commonly seen as an alignment of coarse grains that parallel the dominant mylonitic S_1 fabric. Gold grains also commonly occur associated with thin laminar quartz veins of D_3 origin, which either occur along the S_1 mylonitic foliation or along steep east-trending fractures. Mineralization shows a spatial relationship with D_3 alteration haloes near post-tectonic coarse-grained quartz-feldspar dykes, and fine gold grains typically occur near patches of chlorite, albite and hematite. The east-trending quartz-feldspar veins are locally associated with breccia zones, which in drill core are most prominent at depth in the immediate footwall of high-grade ore zones (Figs. 2.7f,g). At shallower levels where breccia is less common, high-grade mineralization is concentrated in areas of intense laminar D_3 veining (Figs. 2.4i, 2.9a,c).

The quartzo-feldspathic mylonite is locally extremely gold-rich (e.g. up to 3209 ppm @ 0.5 m in DH TH014), and gold grains locally display a characteristic granoblastic texture. Within the high-grade ore zones, gold grains commonly display bimodal grainsize distributions with irregularly shaped larger grains surrounded by a halo of finer grains (e.g. Choy, 1994, Figs. 2.9d,f). A few of these finer grains

contain small amounts of Ag (< 5.3 wt.%) and Cu (< 2 wt.%). Coarse-grained gold is commonly enclosed within recrystallized quartz, with quartz appearing as a metamorphic moat around the gold. Gold also occurs along the grain boundaries between quartz and feldspar grains (Fig. 2.9b). Within calc-silicate units, gold is locally enclosed within granoblastic, hornblende, scapolite and pyroxene grains that are aligned in the peak-metamorphic S_1 fabric (Figs. 2.9d-e). Fine-grained gold occurs either as haloes near larger gold grains or as trails associated with strongly silicified zones and alteration minerals that included bismuth selenides and sulfides (Table 2.2). In general, the sulfide content in the mineralized quartz-feldspar mylonite unit is less than in the other units, and the abundance of sulfides increases towards the footwall of the deposit.

The high-grade core of the Tick Hill deposit shows only minor enrichment in other metals, and sulfides. Available assay data for a restricted number of elements (Cu, Co, Ni, Pb, Zn, As, Fe, Mn) from exploration holes drilled in the 1990s (MIM, 2000) indicate that with few exceptions, on a meter-scale, gold values show no correlation with any of the other metals. On a scale of the entire deposit, a general enrichment in Cu (> 100 ppm), Co (> 40 ppm), S, As, and Bi has been suggested for the immediate footwall of the ore zone (Nano 1999; Tedman-Jones 2001), with minor Co enrichment (> 40 ppm) partly overlapping with the 1 g/t Au envelope. Cu values reach up to several 1000 ppm in the footwall to the ore zone and can be linked to chalcopyrite-pyrite and minor bornite-pyrrhotite mineralization, which is possibly also responsible for an induced polarization anomaly that was observed over the Tick Hill ore body (Nano, 1999). Cu values are rarely high in the ore zone itself. At a larger scale, it is clear that Cu and Co anomalies are not just restricted to the vicinity of the ore zone, but also occur in the hanging wall of the ore zone, where Cu values locally reach 100's ppm away from mineralization and alteration (Fig. 2.10). In general Cu shows moderate to strong correlations with Co and Ni and a spatial relationship with amphibole-rich lithologies.
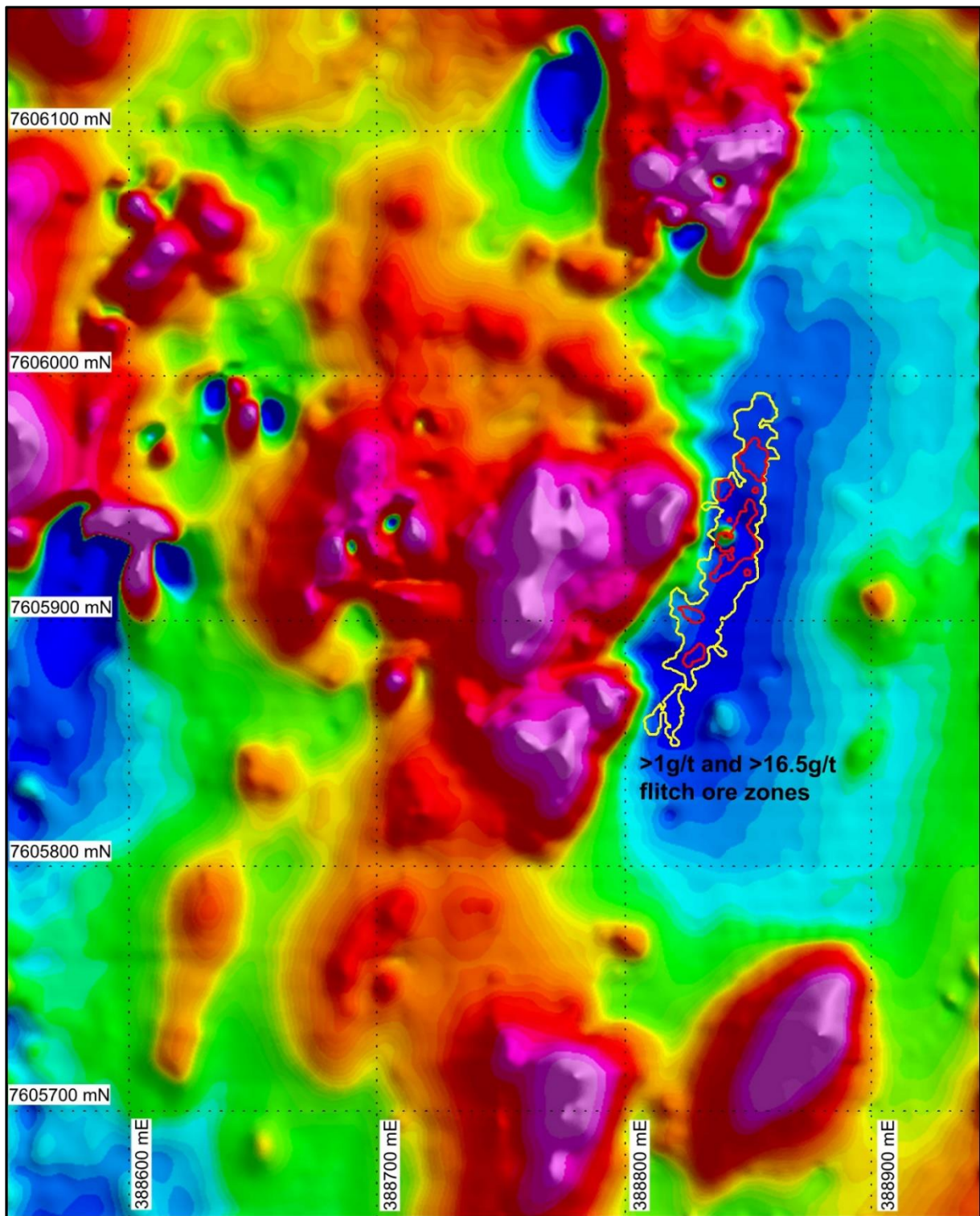
Figure 2.8. Ground magnetic map of the Tick Hill area, overlain with Au grade contours, illustrating the coincidence of gold mineralization with the area of magnetic depletion (Nano et al., 2000).
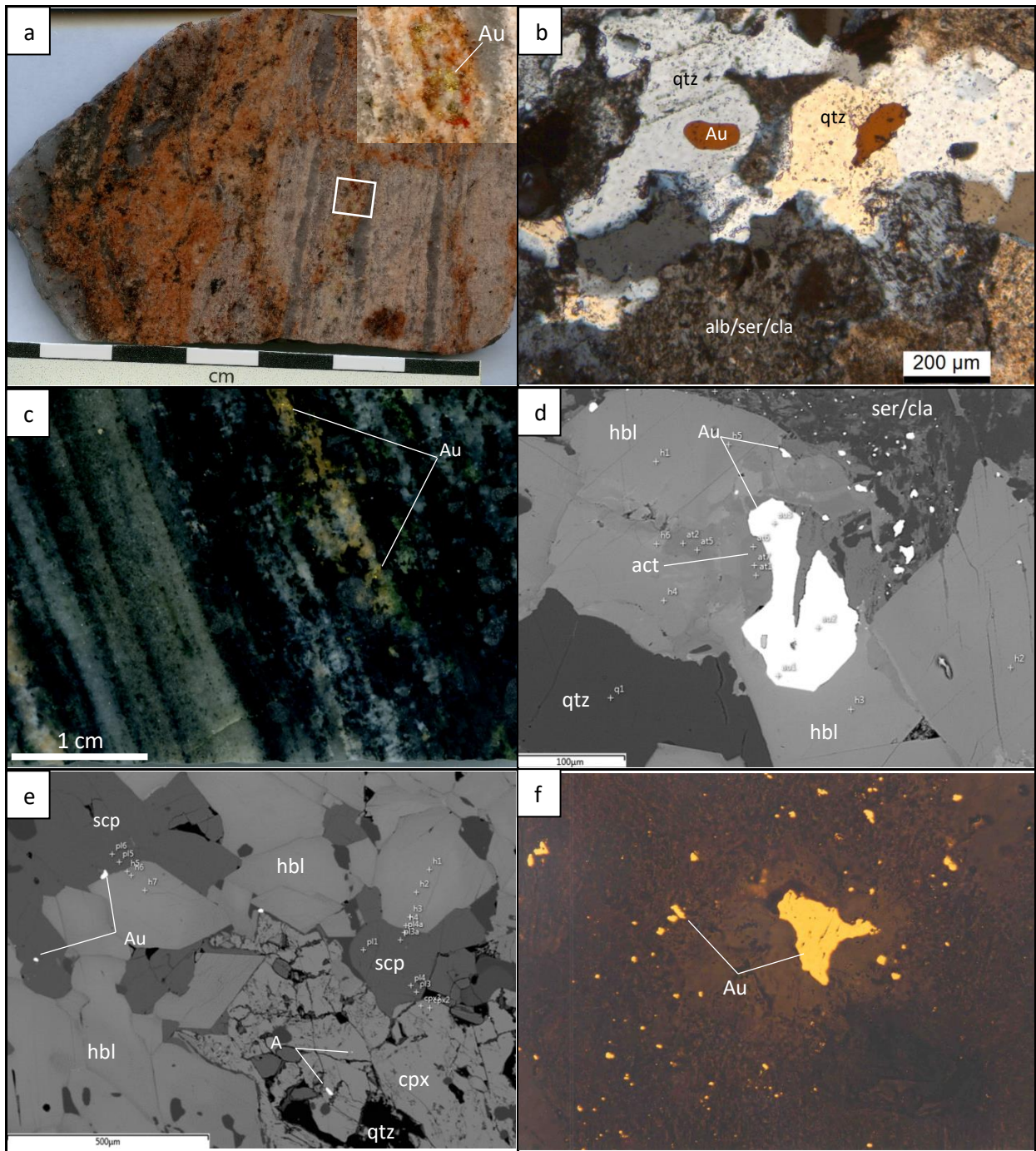
Figure 2.9. Examples of textures associated with gold mineralization. (a) Gold-rich metasomatized quartz-feldspar mylonite, a close-up of the white box is shown in the top right; (b) close-up of coarse-grained gold grains in (a). Gold is commonly contained within quartz or surrounded by a moat of quartz in recrystallised quartzo-feldspathic gneiss in which albite is replaced by late-D_3 sericite and clay minerals; (c) Gold mineralization concentrated along feldspar-rich selvages in strongly foliated amphibole-rich calc-silicate; (d). A SEM image showing coarse-grained gold within peak-metamorphic (D_1) hornblende, while fine-grained gold occurs along grain boundaries where it is associated with sericite (ser) and clay (cla) alteration (after feldspar); (e) A SEM image showing gold inclusions hosted within peak-metamorphic clinopyroxene (cpx) and scapolite (scp) from amphibole-rich calc-silicate; (f) Microphotograph showing a coarse grain of gold with a halo of finer gold grains suggesting local dissolution and remobilisation of early stage gold (image after Choy, 1994).

2.4.2. The spatial distribution of the alteration halo around gold mineralization

The Tick Hill deposit is associated with two periods of alteration: a first that occurred at high temperatures during D_1, and a second that occurred at lower temperatures during D_3. Early high temperature alteration involved the emplacement of gold that was incorporated in hornblende and diopside grains aligned in the S_1 fabric. Evidence for this early event is only partly preserved, because of the intensity of the later stages of hydrothermal overprints during D_3, and the exact spatial distribution of the early alteration halo is uncertain.
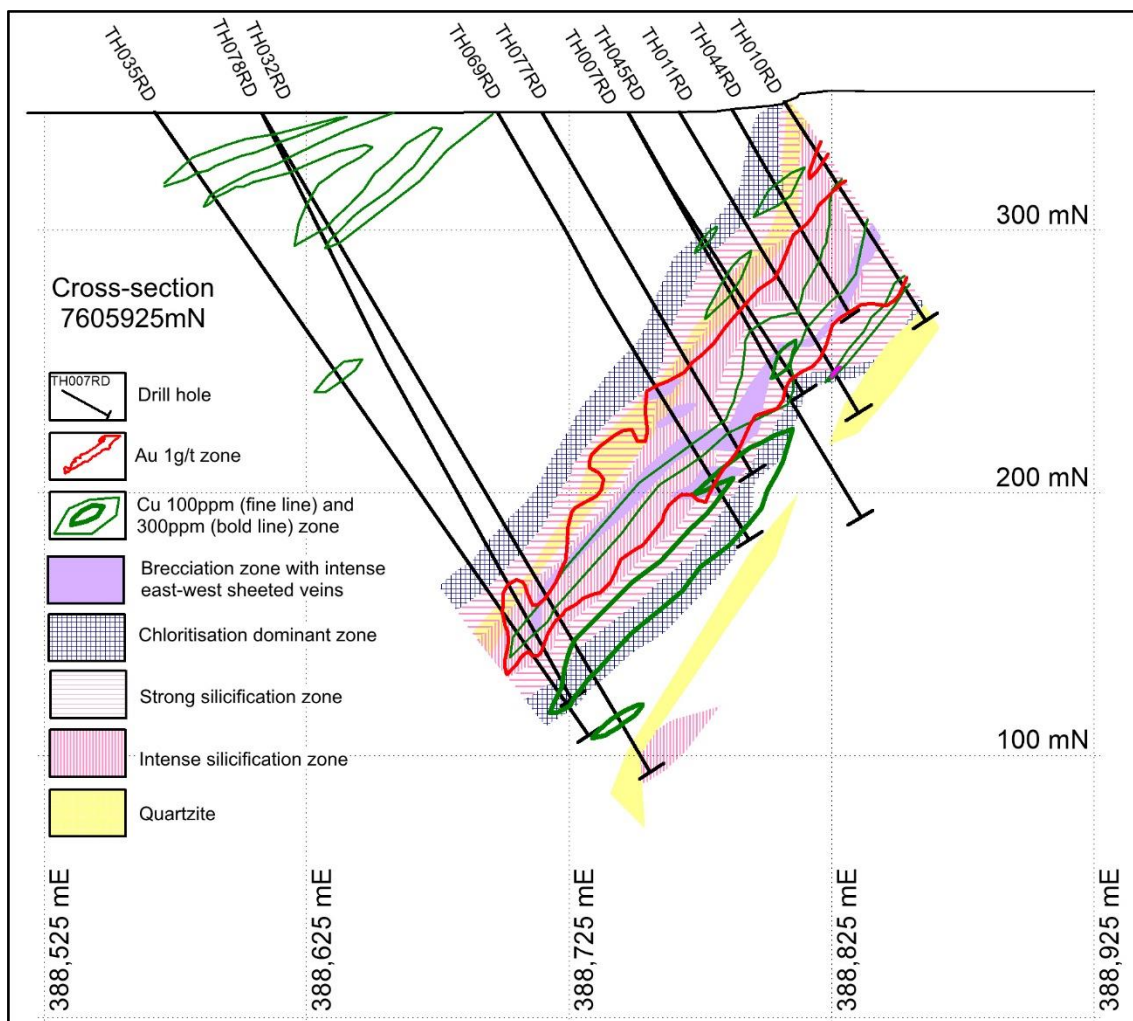
Figure 2.10. Cross-section 7605925mN showing the spatial relationship between various alteration zones, brecciation, 100-300 ppm Cu zone and the 1g/t ore envelope at Tick Hill based on core logging and assay data.

The early alteration event is characterized by intense silicification and magnetite alteration (e.g. Fig. 2.4c; Appendix 6A, page 385) that is most evident within the hanging wall quartzite unit. Within the ore zone, syn-D_1 silicification was intense and involved the growth of quartz at the expense of other silicate phases (Fig. 2.11b), which now occur as inclusion trails in quartz. Early magnetite alteration was largely destroyed by the lower temperature D_3 hydrothermal overprint during which magnetite

was replaced by D_3 hematite. Gold grades in drill core today display a negative correlation with magnetic susceptibility, and this effect is visible on a larger scale by the presence of an aeromagnetic low that coincides with the ore zone and the D_3 alteration halo (Fig. 2.8).

The younger D_3 alteration events resulted in the formation of a clear low- to moderate-temperature alteration zone that is about 100 m in diameter, which developed during D_3 and overprinted the earlier high temperature alteration assemblages as well as the D_1 peak metamorphic mineral assemblages and associated structures (Figs. 2.3, 2.10). This later alteration is most prominently developed in the ore zone and hanging wall rocks to the ore zone above the S_{1-3} foliation truncation plane, whilst the footwall rocks to that surface are significantly less altered (Geological Survey of Queensland, 2015).

The lower temperature alteration assemblages vary with rock type and display a zonal pattern, with most intense alteration occurring along D_3 fracture zones and associated breccia. From the proximal mineralization outward, the alteration zonation includes (Fig. 2.10): (1) intense to (2) strong silicification and associated growth of abite-hematite-chlorite-epidote-sericite-actinolite/hornblende-oligoclase, surrounded by (3) a shell characterized by chlorite and epidote, and (4) an extensive zone with clay alteration. Zonal boundaries are gradual with localized overlaps in alteration assemblages, whilst late clay alteration occurs throughout.

The most extensive expression of low-temperature alteration in drill core includes the presence of smectite and illite with minor hematite and quartz in veins, and as replacement of feldspar. This type of alteration typically occurs in association with quartz-feldspar veins in the hanging wall calc-silicate and amphibolite units. Intense clay alteration is also well developed within the more reactive felsic units and biotite schist in the immediate footwall to gold mineralization (Geological Survey of Queensland, 2015). The clay minerals occured throughout most drill holes, tens of meters from the mineralization zones (e.g. Appendix 1, Geological Survey of Queensland, 2015).
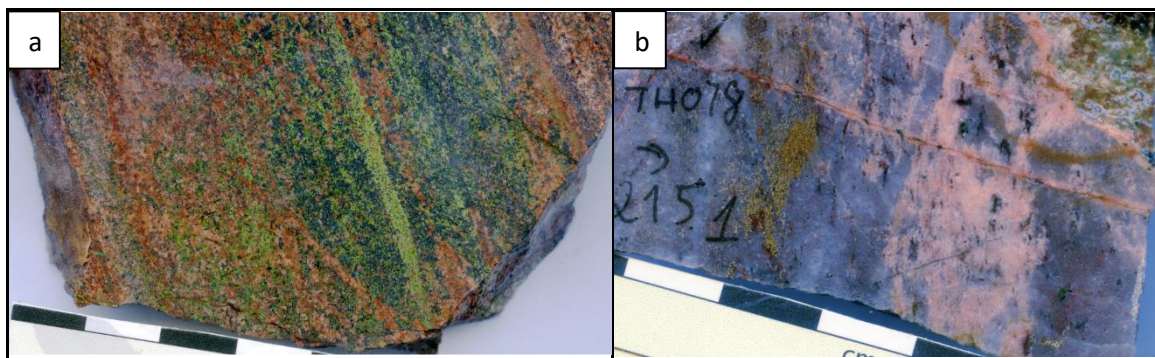
Figure 2.11. Examples alteration from Tick Hill deposit. (a) A cm-scale image of chlorite-epidote alteration in the hanging wall to mineralization; (b) A cm-scale image of the D_{1-2} silicification zone, with relic biotite, overprinted by D_3 pink feldspar-quartz alteration and gold mineralization (gold is found in the sheeted veins in association with chlorite and feldspar at the center of the image).

On the hanging wall side and closer to mineralization, chlorite-epidote alteration overprints the older quartz-magnetite alteration, especially along the contact zone between the calc-silicate unit and hanging wall quartzite, and near the base of the hanging wall quartzite unit (Fig. 2.11a). The immediate halo to the ore zone is characterized by strong silicification that is spatially associated with patches and/or veinlets of pink albite and chlorite-epidote-actinolite-hematite-sericite-calcite alteration, as well as gold and minor sulfides. The alteration is pervasive and is concentrated in veins, along fracture zones and as disseminations along microfracture networks. In this zone, primary feldspar was replaced by sericite, albite and clay minerals (illite, smectite), whilst magnetite and ilmenite were altered to hematite and leucoxene, and chlorite replaced biotite.

Within the high-grade ore zone, intense silicification affected the quartz-feldspar mylonite and biotite-rich schist (Fig. 2.11b). Here, pervasive silicification with quartz growth across the mylonitic fabric occurred early (i.e. pre- or early-D_3), with later silicification linked to the emplacement of thin quartz veins (sub-) parallel to the S_1 foliation, and the growth of quartz in alteration haloes near quartz-feldspar veins and pegmatite dykes. Other alteration minerals in this zone include albite, oligioclase, K-feldspar, hornblende, actinolite, chlorite, epidote, sericite, calcite, hematite, and leucoxene.

Carbonate alteration generally occurs as a late late-D_3 and D_4 fracture fill. In the mineralized zone, calcite locally occurs as secondary growth along sheeted quartz veins and east-trending fractures, but carbonate growth is not pervasive. However, in the keel of the deposit in the lower levels of the mine, gold was mined from east-trending breccia veins that were reported to contain chlorite-hematite-carbonate in the matrix (Tedman-Jones, 2001), i.e. at depth carbonate growth may have been more abundant and it occurred in associated with gold, although we could not confirm this in drill core.

2.4.3. Paragenetic sequence

Most hydrothermal alteration minerals associated with gold mineralization formed during D_3. However, there is clear textural evidence that gold was present during D_1 peak metamorphism when the main gneissic fabric formed and an early stage of high temperature alteration occurred (Table 2.1. The main minerals that characterize early, high temperature alteration are magnetite and quartz, which are best preserved in the hanging wall quartzite unit, where quartz and magnetite largely replaced biotite, feldspar, and in places amphibole (e.g. Geological Survey of Queensland, 2015), which are now only visible as trails of largely resorbed grains aligned along S_1 and included in granoblastic quartz. The magnetite content in the hanging wall quartzite increases upwards and grades into a near-massive magnetite zone towards the upper contact of the quartzite, where magnetite is aligned with S_1 and inter-grown with syn-D_1 high-temperature minerals including scapolite and hornblende, suggesting that much of it formed pre- or syn-D_1 (Table 2.1). Considering that the early magnetite-quartz alteration is prominent in the hanging wall of the high-grade ore zone, and magnetite within the ore zone itself

was largely replaced by D_3 hematite (Fig. 2.8), it is likely that early magnetite alteration was associated with deposition of early gold.

The best evidence for early gold mineralization can be found in mineralized amphibolite-rich, calc-silicate gneiss horizons, where granoblastic gold inclusions occur in peak-metamorphic scapolite, hornblende and diopside grains that were unaffected by later retrograde alteration (Figs. 2.9d-e). There are no obvious micro-fractures in the scapolite, clinopyroxene or hornblende grains that could indicate later remobilization of gold, and the presence of these inclusions strongly suggests that gold was present when the S_1 fabric formed. The presence of early gold is further supported by its bimodal grainsize distribution in some high-grade ore zones, where coarse gold grains that are typically aligned in the S_1 fabric and surrounded by a halo of fine gold (Figs. 2.9d,f; Choy, 1994).

Emplacement of early gold may have been associated with the deposition of sulfides. Texturally early D_1 chalcopyrite has been observed as inclusions inside amphibole, which itself occurs as inclusions inside coarse-grained, peak-metamorphic, almandine garnet (e.g. in drill core TH99, 800 m north of Tick Hill). Away from the main ore zone, chalcopyrite and pyrite are relatively common in amphibolite gneiss, where the sulfides occur along S_1 foliation traces. Thus, a first stage of gold mineralization occurred in association with the peak-metamorphic assemblage and an early stage of magnetite-quartz alteration when chalcopyrite was present within the system (Table 2.1).

The most obvious alteration assemblages visible in the Tick Hill pit today formed during D_3 and D_4, and involved six hydrothermal stages (Table 2.2). During stage 1, magnetite-bearing feldspar veins were emplaced associated with the formation of an alteration assemblage (stage 1) that included quartz-albite (±oligioclase)-hornblende-magnetite-hematite (±leucoxene). This was followed by at least three stages during which gold was either introduced or remobilized, with hematite and chlorite being the most characteristic alteration minerals in outcrop. Stage 2 coincided with the main period of gold enrichment, and involved quartz-feldspar veining and alteration characterized by the growth of quartz-albite-actinolite-chlorite$_1$-hematite (±leucoxene) progressing into stage 3 with the growth of K-feldspar-sericite-chlorite$_2$-epidote-hematite (early stage 3) followed by hematite, smectite and illite (late stage 3). Stage 4 is characterized by minor calcite veining, late chlorite$_3$ growth and the remobilization of some gold along fractures. Stage 5 events postdated mineralization and included late-D_3, pale pink quartz-albite flooding and the renewed growth of magnetite along isolated fractures. During later D_4 events additional quartz-carbonate-clay alteration (stage 6) occurred along late faults, with no evidence that gold was remobilized. The paragenetic sequence and mineral assemblages that formed during each of these six stages are discussed in more detail below and presented in Table 2.2.

The early-D_3 emplacement of *stage 1* feldspar veins marked the onset of younger hydrothermal alteration events that predated the introduction of new gold during D_3, or the re-mobilization of early

gold that had formed during D_1. Most veins of this type are steep and have an east trend (Fig. 2.12a), and they contain magnetite and titanite. They represent the earliest set of veins that form part of the family of laminar, sheeted veins that characterize the ore zone. They are common in the hanging wall sequence, and their occurrence in the footwall sequences is uncertain, due to a paucity of available drill core. Vein emplacement was associated with the formation of a mineral assemblage (stage 1) that included quartz-albite-oligioclase-hornblende-magnetite-hematite (±leucoxene). Intense albite alteration characterized stage 1 and occurred with the formation of oligoclase, hematite and hornblende. Stage 1 magnesio-hornblende (Mg/Mg+Fe = ~0.6, minor Na_2O, K_2O, Cl, and TiO_2) is blue-green in colour (Fig. 2.13a), and either replaces older D_1 hornblende, or occurs as clots overgrowing the dominant fabric.

During *stage 2*, numerous feldspar-rich veins were emplaced that either contained gold, or that were associated with alteration haloes that contained gold (Figs. 2.12b-d). These veins included thin (< 1 mm), east-trending, laminar veins, and north-trending veins that can be up to 10 cm wide and parallel the S_1 foliation. The stage 2 veins were best developed as feldspar-filled fractures within the silicified biotite-rich schist, in quartz-feldspar mylonite and in the hanging wall quartzite (Figs. 2.12b-c). Stage 2 veins consist of pale pink to dark pink feldspar and quartz. The pale pink feldspar is commonly albite with lesser oligioclase, while the darker pink feldspar is either albite or oligoclase with abundant fine-grained hematite inclusions. Overprinting relationships between veins in some drill cores suggest that stage 2 veining commenced with feldspar-rich veins and continued with the emplacement of progressively more silica-rich veins.

Stage 2 veins are associated with extensive feldspar alteration haloes that emanate from the veins, and overgrow and replace the older S_1 fabric (Fig. 2.11b). Alteration textures vary in intensity and include: (a) albite (±oligoclase) replacement with minor quartz that obliterated the older fabric, (b) albite-quartz alteration along thin laminates that generally parallel the S_1 fabric, and (c) replacement alteration along networks of fine fractures that resulted in a spotted and veined alteration texture (Fig. 2.12c). Most gold observed in thin sections occurs in spatial association or is inter-grown with stage 2 alteration assemblages, and it commonly occurs as inclusions within granoblastic, grey quartz grains (Fig. 2.9b). The mineralization was associated with the growth of albite-hematite-actinolite-chlorite$_1$ and later K-feldspar-sericite (Figs. 2.13a-f). Intense albite alteration with oligoclase occurred early during stage 2, and became weaker towards stage 3, as K-feldspar started to develop. In general, K-feldspar formed after albite, and locally appears as reaction rims on albite grains (Fig. 2.13d). K-feldspar is commonly hematite-dusted, and together with hematite-dusted albite forms the red-pink feldspar alteration that characterizes stage 2 alteration zones.
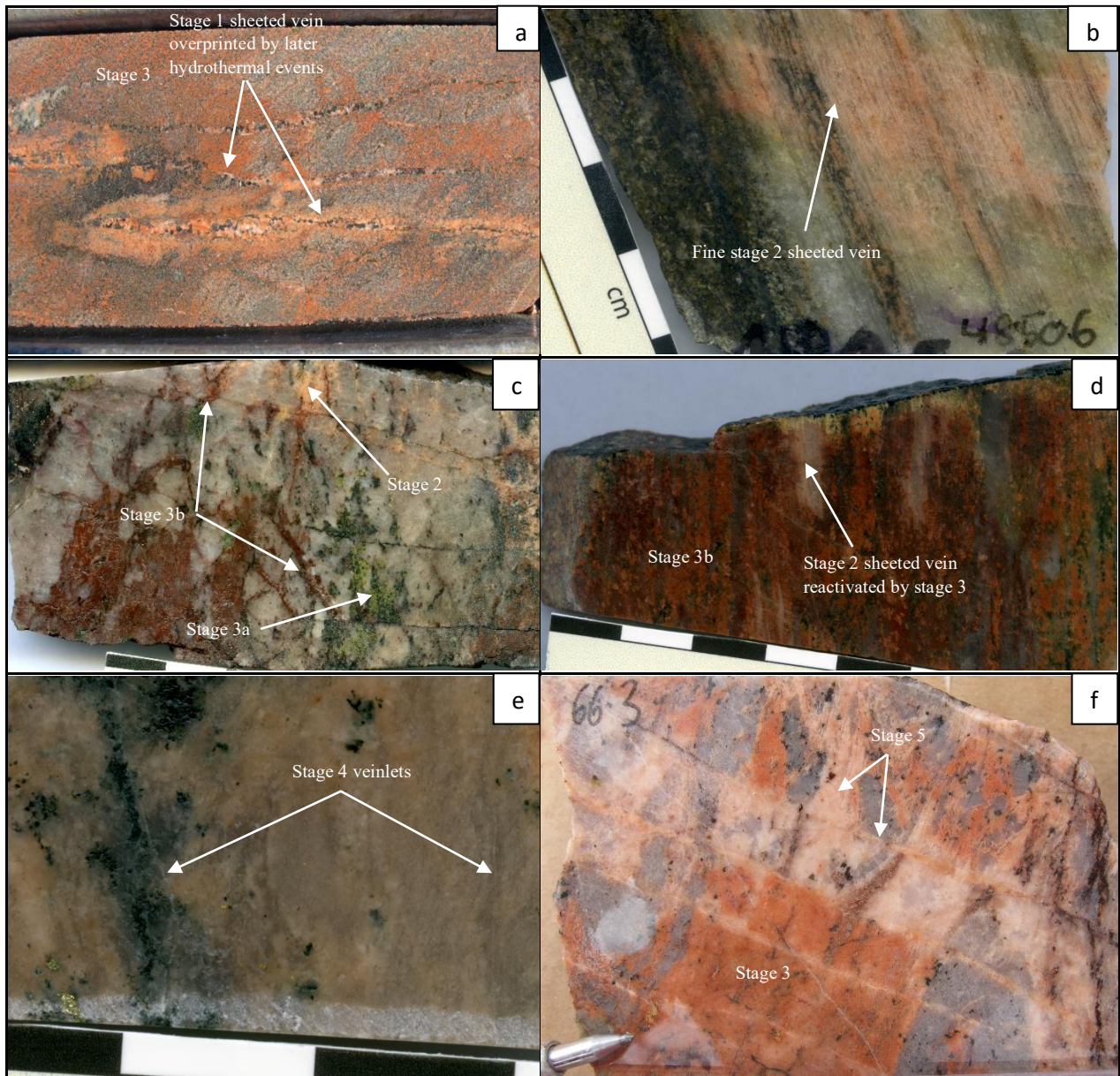
Figure 2.12. Examples of alteration assemblages in drill core from the high-grade ore zone, reflecting the paragenetic stages recognised in Tick Hill. (a) Stage 1 east-trending sheeted veins comprised of quartz, feldspar and magnetite, which were overprinted by stage 3 red rock alteration (RRA). (b) Stage 2, east-trending, finely laminated, sheeted veinlets and associated pink feldspar-quartz alteration haloes overprinting the S_1 fabric. Note that many of the sheeted veins parallel the mylontic fabric and resemble quartz-ribbon grains, thus masking their abundance. (c) High-grade gold mineralization in intensely silicified biotite schist, associated with east-trending, stage 2 sheeted quartz-feldspar veins (pink) overprinted by stage 3a chlorite-epidote and stage 3b hematite-rich alteration. (d). Stage 3 RRA pervasively altered silicified biotite schist with stage 2 sheeted veins. (e) Stage 4 veinlets of calcite overprinting earlier amphibole and quartz-feldspar alteration. (f) Stage 5 light pink feldspar reactivated the stage 1 and 2 sheeted veins and over printed stage 3 RRA.

Stage 2 sericite alteration is common in the mineralized zone and replaced earlier albite and oligoclase (Figs. 2.9b, 2.13a). The intensity of sericite alteration varies with proximity to stage 2 veining and is commonly associated with hematite, fine-grained gold, and minor $pyrite_1$ and chalcopyrite. Hematite formed as fine inclusions in feldspar, as grains replacing magnetite and as separate grains (Fig.

2.13g). Hematite commonly contains some titanium and it is intergrown with leucoxene. Stage 2 chlorite$_1$ replaced peak-metamorphic D$_{1-2}$ biotite (Figs. 2.13b,c), and consists of relatively Fe-rich (~30-35% FeO$_{total}$) ripidolite to picnochlorite. It is characterized by a relatively high Al$_2$O$_3$ (> 18.5 wt.%) and minor MnO (0.1-1.3 wt.%) and TiO$_2$ (< 0.2 wt.%) contents. Stage 2 actinolite is restricted to retrograde rims of stage 1 hornblende (Fig. 2.13a).

Within the ore zone, sulfide minerals are relatively rare, and they typically exhibit irregular, resorbed grain shapes of intergrown pyrite, pyrrhotite and chalcopyrite, with rare bornite, chalcocite, arsenopyrite, and unspecified Ni-Co-Cu-(±Fe) sulfides (possibly (Fe-) Carrollite) that formed during stage 2. Apart from the sulfides, fine gold grains are commonly associated with stage 2 and stage 3 Bi-selenides (e.g. Guanajuatite, Bi$_2$Se$_3$), which in many places are more common than sulfide. Where pyrite is present, texturally early stage 2 pyrite$_1$ is commonly Ni-rich, and overgrown by late stage 2 Se (±As)-rich pyrite$_2$ (stage 2) and late stage 2 and stage 3 Se-rich pyrrhotite.

Table 2.1. Peak-metamorphic mineral assemblages in major rock units.

Minerals	D$_{1-2}$ Biotite schist	D$_{1-2}$ Calc-silicate	D$_{1-2}$ Amphibolite	D$_{1-2}$ Qtz-fsp mylonite
Sillimanite	—			
Biotite	▬ (dominant)		- - - (minor)	
Amphibole	—	▬ (dominant)	▬ (dominant)	
Plagioclase	—	—	—	▬ (dominant)
K-feldspar		- - - (minor)		—
Quartz	—	—	- - - (minor)	▬ (dominant)
Diopside		—	—	
Scapolite		—		
Garnet (Almandine > Pyrope > Grossular)			—	
Apatite			- - - (minor)	
Magnetite	—	—	—	- - - (minor)
Ilmenite (±Mn)	—	—	—	- - - (minor)
Gold (inclusion)		- - - (minor)	- - - (minor)	- - - (minor)
Chalcopyrite	- - - (minor)	- - - (minor)	- - - (minor)	
Pyrite	- - - (minor)	- - - (minor)	- - - (minor)	

Quantity: Dominant ▬▬▬ ——— - - - Minor

Table 2.2. Retrograde mineral paragenesis for high-grade ore zones at Tick Hill

Minerals/ Deformation events	D₃					D₄
	Stage 1	*Stage 2*	*Stage 3*	*Stage 4*	*Stage 5*	*Stage 6*
Quartz	▬▬▬	─ ─ ─	─ ─ ─	─ ─ ─	▬▬▬	▬▬▬
Albite	▬▬▬	───	─		▬▬▬	─
Oligoclase	───	─ ─			───	─ ─
K-feldspar			─ ─ ─			
Hornblende	───	─ ─				
Actinolite		───	─			
Chlorite₁						
Chlorite₂		───	───			
Chlorite₃				───		
Epidote		─ ─	───			
Sericite			─ ─ ─			
Clay minerals (smectite-illite)			─	───		▬▬▬
Calcite				─ ─ ─		▬▬▬
Magnetite	─ ─ ─				─ ─ ─	
Hematite		───	▬▬▬	─ ─		
Leucoxene	─ ─ ─	─ ─				
Gold (Cg matrix)		───	─			
Gold (Fg matrix)		─ ─ ─	─ ─	─ ─		
Gold (Fractures)		───	───	─ ─		
Chalcopyrite	─ ─ ─	─ ─ ─	─ ─ ─	─ ─		
Bornite		─ ─				
(Fe-) Carrollite ? (Ni-Co-Cu-S±Fe)		─ ─				
Pyrrhotite		─ ─ ─	─ ─			
Pyrite₁		─ ─				
Pyrite₂			─ ─			
Pyrite (undifferentiated)				─ ─ ─		─ ─ ─
Guanajuatite, Bi₂Se₃		───	───	─ ─		
Junoite, Pb₃Cu₂Bi₈(S,Se)₁₆				·······		
Cerromojonite; CuPbBiSe₃				·······		
Molybdomenite; PbSeO₃				·······		

Quantity: Dominant ▬▬▬   ─── ─ ─ ─ ······· Trace

Stage 3 alteration is a progression of stage 2 and involved strong green-blue chlorite₂-epidote alteration (stage 3a, Fig. 2.12c) followed by pervasive clay-hematite alteration that overprints the earlier assemblages (stage 3b, Figs. 2.12c-d). The intensity of this alteration as seen in drill core is related to the fracture density and the lithological composition, and, more specifically, the amount of primary (D₁₋₂ and early D₃) plagioclase and magnetite. Stage 3 alteration is associated with gold, which could have

been either remobilized from earlier gold or newly introduced. Alteration minerals include illite and smectite (Appendix 1; Geological Survey of Queensland, 2015), hematite, and leucoxene (after magnetite). Stage 3, chlorite$_2$ formed in spatial associated with gold (Fig. 2.13e) and in the chlorite$_2$-epidote shell surrounding the ore zone. Chlorite$_2$ mostly forms non-orientated clots and is commonly intergrown with epidote, and both minerals have irregular (partly resorbed) grain shapes (Fig. 2.13f). Chlorite$_2$ is relatively Fe-rich (mainly at 25-30% FeO$_{total}$) brunsvigite to diabantite with intermediate Al$_2$O$_3$ (14-19 wt.%) and minor MnO (< 0.25 wt.%), and TiO$_2$ (< 0.2 wt.%) contents.

Stage 4 alteration is characterized by the formation of micro-veins of calcite-quartz±chlorite$_3$ that cut across the S$_1$ fabric (Fig. 2.12e), as well as the continued formation of clay minerals. It is important to note that such veinlets are relatively uncommon, and carbonate growth during stage 4 is not pervasive. Mg-rich stage 4 chlorite$_3$ is locally intergrown with calcite, and is Fe-poor (~10-35% FeO$_{total}$) diabantite to penninite characterized by a low Al$_2$O$_3$ (13-14 wt.%) contents without MnO or TiO$_2$. Stage 4 veins are associated with the deposition of minor gold, bismuth selenide, chalcopyrite (Fig.13h), pyrite and rare Cu-Pb-Bi selenides that resemble junoite (Pb$_3$Cu$_2$Bi$_8$(S,Se)$_{16}$), cerromojonite (CuPbBiSe$_3$) and clausthalite (PbSe). Stage 4 calcite is generally pure CaCO$_3$, but occasionally contains up to 0.5 wt.% MnO.

Stage 5 alteration postdates mineralization and involved the localised growth of late-D$_3$, pale pink feldspar and minor quartz, magnetite, specularite, and titanite (Fig. 2.12f). Feldspar alteration is concentrated along fracture zones that vary in width from a few decimeters to over 20 m, and it resulted in the formation of vein- or dyke-like features (Fig. 2.12f). These are common in both hanging wall and footwall sequences. Assay values from drill core indicate that stage 5 feldspar veins and dykes do not contain gold, and where stage 5 veins intersect mineralization, gold was depleted.

The youngest hydrothermal event at Tick Hill, defined as *Stage 6*, involved the formation of carbonate-quartz-clay assemblages along late veins and D$_4$ faults (Fig. 2.7h). In drill core, stage 6 alteration occurs in both footwall and hanging wall sequences. The veins commonly constitute infill along fault breccia with vuggy quartz, calcite, green clay minerals and minor pyrite.
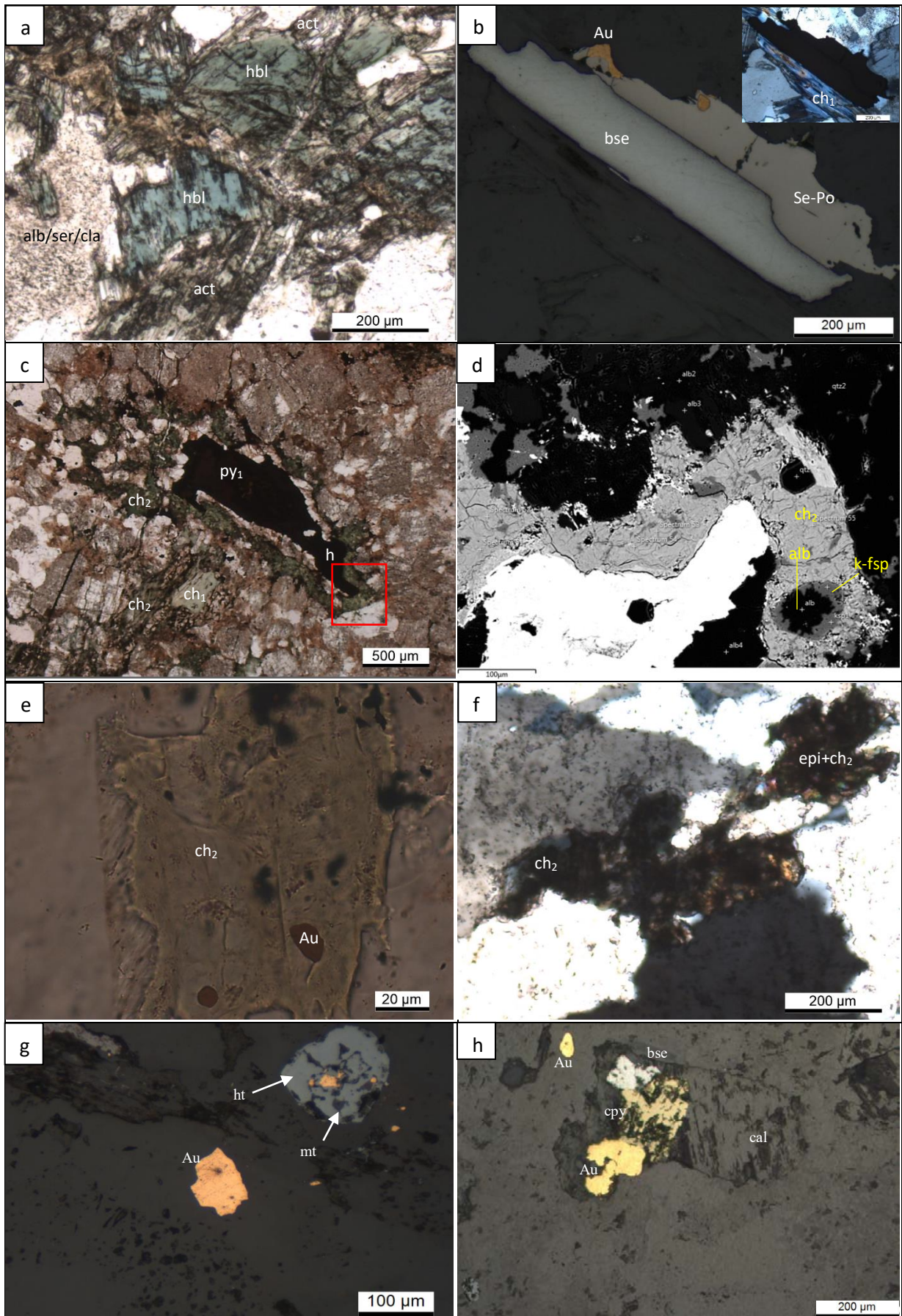
Figure 2.13. Thin section and SEM images of alteration assemblages associated with gold (including stages 1 to 4). (a) Stage 2 actinolite rimmed and replaced stage 1 hornblende that formed along micro veins, with stage 3 clay minerals replacing stage 1 and 2 albite. (b) Stage 2 chlorite$_1$ replacing earlier biotite and was associated with, gold, bismuth selenide (bse) and Se-pyrrhotite (Se-Po). (c) Zoned coronal reaction rim of stage 3 green chlorite (ch$_2$), albite and quartz around an early coarse-grained pyrite (py$_1$). The matrix assemblage preserves earlier, stage 2 chlorite$_1$ (ch$_1$); the red box shows the area shown in (d). (d) SEM image showing more details of the reaction textures in (c) with early stage 3 albite inter-grown with chlorite$_2$ being replaced by later stage 3 K-feldspar. (e) Inclusion of fine-grained gold inside stage 3, chlorite$_2$ (ch$_2$). (f) Stage 3, chlorite$_2$ (ch$_2$) intergrown with epidote (epi). (g) Reflected light image of gold (Au) associated with stage 2 and 3 hematite (ht) after stage 1 magnetite (mt). (h) Stage 4 gold (Au), chalcopyrite (cpy) and bismuth selenide (bse) intergrown with calcite (cal; reflected light).

2.5. Discussion

Since its discovery, intensive exploration in the region around Tick Hill has demonstrated that the deposit has no obvious extensions and, therefore, appears to be unique. What makes it different from other gold deposits in the Mt Isa Block is the high-grade, concentrated nature of the gold mineralization hosted in high-grade metamorphic rocks, the virtual lack of significant enrichment in other metals, the low sulfide content, and the presence of Bi-selenides. As such Tick Hill does not comfortably match the ore deposit models for either gold-rich IOCG deposits (e.g. Williams et al., 2001, 2005; Groves et al., 2010; Duncan et al., 2014) or orogenic lode gold occurrences (e.g. Goldfarb et. al., 2005; Danero et al., 2013).

In mapping the deposit and its associated structure, paragenesis and alteration assemblages a number of controlling factors have been identified that influence how gold-bearing fluids at Tick Hill may have moved to trapping sites, and how these fluids interacted with the host rock to deposit gold. These controls include lithological and structural controls as well as the nature of the far field stress, and the potential role of intrusive activity.

One important and puzzling feature about the Tick Hill deposit is the evidence for texturally early (D$_{1-2}$) and late (D$_3$) gold, together with indications that early gold and sulfide mineralization may have been remobilized (Fig. 2.9), which has led to a variety of mineralization concepts in past exploration campaigns (Tedman-Jones, 2001). The implications for the timing and origin of the Tick Hill deposit will be discussed in more detail below.

When discussing the mineralization events we will make reference to early and late gold. With respect the late gold phase it is important to bear in mind that the evidence shows that gold was mobile during D$_3$ stages 2-4, and that early gold was remobilized. However, we cannot be certain that the late gold stage involved the introduction of new gold.

2.5.1. Controls on the distribution of mineralization at Tick Hill

2.5.1.1. Lithological controls

Mineralization at Tick Hill is not restricted to any one stratigraphic horizon, and the high-grade ore envelope transgresses different lithologies including quartzite, quartz-feldspar mylonite, calc-silicate gneiss, amphibolite and biotite schist (Fig. 2.3). All of these lithologies are characterized by strong-silicification that predated the main stage of mineralization. Thus, from a litho-chemical perspective there does not appear to be a single lithology (e.g., an Fe-rich lithology) that was especially conducive to the precipitation of gold, i.e. it is unlikely that chemical interaction between the host rock and a ligand carrying the gold was of great importance in trapping gold. Having said this, the lithologies in the area contain magnetite, in places at high concentrations, and the high-grade ore zone is characterized by a clear overprint of hematite replacing magnetite. Much of this magnetite formed early (during D_1 and D_3 stage 1 alteration; Table 2.1) as the product of metamorphism and early metasomatism, and its presence clearly played a role in the hematite alteration, and by extension, possibly gold. Thus, early gold precipitation during D_1 may have involved a reaction between magnetite and the altering high temperature fluids, but direct textural evidence for this has not been found.

The most characteristic feature of the high-grade ore zones in all lithologies is the high degree of silicification, which occurred both early (D_1) with silicification concentrated along the hanging wall quartzite and late (D_3) with the formation of a dense network of syn-D_3, laminar veins that are mostly thin (< 0.5 cm) and both parallel and transecting the dominant underlying S_1 mylonitic fabric. The fine, laminar D_3 veins have the appearance of quartz ribbon grains thereby masking the extent of their development in quartz-feldspar mylonite. Sodic, and potassic alteration with the development of albite and later K-feldspar-sericite was part of this process. In most places micro-fractures associated with the veining were healed, but their imprint remains visible as trails of fluid inclusions, alteration minerals, and gold grains.

Thus, the main lithological control on the configuration of the deposit with respect to the late gold stage and the lower temperature D_3 alteration events appears to have been mechanical in nature, in which strongly silicified, and, therefore, more competent lithologies were preferentially fractured. The competency of the lithologies resulted in part from the high-grade metamorphic nature (i.e. coarse-grained, granoblastic, mica-poor) of the rock in combination with the effects of at least two periods of pervasive silicification (early D_1 and early D_3) that affected the ore zone prior to D_3 fracturing and mobilization of the gold.

2.5.1.2. Structural controls

The geometry of the Tick Hill deposit is controlled by structures. $D_{1,2}$ shearing, folding and transposition led to the formation of tight intrafolial folds and the foliation truncation plane, which occur as macroscale shear bands; a phenomenon common in high-grade gneiss belts (e.g. Dirks and Wilson, 1995; Passchier and Trouw, 2005). It also included the formation of laterally discontinuous mylonitic quartz-rich zones interpreted as silicified and altered, syn-D_1 shear horizons (e.g. Laing, 1993; Tedman-Jones, 2001) represented in Tick Hill by the hanging wall quartzite. These structures provided the architecture on which the gold mineralization was imprinted.

On the scale of the deposit (i.e. 100 m scale) the distribution of the ore zone coincided with a D_1 foliation truncation plane (Fig. 2.3), and early gold was probably concentrated along this surface. The D_1 foliation truncation plane was reactivated during D_3, as part of a network of faults and veins that created the fluid pathways through which later hydrothermal fluids were channeled that had the capacity to remobilize or transport gold.

Exploration reports for the deposit have suggested that the linear, east-northeast-plunging, high-grade ore zone parallels the dominant mineral elongation lineation (L_{1x}) and this has been used as an argument for early gold mineralization (e.g. Choy, 1994; Oliver, 1998). Our observations indicate that the linear high-grade ore envelope more-or less parallels the L_{1x} mineral lineation, but it also coincides with the orientation of the intersection lineation between two sets of D_3 faults and associated veins (i.e. north-northeast-trending and east-trending sets; Fig. 2.6c). The main north-northeast-trending fault parallels the D_1 foliation truncation plane and the mylonitic fabric west of the fault, and the high-grade ore envelope coincides with it. The east-trending fracture set provides a second order (10 m scale) control on D_3 fluid migration. The coincidence of low-grade (<0.1 g/t) ore envelopes with some of these east-trending fractures away from the main ore zone, indicate that at least some of the gold moved along these fractures during D_3; the question is "by how much ?".

On the scale of individual outcrops, high-grade gold domains are dominated by numerous, laminar D_3 fractures that either parallel the main S_1 mylonitic fabric or occur as steep, east-trending partings to create the stock work vein pattern that is texturally associated with late gold. Gold occurs inside D_3 fractures and veins, and is commonly intergrown with D_3 alteration assemblages, linking the distribution of gold to D_3 structures as seen today on mm- to m-scales. However, coarse gold aligned in S_1 is commonly surrounded by a halo of fine gold, suggesting that early gold re-mobilized during D_3 did not necessarily travel far to be deposited again as late gold.

The textural observation that late gold may not have moved far, taken together with the spatial coincidence of the ore body with L_{1x} and the D_1 foliation truncation plane, and the sharp boundary of

the high-grade ore shell, indicate that gold remobilization during D_3 may only have had a limited spatial effect. It suggests that the large-scale distribution of gold at Tick Hill must be understood in terms of controlling D_1 structures.

2.5.2. The stress field during mineralization

The nature of the stress field at the time of mineralization may have provided a further control on gold deposition. Early models for the Tick Hill deposit have suggested that the mineralization formed during D_1 in an extensional environment (e.g. Laing, 1993; Choy, 1994). Later, Tedman-Jones (2001) suggested that gold was controlled by activity on the Plumb Mt. and Mt. Bruce faults (Fig. 2.2a), due to the east-west compression during D_3 (Forrestal et al., 1998).

The strongly annealed and complex nature of $D_{1,2}$ structures and lack of kinematic indicators precludes reliable statements regarding the nature of the stress field during deposition of early gold. This is different for D_3 when late gold was deposited. The shear indicators that exist along the main north-northeast-trending D_3 fault suggest a sinistral-normal sense of movement, whilst the east-trending D_3 faults that are well exposed in the northwest corner of the pit, preserve clear normal components of movement (Fig. 2.7e). Given that the mineralization of late gold can be linked to these faults, both within the pit and in drill core, D_3 alteration and mineralization probably occurred during extension. The cause of extension at Tick Hill during D_3 is unresolved. It could reflect a localized effect, e.g. extension above an intrusive body, or it could have resulted from a regional extensional event.

2.5.3. The potential role of intrusions

Exploration reports in the early 1990s have suggested that early gold mineralization was caused by the syn-D_1 emplacement of granites belonging to the Tick Hill intrusive suite (e.g. Tedman-Jones, 2021). This potentially included the quartz-feldspar mylonite that hosts much of the gold at Tick Hill. However, a genetic link between these strongly deformed and altered granites and early gold is hard to be proved other than pointing at a spatial correlation.

Arguments for possible intrusive activity during the formation of late gold are stronger. The occurrence of pegmatite veins and quartz-feldspar metasomatism in the high-grade ore zones, as well as the apparent association of gold with Bi-Cu and oxidizing fluids, can be interpreted as indications of intrusion-related gold mineralization (e.g. Thompson et al., 1999; Hart and Goldfarb, 2005). Aeromagnetic data collected by MIM during their exploration efforts in the 1990s showed that the Tick Hill orebody is located at the northeast margin of a 3x2 km, oval shaped magnetic low that was interpreted as a possible concealed intrusion (Nano, 1999), potentially linking mineralizing fluids to a granite intrusion at depth (Tedman-Jones, 2001). Other than the late pegmatite bodies describe here, no

late-tectonic granite bodies were found in the area (Wyborn 1997; Laing, 1993). The late pegmatite intrusions around Tick Hill are granitic in composition and were emplaced during D_3. The stage 2 (D_3) feldspar-rich sheeted veins are similar in composition and relative timing as the late pegmatite veins, and they are common in drill core below the ore zone. These sheeted veins occur with fracture zones, and in part involved a metasomatic overprint of the surrounding gneiss. They share the same deformation textures and are associated with similar alteration haloes as the late pegmatite bodies visible in the pit, and therefore, late pegmatite and late gold mineralization could be related to syn-D_3 igneous activity. Oxygen isotope data obtained from lithologies in and around the deposit, have been cited as evidence for an intrusive fluid (e.g. Choy, 1994). However, the $\delta\,^{18}O_{VSMOW}$ values vary little (+10.2 to +12.9‰, Hannan, 1994) across a variety of rock types and veins, and they do not unequivocally reflect a magmatic source (e.g. Oliver et al., 2004).

A further argument that can be made for the possible involvement of an intrusive body at depth during late gold mineralization is the stockwork-like geometry of the fracture-networks and veins that host the gold at Tick Hill (Figs. 2.7c,e). Vein distribution patterns can reflect the broader geological setting during fluid migration. For example, intrusion-related, low- and high-sulfidation gold deposits that formed from fluids released by a causative intrusion typically display widespread stockwork veining across all lithologies (Corbett and Leach, 1998; Thompson et al., 1999; Corbett 2002; Rowe and Zhou, 2007; Goldfarb and Groves, 2015; Blenkinsop et al., 2020), rather than showing a systematic distribution of secondary structures near a master fault typical for orogenic gold deposits (e.g. Colvine et al., 1988; Goldfarb et al., 2005; Dirks et al., 2013). At Tick Hill, the mineralized D_3 veins, fracture networks and associated breccia zones are highly localized and stock-work like, whilst any through-going controlling D_3 shear zones are absent. Additionally, the five different stages of alteration and veining observed during D_3, suggest that brecciation and fracturing was a process that repeated itself several times, and involved a number of fluid pulses as the temperature of the altering fluid was cooling (Table 2.2). These observations are consistent with the presence of an igneous intrusion below Tick Hill, which could have driven episodic fluid flow through a network of D_3 structures and remobilized early gold, and/or introduced late gold.

2.5.4. Timing of mineralization

Although most of the mineralization at Tick Hill when viewed on mm- to m- scales is related to D_3 fracture zones and associated laminar veins and quartz-albite-hematite-chlorite alteration (Table 2.2), not all observations fit this pattern. In particular, the presence of coarse-grained, granoblastic gold inclusions in seemingly unaltered peak-metamorphic hornblende and clinopyroxene grains that are aligned within S_1 contradicts D_3 gold mineralization. The presence of early gold in peak-metamorphic minerals was cited by Choy (1994), and has led to speculation during the early exploration stages that the mineralization must have predated the main D_{1-2} events (Laing, 1993; Oliver, 1998; Tedman-Jones,

2001). In various exploration reports, it was suggested that the original source of mineralization could have been sedimentary-alluvial, syn-sedimentary epithermal, or associated with early stage intrusions that were subsequently sheared and mylonitised (Laing, 1993; England, 1993, 1995; Choy, 1994; Oliver, 1998). It is worth looking at each of these scenarios.

If a significant amount of the gold formed prior to or during D_1 it is hard to explain the highly concentrated nature of the mineralization considering the intensity of the S_{1-2} mylonitic, transposition fabric and D_3 metasomatic overprint, unless the early gold forming event itself was highly localized. Regional exploration along strike, in litho-stratigraphic units that are similar to those hosting mineralization at Tick Hill, have not yielded any significant gold enrichment. This would make it unlikely that a significant amount of the gold at Tick Hill would have formed as alluvial gold in a sedimentary environment, or that it was associated with early intrusions, since both of these mechanisms would have likely resulted in a more dispersed distribution of early gold (e.g. Robb and Robb, 1998; Hart and Goldfarb, 2005; Tucker et al., 2016).

The most plausible explanation for the confined early deposition of gold, although based on limited evidence, has been the suggestion that gold was deposited from magmatic fluids in an extensional fault jog along D_1 shears that are represented by the quartzite ridges (e.g. Laing, 1993, Oliver, 1998; Tedman-Jones, 2001), with fluids moving along the L_{1x} mineral elongation direction. This would have happened at the same time that granite was emplaced, which is represented by the quartz-feldspar mylonite that hosts much of the mineralization. Mapping of the quartzite ridges in the Tick Hill area has demonstrated that many of them transgress the dominant gneissic layering, and are strongly metasomatised (e.g. magnetite rich) with lensoidal geometries, gradational margins and fringed terminations suggesting alteration fronts (Coughlin, 1993; Laing, 1993). Few unequivocal sedimentary structures have been described from any of the quartzite ridges in the region, and many are characterized by extensive micro-veining, brecciation and silicification, largely masked by later recrystallization and metasomatism. This is the case for the hanging wall quartzite at Tick Hill, which was, therefore, interpreted as a strongly silicified metasomatised D_1 shear zone with early gold enrichment accompanying silicification in a D_1 dilational jog (e.g. Coughlin, 1993; Laing 1993; Oliver, 1998).

In spite of overwhelming structural evidence that the host rocks are mylonitic, the laminate textures in the Tick Hill ore zone have also been interpreted as primary varve-like deposits from silica gels in an epithermal environment (e.g. England, 1995). This interpretation followed suggestions of an epithermal exhalative origin for the gold-rich IOCG deposits at Starra (e.g. Davidson et al., 1989) ~60 km east of Tick Hill, but there is no evidence to support this.

Given the intensity of the later deformation and D_3 metasomatism, it is impossible to confidently pick the exact model that resulted in the deposition of early gold at Tick Hill. Structural arguments

presented above suggest that the large-scale geometry of the ore zone is primarily controlled by D_1 structural elements, and that D_3, whilst pervasive at outcrop scales, only resulted in localized remobilization of early gold. These observations suggest that most if not all the gold at Tick Hill is early, even though the bulk of the mineralization when viewed in drill core, hand specimen or thin section is hosted by D_3 structures, and has, therefore been remobilized from early gold.

2.5.5. Constraints on the mineralizing fluids and mineralization style

One of the characteristic alteration features associated with late gold mineralization at Tick Hill is the destruction of the magnetic signature in the lithologies that host the gold, as a result of the replacement of D_{1-2} and stage 1 magnetite by hematite (Fig. 2.8). The abundance of hematite over magnetite in association with gold reflects the strongly oxidized nature of the D_3 hydrothermal fluids. In spite of this, the immediate hanging wall to the orebody is strongly enriched in magnetite, but most of this magnetite was texturally early, and probably associated with the formation of early gold, and it predated the pervasive late alteration and gold mineralization.

Similar to magnetite, sulfides appear to have been affected and largely resorbed in the high-grade ore zones, presumably by the same late stage (D_3), hydrothermal fluids. Gold observed in stage 2 to stage 4 assemblages, occurs everywhere as free gold, readily visible under the microscope, and generally associated with little or no sulfide. In some of the more mafic lithologies (e.g. amphibolite-bearing calc-silicate), gold occurs in spatial association with trace amounts of pyrite, chalcopyrite and pyrrhotite, but these sulfides are typically irregular, strongly embayed, and skeletal in shape, although in some places gold is intergrown with newly formed subhedral pyrite or pyrrhotite. Instead, gold is more commonly associated with Bi-selenides. These observations suggest that most sulfides represent the remains of older grains that may have formed with early gold and predated late gold mineralization when sulfide was largely resorbed and removed from the high-grade ore-zones by S-under-saturated fluids.

Pyrite, chalcopyrite and pyrrhotite patches are common in amphibolite and amphibolitic calc-silicate units in the hanging wall and footwall to the deposit. Although there is no obvious metal enrichment other than gold within the ore zone itself, a weak Co (> 30 ppm) anomaly has been observed, whilst the immediate footwall to the high-grade mineralized zone, typically showed enrichment in Cu (> 200 ppm). On a local scale, Cu and Co show a poor spatial correlation with gold in assay data, whilst Co and Cu correlate with each other and with Ni. The observed Cu-Co enrichment correlates with chalcopyrite-pyrite mineralization in the footwall. What is not clear is whether this chalcopyrite-pyrite mineralization formed with the late gold as part of the mineralizing fluids, or whether Cu and Co were present in the host rock prior to oxidizing fluids leaching the host rock of its metals during D_3. In other words, similar to magnetite being largely destroyed by the late stage oxidizing fluids, sulfides in the host rocks may have also been destroyed with S and Cu and to a lesser degree Co being removed from the

high-grade gold zone as early gold was remobilized at a more localized scale. The Cu-sulfides were subsequently redeposited along the edges of the mineralization, presumably as a result of the interaction of the mineralizing fluids with the ambient fluids. This would be consistent with the sulfide textures and the gold-only nature of the ore. It is also consistent with early gold being re-mobilised by the same fluids to be redeposited as late gold along D_3 structures.

Apart from hematite, the gold-rich zone is characterized by quartz-albite-oligoclase-K-feldspar-sericite alteration, which showed a temporal evolution from early sodic alteration dominated by albite (stage 1 and early stage 2) to later, more potassic alteration with the formation of K-feldspar and sericite (late stage 2 and stage 3). The ore zone is further characterized by a recrystallized granoblastic texture in quartzo-feldspathic rocks. The bulk of the gold as preserved today was deposited during D_3 in stage 2, with stage 3 and 4 mineralization being either due to the continued inflow of new gold, or the remobilization of stage 2 gold (Table 2.2). However, as argued above, even stage 2 gold probably largely originated from the remobilization of early gold, and little, if any, gold may have been introduced during D_3.

The alteration mineral assemblage that formed during stage 1 (i.e. magnesio-hornblende, albite, oligoclase) indicates that D_3 metasomatic events started at upper-greenschist facies conditions in the core of the alteration zone. The assemblages that formed during stage 2 (actinolite, albite, chlorite$_1$), stage 3 (chlorite$_2$, epidote, k-feldspar, sericite) and stage 4 (chlorite$_3$, calcite) indicate a progressive drop in temperature of the hydrothermal fluids. The intense hematite alteration, the formation of leucoxene and selenides, and the destruction of magnetite (Fig. 2.8) and sulfide indicate that the mineralized fluids were strongly oxidized and S-under-saturated during stages 2 and 3. Conditions may have varied somewhat with the localized formation of pyrrhotite after pyrite suggesting more reduced conditions in at least parts of the deposit. This type of textural variation could reflect the interplay of reduced mineralizing fluid with a more oxidized ambient fluid considering the regional prevalence of hematite as an alteration phase (e.g. Oliver, 1995; Skirrow and Walshe, 2002). The fact that carbonates are largely absent from the alteration assemblage would further suggest that the mineralizing fluids did not contain CO_2. These constraints on the fluid composition indicate that late gold was not transported as a bisulfide complex, but must instead have moved as halogen complexes at low pH conditions. This is likely to have involved chlorine as is common in IOCG deposits in the Mt Isa district and considering the presence of Cl in stage 1 amphibole (e.g. Williams et al., 2001, 2005; Williams and Pollard, 2001; Oliver et al., 2004). Thus, the late stage, low temperature mineralizing fluids that remobilized early gold during D_3 were saline and oxidized, a characteristic that has been linked to igneous activity (e.g. Oliver et al., 2004; Mark et al., 2006).

One conspicuous feature about the Tick Hill deposit is the presence of a range of selenide minerals and the corresponding general paucity of sulfides in direct association with gold. Selenide minerals are

relatively rare in mineral deposits because Se, which is strongly chalcophile, readily substitutes for sulfur in sulfide minerals. Deposition of selenides, rather than substitution in e.g. pyrite or chalcopyrite, therefore, requires specific conditions, and the selenide mineral assemblage places constraints on the nature the ore forming fluids as well as physical conditions of formation (e.g. Simon and Essene, 1996; Simon et al., 1997; Cook et al., 2009; Cabral et al., 2017). Bi-Cu-Pb bearing selenide deposits with hematite and rare sulfides have been described from vein deposits in schists, where they typically formed at relatively low temperatures from highly oxidized saline fluids within the hematite stability field at a low sulfur fugacity (e.g. Simon et al., 1997; Cabral et al., 2017). A high oxygen fugacity prevents the early incorporation of Se in sulfides and promotes the formation of selenides, which generally occurs between 65 and 300°C, and mostly below 150°C (Simon et al., 1997). Reconstructions of the palaeo-depth of most selenide-bearing deposits indicate that lithostatic pressures were probably less than 0.5 kbar (Simon et al., 1997). The formation of copper selenides require acidic or reducing environments (Cook et al., 2009). Thus, the presence at Tick Hill of Bi-Cu-Pb selenides in association with gold probably indicates a relatively shallow depositional depth at relatively low temperatures and further confirms the involvement of strongly oxidized, acidic, saline fluids in which gold and other metals (Bi, Cu, Ni, Co) were mobilized as chlorine complexes (Simon et al., 1997; Cook et al., 2009). Some of the selenides at Tick Hill contain minor Te as well, and the association Au-Bi-Te-Se, together with other chalcophile elements has been linked to a magmatic signature (e.g. Spooner 1993).

2.5.6. An alternative model for gold at Tick Hill; involvement of Kalkadoon basement

The alteration assemblage and structural setting at Tick Hill display some similarities with IOCG deposits in the Eastern Fold Belt of the Mt Isa Block (e.g. Williams et al., 2005), but these mostly relate to D_3 alteration and the mobilization of late gold. Similarities include the strong structural controls on mineralization, the prevalence of sodic alteration predating late gold mineralization and the shift from sodic to more potassic alteration as gold deposition progresses, the presence of abundant hematite and magnetite together with chlorite in association with gold, and the involvement of oxidized, acidic saline fluids (Williams, 1998; Williams and Pollard, 2001; Oliver et al., 2004; Williams et al., 2005; Groves et al., 2010; Mclellan et al., 2010). But there are important differences with classic IOCG deposits in the eastern fold belt (e.g. Groves et al., 2010). These include the absence of any significant copper mineralization, or any other significant metal enrichment for that matter, the absence of significant sulfide mineralization, the presence of Bi-selenides, and the absence of large volumes of concomitant felsic or mafic intrusions in the area at least during D_3 (Oliver et al., 2004; 2008). The high-grade metamorphic nature of the host rock, high gold-grade mineralization and extremely restricted nature of the deposit also differ from IOCG deposits in the Eastern Fold Belt. Thus, the geological setting of Tick Hill does not provide an easy match with any existing deposit type in the Mt Isa Province.

When considering the Au-rich nature of the Tick Hill deposit, its association with Bi and Se and extensive hematite-chlorite alteration, the Tick Hill deposit displays many similarities with some of the high-grade gold deposits (e.g. Nobles Nob, Eldorado; Skirrow and Walshe, 2002; Groves et al., 2010) in the Tennant Creek area of the Northern Territory, Australia. It is instructive to investigate these similarities in more detail, as it has implications for how to interpret the origin and timing of mineralization at Tick Hill.

The Tennant Creek gold field includes a large range of Au-Cu-Bi deposits that vary significantly in Au:Cu ratios, Fe-oxide and sulfide mineralogy and isotope compositions, and include reduced Cu-rich, and oxidized Au-rich end-members (Skirrow and Walshe, 2002; Groves et al., 2010). The Cu-rich endmember deposits have been considered as possible IOCG deposits (e.g. Skirrow, 2000; Williams et al., 2005). In contrast, the Au-rich end-member deposits do not comfortably fit in the IOCG family (Groves et al., 2010), but they compare favorably with Tick Hill (e.g. Groves et al., 2010). Mineralization in the Tennant Creek area comprises native gold, chalcopyrite, and a range of bismuth minerals including S-Se-Te-Cu-Pb-bearing Bi sulfosalts (Large, 1975; Wedekind et al., 1989; Skirrow and Walshe, 2002). The Au-rich deposits (e.g. Juno, Argo, Nobles Nob, Eldorado) tend to have minor to abundant hematite alteration of pre-existing magnetite and widespread chlorite, muscovite, pyrite alteration (Skirrow and Walshe, 2002). The mineralization is typically hosted by structurally controlled, magnetite/hematite-rich, hydrothermal replacement bodies referred to as 'ironstones' that formed at temperatures of 350-400°C and 2.5-5.0 kbar (Skirrow and Walshe, 2002). These 'ironstones' are hosted by ca. 1860 Ma, low-grade metasedimentary turbidites. The Au-Cu-Bi mineralization was introduced into the ironstone bodies at slightly lower temperatures (~300°C) during the regional Tennant Event at 1860-1845 Ma (Compston and McDougall, 1994; Skirrow and Walshe, 2002). The Au-rich deposits have been linked to the reactions between magnetite ironstone and oxidizing brines that mixed with pulses of intermediate-oxygen fugacity, low- to moderate-salinity ore fluids to deposit gold and Bi sulfosalts whereas Cu deposition was suppressed by increasing solubility of Cu in the mixed fluid (Skirrow and Walshe, 2002). Additional significant 'non-ironstone' deposits of Au-Cu-Bi mineralization occur within shear zones outside the ironstones (e.g. Orlando East, Navigator 6; Skirrow, 2000; Skirrow et al., 2019). Some of the shear zone hosted deposits were dated at ca. 1660 Ma and are thought to have formed through remobilization of the main ironstone-hosted Au-Cu-Bi ore bodies with Au moving up to hundreds of meters (Skirrow et al., 2019). A ubiquitous feature of the gold-bearing veins is the presence of chlorite alteration adjacent to the veins together with hematite, monazite and chalcopyrite.

At Tick Hill it would appear that highly oxidized, Bi-Se-bearing hydrothermal fluids were capable of transporting gold to its current depositional site. The presence of gold in hornblende and clinopyroxene grains that are aligned in the D_1 fabric, indicates that that this gold mineralization may

originally have occurred early. If one considers the parallels that exist with the Tennant Creek gold field, we suggest that there is a genuine possibility that early high-grade Au-Cu-Bi mineralization of the oxidized Au-rich end-member type (Skirrow and Walshe, 2002) may have formed either before or during D_1. During $D_{1,2}$ this early gold mineralization was aligned with or formed in parallelism with D_1 structures and it overprinted syn-D_1 intrusions now preserved as quartzo-feldspathic mylonite. If this early gold mineralization was subsequently reworked and overprinted by low temperature hydrothermal fluids with the capacity to remobilize metals including gold, then the Tick Hill deposit could represent a remobilized, older high-grade gold deposit. The fluids involved in this remobilization were highly saline, oxidized fluids that gave rise to the extensive regional albite-hematite alteration in the area (e.g. Oliver 1995). These fluids would not necessarily have to be gold-rich, but could have scavenged their metal load from the older deposits in a way described for the late Au-vein deposits in the Tennant Creek area (Skirrow et al., 2019).

2.6. Conclusion

Four deformational events have been recorded at Tick Hill and the surrounding rocks including: (1) regional D_1 shearing resulting in the formation of mylonitic textures at high-grade metamorphic conditions; (2) D_2 upright folding that formed the Tick Hill syncline, again at high-grade metamorphic conditions; (3) D_3 oblique-normal faulting with extensional veining and widespread quartz-feldspar alteration near Tick Hill and subsequent regional red rock alteration; and (4) D_4 strike-slip faulting with cataclasite textures. The ore zone at Tick Hill parallels a D_1 foliation truncation plane that was reactivated during D_3 sinistral-normal faulting. Mineralization also approximately parallels the L_{1x} mineral elongation lineation, and the intersection lineation between sets of D_3 faults, with localized brecciation along the faults increasing with depth.

Key features of gold mineralization at Tick Hill include: (1) the high-grade, coarse-grained, gold-only nature of the deposit most of which was deposited in its current textural position during D_3 faulting and associated alteration (late gold); (2) the presence of an early, pre- or syn-D_1 stage of mineralization (early gold); (3) the restricted nature of the deposit, with an abrupt boundary between mineralized and non-mineralized zones; (4) a paucity of sulfides and other metals in the ore zone together with the presence Bi-selenides in association with late gold; (5) a prevalence of magnetite and hematite, with hematite concentrated in the ore zone; (6) early (D_1) high-temperature alteration assemblages characterized by magnetite and quartz, possibly associated with early gold; (7) late (D_3) low-temperature alteration assemblages characterized by proximal amphibole, albite, hematite, chlorite, epidote, sericite, illite, and minor calcite, and associated with late gold; (8) proximal mineralization coincided with D_3 brecciation and intense silicification, bounded by a strongly silicified zone and surrounded by a chlorite-epidote shell; (9) the presence of abundant laminar quartz veins, locally forming breccia associated with

late gold; (10) the involvement of strongly oxidized, acidic, saline, hydrous fluid during late (D_3) low-temperature alteration; and (11) a possible genetic relationship between post-tectonic pegmatite and late-stage alteration fluids.

In terms of alteration assemblages and structural setting the Tick Hill deposit shares many similarities with the ca. 1850 Ma, Au-Cu-Bi mineralization in the Tennant Creek area. In contrast, its high-grade gold-only nature, lack of significant Cu enrichment, presence of Bi-selenides and general absence of associated intrusions make it a unique deposit in the Mt Isa Block. Evidence of early mineralization and D_3 related remobilization of gold and sulfides suggest that early gold enrichment was responsible for the bulk of the mineralization and it was remobilized by later hydrothermal fluids to be deposited as late gold in suitable structural traps during D_3.

Chapter 3: Geochronological constraints on the geological history and gold mineralization in the Tick Hill region, Mt Isa Inlier

Abstract

The Tick Hill Gold deposit in the southern Mary Kathleen Domain of the Mount Isa Inlier is hosted in a strongly deformed, Mesoproterozoic volcano-sedimentary sequence intruded by pre- and syn-tectonic granites. Igneous rocks and quartzite from the Tick Hill region were dated to constrain the age of the lithologies, deformation events, and gold mineralization. LA-ICP-MS, U-Pb zircon ages for these rocks together with field relationship confirm the presence of: (1) 1850-1855 Ma granite belonging to the Kalkadoon Supersuite at ~10 km and ~4 km west of Tick Hill respectively; (2) 1770-1790 Ma, early syn-tectonic granite along the contact zone between mapped Argylla Formation and the Kalkadoon Supersuite west of Tick Hill, and later syn-tectonic leucogranite within the immediate vicinity of Tick Hill including the host rocks to gold mineralization; and (3) late-tectonic, 1520-1525 Ma pegmatite and associated hydrothermal activity in the Tick Hill area that resulted in the mobilization of gold. Quartzite ridges in the hanging wall and footwall of the orebody provide contrasting results with the youngest zircon population groupings at 1781±6 Ma and 1841±15 Ma respectively. Textural evidence suggests that much of the hanging wall quartzite is probably metasomatic in origin, and the 1781±6 Ma age group, which was derived from mostly prismatic, euhedral zircon, reflects the age of a heavily silicified quartzofeldspathic gneiss. Thus, the age of the youngest detrital zircon group, 1841±15 Ma, constrains the maximum age of the sequence at Tick Hill. Field evidence suggests that the 1770-1790 Ma granites intruded into the sedimentary sequence that hosts gold mineralization, indicating that the supra-custal rocks are at least 1790 Ma in age and should not be grouped as Corella Formation. These sediments were affected by intense shearing and upright folding between 1790 Ma and 1770 Ma and younger normal faulting and metasomatism around 1520-1525 Ma. Early gold was introduced during D_1 peak metamorphism at ca. 1770-1790 Ma while the later mineralizing events involved the new introduction of gold or the remobilization of pre-existing older gold around 1520-1525 Ma. One of the major outcomes of this study is that the old schist zones in the south Mary Kathleen Domain are prospective for gold mineralization. The extent of outcrop of these schists needs to be more accurately mapped.

3.1. Introduction

The Mount Isa Inlier is a highly mineralised geological terrain with world-class deposits of lead, zinc, and copper (Withnall and Hutton, 2013). Most major Pb-Zn deposits are concentrated in 1570-1660 Ma shale units in the western part of the inlier (Huston et al., 2005; Denaro et al., 2013). The bulk of IOCG mineralization is concentrated in the eastern part of the inlier where mineralization occurs in supracrustal rocks that are spatially associated with intrusions of the 1550-1490 Ma Williams

and Naraku Suites (Page and Sun, 1998; Perkins and Wyborn, 1998; Williams et al., 2005, Neumann and Fraser, 2007). In the central part of the Mt Isa Inlier, which includes the higher-grade gneisses of the Kalkadoon-Leichhardt Belt and adjacent rocks of the Mary Kathleen Domain (MKD), mineralization appears to be less abundant. Mineral deposits in the MKD include the world-class Dugald River Pb-Zn-Ag deposit, many smaller Cu-Au occurrences (e.g., Elaine Dorothy, Trekelano, Mount Colin, Overlander, Kalman), the Mary Kathleen U-REE deposit (Forrestal et al., 1998; Denaro et al., 2013), and the gold-only, high-grade Tick Hill deposit, which is the focus of this study. The Tick Hill deposit is a relatively small, but an extremely rich, gold-only deposit, and constitutes a unique mineralization style in the Mt Isa inlier. The timing of mineralization and links to other, IOCG-related gold deposits in the Mt Isa inlier have not been established, and the deposit is variably referred to as either an end-member IOCG deposit (e.g., Williams et al., 2005; Groves et al., 2010), or an orogenic, shear zone-hosted deposit (e.g., Denaro et al., 2013).

Compared to other parts of the Mt Isa Province, relatively little geochronological and stratigraphic work has been carried out in the MKD. The current interpretation of stratigraphy and structural evolution of the MKD, including associated mineralization, is largely based on work performed in the central MKD (e.g., Blake et al. 1984; Holcombe et al., 1991; Neumann et. al., 2006, 2009; Southgate et al. 2013; Withnall and Hutton, 2013). Far fewer geochronological constraints are available for rocks in the northern and southern parts of the MKD (e.g., Kositcin et al, 2019; Withnall, 2019; Bodorkos et al., 2020). Rocks in the MKD have been mainly attributed to ca. 1730-1780 volcano-sedimentary sequences (e.g., Oliver et al., 1991; Foster and Austin, 2008; Neumann et. al., 2009; Withnall and Hutton, 2013; Kositcin et al, 2019), with deformation attributed to 1755-1740 Ma extensional and 1600-1500 Ma compressional events (e.g., Holcombe et al., 1991, Blake and Stewart, 1992; Withnall and Hutton, 2013). The MKD is characterised by abundant 1730-1740 Ma Wonga and Burstall Suites. Intrusions of the younger Williams Suite are conspicuously absent (e.g., Kositcin et al, 2019; Withnall, 2019; Bodorkos et al., 2020). In the absence of good age constraints in the southern MKD, the volcano-sedimentary, sequences in the Tick Hill area have generally been correlated with the Argylla and Corella Formations further north (e.g., Blake et al., 1982; Wyborn, 1997; Withnall and Hutton, 2013; Withnall, 2019), whilst upright folding of high-grade gneiss around Tick Hill was linked to east-west compression during the Isan Orogeny by analogy with similar folding in the Mary Kathleen and Duchess areas (e.g., Holcombe et al., 1991, Oliver et al., 1991; Passchier, 1992; Choy, 1994). Blake (1980) and Blake et al. (1982) pointed out that care should be taken when making regional correlations, i.e. the high-grade Corella Formation west of the Wonga belt including gneisses in the Tick Hill area could actually represent pre-1860 Ma basement. The age of mineralization at Tick Hill remains unconstrained and has variably been linked to 1740 Ma extensional events and associated magmatism (Choy, 1994; Forrestal et al., 1998), or undefined younger (ca. 1530 Ma) intrusive activity (e.g., Rutherford, 1999; Tedman-Jones, 2000), with little direct evidence provided in support.

In this chapter, we present new U-Pb zircon ages and whole-rock geochemistry for a range of igneous and quartzitic units with variable relationships to the dominant gneissic fabrics in the Tick Hill area (i.e., pre-, syn- and post D_{1-2}). Samples were obtained from exploration drill core and from outcrops within a 10 km radius of the Tick Hill open pit (Fig. 3.1). In dating the selected rocks we aim to constrain: (1) the age of igneous events in the area; (2) the extent of Kalkadoon-Leichhadt Belt basement gneiss; (3) the age of the main stratigraphic units that host the Tick Hill deposit; (4) the timing of deformation events that affected the deposit; and (5) the timing of mineralization.

3.2. Geological setting

3.2.1. Regional geology

The Mt Isa Inlier preserves a complex mixture of bimodal igneous rocks and Meso-Proterozoic tectono-stratigraphic sequences that formed during a 400-million year period (1890-1500 Ma) in a series of discontinuous basins. These basinal sequences were affected by magmatism and metamorphism related to two major orogenic events, the Barramundi Orogeny (ca. 1870-1840 Ma) and the Isan Orogeny (1600-1500 Ma; Blake and Stewart, 1992; Withnall and Hutton, 2013). Based on the distribution and age of sedimentary sequences and intrusive igneous suites, the Mt Isa Province was subdivided into three north-trending tectonic domains (Blake, 1987; Withnall and Hutton, 2013): the Western Fold Belt; the Kalkadoon-Leichhardt Belt; and the Eastern Fold Belt (Fig. 1.1, Chapter 1). The Kalkadoon-Leichhardt Belt, represents an old (>1850 ma) basement high that exposes rocks affected by the Barramundi Orogeny. It is overlain by younger rocks to the west and east. Post-Barramundi, volcano-sedimentary cover sequences in the inlier have been interpreted as intracratonic rift-sag deposits (e.g., Blake and Stewart, 1992; Foster and Austin, 2008; Withnall and Hutton, 2013) and were described as three separate cover sequences separated by regional unconformities. The age and extent of the cover sequences were later refined with additional geochronological and stratigraphic work and the sequences were subsequently linked to the development of three 'superbasins' (Jackson et al., 2000; Scott et al., 2000; Neumann and Fraser, 2007; Foster and Austin, 2008; Neumann et al., 2009; Withnall and Hutton, 2013). Following the stratigraphic subdivisions as outlined in Foster and Austin (2008), the Mesoproterozoic cover sediments include Cover Sequence 1 (ca. 1870-1850 Ma) which predated the development of the superbasins, is largely composed of felsic volcanics and restricted to the Kalkadoon-Leichhardt Belt (Fig. 2.1). This is overlain by Cover Sequence 2 (ca. 1790-1690), which overlaps with the Leichardt (1800-1750 Ma) and Calvert (1730-1690 Ma) Superbasins and includes felsic volcanics of the Argylla Formation and calc-silicates of the Corella Formation that are prominent in the MKD (Fig. 2.1). Cover Sequence 2 is overlain by Cover Sequence 3 (1680-1590 Ma), which overlaps with the Isa Superbasin (1665-1575 Ma) and is distributed widely across the entire Mt Isa Province (Fig. 2.1). Development of the various superbasins was accompanied by igneous

activity, which involved extensive volcanism and the emplacement of bimodal igneous batholiths along north-trending belts. These include emplacement of the 1860-1850 Ma Kalkadoon Supersuite into basement gneiss of the Kalkadoon-Leichhardt Belt; the 1780-1720 Ma Wonga and Burstall Suites along the western margin of the Eastern Fold Belt and the 1675-1655 Ma Sybella Suite along the western margin of the Western Fold Belt (Fig. 2.1). In addition, post-tectonic suites of the 1550-1490 Ma, Williams and Naraku Suites were emplaced across much of the Eastern Fold Belt, during the final stages of the Isan Orogeny (Page and Sun, 1998; Withnall and Hutton, 2013).

Rocks in the Eastern Fold Belt were further subdivided into a series of mostly north-trending, unconformity and fault-bounded tectono-stratigraphic domains, the westernmost of which is the MKD (e.g., Withnall and Hutton, 2013). The MKD is bounded by the Pilgrim-Rose Bee Fault Zone to the east and comprises 1730-1780 Ma volcano-sedimentary rocks belonging to Cover Sequence 2 (Upper Leichardt Superbasin), which in the northern part of the domain are overlain by rocks of the Mount Albert Group of Cover Sequence 3 (i.e., Isa Superbasin; e.g., Scott et al., 2000; Foster and Austin, 2008; Fig. 2.1)). To the west of the MKD, rocks of Cover sequence 2 overly the Kalkadoon-Leichhardt basement and are intruded by granites and gabbros of the Wonga and Burstall Suites (Withnall and Hutton, 2013; Kositcin et al., 2019; Bodorkos et al., 2020).

The stratigraphic base of Cover Sequence 2 in the Kalkadoon-Leichhardt Belt consists of the ca. 1790 Ma Magna Lynn Metabasalt unit (Blake, 1987; Jackson et al., 2000; Foster and Austin, 2008; Carson et al., 2011; Withnall and Hutton, 2013), which is overlain by felsic volcanics of the 1770-1780 Ma Argylla Formation (Page, 1983; Neumann et al., 2009) that extends into the MKD (Fig. 2.1). The Argylla Formation is overlain by the ca.1755 Ma Ballara Quartzite (Blake, 1987; Neumann et al., 2006, 2009) and the 1730-1760 Ma Corella Formation that covers large parts of the MKD (Blake, 1980; Blake, 1987; Carson et al., 2009; Southgate et al., 2013; Withnall and Hutton, 2013; Fig. 2.1)). At the type locality northeast of Mary Kathleen, the Corella Formation consists of scapolite-bearing calc-silicate and amphibolite, with lesser marble, metapelite, quartzite, and felsic metavolcanics (Blake, 1987; Foster and Austin, 2008). The calc-silicates have been interpreted as metamorphosed, shallow water, mixed siliciclastic-carbonate platform sequences intercalated with evaporite deposits (e.g., Blake, 1987; Jackson et al., 2000; Foster and Austin, 2008).

In the Tick Hill region (Fig. 3.1a), rocks are dominated by calc-silicate and amphibolite, intercalated with quartzite and biotite-schist, which have been correlated with the Corella Formation to the north (Blake et al., 1982; Wyborn, 1997). However, it has been suggested that the metasediments around Tick Hill could represent pre-1860 Ma basement (Blake et al., 1980). Much of the quartzite in the area occurs along discontinuous ridges. Exploration reports mention that these quartzite ridges are characterized by early brecciation and veining, have diffuse boundaries and commonly transect the gneissic layering. Consequently, they were interpreted as early metasomatic alteration zones along

shears, rather than sedimentary units (e.g., Laing, 1993; Oliver, 1995). Felsic metavolcanics, which outcrop along a north-trending zone to the west of the calc-silicates (Fig. 3.1a) were assigned to the Argylla Formation (Blake et al., 1982; Wyborn, 1997). West of the Argylla Formation are a series of north-trending gneissic granites, which mark the transition into Kalkadoon-Leichhardt basement rocks (Fig. 3.1a; Withnall and Hutton, 2013). From east to west, these are the Saint Mungo Granite, the One Tree Granite, the Plum Mountain Gneiss and the Bird Well Granite (Fig. 3.1a; Blake et al., 1982; Wyborn, 1997), which were targeted for geochronology in this study. The metasedimentary units around Tick Hill were intruded by syn-tectonic granite sheets of the Tick Hill Complex, and the syn-tectonic Monument Syenite (Laing, 1993; Wyborn, 1997, Rutherford, 1999, 2000). Inliers of Saint Mungo Granite were locally mapped within intrusions of the Tick Hill Complex immediately west of Tick Hill (Fig. 3.1a; Rutherford, 1999, 2000). Together with the Saint Mungo and Bird Well granites the intrusions of the Tick Hill Complex were assigned to the ca. 1740 Ma Wonga and Burstall Suites (Wyborn, 1997; Rutherford, 1998, 1999). Post-tectonic (post-D_1) intrusions are limited to small outcrops of pegmatite and aplitic granite originally described as granite of unknown age (Blake et al., 1982, Wyborn, 1997) and later assigned to the Williams Suite (Laing, 1993; Rutherford, 2000).

The gneisses around the Tick Hill deposit record four major deformational events (e.g., Blake et al., 1982; Passchier and Williams, 1989; Oliver, 1995; Tedman-Jones, 2000; Chapter 2, this study). D_1 events involved the formation of an upper amphibolite facies mylonitic S_1 fabric associated with isoclinal intrafolial folds, a west-dipping lineation, and a possible east-up sense of movement. D_1 structures were interpreted to result from north-south extension around 1750-1730 Ma equivalent to what has been described for the Wonga-Shinfield zone further north (e.g., Passchier and Williams, 1989; Holcombe et al., 1991; Passchier, 1992; Oliver, 1995; Withnall and Hutton, 2013). During D_2, the S_1 mylonite fabric was folded to form a north-trending steeply dipping high-strain zone and associated tight upright folds that characterize the Tick Hill area (Laing, 1993; 1998; MacCready et al., 1998). The D_2 event resulted from east-west compression at high-grade metamorphic conditions during the Isan Orogeny (Oliver, 1995; Betts et al., 2006), based on correlations with structures in the Mary Kathleen and Duchess areas (e.g., Holcombe et al., 1991; Passchier, 1992). During D_{1-2}, rocks in the MKD were affected by high-temperature, low-pressure metamorphism (550-670°C, 3-4 kbar in the Mary Kathleen area), accompanied by the emplacement of the Wonga and Burstall granites (Oliver et al., 1991). Mineralization and related alteration generally overprinted the S_{1-2} fabrics, although gold has been described from inclusions in peak-metamorphic assemblages (Choy, 1994; Chapters 2 and 5, this study). This has led to suggestions that some of the mineralization may have had an early origin (e.g., Choy, 1994; Oliver, 1995; Tedman-Jones, 2000).
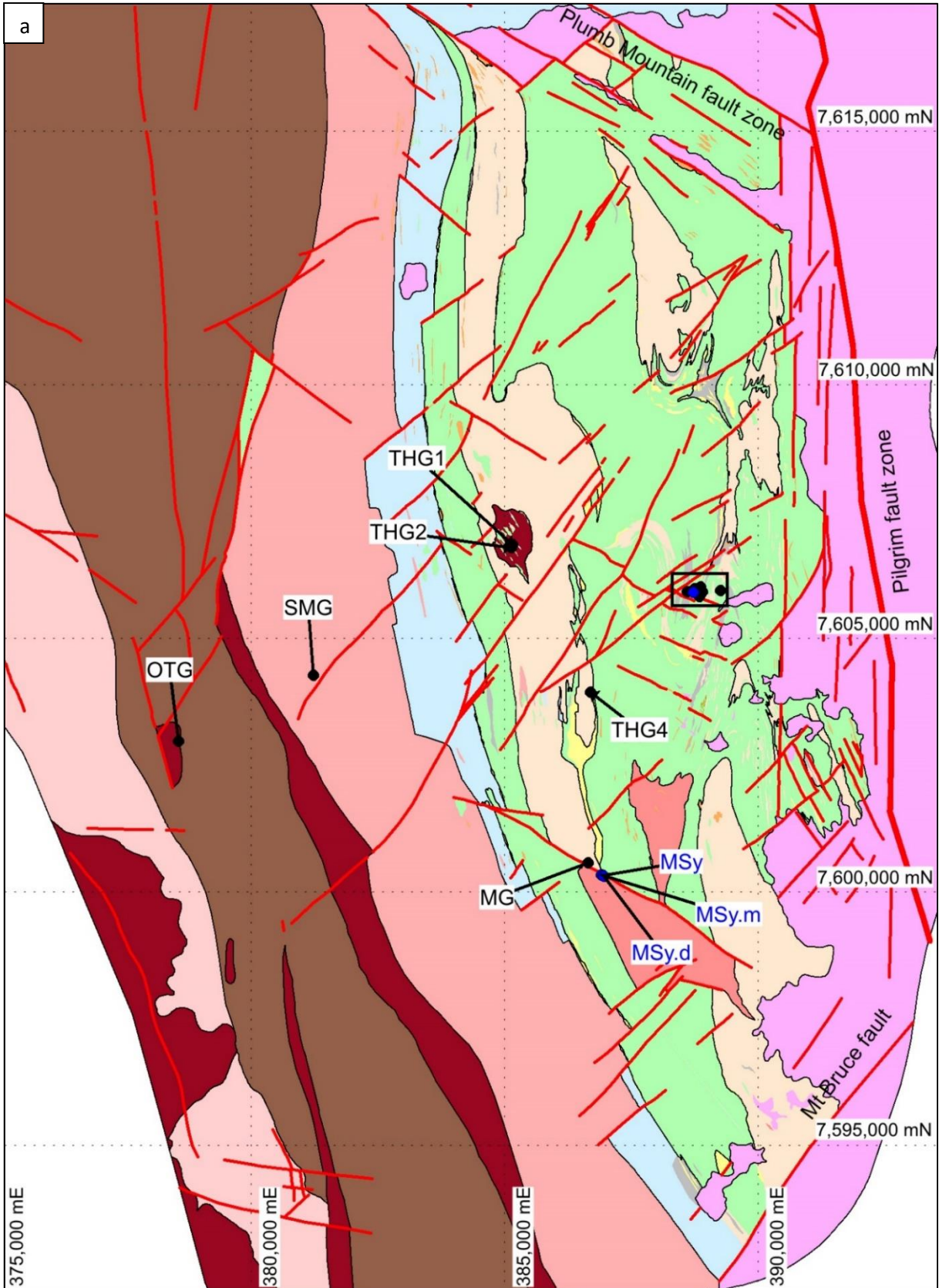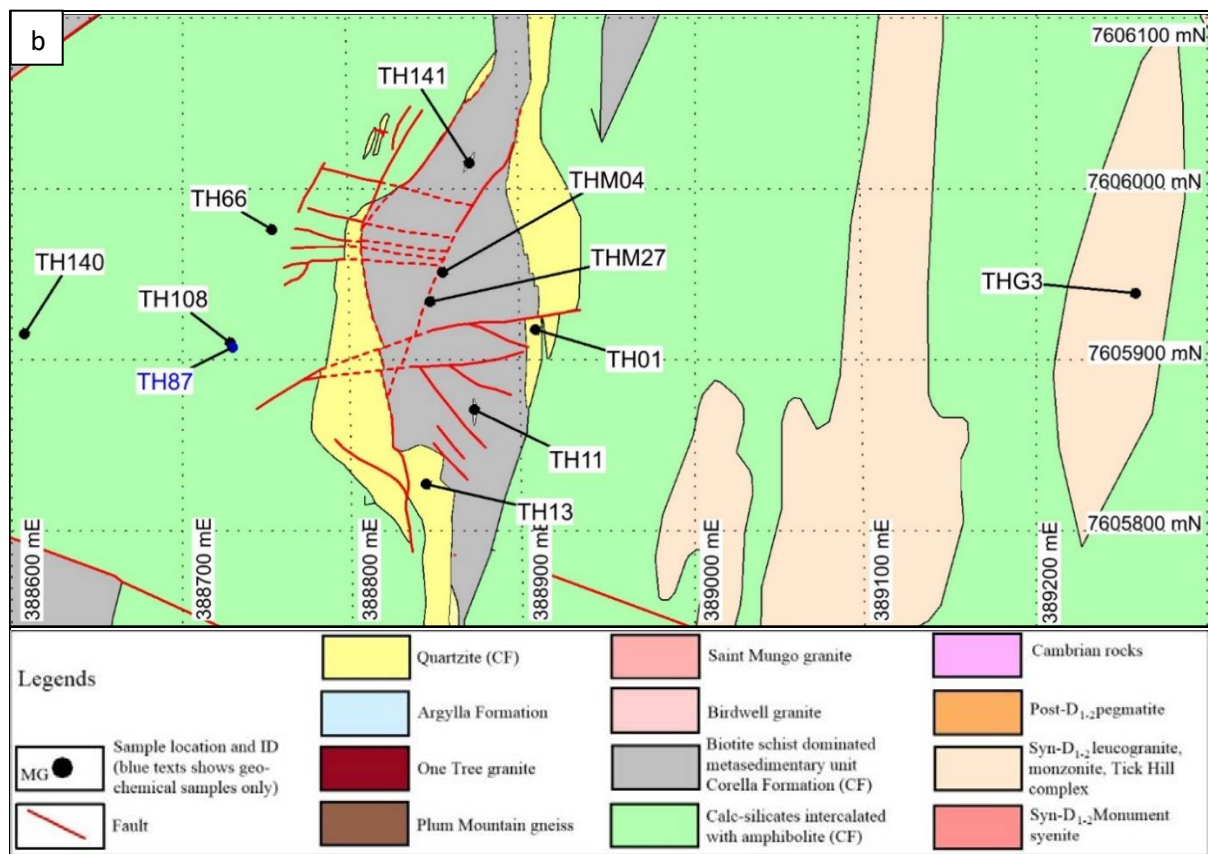
Figure 3.1. Geological map of the Tick Hill region (a; adapted from Blake et al., 1982; Wyborn, 1997; Rutherford 2000) with the locations of geochronological (black lettering) and geochemical samples (blue lettering); The black box shows (b) the lose-up of the pit area. The location of drill core collars from which samples TH66, TH86, TH108 and TH140 were taken, are shown.

D_3 events in the Tick Hill pit are characterized by the formation of brittle-ductile normal faults and breccia formation. Gold mineralization, and associated chlorite-albite-hematite-quartz alteration occurred at this time, probably concomitant with the emplacement of late-tectonic pegmatite (Chapter 2). The regional extent of the D_3 events has not been established.

D_4 events involved the formation of northeast-striking dextral and northwest-striking sinistral faults including the Plum Mountain and Mt Bruce faults (Fig. 3.1a) to the north and south of Tick Hill respectively. D_4 faults post-dated mineralization (Chapter 2) and resulted in cataclasite formation and clay alteration. Regionally, these faults have been linked to east-west compression during the late stages of the Isan Orogeny (O'dea et al., 1997; Forrestal et al., 1998; Betts et al., 2006) coeval with the emplacement of the Williams Suite and widespread sodic-potassic and hematite-rich alteration (Wyborn et al., 1988). Brittle reactivation of these faults occurred at various stages during later events between 1500 Ma-1100 Ma (e.g., Blake and Stewart, 1992; Oliver, 1995).

3.2.2. Previous geochronology in the Mary Kathleen Domain

Past geochronological studies conducted in the MKD defined three main magmatic events: (1) emplacement of the Leichhardt Volcanics and Kalkadoon Supersuite at 1865-1845 Ma (Page 1978; Carson et al., 2011; Kositcin et al., 2019); (2) bi-modal volcanism resulting in deposition of the Magna Lynn Metabasalt and Argylla Formation on top of Kalkadoon-Leichhardt basement at 1800-1775 Ma with associated magmatism during a possible early extensional events (Page, 1978; Page and Sun, 1998; Carson et al., 2009; Neumann et al., 2009; Carson et al., 2011; Magee et al., 2012; Kositcin et al., 2019); and (3) emplacement of granites belonging to the Wonga and Burstall Suites at 1745-1730 Ma (Page, 1978; Page, 1983; Pearson et al., 1992; Page and Sun, 1998; Davis et al., 2001; Carson et al., 2009; Neumann et al., 2009; Kositcin et al., 2019), during further extension (e.g., Holcombe et al., 1991; Withnall and Hutton, 2013). The summary of geochronological study results in the MKD is presented in Appendix 2.

The host rocks of the Tick Hill deposit were mapped as Corella Formation (Blake et al., 1982; Rutherford, 2000), which was dated at 1740-1755 Ma using detrital zircons and intercalated volcanic horizons from samples collected further north (Page and Sun 1998; Carson et al., 2009; Neumann et al., 2009; Kositcin et al., 2019). From north to south in the MKD, available ages for the Corella Formation are as follows: Felsic rocks in the Corella Formation near Dugald River mine, provide an age of 1750±7 Ma (Page and Sun 1998), whilst two samples collected from sandstone units in the Corella Formation, 25 km northwest of Mary Kathleen yielded age estimates of 1770±6 Ma and 1776±3 Ma respectively based on the weighted mean age of the youngest zircons (Neumann et al., 2009). These ages were interpreted as maximum depositional ages noting that the youngest zircons in these samples yield ages of 1742±58 Ma and 1744±32 Ma (Neumann et al., 2009). Two samples of meta-rhyolite in the Corella Formation ~40 km north of Duchess yielded crystallisation ages of 1739±5 Ma and 1740±5 Ma (Kositcin et al., 2019), similar to the magmatic emplacement age of 1738±2 Ma for a meta-rhyolite exposed in the Corella Formation ~10 km further south (Neumann et al., 2009). A sample from mapped Corella Formation near Mt Morah mine in the Duchess area yielded a maximum depositional age of 1740±20 Ma (Neumann et al., 2009). Another sample for the Corella Formation from feldspathic quartzite three km east of Duchess yielded a maximum depositional age of 1752±2 Ma (Kositcin et al., 2019). The Corella Formation near Duchess is intruded by granite of the Mount Erle Igneous Complex dated at 1735±3 Ma (Kositcin et al., 2019), providing a minimum age constraint in this area.

Metamorphic ages in the MKD were obtained from rim overgrowths on primary zircon grains including a 1515±13 Ma age from rhyolite in the Corella Formation north of Duchess (Kositcin et al., 2019). In addition, titanite from the Mt Erle Igneous Complex near Duchess and Mt Philp Breccia ~40 km north of Dutchess yield ages of 1500±6 Ma, 1503±7 Ma and 1527±16 Ma, reflecting metamorphic-thermal events (Kositcin et al., 2019).

Little age dating has been done in the immediate vicinity of the Tick Hill mine. An imprecise K-Ar biotite age of ca.1420 Ma (Richards et al., 1963) was reported for the Monument Syenite, 20 km south of Tick Hill, whilst a sample of Plum Mountain gneiss in the Kalkadoon-Leichhardt basement ~20 km northwest of Tick Hill yielded a U-Pb zircon age of 1862±3 Ma (Carson et al., 2011). Poorly constrained titanite ages mentioned in consulting reports (Tedman-Jones, 2001) include a 1517±10 Ma titanite age interpreted to predate mineralization, and a 1433±85 Ma titanite age interpreted to postdate mineralization. In addition, lead isotopic data for pyrite associated with gold mineralization yielded an isochron age of 1530±100Ma (Tedman-Jones, 2001).

3.3. Methodologies

3.3.1 Sample descriptions

Sixteen samples from rock units in the immediate vicinity of the Tick Hill deposit (10 samples) and surrounding areas (six samples, Fig. 3.1) were collected for dating. In collecting the samples, reference for unit names was made to the 1:100,000 geological maps compiled by Blake et al. (1982), Wyborn (1997) and later digital versions. Two of the regional samples were taken from granitic gneiss to the west of the mapped western boundary of the Argylla Formation. These samples could represent a part of the Kalkadoon-Leichhardt basement and were taken to establish the age of the older igneous intrusions in the area. The two samples include granitic gneiss mapped as One Tree Granite (OTG), which intruded the ca. 1860 Ma Plum Mountain gneiss, 10 km west of the pit (Blake et al., 1982; Carson et al., 2011), and a granitic gneiss of the Saint Mungo Granite (SMG) eight km west of the pit, which was interpreted to have intruded the Corella Formation (Blake et al., 1982). Four regional samples were taken from intrusions to the east of the mapped outcrop of Argylla Formation, including two phases of granitic gneiss variably mapped as Tick Hill Granite or Saint Mungo Granite (THG1, THG2) 3.7 km west of the pit, which contain rafts of Corella Formation (Blake et al., 1982; Wyborn, 1997) and two samples from variably foliated, late tectonic intrusions, which were emplaced into strongly sheared and folded (D_{1-2}) mylonitic gneiss mapped as Corella Formation (THG4, MG). These samples were taken to constrain the minimum age of D_{1-2} deformation event and associated high-temperature metamorphism, and include foliated granite mapped as Tick Hill Granite, 3.5 km southwest of the pit (THG4), and a thin monzonite dyke (MG), which intruded strongly foliated gneiss immediately north of the Monument Syenite, 23 km south-southwest of Tick Hill pit.

Samples collected in and around the Tick Hill pit are hosted within rocks mapped as Corella Formation and include one sample of mylonitic, syn-tectonic granite mapped as Tick Hill Granite (THG3) and two samples of gold-rich quartz-feldspar mylonite (galahstone) from the core of the deposit (THM04, THM27) that are similar in appearance to altered Tick Hill Granite. These samples were taken to constrain the age of D_{1-2} deformation event and provide a maximum age for

mineralization, and a minimum age for the host rocks in which they intruded. An additional five samples were taken of largely undeformed, post-tectonic pegmatite veins and associated metasomatic overgrowths that overprint the mylonitic D_{1-2} fabric, and are interpreted to be emplaced during D_3 at the time of main stage of mineralization. Two pegmatite veins were sampled within the pit (TH141 in the north wall and TH11 in the east wall) and three were obtained from drill core directly below mineralization (TH66, TH106, TH140). A further two samples were taken for provenance dating of the hanging wall (TH13) and footwall quartzite (TH01) units that bound the ore zone. In addition, 12 samples from igneous rocks that were used for dating together with four samples from post-tectonic pegmatite and Monument Syenite that did not yield (sufficient) zircon grains were used for major and trace element geochemistry to further characterize the igneous suites in the Tick Hill area.

3.3.1.1 Regional samples

Sample OTG is a granitic gneiss that was collected from the One Tree granite, 10 km west of the Tick Hill pit (Fig. 3.2a). The granite preserves a well-developed, north-trending foliation (Fig. 3.2a) with a steeply plunging lineation defined by aligned biotite, amphibole and elongated quartz-feldspar aggregates. The sample is composed of ~30% quartz and ~50% feldspar (plagioclase and K-feldspar), ~15% amphibole and biotite, and ~5% magnetite. In places, plagioclase was altered to sericite while biotite was replaced by chlorite.

Sample SMG was collected from outcrops of granitic gneiss mapped as Saint Mungo Granite (Blake et al., 1982; Rutherford, 2000) along the main farm track, eight km west of the Tick Hill pit (Fig. 3.2a). The SMG intruded Plum Mountain Gneiss and the Corella Formation, with outcrops of Corella schist occurring west of the intrusion in conformable contact with Plum Mountain Gneiss (Blake et al., 1982). The rock preserves a foliation (Fig. 3.2b) defined by biotite, that wraps around partly recrystallized, cm-large feldspar grains. It is composed of ~35% quartz and ~40% feldspar (K-feldspar and plagioclase), ~20% amphibole and biotite and ~5% magnetite. Alteration of plagioclase to sericite and silicification of amphibole was common.

Samples THG1 and THG2 were collected from low outcrops along a farm road, ~4 km west of the pit. Sample THG1 was collected from a northwest-trending 5-10 m wide granitic dyke that intruded older granitic gneiss that was sampled as THG2 (Fig. 3.2c). Both phases of granite are strongly foliated, and the dyke from which THG1 was taken truncates the foliation in the older granite at a low angle (<10°). THG1 consists of well-foliated granitic gneiss (Fig. 3.2d) composed of <5 cm large subhedral K-feldspar porphyroclasts in a matrix of quartz, plagioclase and biotite, with minor hornblende. The dispersed, large, rounded feldspar clasts form the most conspicuous aspect of this rock. They are wrapped in a foliation that is defined by biotite and hornblende. Epidote, chlorite and sericite alteration is common in this sample. THG2 consists of a strongly foliated granitic gneiss that

is slightly more mafic than THG1, in which < 1cm large K-feldspar porphyroclasts with dynamically recrystallized margins are aligned within in a matrix of strongly foliated, quartz biotite and hornblende (Fig. 3.2e). The gneisses (i.e. THG1 and THG2) have been mapped as part of the Tick Hill Complex (Blake et al., 1982; Wyborn, 1997) or as Saint Mungo Granite outcrop surrounded by Tick Hill Complex in a more detailed exploration project (Rutherford, 1999, 2000). In the light of new geochronological data from the THG2 in this study, the THG2 outcrop is mapped as remnant Kalkadoon Supersuite (Fig. 3.1a). The Tick Hill complex intrudes the Corella Formation, showing rafts of Corella contained within the gneiss (Wyborn, 1997). The rock consists of quartz, plagioclase, microcline, biotite and minor hornblende (<1%), with a foliation defined by biotite. Compared to sample THG1, alteration is stronger in sample THG2, with plagioclase replaced by sericite, and microcline and biotite weakly altered to sericite and chlorite respectively. Near the sampling site, the THG2 gneiss unit contains numerous large (up to 10's of meters) enclaves of strongly folded amphibolitic gneiss in which the gneissic layering preserved in THG2 is axial planar to the folds within the mafic enclaves. The mafic rafts are similar in appearance to amphibolite units in the Corella Formation.

THG4 was collected from a low set of hills, 3.5 km southwest of the pit and consists of a relatively undeformed leucogranite, characterized by weakly flattened quartz phenocrysts that are <5 mm in size, and partly recrystallized, slightly elongated K-feldspar grains that together with quartz define a weak foliation (Fig. 3.2f), which intensifies towards the margins of the intrusion. Internal to the intrusion the grainsize locally coarsens into pegmatoidal pockets that typically display graphic intergrowths between K-feldspar and quartz. The intrusion was mapped as part of the Tick Hill Complex (e.g., Wyborn, 1997), and has a sharp intrusive contact that transects D_{1-2} folding in the surrounding mylonitic gneiss units. Therefore, THG4 represents a late-syntectonic granite relative to the dominant D_{1-2} fabric and was probably emplaced late during D_2. THG4 consists of quartz, plagioclase and K-feldspar with rare biotite and no other mafic phases, in which plagioclase and K-feldspar were replaced by sericite (±albite, clay minerals).

Sample MG was obtained from a thin (<20 cm), quartz-poor monzonite dyke, that cuts across intensely folded, sheared and migmatised (D_{1-2}) amphibolitic calc-silicate gneiss ~6 km south-southwest of Tick Hill pit (Figs. 3.2g, h). The dyke pinches and swells as it transects isoclinal folds and the S_{1-2} layering at a 20-30° angle across platform outcrops in the river. The monzonite preserves a weak foliation and lineation (Figs. 3.2g, h), which is similar in orientation to the regional L_{1-2}, and indicates that the dyke was emplaced late during D_2. Sample MG comprises roughly equal amounts of plagioclase and K-feldspar, with biotite and amphibole and minor quartz. Plagioclase was strongly altered by sericite whilst biotite was replaced by chlorite.
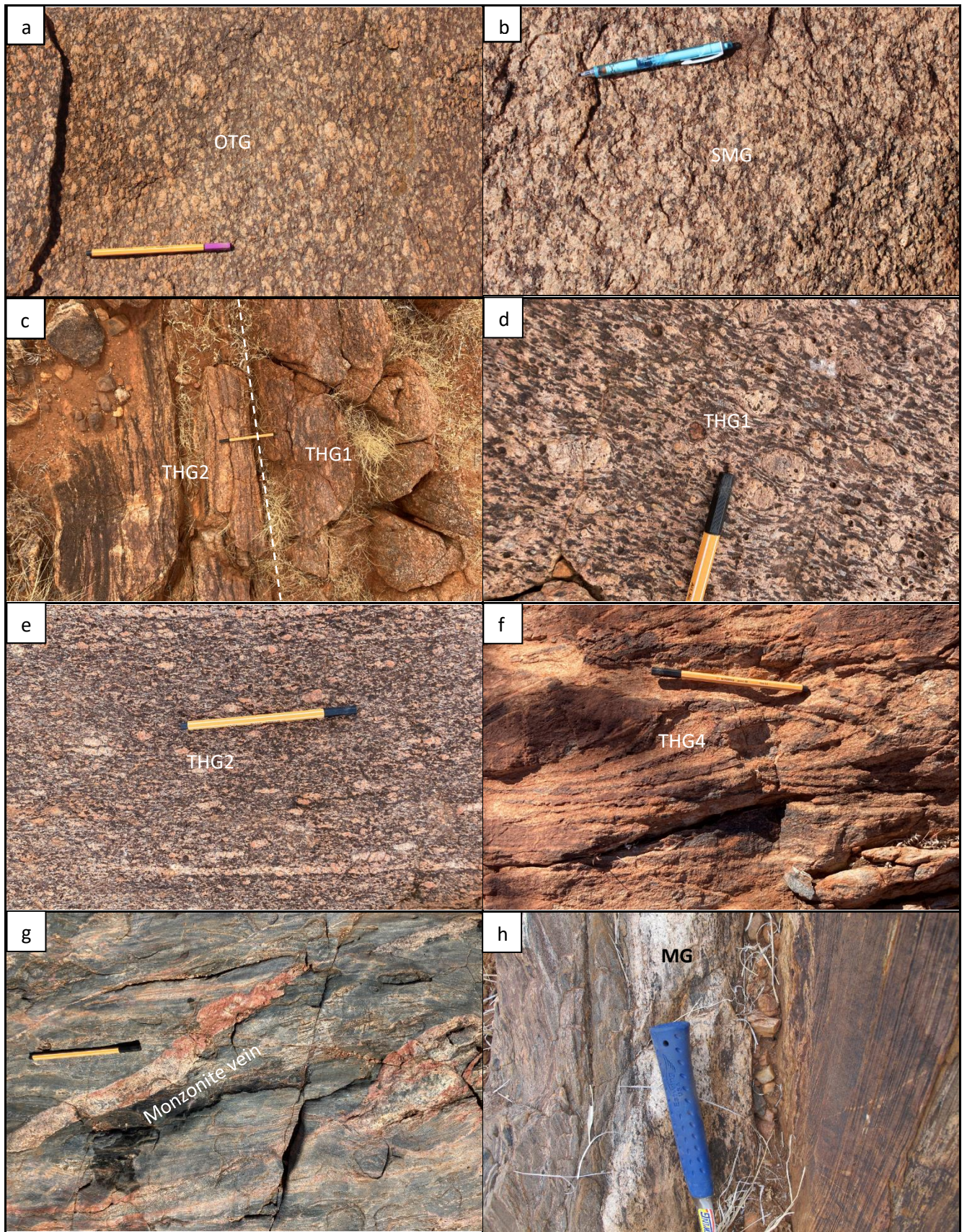
Figure 3.2. Photographs of samples collected from differently intrusive units in the Tick Hill region: (a) Foliated granodiorite of One Tree Granite (sample OTG); (b) Foliated granodiorite of Saint Mungo Granite (sample SMG); (c) Contact of granitic dyke (THG1) and older granite (THG2); (d) Strongly foliated granite (sample THG1) mapped as either Saint Mungo Granite or Tick Hill Granite; (e)

Foliated granite (sample THG2), which was intruded by THG1 and was mapped as either Saint Mungo Granite or Tick Hill Granite; (f) Foliated late-tectonic leucogranite mapped as Tick Hill Granite (sample THG4); (g) Late tectonic, monzonite vein and dyke (bottom right), which intruded strongly foliated calc-silicate and amphibolite gneiss (sample MG).

3.3.1.2. Local samples

Sample THG3 was collected from strongly deformed leucogranite belonging to the Tick Hill Complex at the foot of the hill, 300 m east of Tick Hill pit. It consists of mylonitic, quartzo-feldspatic gneiss that is intercalated with the surrounding metasediments (Fig. 3.3a) as a result of intense D_{1-2} deformation (Chapter 2). The rock consists of granoblastic quartz, plagioclase, and K-feldspar (now largely replaced by albite) and is characterized by well-developed quartz ribbon grains, and a strong lineation defined by feldspar-quartz rodding. The outcrop from which sample THG3 was taken is part of a larger lensoidal granite body that displays strain gradients, with less intensely mylonitised granite towards its core, i.e. the rock is interpreted as a syn-tectonic intrusive leucogranite that was emplaced into the surrounding metasediments during D_1. THG3 was collected to obtain an age of granite emplacement and concomitant D_1 shearing. Plagioclase was strongly altered by albite, k-feldspar and sericite.

Samples THM04 and THM27 of gold-rich, quartz-feldspar mylonite (galahstone) that constitute the principle host rock to mineralization were provided by MIM and Nick Oliver. These samples were collected from the high-grade mineralized zone at the time of mining and the exact location of the samples is not known. The two samples are near identical in composition and consist of metasomatized quartzo-feldspathic mylonite with a composite S_{1-2} foliation characterized by quartz and feldspar ribbon grains (Figs. 3.3b,c) similar to sample THG3, but more strongly altered. The samples are dominated by quartz, K-feldspar and plagioclase with few dark minerals, most of which formed during various stages of alteration events (i.e., amphibole, chlorite, epidote and hematite). K-feldspar and plagioclase were largely replaced by albite, which in turn is generally strongly altered to sericite (+ clay minerals), and the both samples contained abundant gold. The rock is characterized by a sugary, granoblastic texture reflecting post-deformational annealing and recovery (Figs. 3.3b,c; Chapter 2).
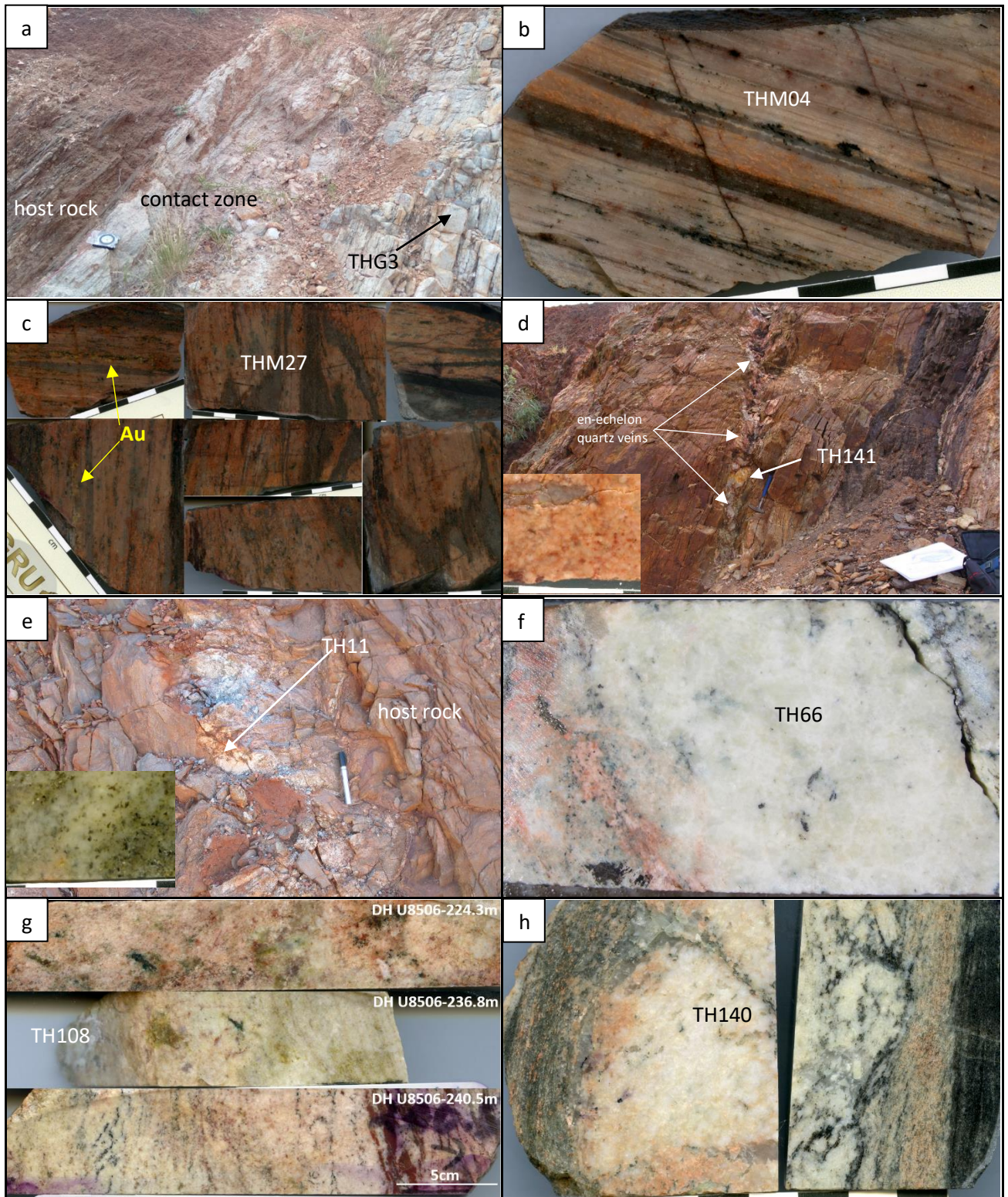
Figure 3.3. Photographs of samples taken from around the Tick Hill deposit. (a) Strongly deformed (mylonitic) contact zone between syn-tectonic leucogranite (sample THG3) and gneissic host rock at Tick Hil; (b) Strongly altered, Au-rich quartz-feldspar mylonite (sample THM04); (c) Offcuts of strongly altered Au-rich quartz-feldspar mylonite (collective sample THM27); (d) Pegmatite associated with en-echelon quartz veins in the north wall of the pit (sample TH141); (e) Boudinaged pegmatite dyke in the east pit wall of the pit below the main ore zone (sample TH11); (f) Metasomatic feldspar-dominant vein underneath the Au-rich mineralization zone in DH U9205 (sample TH66); (g) Metasomatic feldspar-dominant zones overprinting gneissic layering in three intervals from DH U8506 (collectively sampled

as TH108); (h) Contact of late-tectonic (D$_3$) pegmatite dyke (sample TH140) and host rock from drill core underneath the ore zone.

Five samples of weakly deformed and undeformed, syn-D$_3$ pegmatite veins were sampled in the pit (TH11, TH141,) and in drill core (TH66, TH140, TH108). These samples were targeted because their emplacement is interpreted to coincide with the timing of the main stage of gold mineralization (Chapter 2). Sample TH141 was taken from a felsic pegmatite vein in the north wall of the pit, where it transects the dominant composite S$_{1-2}$ fabric in biotite-chlorite schist at a low angle across sharp intrusive boundaries (Fig. 3.3d). The pegmatite intruded along the main D$_3$ shear zone that forms the host to mineralization (Chapter 2), and is associated with an array of en-echelon quartz veins consistent with a normal-sinistral sense of movement (Fig. 3.3d; Chapter 2), i.e. the pegmatite will provide an age for D$_3$ normal faulting. Sample TH141 is not foliated and largely consists of coarse-grained albite and K-feldspar with subordinate quartz and minor biotite. Much of the feldspar was strongly altered to albite, epidote, sericite and clay minerals while biotite was replaced by chlorite. Sample TH11 was collected from a weakly-deformed and partly boudinaged granitic pegmatite that intruded into the S$_{1-2}$ mylonitic fabric in the east wall of the Tick Hill pit in the footwall to the mineralization (Fig. 3.3e). The pegmatite preserves a weak foliation defined by biotite and is dominated by feldspar with subordinate quartz (including minor quartz veins inside the feldspar-rich groundmass), biotite and traces of magnetite. The feldspar was strongly altered to sericite, albite and clay minerals while the magnetite was altered to hematite. Samples TH66 (Fig. 3.3f), TH108 (Fig. 3.3g) and TH140 (Fig. 3.3h), were collected from drill core. All samples were taken from pegmatite dykes and metasomatic veins that truncate and overprint the footwall sequence between 80-180m below the mineralized zone. Sample TH108 combines three separate intersections of post-tectonic pegmatite with similar compositions (feldspar-quartz) and textures (fine grained, non-foliated), sampled across a 16m interval. The three pegmatite samples consist of medium-grained plagioclase and K-feldspar with minor quartz and biotite. The boundaries of the veins are generally diffuse, with feldspar-quartz overprinting and seemingly replacing the older gneissic fabric (Fig. 3.3h). The veins themselves are generally undeformed, but the feldspar in the veins was altered to sericite and albite (clay minerals) while biotite was altered to chlorite.

Two samples from the hanging wall (TH13) and footwall (TH01) quartzite units were collected from outcrops in the pit. The hanging wall quartzite forms the immediate hanging wall to mineralization, and is locally mineralized. It is a composite unit that varies in thickness, and it has diffuse boundaries and significant internal lithological variation (Laing 1993; Tedman-Jones, 2001). The hanging wall contact with overlying calc-silicates is magnetite rich, whilst the main body of quartzite includes zones dominated by oriented grains of either biotite, hornblende-epidote-feldspar or altered feldspar that are aligned within S$_{1-2}$ to resemble silicified biotite schist, calc-silicate or quartzofeldpathic gneiss respectively. The amount of biotite, hornblende, epidote and feldspar vs

quartz is variable, and portions of almost pure white quartzite occur. Within the hanging wall quartzite evidence for brecciation and intense stockwork veining, now largely annealed, is common, and the unit has been variably interpreted as a primary sedimentary horizon or as alteration along a D_1 shear zone (Laing 1993; Tedman-Jones, 2001). Dates from this unit may, therefore, either provide an upper age limit for the sedimentary sequence, or an age for D_1 metasomatism. Sample TH13 was taken from hanging wall quartzite in the SE corner of the pit (Fig. 3.4a). The sample has a spotted texture as a result of abundant (~10%) feldspar grains with minor biotite that are aligned within the S_{1-2} foliation, and that are largely overgrown and replaced by quartz (Fig. 3.4b). As such, this unit could represent strongly silicified quartzo-feldspathic gneiss. The quartz is extremely coarse-grained as a result of post-tectonic annealing and grain growth, but inclusion trails of tourmaline, amphibole, and other accessory minerals preserve evidence for the underlying older fabric. The sample was strongly metasomatised which resulted in the growth of quartz at the expense of feldspar and biotite (Fig. 3.4b), the replacement of feldspar by sericite and abundant fluid inclusion trails in quartz, whilst biotite was altered to chlorite. The footwall quartzite is thickly bedded (>30cm), and appears less deformed and altered and more quartz-rich than the hanging wall quartzite (Figs. 3.4c,d). Sample TH01 was collected in the northeast corner of the pit. The sample consists almost completely of grey-white translucent quartz with a little biotite and magnetite. The quartz is extremely coarse-grained (up to 1 cm) due to post tectonic annealing and D_3 metasomatism as indicated by the abundance of fluid inclusion trails along healed fractures, but the underlying gneissic fabric has been preserved by the alignment of accessory minerals. Similar to the hanging wall quartzite, the footwall quartzite was variably interpreted as a sedimentary unit or a silicified D_1 shear zone (Laing 1993; Tedman-Jones, 2001), and dates from this unit may either reflect an upper age limit for the sedimentary sequence, or an age for D_1 metasomatism.

3.3.1.3 Additional samples for geochemistry

In addition to the geochronology samples described above, a further two samples were collected from the main body of Monument Syenite (MSy, MSy.m) and one sample from an associated intrusive syenite dyke (MSy.d), which intruded ~6 km south of Tick Hill (Fig. 3.1a). These samples did not yield zircon but were included for geochemical analyses. The Monument Syenite intrusions preserve a well-developed linear fabric (L-tectonite) with the lineation parallel to the regional mylonitic L_1 fabric. It consists of K-feldspar and plagioclase with little quartz and abundant magnetite. The syenite dyke is weakly foliated with a fine-grained aphanitic texture, with amphibole and magnetite in a matrix of intergrown plagioclase and K-feldspar. In addition, one further sample of undeformed, late-tectonic pegmatite was taken from drill core below the ore zone (TH87). This sample did not provide sufficient concordant zircon in dating, but it has been used to supplement the geochemistry data for the late pegmatite group.
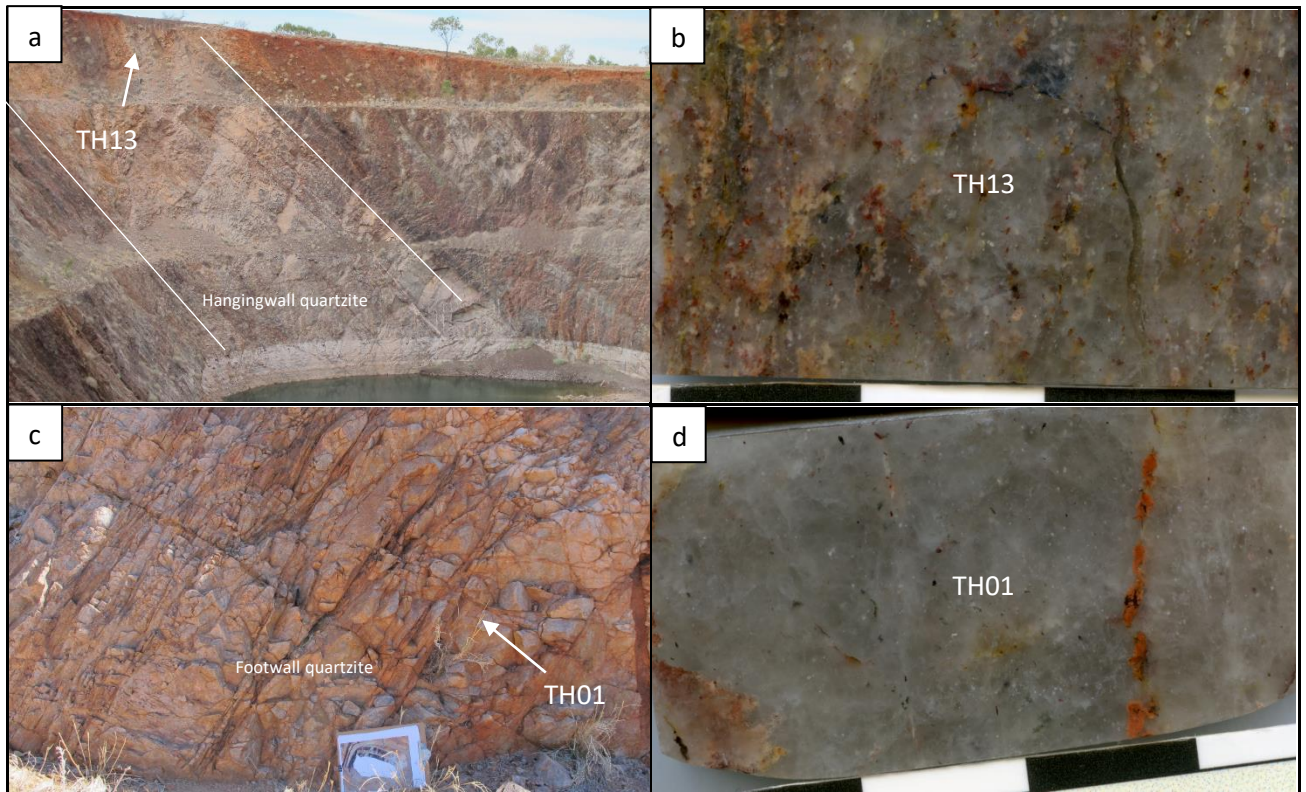
Figure 3.4. Photographs of hanging wall and footwall quartzite samples taken from the open pit. (a) Hanging wall quartzite exposed in the southeast corner of the pit with the location of sample TH13 indicated. (b) close-up of sample TH13 (scale bar in centimeters) illustrating the spotty feldspar texture, with feldspar aligned along S_{1-2} and overprinted by quartz. (c) Footwall quartzite exposed in the northeast corner of the pit with the location of sample TH01 indicated. (d) Close-up of quartzite sample TH01 showing the coarse-grained recrystallized nature of quartz.

3.3.2. Analytical methods

3.3.2.1. Major and trace element analyses

Intrusive rock units targeted for age dating were analyzed for major and trace element geochemistry. Selected samples were crushed and milled to powders that were fused in beads for analysis. Major elements for most samples were obtained by the Advance Analytical Centre at James Cook University, using a Bruker-AXS, S4 Pioneer XRF Spectrometer. FeO and trace elements including fluorine were analyzed at Bureau Veritas Canada Inc. in Vancouver, British Columbia. Both major and trace elements for samples TH140 and TH141, were analyzed at Bureau Veritas. Samples TH108 and TH87 were analyzed for major-elements only. Major and trace element values were processed and analyzed in IOGas software. All values below detection limits were assigned half the value of the lower detection limits.

Prior to the geochemical analysis, rock samples were crushed and milled to powders, and then mixed with $LiBO_2$ / $Li_2B_4O_7$ flux and fused in a furnace. The cooled bead was then dissolved in ACS grade nitric acid and analysed by ICP-OES and/or ICP-MS. For the analysis of ultra-trace elements,

the prepared samples were digested with a modified Aqua Regia solution of equal parts concentrated HCl, HNO_3 and de-ionized H_2O for one hour in a heating block or hot water bath. The sample solution was made up to volume with dilute HCl. Loss on ignition (LOI) was determined by heating a sample split, and then measuring the LOI.

FeO concentrations were determined by a titration method. Samples were first digested with sulfuric acid (H_2SO_4), then allowed to cool, and digested with hydrofluoric acid. An indicator solution consisting of distilled water, sulfuric acid, phosphoric acid, boric acid and diphenylamine sulfonate was added to every sample solution. The solutions were then titrated using a standard dichromate ($K_2Cr_2O_7$) solution.

Fluorine concentrations were determined by decomposing the samples by fusion with sodium hydroxide, and then digesting the produced melt in water. The solution was acidified with citric acid and ultimately buffered with ammonium citrate solution. Fluoride was determined using an electrode composed of lanthanum fluoride crystal membrane that is an ionic conductor selective for un-complexed fluoride ions. The electrode was placed in the sample solution after the ion strength was adjusted to pH of 6.5, and the potential was measured by an mV/pH meter. Fluorine concentrations were derived from a standard graph of potential vs. concentration of fluorine.

3.3.2.2. U-Pb dating of zircon by LA-ICP-MS

Zircon grains were separated from rock powders with heavy liquid followed by hand picking under the microscope. Selected zircon grains were mounted in 2.5cm epoxy-resin mounts, which were polished and imaged with a cathodoluminescence microscope to classify zircon types and detect internal textures (Corfu et al., 2003).

Individual grains were analysed by LA-ICP-MS, using a Geolas Pro 193nm ArF excimer laser system coupled with a Bruker 820-MS ICP-MS at the Advanced Analytical Centre, James Cook University, Townsville. Ablation was conducted in a large volume cell using high-purity He as the carrier gas (Fricker et al., 2011), which was subsequently mixed with Ar prior to introduction into the ICP-MS. Full analytical details are described in Tucker et al. (2013). Analytes collected were ^{29}Si, ^{90}Zr, ^{202}Hg, ^{204}Pb, ^{206}Pb, ^{207}Pb, ^{208}Pb, ^{232}Th, ^{235}U, and ^{238}U. The ICP-MS was tuned to ensure low oxide production levels (ThO/Th <0.5%) and approximately equal sensitivity of U, Th and Pb to minimize isotope fractionation due to matrix effects (Pettke, 2008). Fractionation and mass bias were corrected by using standard bracketing techniques with every eight to ten zircon sample measurements bracketed by measurements of GJ1 (primary calibration standard, Jackson et al., 2004), with FC1 (Paces and Miller Jr., 1993) and 91500 (Wiedenbeck et al., 1995) as secondary standards. All zircons were analyzed with a beam spot diameter of 25 to 36 μm depending on the size of the zircon and selection of analytical

sample spots was guided by CL images. Individual analyses consist of approximately 30 seconds of signal of the gas background followed by 30 seconds of signal collected during zircon ablation. Analysis of the NIST 610 reference glass was conducted at the beginning and end of every analytical session to monitor instrument stability.

The obtained data were processed using Iolite software (Paton et al., 2011). All time-resolved single isotope signals from standards and samples were filtered for signal spikes or perturbations related to inclusions and fractures. The most stable and representative isotopic ratios were selected taking into account possible mixing of different age domains and zoning. Drift in instrumental measurements was corrected following analysis of drift trends in the raw data using measured values for the GJ1 primary zircon standard. Age calculations based on measured isotope ratios were done for zircon grains with a discordance < 10%, using Isoplot/Ex version 4.15 (Ludwig, 2011). Analyses of the secondary zircon standards were used for verification of GJ1 following drift correction. The $^{206}Pb/^{238}U$ age for the primary standard GJ1 in this study (600.24±0.44 Ma; n = 322, MSWD = 0.62) was similar to ages reported byAlagna et al. (2008) and Jackson et al. (2004). The $^{207}Pb/^{206}Pb$ age for sample FC1 (1093.2±2.3 Ma; n = 146, MSWD = 0.88) is ~0.5% younger than the age reported by Paces and Miller Jr. (1993) whilst the $^{207}Pb/^{206}Pb$ age for 91500 (1048.5±3.6 Ma; n = 210, MSWD = 0.48) is ca. 1.5% younger than the age reported by Wiedenbeck et al. (1995).

3.4. Results

3.4.1. Whole rock geochemistry

Whole rock geochemistry results are summarized in Table 3.1, with various rock classification plots shown in Figs. 3.5-3.7. Based on their relationship with deformation events and their age as reported in Table 3.2, the sampled intrusive rock types have been sub-divided and plotted in relation to the deformation events as: (1) pre-D1; (2) syn-D_1, (3) syn-D_1 to syn-D2; and (4) syn-D_3 intrusions (Figs. 3.5-3.7).

The pre-D_1 intrusions include granite samples OTG and THG2, which were interpreted to belong to Kalkadoon basement (Blake et al., 1982; Rutherford, 2000), and contain a strong composite S_{1-2} fabric. The rocks plot in the granodiorite field (Fig. 3.5a), and have relatively high TiO_2 and REE values with elevated Y and MgO contents. They plot as a distinct group in the Y-Nb variation diagram (Fig. 3.5d), the chrondrite-normalized REE distribution diagram (Fig. 3.6a), and the SiO_2 vs (Cao, MgO, Ba) diagrams (Fig. 3.7). Their composition is akin to the syn-D_1 granites.

Table 3.1. Content of major (wt/%) and trace (ppm, except for Au which is in ppb) elements for samples from the Tick Hill region. Samples TH87 and TH108 were not analysed for trace elements and FeO.

Sp./ ox./el..	OTG	THG2	SMG	THG1	MG	THG4	THG3	THM04	THM27	TH141	TH11	TH140	TH66	TH108	TH87	Msy	Msy.m	Msy.d
SiO2	69.32	68.13	70.40	70.36	60.90	74.56	75.12	80.63	76.21	64.06	61.42	67.19	76.23	59.26	64.81	51.76	52.49	49.79
Al2O3	13.01	14.51	13.81	13.54	21.30	14.93	14.71	10.52	13.04	20.9	20.36	18.57	13.14	22.46	19.76	20.64	22.43	23.17
Fe2O3	6.21	3.60	4.18	3.74	1.56	0.12	0.09	1.68	1.75	1.27	2.70	1.14	0.89	0.23	0.49	8.15	5.11	5.66
FeO	5.78	3.28	3.61	2.96	0.67	0.36	0.35	1.07	0.95	0.44	2.19	1.09	0.6	-	-	5.04	3.07	3.78
MgO	1.18	1.00	0.41	0.84	0.88	0.19	0.20	0.47	0.65	0.7	1.42	1.19	0.29	1.31	0.78	1.45	0.78	1.03
CaO	2.30	2.34	1.82	2.39	3.55	1.35	1.41	0.44	0.66	0.76	2.68	2.62	1.06	3.08	2.53	3.97	2.45	3.19
Na2O	1.66	2.27	1.56	2.96	5.63	6.33	5.94	5.13	5.53	6.2	4.04	5.81	1.29	6.54	5.40	8.34	10.87	9.73
K2O	3.30	4.49	5.73	5.14	1.44	0.94	0.80	0.54	1.03	4.26	3.04	1.81	6.89	2.05	1.63	3.14	3.40	3.37
TiO2	0.75	0.54	0.40	0.59	0.44	0.03	0.03	0.02	0.13	0.03	0.47	0.21	0.08	0.65	0.07	0.77	0.51	0.56
P2O5	0.21	0.25	0.15	0.21	0.07	0.15	0.13	0.01	<0.01	<0.01	0.07	0.01	0.08	0.07	0.10	0.36	0.25	0.35
MnO	0.07	0.02	0.04	0.03	0.02	0.01	0.01	0.02	0.02	0.02	0.02	0.02	0.01	0.03	0.03	0.16	0.10	0.11
LOI	0.43	0.63	0.45	0.53	1.55	0.51	0.62	0.5	0.9	1.6	1.85	1.3	0.50	2.91	1.81	0.80	0.40	0.77
Sum	98.46	97.80	98.96	100.37	97.40	99.15	99.10	99.98	99.97	99.86	98.11	99.9	100.48	98.62	97.44	99.69	98.95	97.93
Ba	920	706	699	817	808	110	118	36	111	371	307	197	147	-	-	1232	1656	1737
Cs	9.9	4.1	9.7	2.1	3.9	<0.1	0.2	<0.1	1.2	0.6	3.1	1.4	0.7	-	-	1.5	0.5	1.1
Ga	16.6	20.1	18.8	18.1	12.5	11.9	12.2	10.6	13.9	17.5	20.6	18.1	18.8	-	-	16.8	15.6	15.4
Hf	8.3	3.9	9	8.7	6.7	1.5	2.2	0.2	1.2	10.9	3.4	7.2	2.9	-	-	2.3	1.3	1.4
Nb	14.2	15.1	13.2	19.4	6.2	2	0.8	1.6	3.7	0.4	4.7	2.7	4.2	-	-	26.5	16.7	16.5
Rb	126.9	192.8	229.4	165.4	176.6	17.4	11.5	10.3	34	223.8	159.1	66.4	109.1	-	-	72.8	63.7	61.9
Sn	6	<1	7	1	<1	<1	<1	<1	<1	<1	<1	<1	<1	-	-	<1	<1	<1
Sr	130.2	140.3	79	128.5	98	135.4	154.7	25.3	79.1	230.8	230.6	240.1	297.4	-	-	576.1	614.1	711.6
Ta	1	1.6	1.3	1.7	1.3	0.3	0.1	<0.1	0.2	<0.1	0.6	1.3	0.5	-	-	1.2	0.7	0.8
Th	18.7	10.8	31.4	31.3	130.7	3.3	2.9	0.5	2.8	5.4	3.1	2.9	0.5	-	-	1.4	1	0.7
U	2.3	7.7	5.8	7.4	35.7	0.6	0.5	0.4	2.7	1.7	1	1.5	0.7	-	-	0.3	0.2	0.1
V	41	40	13	23	<8	<8	<8	<8	16	9	61	34	<8	-	-	49	28	34
W	1.6	10.7	5	0.7	<0.5	0.5	1	<0.5	<0.5	<0.5	1.4	1	1.4	-	-	<0.5	0.7	<0.5
Zr	318.2	144.2	322	322.1	187.7	36.7	49.4	9.1	49.1	428.5	120.1	215.7	100.1	-	-	80.5	46.1	48.2
Y	26.9	22.2	52.1	54.7	9	4.2	3	0.8	3	7.1	4	4.1	0.9	-	-	16.3	9.8	13.2
La	82.3	26.5	86.2	76.3	70.5	1.3	2.8	1	4.6	16	5.9	5.4	4.1	-	-	18.7	12.2	16.6
Ce	144.2	52	167.1	149.3	95	2.3	3.4	1.8	8.5	47.7	8.1	8.9	5.6	-	-	35	22.4	31.5

Table 3.1. Content of major (wt/%) and trace (ppm, except for Au which is in ppb) elements for samples from the Tick Hill region. Samples TH87 and TH108 were not analysed for trace elements and FeO (cont.).

Sp./ ox./el..	OTG	THG2	SMG	THG1	MG	THG4	THG3	THM04	THM27	TH141	TH11	TH140	TH66	TH108	TH87	Msy	Msy.m	Msy.d
Pr	15.73	5.84	18.89	16.8	7.27	0.29	0.47	0.19	0.95	4.27	0.93	0.81	0.46	-	-	4.03	2.5	3.49
Nd	54.5	21	66.5	60.8	18.3	1.3	1.6	0.9	3.5	16	3	2.8	1.4	-	-	14.5	9.2	11.9
Sm	8.06	4.43	11.35	11.92	2.13	0.33	0.39	0.07	0.56	2.49	0.52	0.5	0.2	-	-	2.78	1.66	2.28
Eu	1.65	0.7	1.24	1.39	0.55	0.14	0.21	0.06	0.18	0.55	0.89	0.55	0.69	-	-	0.87	0.71	0.86
Gd	6.89	4.53	10.09	11.07	1.73	0.51	0.42	0.16	0.7	1.74	0.54	0.53	0.18	-	-	2.78	1.64	2.39
Tb	0.92	0.83	1.51	1.75	0.23	0.09	0.07	0.02	0.1	0.23	0.1	0.09	0.03	-	-	0.47	0.28	0.39
Dy	5.19	4.82	9.11	10.59	1.31	0.54	0.45	0.12	0.71	1.05	0.57	0.56	0.16	-	-	2.94	1.8	2.42
Ho	1.05	0.86	1.87	2.06	0.28	0.12	0.09	0.03	0.12	0.2	0.15	0.14	0.04	-	-	0.63	0.37	0.55
Er	2.81	1.97	5.79	5.94	1.01	0.33	0.26	0.08	0.32	0.6	0.48	0.4	0.09	-	-	1.91	1.13	1.45
Tm	0.37	0.23	0.78	0.85	0.15	0.06	0.04	<0.01	0.04	0.09	0.08	0.07	0.01	-	-	0.26	0.16	0.19
Yb	2.55	1.15	4.99	5.1	1.14	0.46	0.31	0.09	0.33	0.72	0.63	0.49	0.15	-	-	1.82	1.01	1.28
Lu	0.38	0.14	0.76	0.77	0.18	0.06	0.05	0.01	0.04	0.13	0.11	0.07	0.03	-	-	0.3	0.17	0.19
Mo	1.4	1.2	1.3	1.1	2.2	0.9	1.1	1.93	4.59	<0.1	0.6	0.1	2.6	-	-	1.2	1.1	0.8
Cu	20.5	8	20.2	9.6	4.7	5	3.8	14.37	43.99	5.2	6.2	5.4	4.2	-	-	8.8	14.1	2.4
Pb	11.7	9.1	25.7	8.8	23	1	2.6	7.06	3.68	0.5	2.1	2.3	1.4	-	-	2.3	4.8	2.5
Zn	151	34	33	26	20	8	12	20.7	16.2	4	14	45	22	-	-	60	35	37
Ni	11.4	11.8	3.1	7.9	2.5	1.7	2.2	6	16.9	2.6	25.9	10.4	3.2	-	-	1.8	1.2	1.9
Co	12.2	11.7	7.8	11.7	1.7	0.5	0.9	6.4	10	2	7	6	0.6	-	-	14.2	8.3	13.6
As	<0.5	0.6	6.5	0.8	0.5	<0.5	0.6	0.9	2.8	0.7	0.5	2.1	<0.5	-	-	1	0.8	1
Au	<0.5	<0.5	<0.5	<0.5	<0.5	<0.5	<0.5	33082.4	>100000	0.7	<0.5	<0.5	<0.5	-	-	<0.5	<0.5	<0.5
Cd	0.1	<0.1	<0.1	<0.1	<0.1	<0.1	<0.1	0.04	<0.01	<0.1	<0.1	0.1	<0.1	-	-	<0.1	<0.1	<0.1
Sb	<0.1	<0.1	0.2	<0.1	<0.1	<0.1	<0.1	0.09	0.11	<0.1	<0.1	<0.1	<0.1	-	-	<0.1	<0.1	<0.1
Bi	0.2	<0.1	0.6	<0.1	<0.1	<0.1	<0.1	1.56	4.38	<0.1	<0.1	<0.1	<0.1	-	-	<0.1	<0.1	<0.1
Tl	0.7	0.4	0.5	<0.1	<0.1	<0.1	<0.1	<0.02	0.08	<0.1	0.2	<0.1	<0.1	-	-	0.2	0.2	0.1
Se	<0.5	<0.5	<0.5	<0.5	<0.5	<0.5	<0.5	0.4	1.1	<0.5	<0.5	<0.5	<0.5	-	-	<0.5	<0.5	<0.5
Be	4	<1	3	2	3	<1	<1	<0.1	0.8	8	5	4	5	-	-	3	2	1
F	769	380	841	295	79	98	42	48	50		580		57	-	-	1284	1171	971
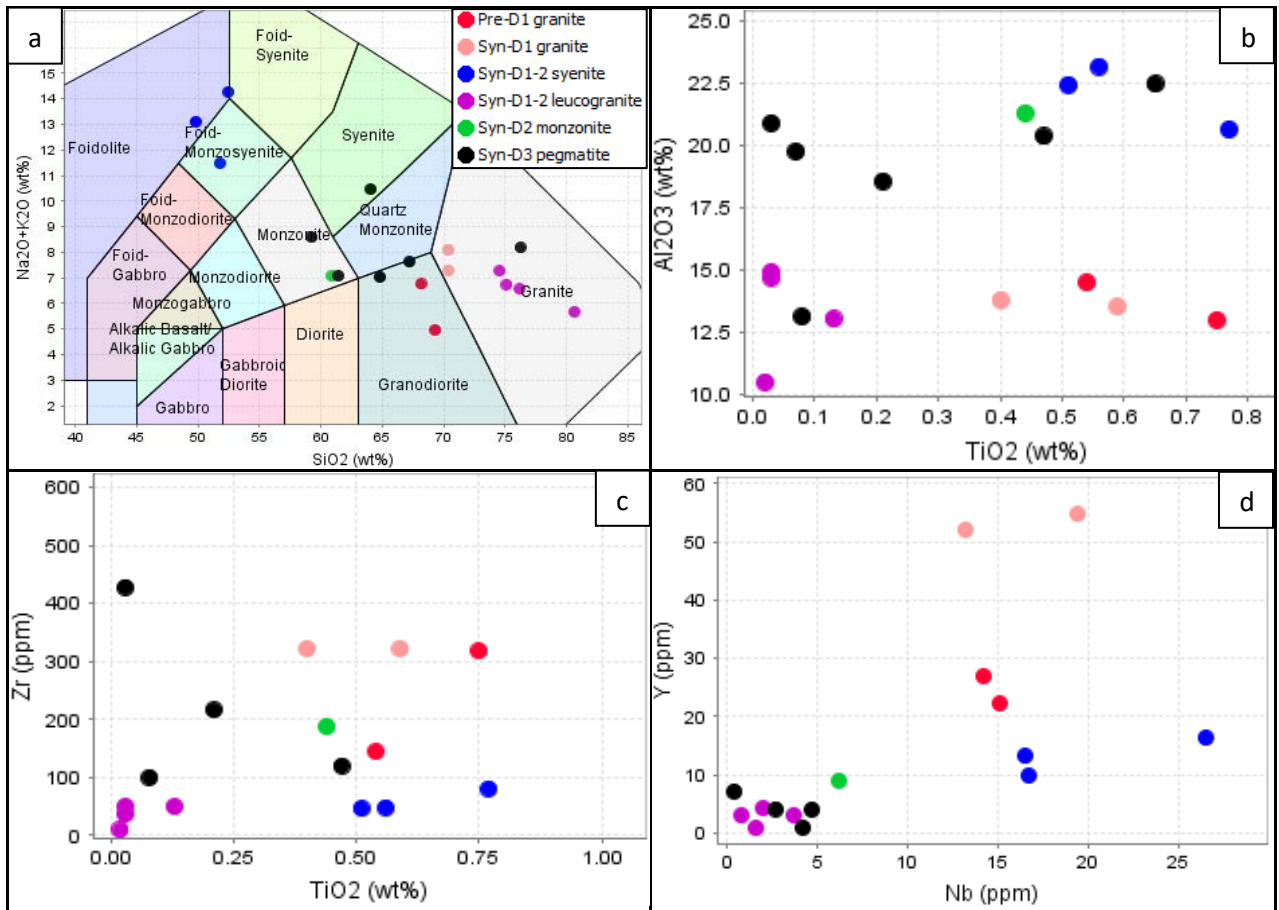
Figure 3.5. Rock classification diagrams (Middlemost, 1994) for major elements (a) and variation diagrams of least-mobile elements including Al_2O_3 vs. TiO_2, Zr vs. TiO_2, and Y vs. Nb (b, c, and d, respectively) for rocks from the Tick Hill region.
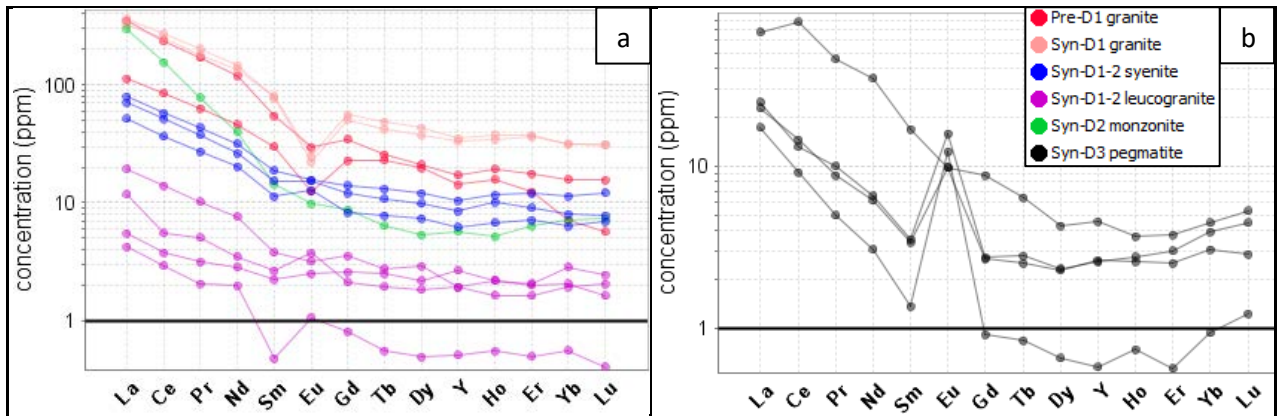
Figure 3.6. Chrondrite-normalized REE patterns for (a) pre-D_1 and syn-D_1 to (b) D_3 intrusions in the Tick Hill region. Chondrite normalization values after McDonough and Sun (1995).

Syn-D_1 intrusions include two granite samples (SMG, THG1) that have been dated and three samples of Monument Syenite (Msy, Msy.m, Msy.d) for which no dates could be obtained. Samples SMG and THG1 plot in the granite field and are broadly similar in composition to the pre-D_1 granites with which they are spatially associated (Figs. 3.5b, 3.7). The granites preserve relatively high concentrations of high-field-strength elements (HFSE) including REE, Zr and Y, and plot as a discrete

group on Y-Nb and REE diagrams (Figs. 3.6, 3.7). The syn-D_1 intrusions from the Monument Syenite form a separate group that is distinct from all other lithologies. They are silica-poor to silica-under-saturated syenite to monzosyenite (Fig. 3.5a) with relatively high Al_2O_3, TiO_2, CaO, Nb, Na, Sr and Ba contents (Figs. 3.5b,d, 3.7), intermediate REE enrichment, and a relatively flat REE pattern without a negative Eu anomaly (Fig. 3.6a).
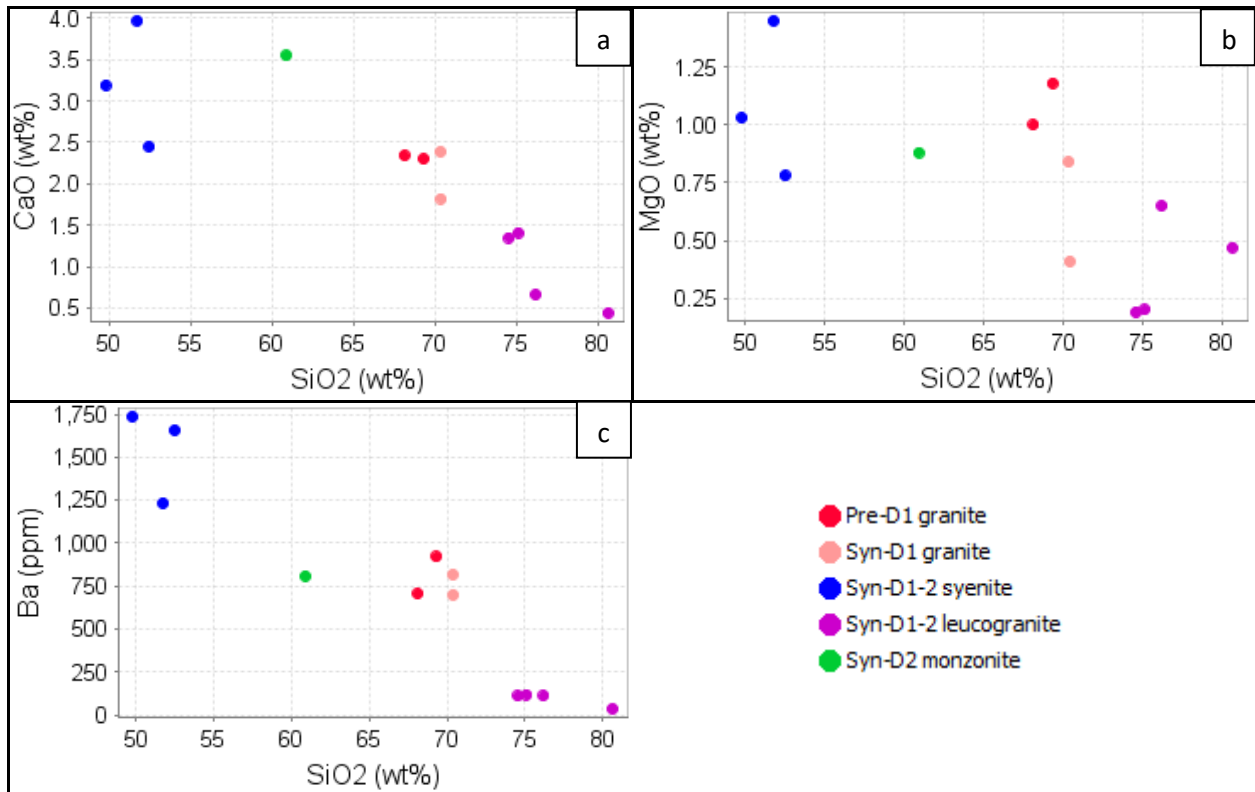
Figure 3.7. Variation diagrams for (a) SiO₂ vs. CaO, (b) SiO₂ vs. MgO, and (c) SiO₂ vs. Ba for pre-D₁ to syn-D₂ intrusions in the Tick Hill region.

The late syn-D_1 and syn-D_2 intrusions include the monzonite dyke sample (MG), variably deformed leucogranite samples (THG3, THG4), and gold-bearing quartz-feldspar mylonite samples (THM04 and THM27). The composition and texture of quartz-feldspar mylonite is similar to that of the leucogranite, and consequently it is grouped with the leucogranite unit. The four leucogranite samples are relatively quartz-rich and plot in the granite field (Fig. 3.5a). They form a discrete group in all variation diagrams (Figs. 3.5-3.7). The rocks are depleted in REE with relatively flat chondrite normalized distribution patterns and only minor enrichment of LREE with no clear Eu anomaly. They are also low in incompatible LILE (K, Ba, Rb Cs) and HFSE (Al, Ti, Zr, Y, Nb and Hf ; Fig 5), and they are relatively enriched in Na and depleted in Ca and K reflecting the abundance of albite in these rocks (Fig. 3.7, Table 3.1). The syn-D_2 monzonite dyke (MG, Fig. 3.5a) is enriched in LILE except for Sr, and strongly enriched in U and Th (Table 3.1). The sample has a distinct REE pattern with strong enrichment in LREE (Fig. 3.6a), but with a relatively low phosphate content. It is relatively enriched in Al_2O_3, MgO, CaO, Zr, Rb, Hf and Ba (Figs. 3.5b,c, 3.7a; Table 3.1).

The syn-D_3 intrusions include all the late-tectonic pegmatites. These form a distinct group with variable compositions and trace element patterns. Compositionally they vary from quartz-monzonite and syenite to granite, with strong enrichment in Na (Table 1). Some samples consist of coarse-grained pegmatite, and their compositional variation is most likely due to the fact that they were incompletely sampled. Nevertheless, the pegmatites plot close together on the Nb-Y diagram (Fig. 3.5d) and show distinct REE patterns with positive Eu anomalies.

Because the rock in the Tick Hill region undergone peak metamorphism (i.e. Syn-D_{1-2} samples) and strong red-rock alteration (Syn-D_3 and some Syn-D_{1-2} samples), the available tectonic discrimination diagrams of based on geochemical compositions possibly do not provide correct conclusion. However, the tectonic environments for studied samples have been tested by diagram of Whalen et al. (1987) using Ga/Al vs Nb contents, in which most of samples are plotted in the "I-, S- and M-type granites" domain.

3.4.2. Geochronology

The geochronological results are summarized in the Table 3.2 and Fig. 3.8, and shown for the individual samples in Figs 9 to 17. The details for each analysis, including standard analysis is presented in Appendix 3 while the CL images for dated zircons are presented in Appendix 4. All reported ages are based on the weighted mean age of the youngest distinct age group in each sample, and only includes zircon ages that are <10% discordant. All reported error margins are given as 2σ.

3.4.2.1. Regional samples

Zircon grains from the pre-D_1 granite sample ***OTG*** are euhedral with prismatic to needle-like shapes. About 70% of zircon grains are dominated by metamict zircon domains with a relatively uniform texture, with the remainder being unaltered zircon domains with well-developed growth zoning (Fig. 3.9a). Some grains have metamorphic overgrowths that are generally irregular in outline and too narrow to be measured by LA-ICP-MS (Fig. 3.9a). A total of 37 analyses were conducted on unaltered and the least metamict zircon domains, that yield a single cluster of concordant ages with a weighted mean age of 1857±5 Ma (n = 20, MSWD = 0.96; Fig. 3.9c), interpreted as the age of emplacement of the granite. Two inherited zircon grains yield near-concordant ages of 1882±22 Ma and 1895±25 Ma.

Sample ***SMG*** of syn-D_1 granite contains largely unaltered, zoned prismatic zircon grains of magmatic origin that are up to 500 μm in length (Fig. 3.9d; Corfu et al., 2003). Some are slightly metamict with thin overgrowths of hydrothermal/metamorphic zircon (Fig. 3.9d; Corfu et al., 2003). Only unaltered or slightly metamict zircon domains were analyzed, whilst metamorphic rims were too

thin to be measured. A total of 53 analyses yield three discrete age populations, with a weighted mean ages of 1790±7 Ma (n = 21, MSWD = 0.42; Fig. 3.9f), 1826±9 Ma (n = 11, MSWD = 0.77) and 1865±11 Ma (n = 6, MSWD = 0.82). The youngest age is interpreted as the magma emplacement age, whilst the older age groups probably reflect inheritance.

Sample *THG1* of syn-D$_{1-2}$ granite contains zircons that are similar in morphology to those described for SMG (e.g., Fig. 3.10a). A dominant population of concordant ages with a weighted mean of 1777±3 Ma (n = 38, MSWD = 1.04; Figs. 3.10b,c), was obtained from a total of 53 analyses, and has been interpreted as the magmatic emplacement age. A further five concordant zircon grains yield age groupings at 1796±12 Ma (n = 2, MSWD = 0.00) to 1834±11 Ma (n = 3, MSWD = 0.14), interpreted to reflect inheritance.
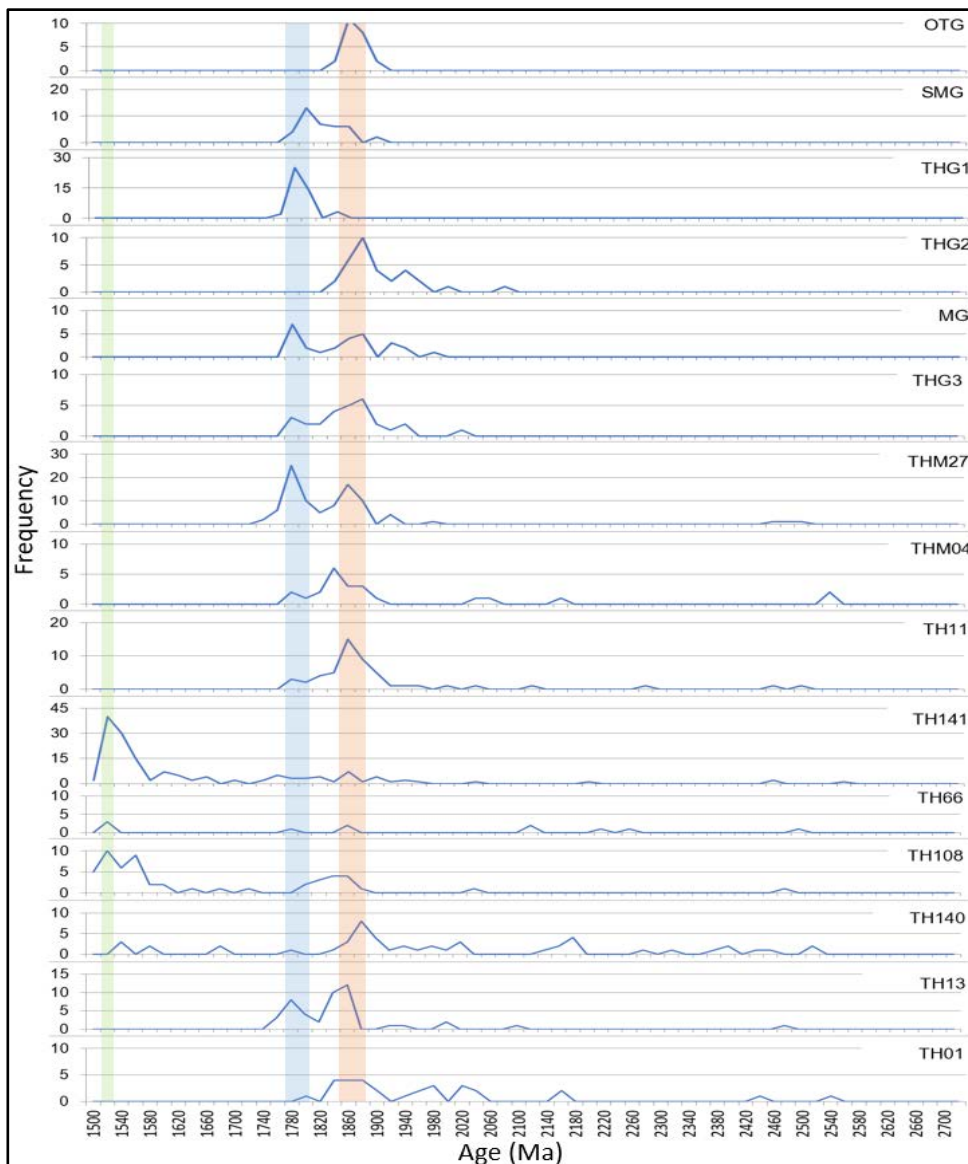
Figure 3.8. Frequency plots showing near-concordant and concordant ages (Ma) for samples from the Tick Hill region. Bin sizes are 20 Ma with the age label for each bin corresponding to the middle age of the bin. Major tectonic events are indicated as coloured bars.

Table 3.2. Sample locations for all samples used in this study, together with a summary of the U-Pb zircon $^{207}Pb/^{206}Pb$ ages for key rock units in the Tick Hill region. The ages are based on weighted mean averages of grains with <10% discordance. Errors are shown as 2σ; photos and plots are shown in Figs.3.8-3.16.

Mapped rock unit (Fig. 1)		Sample ID	Location	Zone 54-GDA94		Age (Ma)	Age comment
				East (m)	North (m)		
Pre-D$_1$	One Tree granite	OTG	10 km W of Tick Hill	378,568	7,602,967	1857±5	n=20; MSWQ=0.96
	Saint Mungo granite	THG2	3,7 km W of Tick Hill	385,138	7,606,776	1850±6	n=10; MSWD=1.6
Syn-D$_1$	Saint Mungo granite	SMG	8 km W of Tick Hill	381,233	7,604,274	1790±7	n=21; MSWD=0.42
	Tick Hill granite	THG1	3,5 km W of Tick Hill	385,156	7,606,851	1777±3	n=38; MSWD=1.04
Syn-D$_{1-2}$	Tick Hill granite	THG4	3,5 km SW of Tick Hill	386,702	7,603,938	1777±14	n=1
	Tick Hill granite	THG3	0,5 km E of Tick Hill	389,258	7,605,939	1778±10	n=7; MSWD=1.5
	Tick Hill quartz-feldspar mylonite	THM27	Tick Hill, underground	388,842	7,605,934	1771±5	n=43; MSWD=0.82
	Tick Hill quartz-feldspar mylonite	THM04	Tick Hill, underground	388,850	7,605,950	1789±16	n=5; MSWD=1.18
Syn-D$_2$	Monzonite dyke	MG	23 km SSW of Tick Hill	386,650	7,600,566	1773±7	n=8; MSWD=1.2
Syn-D$_3$	Tick Hill syn-D$_3$ pegmatite (possibly syn-D$_2$)	TH11	Tick Hill pit	388,869	7,605,868	1772±19	n=4; MSWD=2.1
	Tick Hill syn-D$_3$ pegmatite	TH141	Tick Hill pit	388,867	7,606,015	1522±3	n=81; MSWD=0.79
	Tick Hill syn-D$_3$ pegmatite	TH108	Tick Hill, DH U8506: 224-224.3 m; 236.5-236.8 m; 240.3-240.5 m;	388,728	7,605,910	1524±6	n=27; MSWD=1.14
	Tick Hill syn-D$_3$ pegmatite	TH140	Tick Hill, DH TH032: 285.5-286.1 m	388,607	7,605,915	1530±19	n=3; MSWD=0.2
	Tick Hill syn-D$_3$ pegmatite	TH66	Tick Hill, DH U9205: 149.45-149.9 m	388,752	7,605,976	1517±45	n=3; MSWD=0.021
Pre- or syn-D$_1$?	Hangingwall quartzite	TH13	Tick Hill pit	388,842	7,605,827	1781±6	n=19; MSWD = 1.2
	Footwall quartzite	TH01	Tick Hill pit	388,913	7,605,912	1841±15	n=11, MSWD = 0.74
Syn-D$_{1-2}$	Monument syenite	Msy	6.1 km SSW of Tick Hill	386953	7600313		
	Monument syenite	Msy.m	6.1 km SSW of Tick Hill	386914	7600329		Whole rock geochemistry only
	Syenite dyke	Msy.d	6.1 km SSW of Tick Hill	386953	7600313		
Syn-D$_3$	Tick Hill post-D$_3$ pegmatite	TH87	Tick Hill, underground; DH U8506: 144.1-144.4 m	388,728	7,605,910		
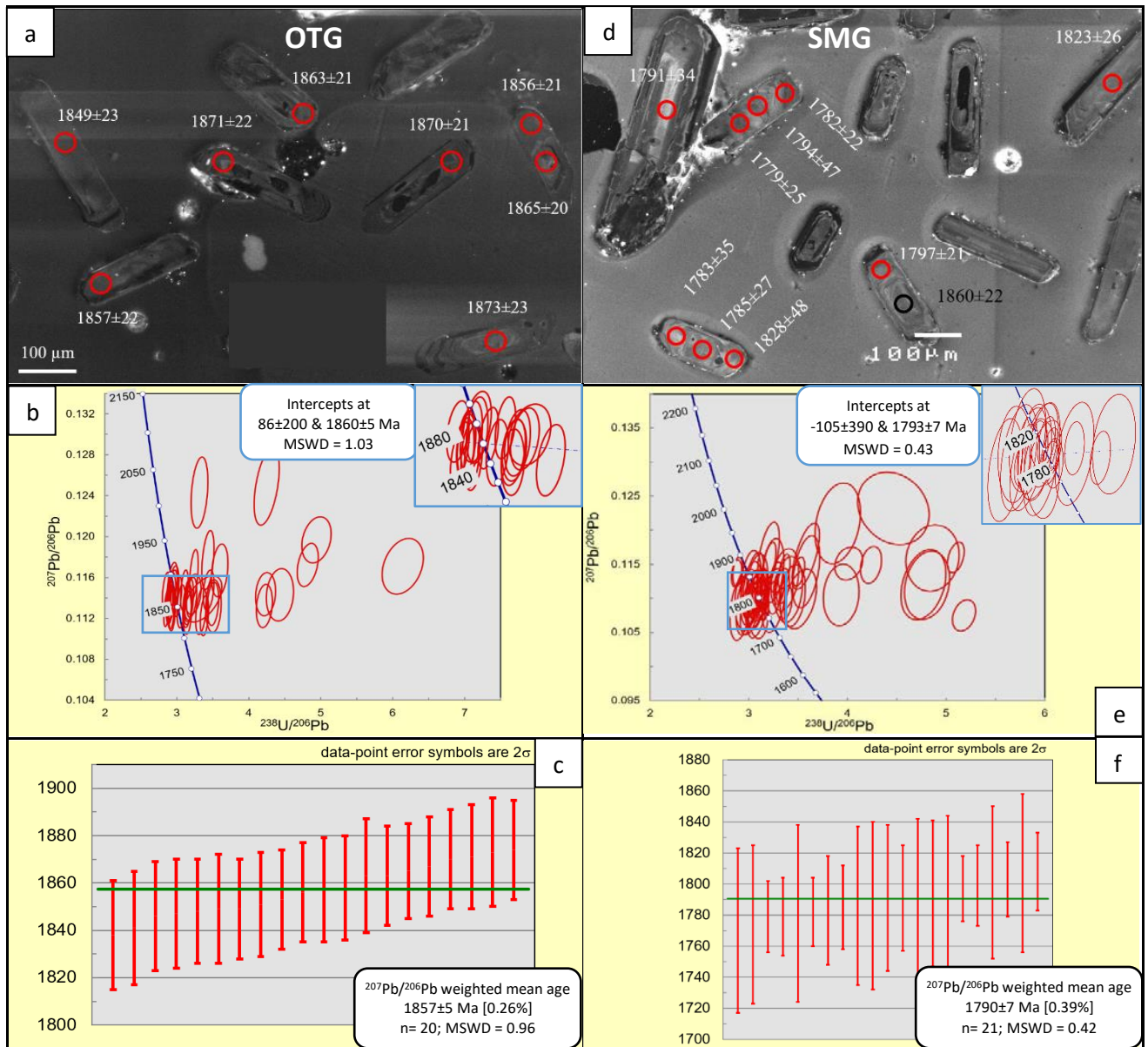
Figure 3.9. Cathodoluminescence images for zircon grains from the youngest age group, concordia diagrams for all analyses, and concordant grains in the youngest age group (inset), and weighted mean age diagram for the youngest zircon group for samples OTG (a, b, and c, respectively) and SMG (d, e, and f, respectively).

Sample **THG2** of pre-D$_1$ granite yielded a morphologically similar sample of zircons as OTG, with both metamict and zoned zircon grains, some with thin metamorphic overgrowths (Fig. 3.10d). A total of 77 analyses provided a weighted mean age for the youngest population group of 1850±6 Ma (n = 10, MSWD = 1.6; Fig. 3.10f). This age has been interpreted as the magma emplacement age. Inherited concordant zircon grains in this sample yield two main groupings at 1876±6 Ma (n = 12, MSWD = 1.6) and 1925±11 Ma (n = 7, MSWD = 1.7) and three single ages ranging from 1947±14 Ma to 2064±18 Ma (Fig. 3.10e).
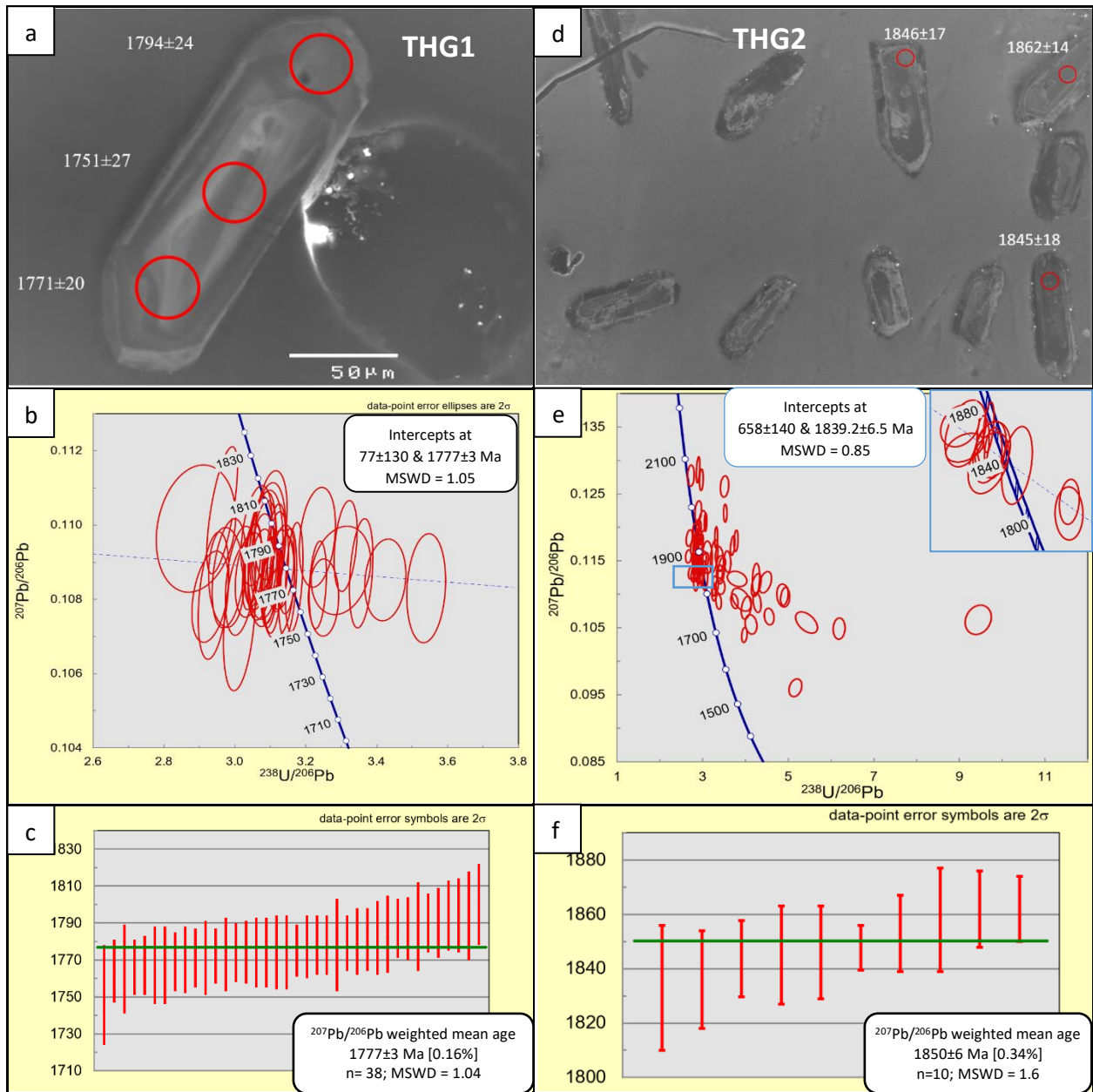
Figure 3.10. Cathodoluminescence images for zircon grains from the youngest age group, concordia diagrams for all analyses and concordant grains in the youngest age group (inset), and weighted mean age diagram for the youngest zircon group for samples THG1 (a, b, and c, respectively) and THG2 (d, e, and f, respectively).

Syn-D$_2$ monzonite sample **MG** contains well-zoned prismatic zircons that are locally metamict with minor metamorphic/hydrothermal overgrowths (e.g., Fig. 3.11a). A total of 46 analyses from unaltered and metamict zircon grains, provide a weighted mean age of 1773±7 Ma (n = 8, MSWD = 1.2; Fig. 3.11c) for the youngest group of concordant zircon grains (Fig. 3.11b), which has been interpreted as the age of emplacement of the monzonite dyke. An additional 18 concordant analyses define three further age groupings at 1842±8 Ma (n = 9, MSWD = 1.3), 1874±7Ma (n = 3, MSWD = 0.41) and 1918±8 Ma (n = 5, MSWD = 0.29), interpreted to reflect inheritance.
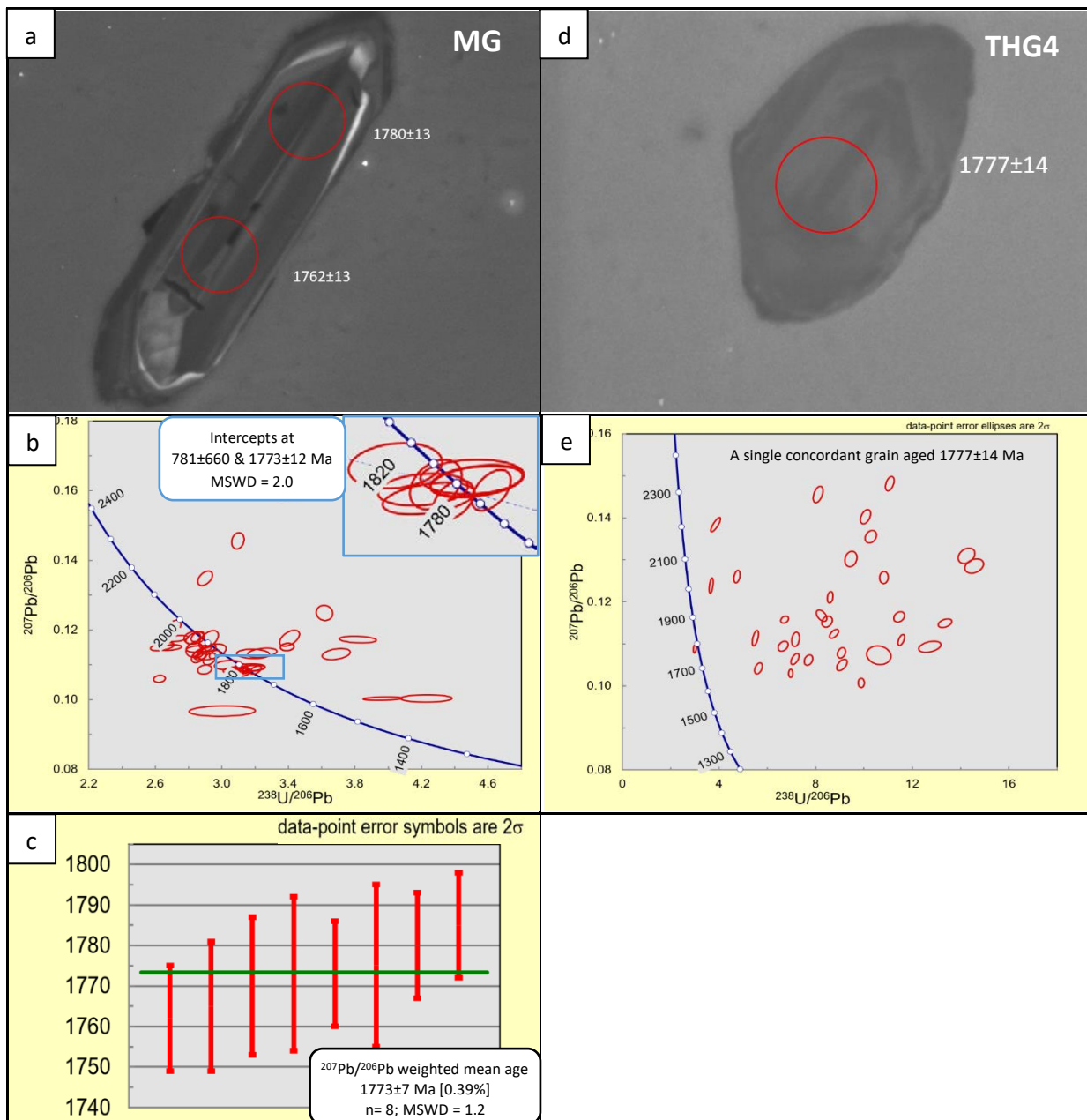
Figure 3.11. (a, b and c respectively) Cathodoluminescence image for a representative zircon grain from the youngest age group, concordia diagram for all analyses and concordant grains in the youngest age group (inset), and weighted mean age diagrams for the youngest zircon group for sample MG. (d and e respectively) Cathodoluminescence image and the concordia diagram of the only concordant zircon grain for sample THG4.

Almost all zircon grains in the syn-D_2 leucogranite sample **THG4** are strongly recrystallised and altered with no internal zonation (Appendix 4), and many have irregular, almost skeletal outlines suggesting partial resorption. Many of these texturally complex grains are completely metamict, and some grains preserve thin metamorphic overgrowths. Only relatively unaltered grains were sampled (Fig. 3.11d), and 34 analyses produced a single concordant age of 1777±14 Ma (Fig. 3.11e), interpreted as the age of granite emplacement.

3.4.2.2. Local samples

Most zircon grains in the syn-D_{1-2} leucogranite sample ***THG3***, were strongly recrystallised and altered (Appendix 4), and many have irregular, almost skeletal outlines suggesting partial resorption, rendering the zircons with complex internal textures that have destroyed all evidence of earlier zoning. Some grains preserve thin metamorphic overgrowths. The strongly recrystallized, metamict zircon grains either do not provide a proper data signal or yield extremely discordant ages. The sample contains a small proportion of prismatic, zoned zircon grains (Fig. 3.12a) for which 65 analyses in a distinct young grouping yield concordant ages with a weighted mean of 1778±10 Ma (n = 7, MSWD = 1.5; Fig. 3.12c), interpreted as the age of emplacement. An additional 21 concordant analyses for older inherited zircon grains, define an age grouping at 1848±7 Ma (n = 14, MSWD = 1.09) with further ages ranging from 1875±10 Ma to 1939±28 Ma.
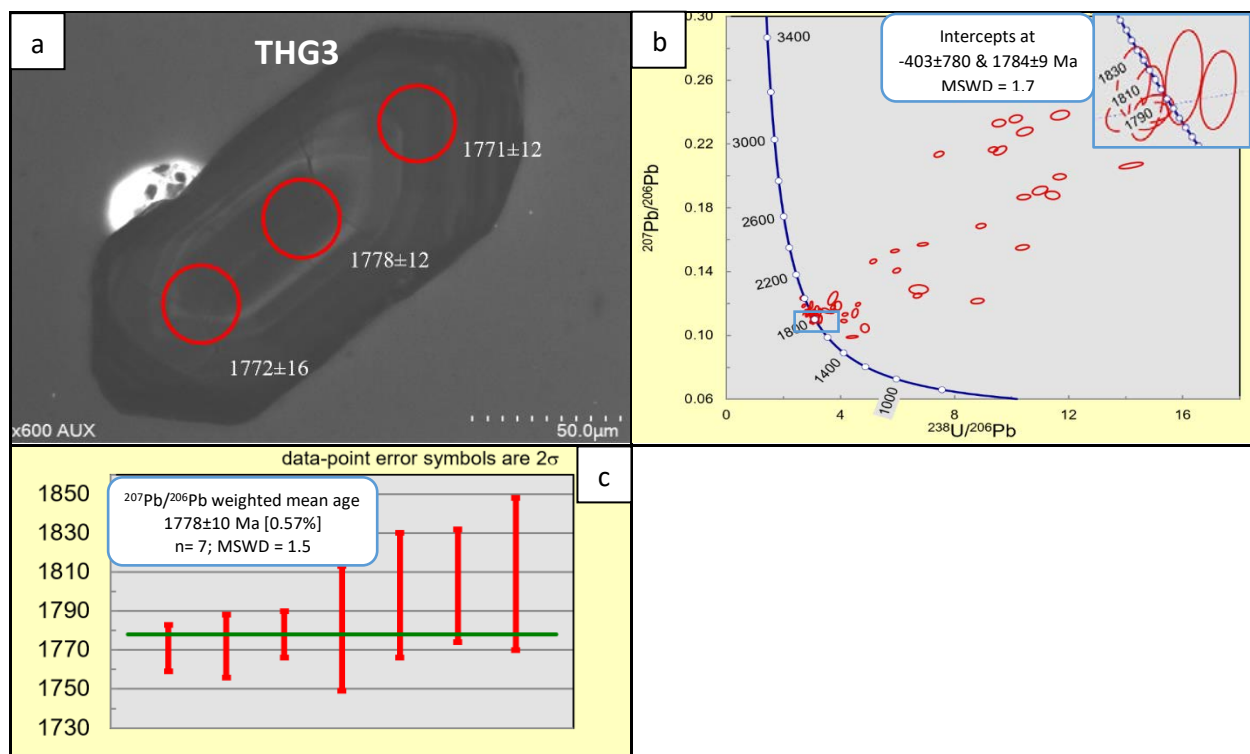
Figure 3.12. Cathodoluminescence image for a representative zircon grain from the youngest age group, concordia diagram for all analyses, and concordant grains in the youngest age group (inset), and weighted mean age diagrams for the youngest zircon group for sample THG3 (a, b, and c, respectively).

The syn-D_{1-2} gold-bearing quartzo-feldspathic mylonite samples ***THM04*** and ***THM27***, are dominated by weakly metamict zircon grains characterized by homogenized internal textures, with metamorphic rims that are too thin to measure (Figs. 3.13a, d). Based on 109 analyses for zircon grains from sample ***THM27***, the youngest population of concordant ages has a weighted mean of 1771±5 Ma (n = 43, MSWD = 0.82; Fig. 3.13c), which is interpreted as the age of emplacement of the original quartz-feldspathic leucogranite. An additional 48 concordant analyses provide a further inherited age

grouping at 1845±6 Ma (n = 40, MSWD = 1.2) and other ages that range from 1915±17 Ma (n = 4, MSWD = 0.08) to 2473±48 Ma (n = 3, MSWD = 2.2). The youngest age grouping for concordant zircon grains from 38 analyses for sample **THM04** provides a weighted mean age of 1789±16 Ma (n = 5, MSWD = 1.18; Fig. 3.13f), again interpreted as the age of emplacement of the original quartz-feldspathic leucogranite. An additional 15 inherited concordant grains yield a cluster at 1848±9 Ma (n = 13, MSWD = 0.96) with further ages ranging from 2036±24 Ma (n = 2, MSWD = 0.61) to 2530±22 Ma (n = 2, MSWD = 0.00).
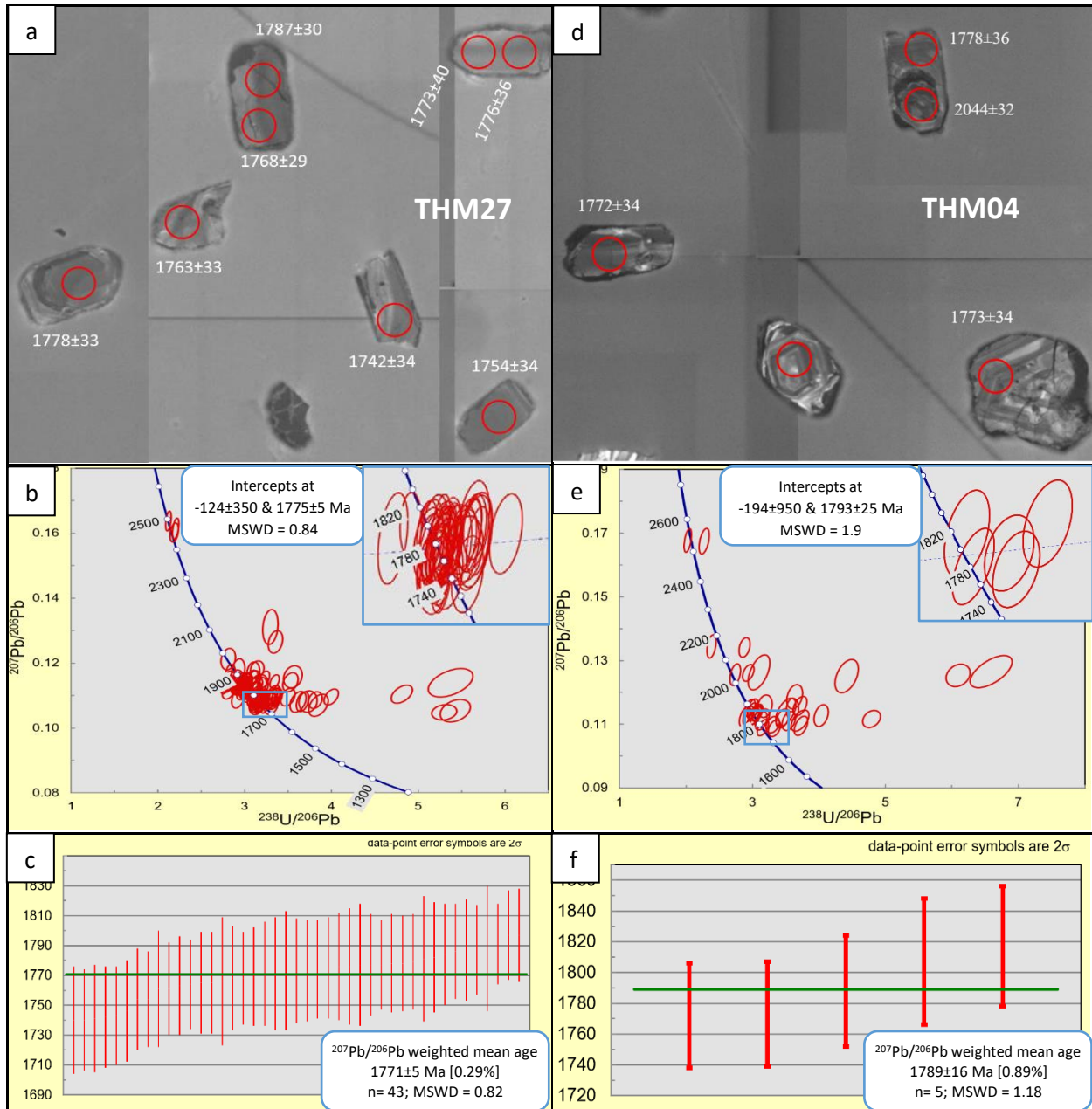
Figure 3.13. Cathodoluminescence images for zircon grains from the youngest age group. Concordia diagrams for all analyses and concordant grains in the youngest age group (inset), and weighted mean age diagrams for the youngest zircon group for samples THM27 (a, b, and c, respectively) and THM04 (d, e, and f, respectively).

The syn-D_3 pegmatite samples (TH11, TH141, TH66, TH108 and TH140) yield complex zircon populations dominated by hydrothermal zircon characterized by a framework texture of bright seams surrounding black domains (e.g., Fig. 3.14d). Other zircon grains show partly zoned and metamict domains, locally recrystallized and overgrown by zircon domains with complex framework textures (e.g., Fig. 3.14a) that indicates hydrothermal and metamorphic zircon. Analyses of metamorphic zircon domains yielded only discordant ages. Hydrothermal and metamict zircon domains in each of the samples provided similar ages. In sample *TH11*, 87 analyses for the least altered zircons (i.e., metamict zircon domains with homogenous texture, Fig. 3.14a) provide a large spread of ages, reflecting inheritance. The youngest four concordant grains provide a weighted mean age of 1772±19 Ma (n = 4, MSWD = 2.1; Fig. 3.14c), but it is not clear if this age whether represents an emplacement age or it reflects inheritance from the surrounding gneiss units because the sample is considered as syn-D_3 pegmatite based on its texture and geochemical signatures as being discussed above. A further 48 concordant analyses from TH11 provided three distinct age groupings at 1824±11Ma (n = 8, MSWD = 2), 1854±4 MA (n = 21, MSWD = 0.67) and 1883±7 Ma (n = 10; MSWD = 0.64), and additional individual ages that range from 1924±24 to 2498±11 Ma (n = 8; Fig. 3.14b).

Sample *TH141*, with 219 analyses (of which 150 were concordant) mostly taken from hydrothermal zircon and metamict zircon provided a weighted mean age of 1522±3 Ma (n = 81, MSWD = 0.79; Fig. 3.14f) for the youngest grouping of concordant zircon grains. This age is well constrained and has been interpreted as the age of pegmatite emplacement and related hydrothermal events during D_3. Other groupings of (near-)concordant analyses for hydrothermal zircons provide mean ages of 1557±11 Ma (n = 8, MSWD = 0.075), 1602±8 (n = 11; MSWD = 0.6), 1649±16 Ma (n = 4; MSWD = 0.083), 1743±12 Ma (n = 7, MSDW=0.8), 1788±13 Ma (n = 8, MSWD = 0.99), 1841±12 Ma (n = 9; MSWD = 0.79), 1880±12 (n = 7, MSWD = 1.05), with an additional eight analyses yielding individual ages of between 1922±28 Ma and 2558±34 Ma.

Sample *TH66* with 28 analyses from hydrothermal and metamict zircon (Fig. 3.15a), provided a weighted mean age of 1517±45 Ma (n = 3; MSWD = 0.021, Fig. 3.15c) for the youngest three concordant analyses of hydrothermal zircon, which is interpreted to approximate the hydrothermal age and probably also the pegmatite emplacement age. Another eight concordant grains provide inherited ages ranging from 1796±74 Ma to 2496±96 Ma. Sample *TH108* (121 analyses) from hydrothermal and metamict zircon (Fig. 3.15d), yielded a weighted mean age of 1524±6 Ma (n = 27; MSWD = 1.14, Fig. 3.15f) for the youngest population of concordant zircon grains. This age has been interpreted as the age of pegmatite emplacement and associated hydrothermal events during D_3. An additional 26 concordant ages range from 1547±21 Ma to 2480±72 Ma, and define three main groupings at 1557±12 Ma (n = 5, MSWD = 0.55), 1795±11 Ma (n = 5, MSWD = 0.6) and 1834.1±10 Ma (n = 8, MSWD = 1.3), all indicative of inheritance from the surrounding host rocks. Sample *TH140* (76 analyses)

contains only few near-concordant grains with a weighted mean age of 1530±19 Ma (n = 3; MSWD = 0.2, Fig. 3.16c) for the youngest three concordant grains of hydrothermal zircon. An additional five concordant analyses for hydrothermal grains yield ages between 1572±32 Ma and 1675±30 Ma, and another 45 concordant analyses from metamict grains give inherited ages ranging between 1777±56 Ma and 3190+31 Ma, including four age clusters around 1869±8 Ma (n = 16, MSWD = 1.12), 1948±13 Ma (n = 6, MSWD = 1.07), 2008±15 Ma (n = 4, MSWD = 0.3) and 2158±12 Ma (n = 7, MSWD =1.01).
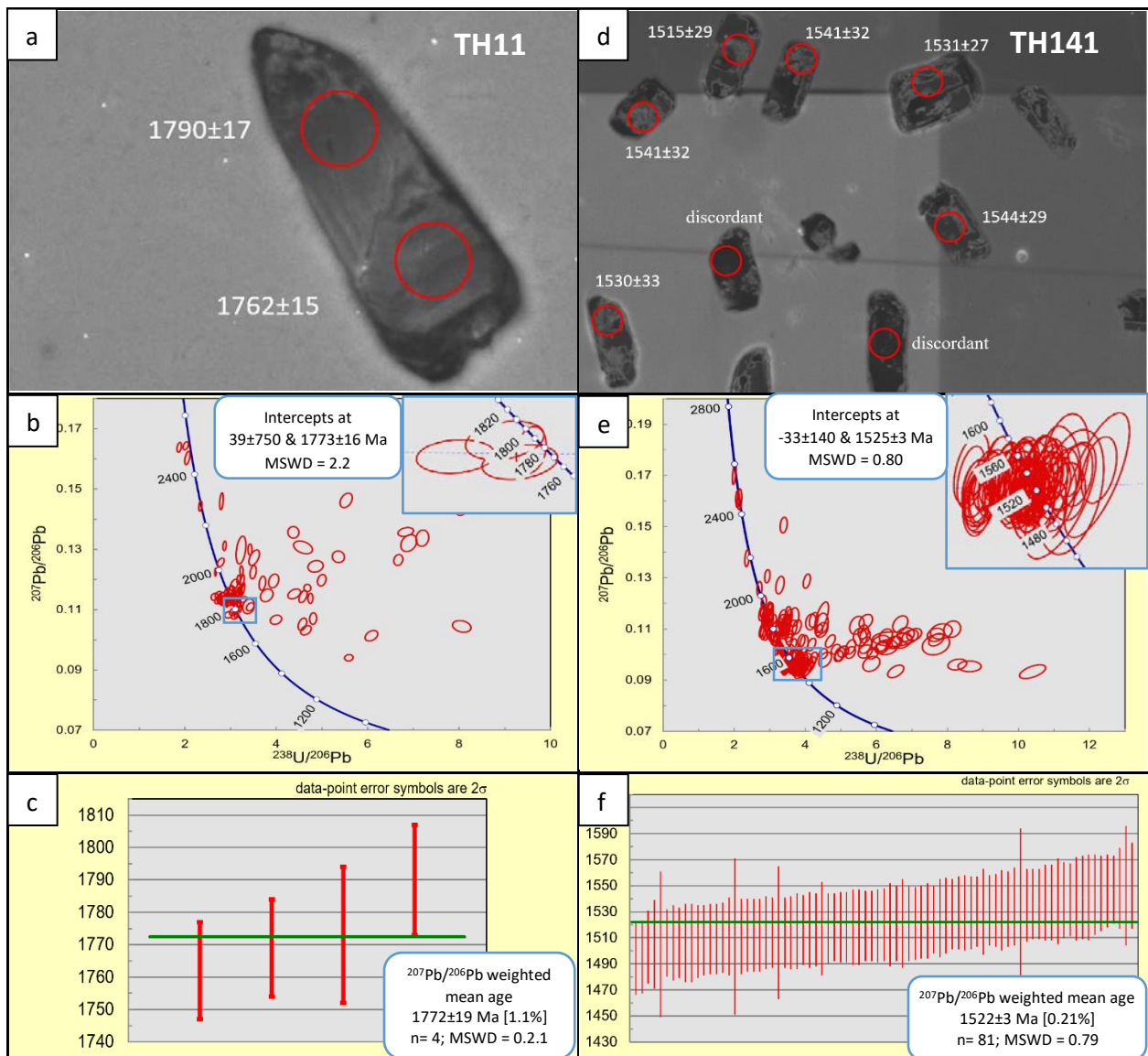
Figure 3.14. Cathodoluminescence images for zircon grains from the youngest age group; concordia diagrams for all analyses and concordant grains in the youngest age group (inset); and weighted mean age diagrams for the youngest zircon group for samples TH11 (a, b, and c, respectively) and TH1141 (d, e, and f, respectively).
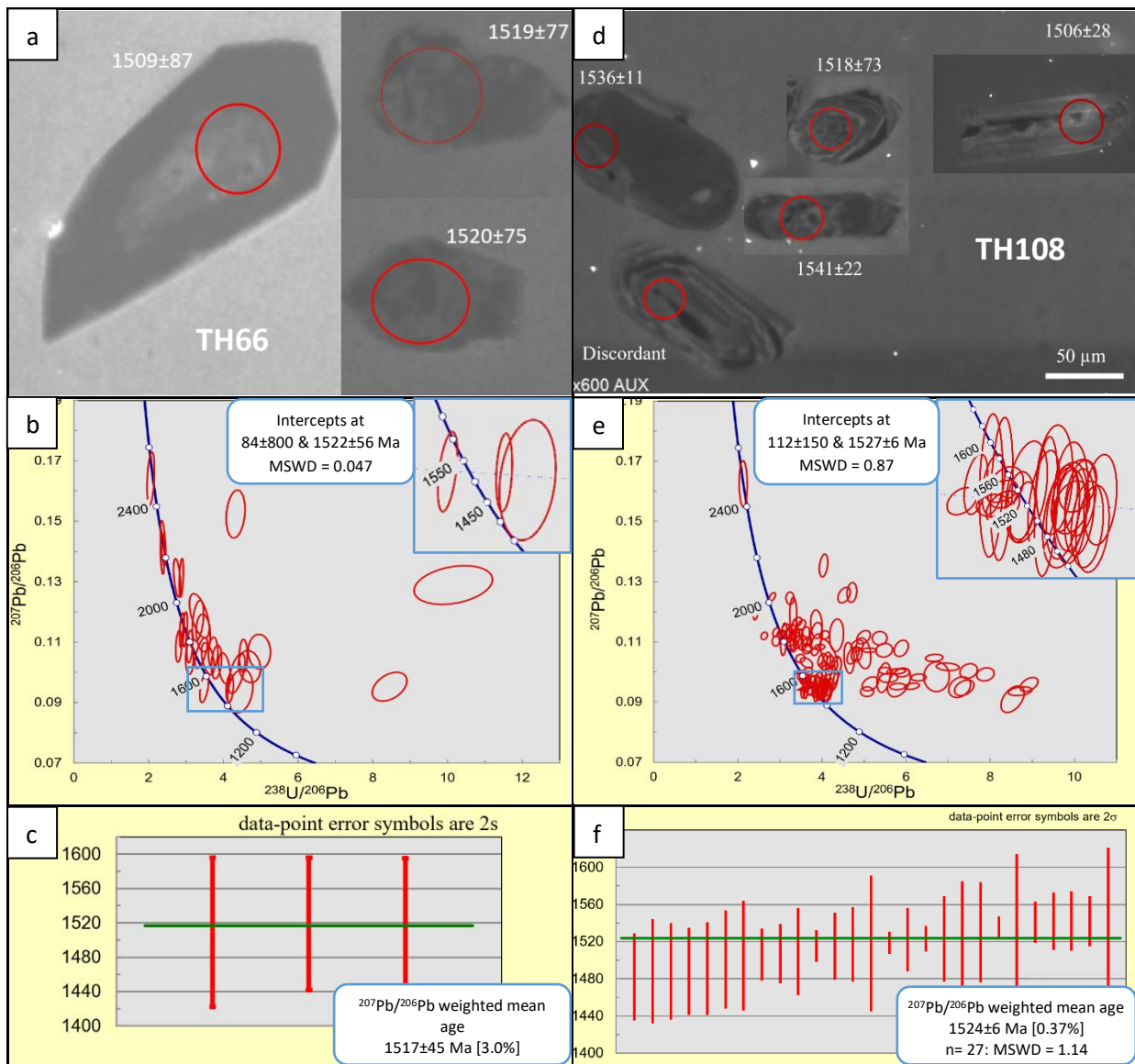
Figure 3.15. Cathodoluminescence images for zircon grains from the youngest age group; concordia diagrams for all analyses and concordant grains in the youngest age group (inset), and weighted mean age diagrams for the youngest zircon group for samples TH66 (a, b, and c, respectively) and TH108 (d, e, and f, respectively).

Sample **TH13** of hanging wall quartzite comprises zircon grains showing (sub)rounded to prismatic and needle-like shapes. Some grains preserve cores of zoned zircon or metamict domains with uniform textures, and thin metamorphic rims are common (Fig. 3.17a). Results for 124 analyses from elongated, euhedral to slightly anhedral prismatic grains fall into two main concordant populations with weighted mean ages of 1781±6 Ma (n = 19, MSWD = 1.2; Fig. 3.17c) and 1841±4 Ma (n = 20, MSWD = 0.98). The mean age for the youngest age grouping can be interpreted as the maximum age of quartzite deposition if the quartzite is interpreted as a sedimentary horizon. Alternatively the quartzite in sample TH13 can be interpreted as strongly silicified quartzo-feldspathic gneiss similar to quartzo-feldspathic mylonite (e.g., Laing, 1993; Tedman-Jones, 2001), in which case the age may represent the age of emplacement of an original leucogranite. The latter interpretation is

more consistent with the needle-like prismatic morphology of many of the grains. An additional six concordant ages provide inherited ages that range from 1919±12 Ma to 2467±45 Ma.
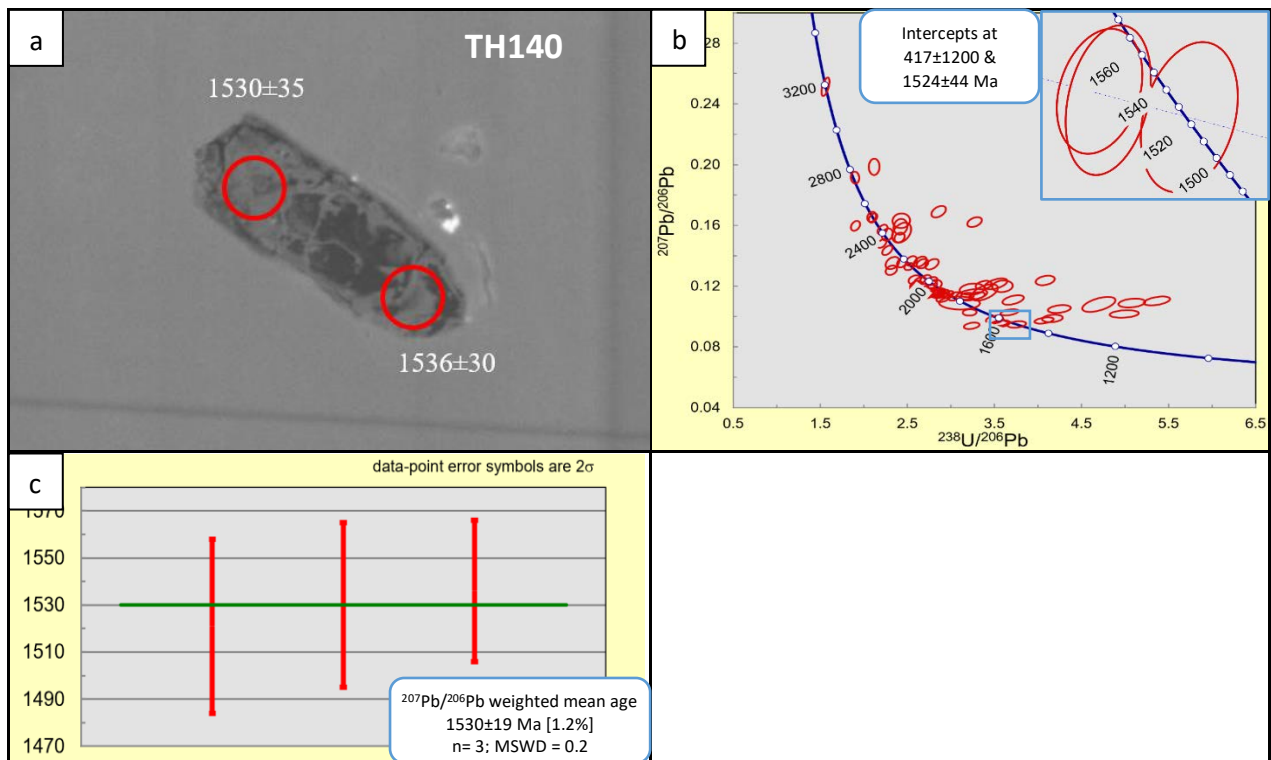
Figure 3.16. Cathodoluminescence image for a representative zircon grain from the youngest age group, concordia diagram for all analyses and concordant grains in the youngest age group (inset), and weighted mean age diagrams for the youngest zircon group for sample TH140 (a, b, and c, respectively).

Sample ***TH01*** of footwall quartzite show rounded to prismatic and needle-like zircon grains (Appendix 4), with individual grains exhibiting either internal growth zoning or uniform metamict textures with concentric metamorphic domains replacing original growth zoning (Fig. 3.17d). Some zircon grains have thin metamorphic rims that are too thin to measure with the laser. About 10% of zircon grains from this sample are extremely metamict, leaving the grains homogenously black in color (Appendix 4). These grains do not yield any concordant ages. Results for 77 analyses for rounded to euhedral grains yielded three concordant zircon groupings with weighted mean ages of 1841±15 Ma (n = 11, MSWD = 0.74; Fig. 3.17f), 1883±24 Ma (n = 4; MSWD = 0.1) and 1984±22 Ma (n = 11, MSWD = 1.7). Additional older ages for individual concordant granis range from 2146±51 Ma to 2532±46 Ma (Figs. 17e, f). The mean age for the youngest age grouping can be interpreted as the maximum age of quartzite deposition if the quartzite is interpreted as a sedimentary horizon and the zircons to be detrital. However, if the quartzite formed as a result of early silicification of a D_1 shear zone, the age may actually represent a detrital age for the underlying sediments that were silicified.
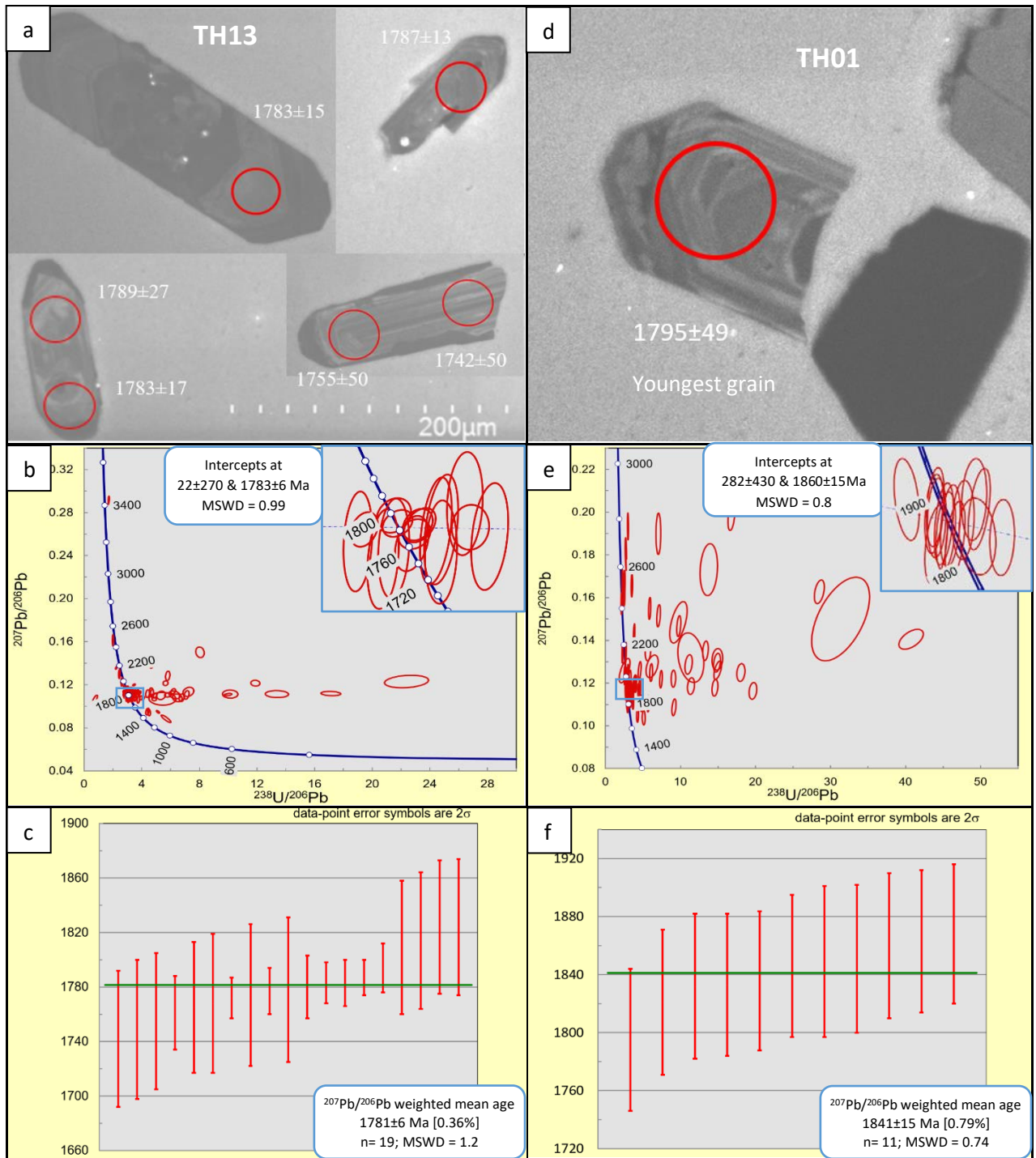
Figure 3.17. Cathodoluminescence images for zircon grains from the youngest age group, concordia diagrams for all analyses and concordant grains in the youngest age group (inset), and weighted mean age diagrams for the youngest zircon group for samples TH13 (a, b, and c, respectively) and TH01 (d, e, and f, respectively).

3.5. Discussion

The presence of coarse gold grains as inclusions in peak-metamorphic hornblende and pyroxene suggests that at least some of the gold at Tick Hill was present prior to or during D_1 events (Laing, 1993; Choy, 1994; Chapter 2). However, on outcrop-scale the bulk of the gold is associated

with syn-D_3 alteration assemblages and D_3 fracture zones. This indicates that most of the gold was either emplaced during D_3 events, or redistributed from an earlier gold deposit when large volumes of acidic, saline, oxidizing, aqueous fluids with the capacity to carry metals moved through much of the rock pile (Oliver et al., 1991; Laing, 1993; Tedman-Jones, 2001; Williams et al., 2005; Groves et al., 2010). Both early-gold and late-gold models have been pursued at some stage during the exploration history of Tick Hill and in either case intrusive activity was invoked as an underlying mechanism. Based on comparisons with the geology in the MKD north of Tick Hill, the early D_1 events were assumed to have occurred within the Corella Formation around 1740 Ma, accompanied by the intrusion of Wonga and Burstall Suites (Blake et al., 1982; Wyborn et al., 1997). D_2 folding and D_{3-4} faulting with gold mineralization was linked to Isan events between 1600-1500 Ma (e.g., Laing, 1993; Choy, 1994; Forrestal et al., 1998; Tedman-Jones, 2001). Whilst seemingly consistent with deformation and mineralization histories for IOCG deposits elsewhere in the Eastern Fold Belt (e.g., Williams et al., 2005), these interpretations are not consistent with the age data presented here.

The U-Pb zircon ages presented for igneous and quartzite units near the Tick Hill deposit, provide evidence for three distinct episodes of magmatic and/or metamorphic activity between ca. 1855 Ma to 1520 Ma. These episodes include: (1) the emplacement of pre-D_1 granitic rocks at 1850-1855 Ma; (2) the emplacement of granite at 1790-1770 Ma concomitant with D_1 shearing and D_2 upright folding; and (3) 1520-1525 Ma, syn-D_3 pegmatite emplacement and related hydrothermal activity. Inheritance in many of the zircon populations suggests that older basement was present throughout much of the area, and there is a general lack of zircons with ages between 1720-1740 Ma, although a few appear in some of the younger pegmatite samples.

3.5.1. The age of early igneous activity and deformation in the Tick Hill area

Samples OTG and THG2 from granodiorite gneiss west of Tick Hill, have ages of 1857±5 Ma and 1850±6 Ma, respectively, which are comparable to the age of the Kalkadoon Granodiorite that intruded the Leichhardt Volcanics (Wyborn and Page, 1983; Withnall and Hutton, 2013). Sample OTG was originally mapped as part of the Kalkadoon Supersuite (Blake et al., 1982) intruding the Plum Mountain Gneiss dated at 1863 Ma (Carson et al., 2011), which is consistent with our obtained age. Sample THG2 was collected from an outcrop originally mapped as part of the Wonga age (i.e., 1740 Ma) Tick Hill Complex (Blake et al., 1982; Wyborn et al., 1997). It was subsequently re-mapped as a small inlier of Burstall Suite (i.e., 1740 Ma), Saint Mungo Granite within the Tick Hill Complex (Rutherford, 2000, Fig. 3.1a). Based on field relationships both the Tick Hill Complex and Saint Mungo Granite were interpreted to intrude the Corella Formation, and rafts of Corella Formation gneiss occur within them. The new age data and geochemistry for THG2 indicate that the rock compares with the One Tree Granite, and that the unit is part of the Kalkadoon basement gneiss. The local outcrop of Kalkadoon basement surrounded by younger rocks (i.e. Tick Hill Complex) could be the remnant

basement in the Tick Hill area or the basement block trapped into the intrusion of Tick Hill Complex. The aeromagnetic signature of the unit from which THG2 was taken is homogenous and similar to Kalkadoon basement gneiss further west. This suggests that the large unit of Tick Hill granite mapped west of Tick Hill (Fig. 3.1a; Blake et al., 1982; Wyborn, 1997) consists largely of basement gneiss, i.e. the Kalkadoon basement extends further east then previously mapped and it locally occurs east of the mapped extent of Argylla Formation (Blake et al., 1982).

Sample SMG of Saint Mungo Granite was originally mapped as part of the 1740 Ma Burstall Suite emplaced immediately west of the Argylla Formation (Blake et al., 1982; Wyborn et al., 1997). The new age (1790±7 Ma) is well constrained and corresponds with the age of opening of the Leichhardt Superbasin in the Western Fold Belt (e.g., Foster and Austin, 2008; Withnall and Hutton, 2013), and particularly with the Big Toby-Yeldham-Bottletree igneous event (Carson et al., 2011; Withnall and Hutton, 2013). Geochemically and texturally, the sample is similar to THG1 (Figs. 3.5-3.7), which yields a well-constrained age of 1777±3 Ma and the two granites are probably related. THG1 was mapped as part of the Tick Hill Complex, but it occurs as a dyke intruding the remnant Kalkadoon Supersuit basement (i.e. THG2). It is texturally and chemically it is distinct from the leucogranites of the Tick Hill Complex that occur to the east (i.e., samples THG3, THG4, THM04, THM27, Figs. 3.5-3.7), and it is better described as part of the Saint Mungo Granite, to which it is geochemically similar. Both SMG and THG1 have a well-developed gneissic layering, which is a composite S_{1-2} foliation. The units were probably emplaced at some stage during D_1 and provide an age estimate for the earlier stages of this deformation event.

The four leucocratic granite samples (THG3, THG4, THM04, THM27) belonging to the Tick Hill Complex (Blake et al., 1982, Wyborn, 1997) are geochemically similar (Figs. 3.5-3.7). Their Si-rich nature and depletion in Ca, Mg, Ti, Zr and total REE, as well as the flat REE patterns with weak positive Eu anomalies are similar to the chemistry described for low-temperature migmatites in which accessory phases were not fully resorbed in the melt (e.g., Solar and Brown, 2001; Bhadra et al., 2007). The leucogranites are interpreted as migmatitic segregations that were probably derived from the surrounding meta-pelite through partial melting. The close geochemical similarity between the leucogranites outside the pit (i.e., THG3 and THG4), which are of unambiguous granitic origin, and the heavily altered and mineralized quartzo-feldspathic mylonite (i.e., THM04, THM27) hosting the ore body, confirms that the latter originated as intrusions and not as immature sediments or laminated epithermal sinter deposits as has been proposed (e.g., England 1993, 1995). The leucogranites from which the samples were taken vary texturally from strongly mylonitic (THM04, THM27) to almost undeformed with well-preserved graphic textures in which granite bodies appear to cross-cut the S_{1-2} foliation and D_2 folds (e.g., THG4; Blake et al., 1982). The leucogranite pockets also display strong strain gradients with individual intrusive bodies characterized by mylonitic rims surrounding weakly

deformed cores with characteristic coarse-grained graphic to pegmatoidal textures (THG3), whilst the fabric external to the granite bodies is mylonitic throughout. The field relationships, therefore, indicate that the Tick Hill granites intruded syn-tectonically during D_1 through to late-D_2 and their relatively uniform age of 1770-1790 Ma provides an upper age limit of D_{1-2} deformation and metamorphism in the area. These relationships are confirmed by the 1773±7 Ma age of the late tectonic (i.e., late-D_2) monzonite dyke (MG), which largely cuts the composite S_{1-2} fabric and associated folding. The monzonite has a geochemical signature that is distinct from all other intrusions including the Monument Syenite (Figs. 3.5-3.7), and probably represents a separate late-tectonic intrusive phase.

In summary, it appears that most of the ductile deformation and igneous activity in the Tick Hill area occurred before 1770 Ma and involved two clear events, one around 1850-1855 Ma at the west of Tick Hill (~10km, western side of the Saint Mungo Granite) that can be linked to formation of the Leichhardt Volcanics at the end of the Barramundi Orogeny, and one around 1770-1790 Ma at near Tick Hill area that can be linked to early Wonga events and regional deposition of Argylla volcanics during opening of the Leichhard Basin (e.g., Page, 1978; Foster and Austin, 2008; Neumann et al., 2009; Carson et al., 2011; Magee et al., 2012; Withnall and Hutton, 2013; Kositcin et al., 2019). We have found no clear evidence for 1740 events, and the age of the syn-D_{1-2} intrusions into the volcano-sedimentary pile around Tick Hill clearly indicates that these sediments cannot be part of the Corella Formation. The remnant Kalkadoon basement gneiss units locally cropout further east than previously mapped (Blake et al., 1982, Wyborn, 1997), and appear to underlie the south MKD.

3.5.2. The age of the sedimentary sequence in the Tick Hill area

The sediments hosting the Tick Hill deposit were mapped as Corella Formation (Blake et al., 1982) and were, therefore, assumed to be 1740-1760 Ma (e.g., Tedman-Jones, 2001; Wyborn, 1997), despite an alternative interpretation in which the Corella Formation south of the Plum Mountain Fault Zone was correlated with >1860 Ma Plum Mountain Gneiss (Blake, 1980). The age of the Tick Hill granites and Saint Mungo Granite that intrude the sediments indicates that they must be older than at least 1790 Ma, and, therefore, cannot be part of the Corella Formation. The two quartzitite samples were collected to constrain a maximum depositional age for the sediments, but the results are equivocal. The hanging wall quartzite yields a youngest age grouping with a weighted mean age of 1781±6 Ma, but the ages were derived from mostly long-prismatic, zoned zircons that do not resemble detrital grains. In contrast, the footwall quartzite yields a youngest age population of 1841±15 Ma, which does include zircon grains with a sedimentary appearance. This discrepency in ages suggests that the two parallel ridges are not related to one another and represent different units, and can be interpreted in several ways. If the youngest age population in each quartzite unit is interpreted as a sedimentary detrital population than the sediments must be younger than ca. 1781 Ma and could be the equivalent of the Ballara Quartzite (e.g., Page and Sun, 1998; Neumann et al., 2006). In this case they would have

been deposited around the same time as deformation and metamorphism of the sediments invoking a very active tectinic regime for the paleo-basinal sequence. It also means that the data does not fit the intrusive relationships observed west of the pit suggesting that different aged volcano-sedimentary rocks were infolded with each other along the D_1 high strain zone.

However, the quartzite ridges do not preserve unambiguous sedimentary features, and they were mapped by exploration teams in the 1990s as silicified shear zones, citing their disconinuous transgressive nature, diffuse boundaries, ghost gneiss fabrics and associated veining and fracturing (e.g., Laing 1993). The sample dated for the hanging wall quartzite, contains ~10% feldspar and acessory tourmaline that are alined in S_1, and were overprinted and largely replaced by quartz, with subsequent annealing and grain growth resulting in a coarse-grained massive texture. The sample displays similarities with heavily silicified quartz-feldspar mylonite in the same way that other samples collected from the same quartzite display similarities with silicified biotite schist or silicified calc-silicate (Wyborn, 1997). If the hanging wall quartzite sample is silicified leucogranite, then the zircons it contains will preserve prismatic igneous forms, and the minimum age (as well as older inherited ages) will be similar to other leucogranites; which is consistent with our observations (i.e., samples THM27 and TH13 have near-identical zircon populations). The footwall quartzite in contrast does not resemble silicified older lithologies, but looks more like a primary bedded sedimentary unit, and it preserves a different age population with a minimum age grouping of 1841±15 Ma obtained from grains that inlude rounded grains (Appendix 4). The hanging wall quartzite also contains a major zircon grouping around 1841±15 Ma and both samples contain significant numbers of pre-Barramundi grains. Considering this as well as the fact that the 1790 Ma Saint Mungo Granite was described as intruding the Corella Formation (Blake et al., 1982), there is a strong possibility that the sedimentary sequence that hosts Tick Hill was formed some time at ca. 1841-1790 Ma and the equivalent of the "old Corella Formation" as originally suggested by Blake (1980) and argued in Blake et al (1982). However the extent od this "old Corella Formation" needs to be more accurately mapped in the south MKD.

3.5.3. *The timing of gold mineralization in the Tick Hill area*

The presence of coarse gold grains as inclusions in D_1 green hornblende, scapolite and clinopyroxene in calc-silicate gneiss (Chapter 2) indicates that the metasedimentary rocks contained gold during D_1. It suggests that the gold was introduced during D_1 events at ca. 1770-1790 Ma. However, the pre-existed gold was remobilized during the D_1 events should be considered at Tick Hill and if this is the case, the age for the early gold stage is poorly constrained to sometime between ca. 1855 Ma and ca. 1770 Ma.

The main phase during which gold was either introduced or remobilized occurred during D_3 normal faulting and the associated fluid flux. The fluid flux resulted in the emplacement of en echelon

arrays of pegmatite and quartz veins along the D_3 shear zones as well the formation of metasomatic, quartzo-feldspatic overgrowths replacing the earlier gneissic layering along the margins of some D_3 faults (Fig. 3.3d). Four of the five syn-D_3 pegmatite samples that were dated contain hydrothermal and metamict zircons with ages of around 1520-1525 Ma. Whilst some of these pegmatites contain a wide range of discordant zircon grains with few concordant ages, TH141 and TH108 returned robust ages of 1522±3 Ma and 1524±6 Ma respectively, in which hydrothermal zircon interpreted to reflect metasomatic events and metamict zircon interpreted to reflect magmatic events yielded near-identical results. This suggests that the different episode of zircon growths were formed when pegmatite veins were emplaced and hydrothermal fluids passed through, to alter the pegmatites and deposit gold. The ages are also consistent with a poorly-constrained titanite age of 1517±10 Ma, which was linked to mineralization (Tedman-Jones, 2001). The fifth pegmatite vein (TH11) only contained older concordant grains with an age of 1772±19 Ma. The weakedly deformed texture of this pegmatite sample was likely resulted from the D_3 deformation event, and the youngest zircon cluster of 1772±19 Ma possibly present the inherited age.

Metamorphic-hydrothermal events dated at 1500-1530 Ma have been recorded by metamorphic titanite or zircon from a number of localities in the MKD to the north of Tick Hill (Page and Sun, 1998; Davis et al., 2001; Kositcin et al., 2019). Similar events are also widespread in the Easten Fold Belt where they have been linked to the emplacement of the Williams and Naraku granite suites and a regional fluid flux of highy oxidizing, saline fluids resulting in regional albite-hematite-scapolite alteration and IOCG type mineralization (e.g., Oliver, 1995; Oliver et al., 2004; Williams et al., 2005; Withnall and Hutton, 2013). In the Tick Hill area, there are no major 1520 Ma intrusions associated with the observed albite-hematite alteration, but late pegmatites are common (Blake et al., 1982; Coughlin, 1993). The positive Eu anomalies recorded in the pegmatite samples (Fig. 3.6b;) possibly reflect the elevated content of feldspar in pegmatite (Rollinson, 1993).

3.6. Conclusion

Dating of intrusive rocks and quartzite units around Tick Hill has placed constraints on the age of the main stratigraphic units in the area and has shown that existing stratigraphic and structural interpretations must be reviewed. Major igneous events occurred around 1850-1855 Ma and 1770-1790 Ma, and were followed by later hydrothermal events with pegmatite emplacement around 1520-1525 Ma. The age of the sediments intruded by 1790-1770 Ma intrusions is therefore >1790 Ma. This is consistent with the maximum age (ca. 1841±15 Ma) for a provenance zircon sample from footwall quartzite. Hanging wall quartzite contains a younger 1780 Ma zircon population suggesting a younger age for the sediments, but this population can be interpreted differently if one considers that the quartzite is possibly metasomatic in origin, with silicification overprinting an intrusive quartzo-

feldspathic gneiss. Major deformation and metamorphic events occurred between 1770 and 1790 Ma with the development of an upper amphibolite facies, mylonitic fabric (D_1), migmatization, and later upright folding (D_2). There probably were earlier fabrics associated with ca. 1850 Ma events, considering the composite nature of S_1, but these were transposed in the high strain D_1 fabric. Later extensional faulting and hydrothermal alteration events took place at ca. 1520-1525 Ma during D_3, followed by younger strike-slip faulting (D_4) with an unconstrained age. The presence of hydrothermal zircon grains in pegmatite with a variety of ages between 1650 and 1520 Ma, suggests that Isan events affected the area to some degree, but these events did not leave a clear deformation imprint.

Formation of the gold ore body advanced in at least two stages: an early stage after deposition of the sediments and (before or) during D_1 events (1770-1790 Ma); and a late stage concomitant with D_3 events at 1520-1525 Ma. The later gold event left the clearest footprint and determined the current distribution pattern of the gold. The geochemistry of the quartzo-feldspathic mylonites that host the main ore zones, is consistent with that of D_{1-2} leucogranite migmatitic origin. Therefore, the quartzo-feldspathic mylonites were probably emplaced as leucogranite sills during D_1 and D_2.

One of the major outcomes of this study is that the "Old Corella Formation" or a new unnamed formation aged sometime between 1841 Ma and 1790 Ma appears to host the Tick Hill deposit, and the similar host rocks in the region is, therefore, prospective for gold mineralization (with anomalous Bi; Le et al., 2021).

Chapter 4: Trace element geochemistry of zircons used in geochronology

Abstract

Next to the zircon morphology, zircon geochemistry can be used as an additional method to distinguish between magmatic and hydrothermal zircon. At Tick Hill, zircon grains dated at 1520-1600 Ma, have a morphology consistent with hydrothermal zircon, and they show a distinct trace element composition when compared to zircon grains dated at 1770-1780 Ma that have typical magmatic morphologies. The younger zircons have an increased Na, Ca, Cu, Mn, Sr and U content, whilst the older zircons are enriched in HREE, Ti and Co. The young zircon population has Th/U ratios of <0.1, which is an important geochemical indication for hydrothermal zircon, and is consistent with the hydrothermal zircon morphology. In contrast, the older zircon grains have high Th/U ratios, mainly >0.2, which is consistent with a magmatic origin as shown by the magmatic zircon morphologies. Within the 1770-1780 Ma zircon population, the similarity in trace-element compositions between zircon from granite and hanging wall quartzite further confirms the interpretation (based on zircon morphology, age, rock composition and textures) presented in Chapter 3 that the so-called hanging wall quartzite originated as an intrusive quartz-feldspar unit and was strongly affected by D_{1-2} silicification events.

4.1. Introduction

Zircon is a common accessory mineral in intermediate to felsic igneous rocks, and can survive high temperature metamorphism without significant adjustments to its chemistry (e.g. Heaman et al., 1990; Hoskin & Schaltegger, 2003). Therefore, zircon is an important mineral for geochronological studies to constrain the age of the host rocks, or earlier provenance.

In this section, we present zircon geochemistry data for 4 groups of zircon grains that were used for U-Pb dating as presented in Chapter 3. These four groups include: Group 1 grains of hydrothermal zircon obtained from syn-D_3 pegmatite dated at 1520-1525 Ma (n=51; samples TH66, TH108, TH140 and TH141; Chapter 3); Group 2 grains of inherited zircon dated at 1550-1600 Ma obtained from syn-D_3 pegmatite (n=15; samples TH66, TH108, TH140 and TH141; Chapter 3); Group 3 magmatic zircon grains dated at 1770-1780 Ma obtained from syn-D_{1-2} intrusive granites (n=55; samples THG1, THG3, THG4, THM04 and THM27; Chapter 3); and Group 4, ca. 1780 Ma zircon grains obtained from the hanging wall quartzite (n=14; sample TH13; Chapter 3).

The hydrothermal and magmatic origins of zircon grains were interpreted based on the zircon morphology and the geology framework in the Tick Hill region. The data presented here has been obtained to examine if the different zircon groups are representative for chemically distinct source

reservoirs, be it metamorphic/hydrothermal or igneous/magmatic. More specifically we aim to investigate four points:

1. Are the 1520-1600 Ma zircon populations chemically distinct from the 1770-1780 Ma zircon grains ?

2. Is the zircon chemistry for the different groups consistent with a metamorphic, igneous or hydrothermal origin ?

3. Can zircon chemistry assist in determining the origin of the hanging wall quartzite ?

The data presented here have been used in support of some of the geochronological interpretations presented in Chapter 3.

4.2. Methodology

The zircon geochemistry was obtained with the use of LA-ICP-MS conducted at the Advanced Analytical Centre, James Cook University, using a Teledyne Analyte G2 193nm ArF Excimer laser ablation system combined with a Thermo iCAP-RQ ICP-MS. The HelExII ablation cell was connected to the iCAP-RQ via Tygon tubing and a 3-way mixing bulb (volume ~5 cm^3). Ultra-high purity Nitrogen (N2) was introduced close to the torch to increase the instrumental sensitivity. All instrument tuning was performed using a 5 Hz repetition rate, 50 μm beam aperture and 3 J/cm2 energy density, as determined by an energy meter at the ablation site. Tuning was achieved by iteratively adjusting the He carrier gas (MFC1&MFC2), Ar sampling gas, N$_2$ gas flow rate, RF Power, torch positions (X, Y, Z) and extraction lens to achieve an ^{238}U/^{232}Th ratio of ~1, and a ThO/Th ratio of < 1%; typically < 0.5% in NIST610.

For a single analysis, the total measurement time was set at 80 seconds. The first 30 seconds were for gas blank measurements (the laser starts firing from 20th second while the shutter is closed), with the shutter opened at the 30th second to allow sample ablation for the final 30 seconds. The NIST 612&610 and GED&GSE standards were used for calibration. The concentration of thirty-eight elements in zircon were investigated, in which Pb was examined for four isotopes including ^{204}Pb, ^{206}Pb, ^{207}Pb and ^{208}Pb. The data were analyzed and presented using IOGas software.

4.3. Results

The trace element content of zircon from the four groups has been presented in Fig. 4.1a with data provided in Appendix 5. Element concentrations in the various zircons group appear to vary in a systematic manner. To illustrate this better, a group of 17 elements was selected to highlight the differences between the young and old zircon groups (Fig. 4.1b). Elements used for this include: the HREE plus Y; major elements that are also associated with widespread alteration including Na, Ca and Sr; several redox sensitive transition metals common in IOCG's including Cu, Co, Mn; and the incompatible elements U and Ti (Fig. 4.1b).

In general, the trace element patterns can be used to divide the zircon grains into two discrete populations including the younger group 1 and group 2 zircons, and the older group 3 and group 4 zircons. Relative to the older zircon groups, the young zircon groups are enriched in U, Na, Ca, Sr, Mn and Cu, but depleted in Ti, Co, and the HREE (i.e. Gd, Tb, Dy, Ho, Er, Tm, Yb, Lu) including Y (Fig. 4.1).

Among the two younger age groups, the trace elements of zircon from the 1522Ma group show similar values to those from the ca. 1550-1560 Ma group. Similarly in the older zircon groups, the trace element content for magmatic zircon from group 3 (ca. 1770-1780 Ma) is comparable to that of zircon from the hanging wall quartzite in group 4 (ca. 1780 Ma; Fig. 4.1).

The geochemical differences between the younger and older zircon groups can be further illustrated by plotting Mn vs Ca, and the Th/U ratio for the various groups (Fig. 4.2). Mn and Ca correlate well for zircon grains from groups 1 and 2, but this correlation is less clear for zircons from groups 3 and 4 (Fig. 4.2a). The Th/U ratio of 84% of group 1 zircon grains and almost all of group 2 grains is less than 0.1 (Fig. 4.2b), which reflects the high concentration of U in these zircon grains (mostly >800 ppm, Fig. 4.2b). In contrast, the Th/U ratio in zircon grains from the older groups 3 and 4 is higher than 0.2 (Fig. 4.2b), reflecting the low concentration of U (mostly from 100 to 300 ppm) in these zircons.

The chondrite-normalized REE patterns for zircon from all groups are relatively flat with weak positive anomalies for Ce and a general trend of increasing values from the LREE to the HREE (Fig. 4.3). The chondrite-normalized REE patterns of the younger zircon groups 1 and 2 show variable Eu anomalies or no Eu anomaly, whilst the older zircon groups generally show negative Eu anomalies (Fig. 4.3). The average concentrations of HREE in zircons from groups 3 and 4 are significantly higher than those in zircons from groups 1 and 2 (Fig. 4.3e).
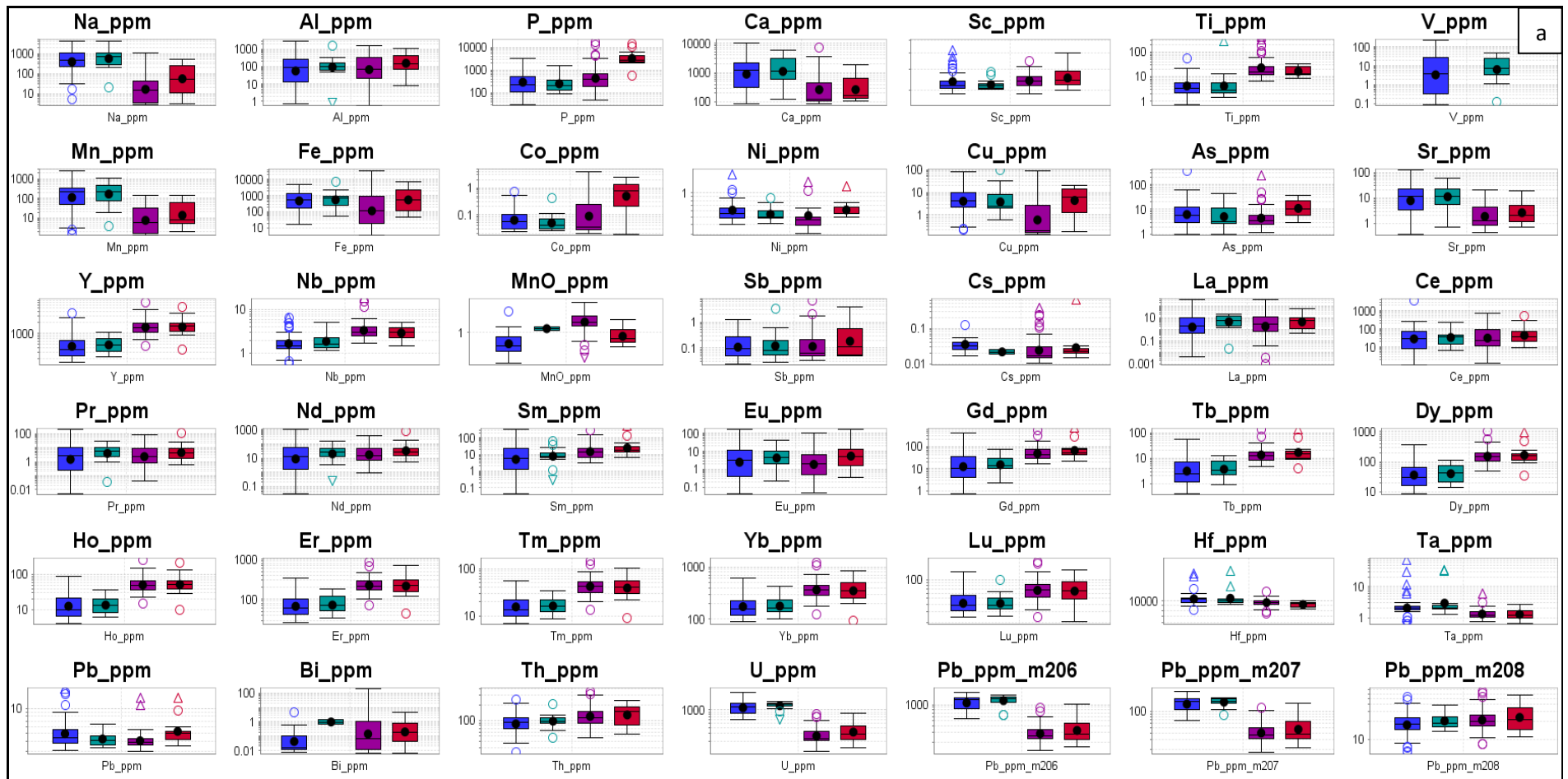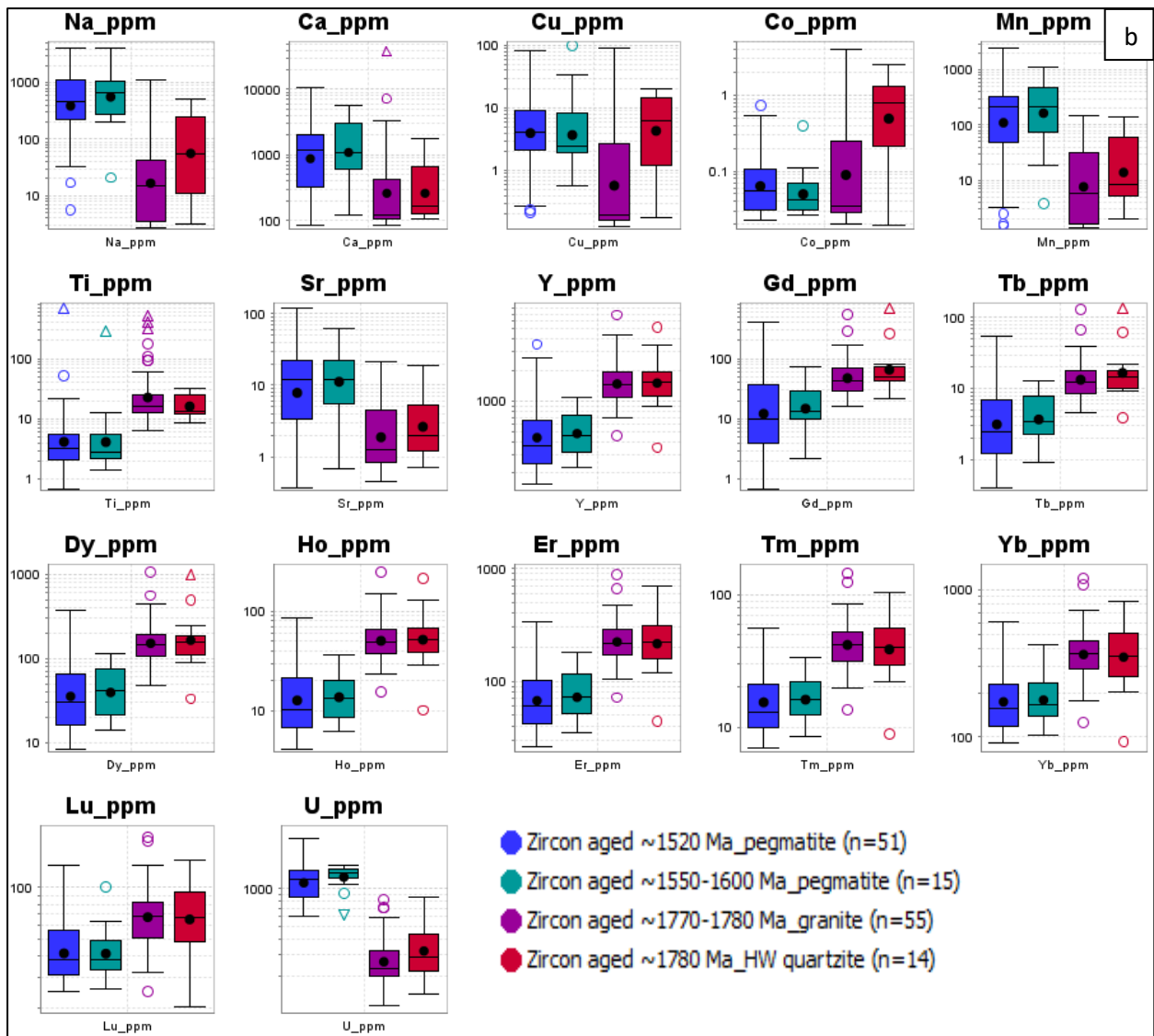
Figure 4.1. (a) Plots showing trace element concentrations in zircon grains from four groups; (b) Plots of selected elements that best illustrate the compositional differences between younger and older zircon groups. Turkey box plots: the central box covers the middle 50% of the data; the black circle shows the mean value; the middle black line shows the median value; the bottom and top black lines (whiskers) show minimum and maximum values within the regular data range; circles and triangles indicate outliers and far outliers respectively. HW = Hanging wall.
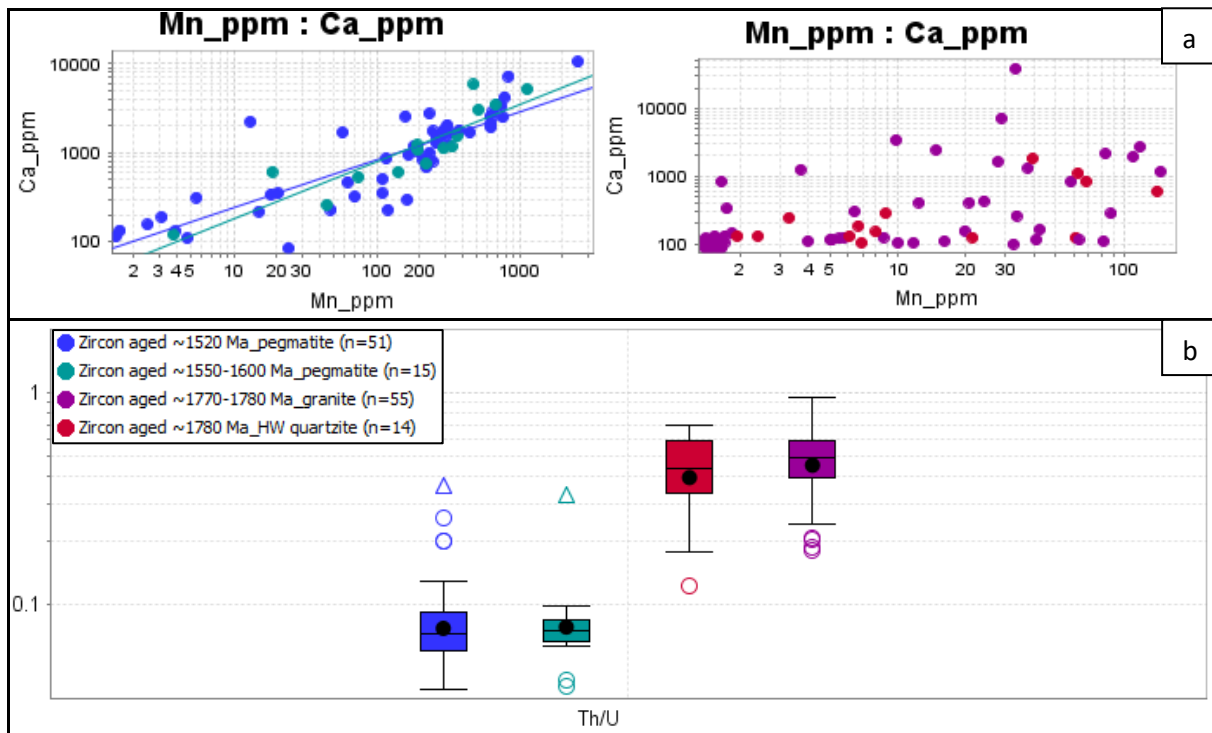
Figure 4.2 shows (a) the differences in Mn-Ca correlations and (b) Th/U ratios from the four zircon groups.

4.4. Discussion

4.4.1. Are the 1520-1600 and 1770-1790 Ma zircon populations chemically distinct?

Results show that the zircon grains from the two younger age groups, clearly and systematically differ from those of the two older zircon groups. While the zircon grains from the older groups are enriched in heavy REE and some metals, the younger groups contain zircons that are enriched in U and major elements such as Na, Ca, Sr, Mn and Cu (Fig. 4.1). This enrichment of major elements in the younger zircons could reflect the chemistry of the host rocks and/ or overprinting alteration/mineralization events. The enrichment pattern appears to mimic the regional alteration assemblages that affected the rock during the Isan Orogeny between 1500-1600 Ma (Fig. 4.1b). This suggests that the zircon chemistry is linked to the same fluid reservoir that resulted in regional alteration across large parts of the Mt Isa Block.

4.4.2. Is the zircon chemistry for the different groups consistent with a metamorphic, igneous or hydrothermal origin ?

Historical reviews of zircon Th/U ratios suggest that a value of 0.1 can be used to differentiate between metamorphic (<0.1) and igneous (>0.1) zircon (e.g. Hoskin & Schaltegger, 2003; Kirkland et al., 2015; Rubatto, 2002; Yakymchuk et al., 2018). A Th/U ratio compilation of zircon grains from Western Australia shows that Th/U ratios < 0.1 tend to occur in metamorphic zircon while Th/U ratios

> 0.1 reflect both igneous and metamorphic, rocks but usually igneous rocks (e.g. Yakymchuk et al., 2018).

In the Tick Hill region almost all zircon grains in the younger groups 1 and 2 have Th/U ratios of < 0.1 suggesting a metamorphic or hydrothermal origin for the zircon. These low Th/U ratios are consistent with the morphology for these zircons (Chapter 3). Almost all zircon grains in group 1 display framework textures with bright seams surrounding black domains, or partly zoned and metamict domains. These textures indicate that the zircon has been locally recrystallized and overgrown by hydrothermal/metamorphic zircon (Corfu, 2003). The hydrothermal zircon grains could represent hydrothermally altered older zircon grains (>1770 Ma) or could be altered zircon that formed during the same events (i.e. during the emplacement of D_3 pegmatites along D_3 structures; more detailed in Chapter 3).

The 1520-1525 Ma hydrothermal events recorded by zircon grains in group 1 are most likely related to the regional 1500-1530 Ma metamorphic-hydrothermal events recorded with titanite and hydrothermal/ metamorphic zircon to the north of Tick Hill (e.g. Page and Sun, 1998; Davis et al., 2001; Kositcin et al., 2019). In the Eastern Fold Belt, coeval magmatic-hydrothermal events have been recorded, which were linked to the emplacement of 1500-1530 Ma Williams-Naraku Batholith and an associated regional fluid flux that resulted in albite-hematite-scapolite alteration and IOCG type mineralization (e.g. Oliver, 1995; Oliver et al., 2004; Williams et al., 2005; Withnall and Hutton, 2013).

In contrast to the younger zircon grains, the older zircon grains in groups 3 and 4 have Th/U ratios that are consistently >0.2. This trend reflects an igneous origin for the zircon grains (e.g. Hoskin & Schaltegger, 2003; Kirkland et al., 2015; Rubatto, 2017). The ca. 1770-1780 Ma zircon grains at Tick Hill commonly display needle-like morphologies with clear internal growth zoning or homogenous textures (Chapter 3). This type of morphology is a good indication for a magmatic origin (Corfu, 2003). On a regional scale, ca. 1770-1780 Ma magmatic events involved the deposition of felsic volcanic rocks of the Argylla Formation and the emplacement of granites along the length of the Mary Kathleen Domain (Page, 1978; Page and Sun, 1998; Carson et al., 2009, 2011; Neumann et al., 2009; Magee et al., 2012; Kositcin et al., 2019).
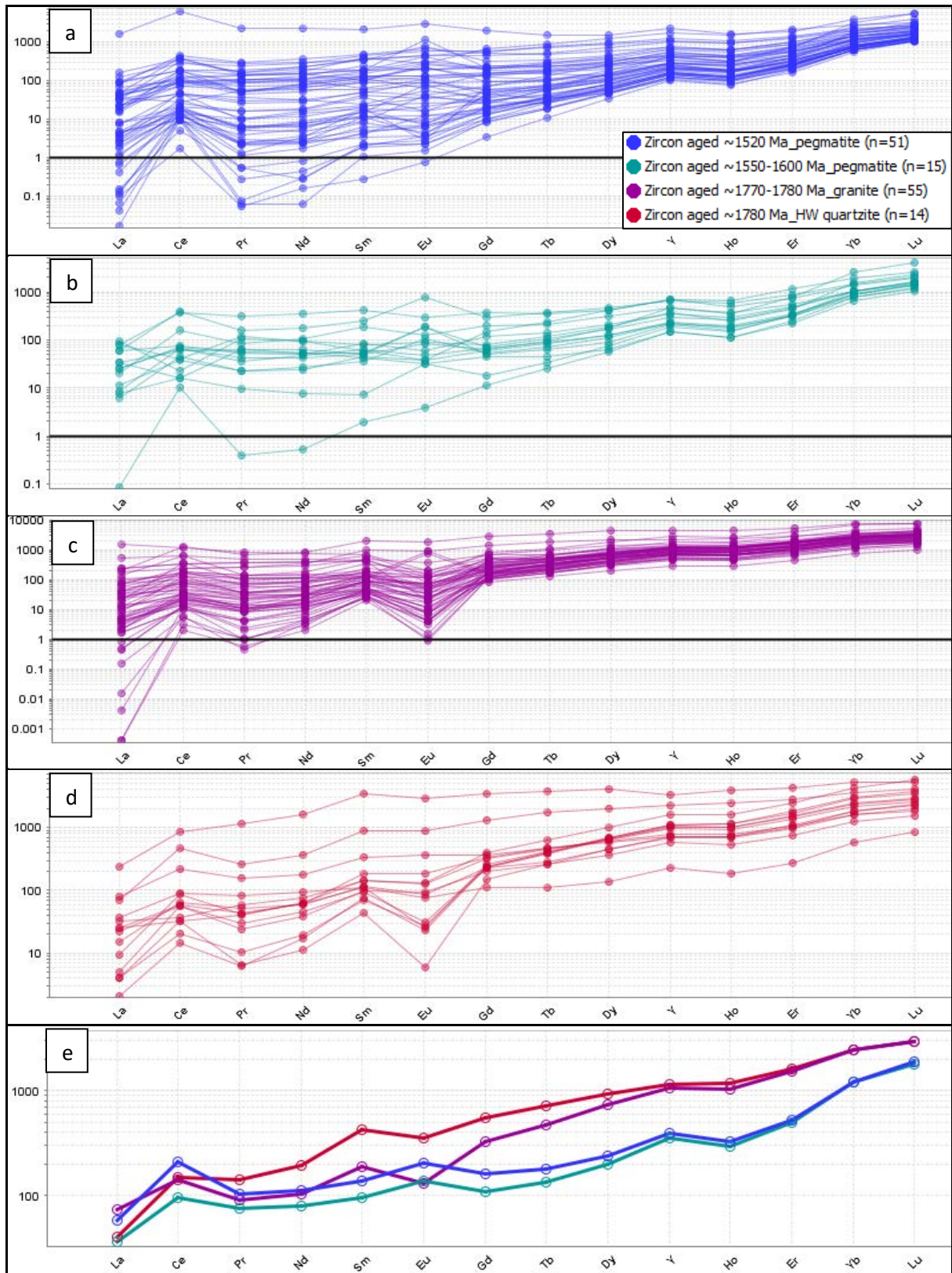
Figure 4.3. Chrondrite-normalized REE patterns (after McDonough and Sun, 1995) for zircon from: (a) ca. 1520-1525 Ma group 1 zircons; (b) ca.1550-1600 Ma group 2 zircons; (c)ca. 1770-1780 Ma group 3 zircons; and (d) ca. 1780 Ma hanging wall quartzite. (e) The average REE contents for each of the four groups.

4.4.3. Can zircon chemistry assist in determining the origin of the hanging wall quartzite ?

Group 4 zircon grains were obtained from a feldspar-rich portion of hangingwall quartzite with a possible sedimentary origin. If the hanging wall quartzite is a sedimentary unit and the zircons within it are detrital, then the geochemistry of the ca. 1780 Ma zircon population is expected to be different and more diverse than the zircons obtained from similar aged granites. However, if the hanging wall quartzite is interpreted as silicified quartzo-feldspathic mylonite, as argued in Chapter 3 and in earlier exploration reports (e.g. see Tedman-Jones 2001 for a summary), then its zircon chemistry is expected to mimic that of the 1770-1780 Ma granites.

Zircon grains from group 3, with clear magmatic morphologies, are near-identical in morphology, age and chemistry to zircon grains from group 4 (Fig. 4.1). Similarities include: (1) needle-shaped zircon morphologies with clear growth zoning for a large proportion of the grains (Chapter 3); (2) similar age distributions for the zircon grains in each group (ca. 1780 Ma; see Chapter 3); (3) high Th/U ratios (>0.2, largely at 0.3-0.5; Fig 2b), and (4) near identical trace element compositions (Fig. 4.1). These similarities support our interpretation that the zircons in group 4 are magmatic in origin, and that the analyzed hanging wall quartzite sample (and probably the quartzite more generally) represents intensely silicified quartz-feldspar mylonite, similar in origin to the quartz-feldspar mylonite that host much of the gold.

4.5. Conclusion

The 1520-1600 Ma zircon populations are chemically distinct from the 1770-1780 Ma zircon populations that were tested in this study. The younger zircon grains display elevated concentrations in Na, Ca, Cu, Mn Sr and U, while the older zircon grains are enriched REE, Ti and Co. Additionally, the younger zircon grains show a good correlation between Mn and Ca, which does not occur in the older zircon grains. The elevated Na content in the younger zircon populations is possibly related to the coeval, widespread and intense albite alteration in the region. The Th/U ratio for the 1520-1600 Ma zircon populations is generally <0.1, which indicates a hydrothermal origin, and is consistent with the complex framework textures that are commonly preserved within these zircon grains (Chapter 3). In contrast, the older zircon grains have higher Th/U ratios (mainly >0.2), which are consistent with a magmatic source, and is comparable with the generally prismatic and clearly zoned nature of these zircon grains. Within the 1770-1780 Ma zircon population, the similarity in trace-element content for zircon grains sourced from syn-D_{1-2} granite, quartz-feldspar mylonite and hangingwall quartzite, together with the magmatic zircon morphologies for these grains and the intensely silicified, altered nature of the hanging wall quartzite (Chapter 3), suggest that the hanging wall quartzite originated as an intrusive quartz-feldspar unit during the D_1 that was affected by intense silicification, possibly as a result of its position along an early-tectonic shear zone.

Chapter 5: Mineral chemistry and P-T analyses

Abstract

With the use of SEM and EPMA, the chemical compositions of critical mineral assemblages formed during the D_{1-2} metamorphism and D_3 alteration events, were determined. Gold occurs as inclusions or coarse grains hosted within D_1 metamorphic diopside, scapolite and hornblende. P-T analyses for a syn-D_1 garnet-biotite-hornblende (tschemakite)-plagioclase (andesine)-quartz assemblage indicate that the peak metamorphic conditions at Tick Hill reached 6-7.6 kbar and ~720-760 °C. The gold at Tick Hill, including gold hosted in D_1 metamorphic minerals and D_3 mineralization zones, is generally pure with zero Ag and Cu. Gold mobilized during D_3 is closely associated with bismuth selenide, chlorite, albite, sericite and K-feldspar. The D_3 chlorite which formed during stage 2 to stage 4 mineralization events displays a wide range of compositions (mainly shifts in Al, Si, Mg and Fe) that reflect a gradual retrograde temperature change from ~380°C to ~130°C. Pressures during D_3 events could not be reliably determined, but the presence of various Bi-selenides, suggest that towards the waning stages of D_3, rocks may have been exhumed to <1kbar.

5. 1. Introduction

The Tick Hill area experienced high-grade D_{1-2} events at ca. 1770-1790 Ma and possibly earlier, and a retrograde metamorphic/hydrothermal overprint during D_3 events around 1520-1525 Ma (Chapters 2 and 3). Minerals aligned in the early D_1 fabric define the peak-metamorphic assemblage (e.g. garnet-amphibole-biotite-plagioclase in meta-amphibolite; diopside-scapolite-amphibole-plagioclase in calc-silicate; sill-biotite-K-feldspar-plagioclase-quartz in metapelite; Chapter 2) in which gold was locally hosted in diopside or hornblende grains aligned in S_1. During D_3 events, the peak assemblages were overprinted by retrograde assemblages that typically include albite- hornblende/actinolite-epidote-chlorite-hematite-quartz and later sericite-K-feldspar-calcite-clay minerals, both associated with the redistribution of earlier gold and the possible introduction of a new phase of gold (Chapter 2). The D_3 alteration involved the local destruction of magnetite, the emplacement of abundant laminar quartz veins, and the deposition of multi-stage alteration assemblages (Chapter 2), including:

- Stage 1: quartz-oligoclase-albite-hornblende-hematite (±leucoxene, chalcopyrite);
- Stage 2: albite-actinolite-chlorite$_1$-hematite (±leucoxene)-pyrrhotite-pyrite$_1$-chalcopyrite-gold-bismuth selenide;
- Stage 3: quartz-K-feldspar-chlorite$_2$-epidote-sericite-hematite (±leucoxene)-gold-bismuth selenide-pyrite$_2$-chalcopyrite;

- Stage 4: quartz-calcite-chlorite$_3$-clay minerals-hematite ($\pm$leucoxene)-gold-pyrite-chalcopyrite -Bi, Pb, Cu selenides including junoite ($Pb_3Cu_2Bi_8(S,Se)_{16}$), cerromojonite ($CuPbBiSe_3$) and molybdomenite ($PbSeO_3$); and

- Stage 5: quartz-albite-oligoclase-magnetite.

In this section, we present the details of SEM and EPMA mineral geochemistry for the D_{1-2} peak metamorphic minerals and multi-staged D_3 alteration mineral assemblages, and discuss their significance in terms of evolving P-T conditions and fluid chemistry. The aim of this study is to:

1. determine the chemical composition of the various mineral assemblages that formed during D_{1-3} events;

2. geochemically characterize the progressive changes in mineral composition for silicate minerals (esp. chlorite, amphibole and feldspar) that formed in association with gold during the various stages of D_3 events; and

3. estimate the P-T conditions of formation for some of the metamorphic and alteration minerals.

5.2. Methodologies

In conducting the metamorphic study, we have focused our work on three rocks types that contain reactive mineral assemblages, are pervasive in the area and occur in direct association with gold namely: amphibolitic gneiss (amphibolite for short), amphibole-bearing calc-silicate and amphibole-chlorite-epidote-bearing, quartz-feldspar mylonite (a variety of 'galahstone'). We note that some meta-pelitic biotite schists in the pit and in drill cores contain sillimanite, but in all meta-pelite samples selected for analyses this sillimanite had been replaced by muscovite, and no further mineral chemistry analyses were conducted for these rocks.

5.2.1. Sample description

The samples selected for the mineral geochemistry investigation are summarized in the Table 5.1, together with their characteristic mineral assemblages. Two samples containing D_{1-2} peak-metamorphic mineral assemblages were selected for this study. One sample (TH99) which contains coarse-grained garnet overgrowing hornblende-biotite-plagioclase-quartz-apatite-ilmenite-magnetite as well as pyrite and chalcopyrite (Chapter 2) was selected from an amphibolite unit in the drill core, ~800 m north of Tick Hill pit (Fig. 5.1a). The garnet in this sample is coarse-grained (1-3 cm diameter) with a granoblastic texture (Fig. 5.1a), and it contains inclusion trails of hornblende, quartz and ilmenite, with minor apatite, biotite, pyrite and chalcopyrite (e.g. Figs. 5.2a,b). Hornblende is commonly coarse-grained, granoblastic and aligned in the S_{1-2} fabric (Fig. 5.2a), with contacts to plagioclase, quartz and garnet. Plagioclase mainly in contact with hornblende, quartz and garnet. Biotite in this sample only

occurred as inclusions intergrown with garnet. Garnet, biotite, hornblende, plagioclase, ilmenite and quartz were geochemically analyzed with SEM and EPMA to provide constraints on early D_1 mineral geochemistry and P-T conditions based on garnet-plagioclase-hornblende-quartz barometry and hornblende-plagioclase, garnet-hornblende and garnet-biotite thermometry (e.g. Ferry and Spear 1978; Hodges and Spear, 1982; Kohn and Spear, 1990; Holland and Blundy, 1994). Mineral grains were tested for compositional homogeneity and analyses near the rims of grains that are in contact with each other were preferentially used for P-T estimates. The amphibolite was locally cut by D_3 micro veins of chalcopyrite-chlorite, but the peak metamorphic minerals selected for geothermobarometry were not affected by D_3 events.

Table 5.1. List of samples and minerals that were geochemically investigated with SEM and EPMA

Tectonic event	Sample	Rock type	Mineral	Technique
D_{1-2}	TH99	Amphibolite	Garnet, hornblende, biotite, plagioclase, ilmenite	SEM/EPMA
D_{1-2} /D_3	TH46	Amphibole-rich calc-silicate	Diopside, scapolite, plagioclase, hornblende (D_{1-2}); actinolite, albite, k-feldspar (D_3)	SEM/EPMA
D_3	TH55	Quartz-feldspar mylonite	Hornblende, feldspar, chlorite, calcite, gold, bismuth selenide, Bi minerals, chalcopyrite, pyrrhotite, pyrite	SEM/EPMA
D_3	THM51C	Quartz-feldspar mylonite	Hornblende, actinolite, feldspar, chlorite, hematite, calcite, gold, bismuth selenide, chalcopyrite	SEM/EPMA
D_3	THM22	Quartz-feldspar mylonite	Feldspar, chlorite, hematite, gold, bornite, Fe-Carrollite, chalcopyrite, pyrite	SEM/EPMA
D_3	TH137	Intense silicified unit	Chlorite, epidote, gold	SEM

A second gold-rich sample with a strongly developed S_{1-2} fabric affected by a D_3 hydrothermal overprint was collected from an amphibole-rich calc-silicate unit within the ore zone, in which hornblende, pyroxene and scapolite host gold grains as inclusions (TH46; Figs. 5.1b, 5.2c-f, 5.3). Gold inclusions in peak assemblages occur in two forms: (1) as fine inclusions concentrated along microfractures cutting the matrix grains and (2) as fine- to coarse-grained inclusions contained within compositionally homogenous grains with no evidence of micro-fracturing. The latter situation includes gold contained as inclusions in amphibole, which itself is contained as an inclusion in diopside; i.e. gold was present during growth of the peak-metamorphic assemblage (Chapter 2). The rock has a mineral assemblage of diopside-scapolite-hornblende-actinolite-plagioclase-quartz with alternating domains of amphibole-diopside, and plagioclase-scapolite-quartz defining a gneisic S_{1-2} fabric (e.g. Fig. 5.2c). Diopside and scapolite have a granoblastic texture (Fig. 5.3) aligned in the S_{1-2} fabric (Fig. 5.1b). Actinolite in this sample, locally replaces granoblastic amphibole in a domainal manner. This includes areas of hornblende grains that host gold grains (Fig. 5.2e). The mineral composition of hornblende-plagioclase pairs in this sample was used for the temperature estimates.
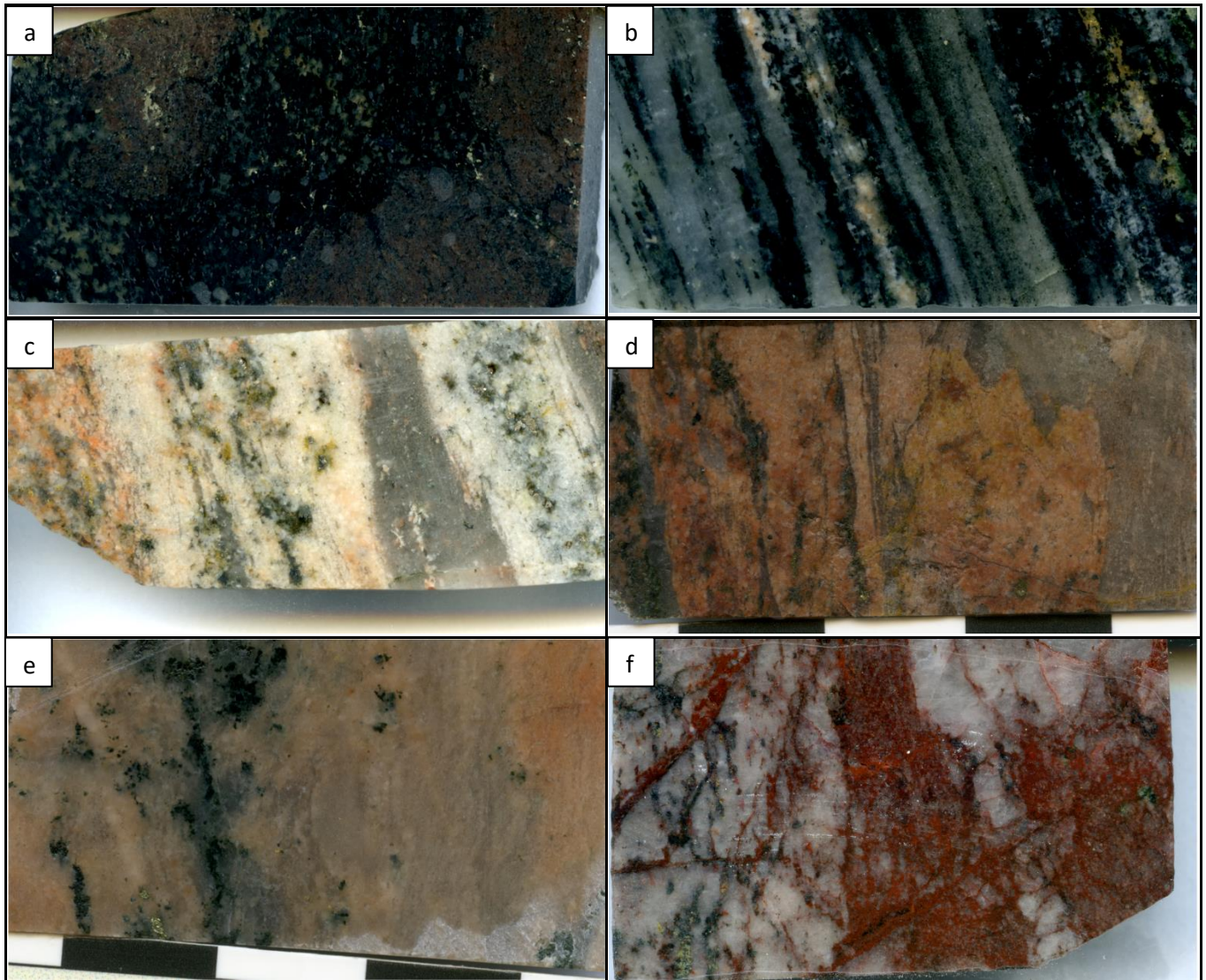
Figure 5.1. Images of samples selected for mineral geochemistry and P-T work including: (a) garnet-bearing amphibolite at ~800m north of Tick Hill pit (sample TH99); (b) gold-bearing, amphibole-rich calc-silicate (sample TH46); (c-e) quartz-feldspar mylonite (sample TH55, THM22 and THM51C respectively); and (f) intensely silicified unit (possibly altered biotite schist, now hanging wall quartzite sample TH137).

Four samples containing D_3 amphibole-actinolite-chlorite-epidote-albite-K-feldspar-hematite-calcite alteration assemblages in the Au-rich zone, including three samples from quartz-feldspar mylonite (TH55, THM22 and TH51C; Figs. 5.1c-e) and a sample from an intensely silicified unit (possibly after biotite-rich schist, TH137; Fig. 5.1f), were selected to investigate the D_3 retrograde alteration assemblages and associated ore minerals. Amphibole in this rock unit includes D_{1-2} relic hornblende (sample TH55) and D_3 hornblende and actinolite alteration (sample THM51C). The D_3 hornblende alteration shows irregular textures and was rimmed and replaced by actinolite along micro fractures (e.g. Fig. 5.4a). Chlorite alteration occurred in all four samples during D_3 events, and shows a gradual shift in morphology from chlorite$_1$ (after biotite) to chlorite$_2$ (after chlorite$_1$; Chapter 2). Chlorite$_1$ formed during stage 2 and replaced (peak-metamorphic) biotite, and usually preserves the

crystal habit of the original biotite flakes while chlorite$_2$ formed during stage 3, one of two main stages during which gold was remobilized. Chlorite$_2$ commonly occurs in association with gold and can contain fine gold inclusions (e.g. Fig. 5.4c). This chlorite$_2$ shows complex textures with irregular shapes (e.g. forming reaction-rims around earlier sulphides; Fig. 5.4b). Chlorite$_3$ formed during stage 4, is inter-grown with calcite, and occurs only in small amounts compared to the chlorite$_2$. Epidote occurs in association with chlorite$_2$ and formed during D$_3$ stage 3, with the remobilization of Au. Epidote selected for mineral geochemistry is hosted in the intensely silicified hanging wall quartzite sample, and is commonly intergrown with chlorite$_2$ (Fig. 5.4d). Albite and K-feldspar are part of the D$_3$ albitization and K-feldspar alteration respectively, occur with gold and chlorite$_2$ (e.g. stage 3, Fig. 5.5) in association with stage 2-3 assemblages. Chlorite$_{1-3}$ compositions have been used in the geothermometry study to constrain the evolving D$_3$ mineralization temperatures.
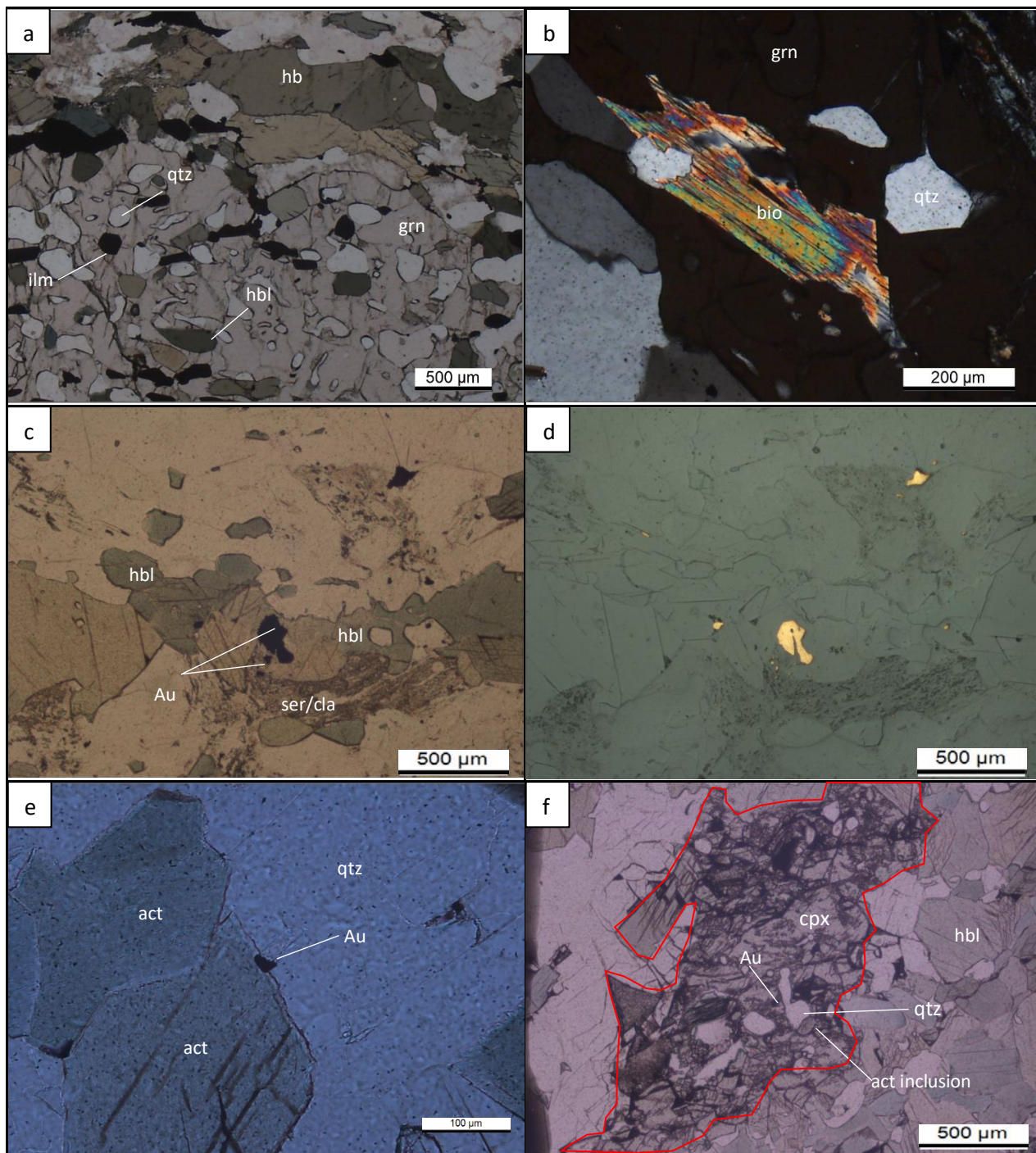
Figure 5.2. Microphotographs of D_{1-2} assemblages in samples TH99 (a, b) and TH46 (d-f) showing: (a) granoblastic hornblende (hbl) aligned in S_{1-2}, bounding a large garnet grain (grn) with inclusions of hornblende, quartz (qtz) and ilmenite (ilm) under plane polarized light; (b) biotite (bio) and quartz (qtz) inclusions in garnet (grn) under cross-polarized light; (c & d) weakly foliated D_{1-2} Au-bearing hornblende (hbl) in amphibole-rich calc-silicate overprinted by D_3 hydrothermal events that caused fine-grained gold to remobilize along grain boundaries where it is associated with sericite (ser) and clay (cla) alteration under (c) transmitted and (d) reflected light; (e) Actinolite (act) in association with gold; (f) a diopside grain (cpx) containing Au and actinolite inclusion (act) appears to occur with hornblende (hbl) during D_{1-2} event and is overprinted by D_3 hydrothermal events.

111
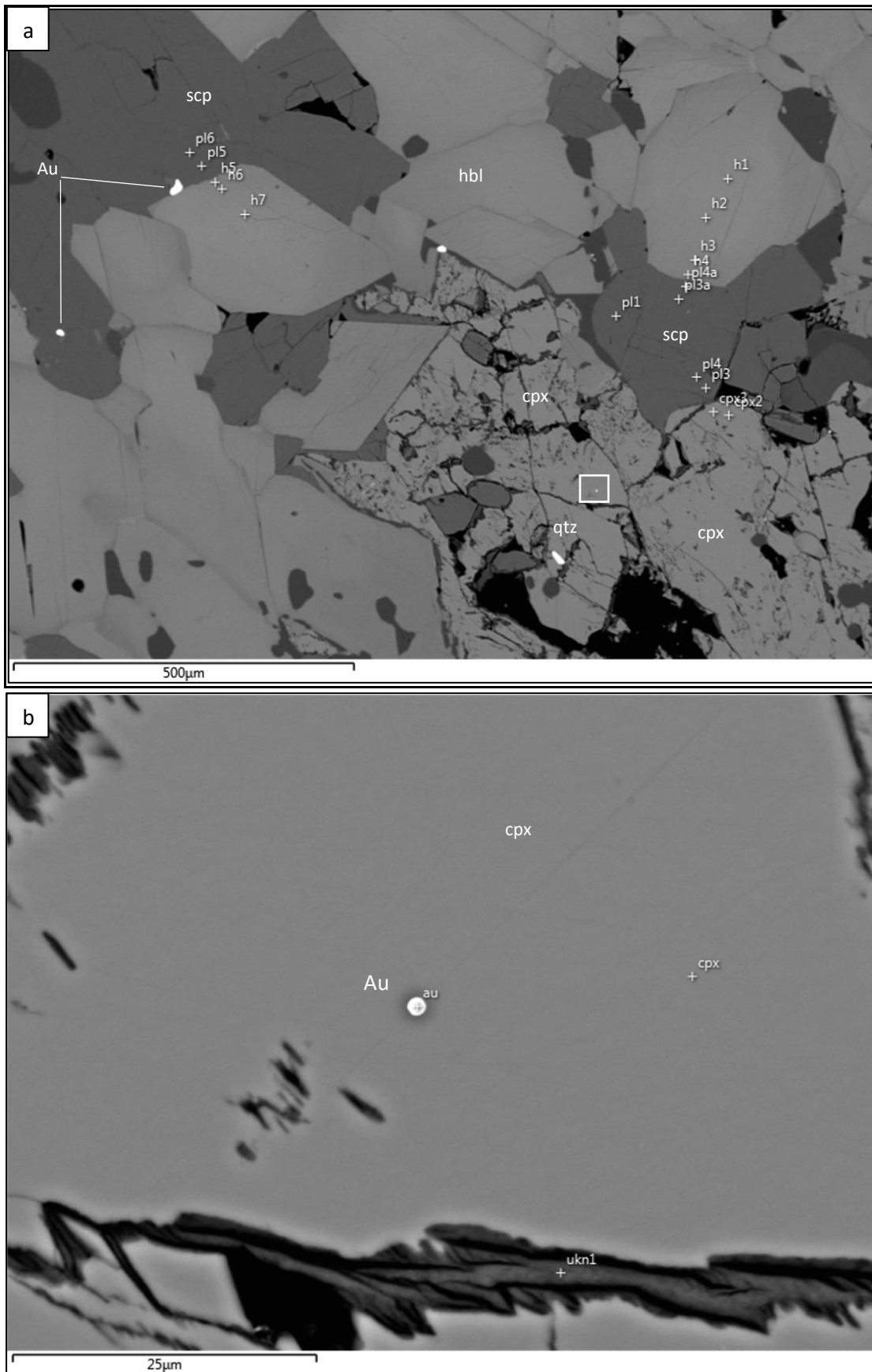
Figure 5.3. SEM images of (a) gold inclusions in scapolite (scp) and diopside (cpx) in amphibole-rich calc-silicate, sample TH46. The white box show area in (b) that shows a gold inclusion in clean diopside.
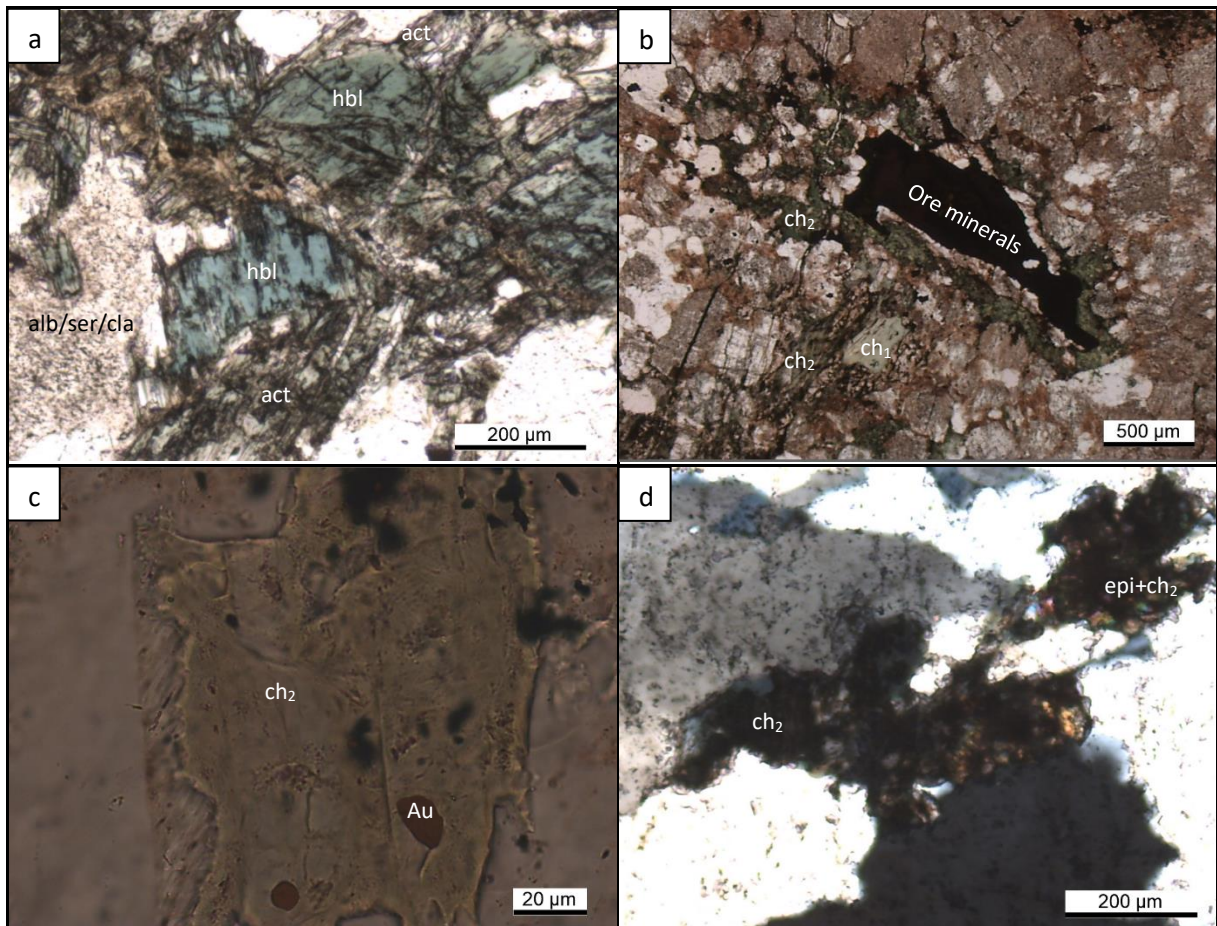
Figure 5.4. Microphotographs showing D_3 alteration minerals in various quartz-feldspar mylonite units in the most strongly altered core of the ore zone: (a) early D_3 hornblende (hbl) is rimmed and replaced by actinolite (act) along micro-fractures (sample THM51C); (b) chlorite$_2$ (ch$_2$) replaces chlorite$_1$ (ch$_1$) and occurrs around an ore mineral (pyrite-chalcopyrite intergrowth) as a reaction rim (sample THM22); (c) chlorite$_2$ (ch$_2$) hosting inclusions of gold (sample TH55); (d); epidote (epi) intergrown with chlorite$_2$ (ch$_2$; sample TH137).

5.2.2. Methodology

All analyses were conducted at the Advanced Analytical Centre (AAC), James Cook University (JCU), using a scanning electron microscope (SEM) and an electron probe micro-analyzer (EPMA). In *SEM analyses*, the microstructural characterization and the major and minor element composition of minerals were determined using a Philips XL30 SFEG scanning electron microscope coupled to an energy dispersive spectrometer by EDAX. The SEM was operated at 15 kV accelerating voltage and magnifications of 250x, 2000x, and 20000x. The thin sections were coated with carbon to increase the conductivity of the samples before analysis by SEM. For H_2O-bearing minerals, compositional estimates obtained with the SEM were corrected based on calculated H_2O content (and Li in some minerals). In *EPMA analyses*, the thin section sample was prepared in a similar way as samples analyzed by SEM, and the element composition was determined by the wavelength-dispersive spectrometer using Jeol JXA8200 "superprobe" housed at the AAC, JCU. Analyses were done utilizing a focus beam (<1µm) with an accelerating voltages of 20kV and a beam current of 20nA. The details of this technique are

presented in Jercinovic et al. (2008). The output data expressed in weight percentages were calculated to determine the mineral formulars for feldspar, garnet, amphibole, pyroxene, biotite, chlorite and epidote.
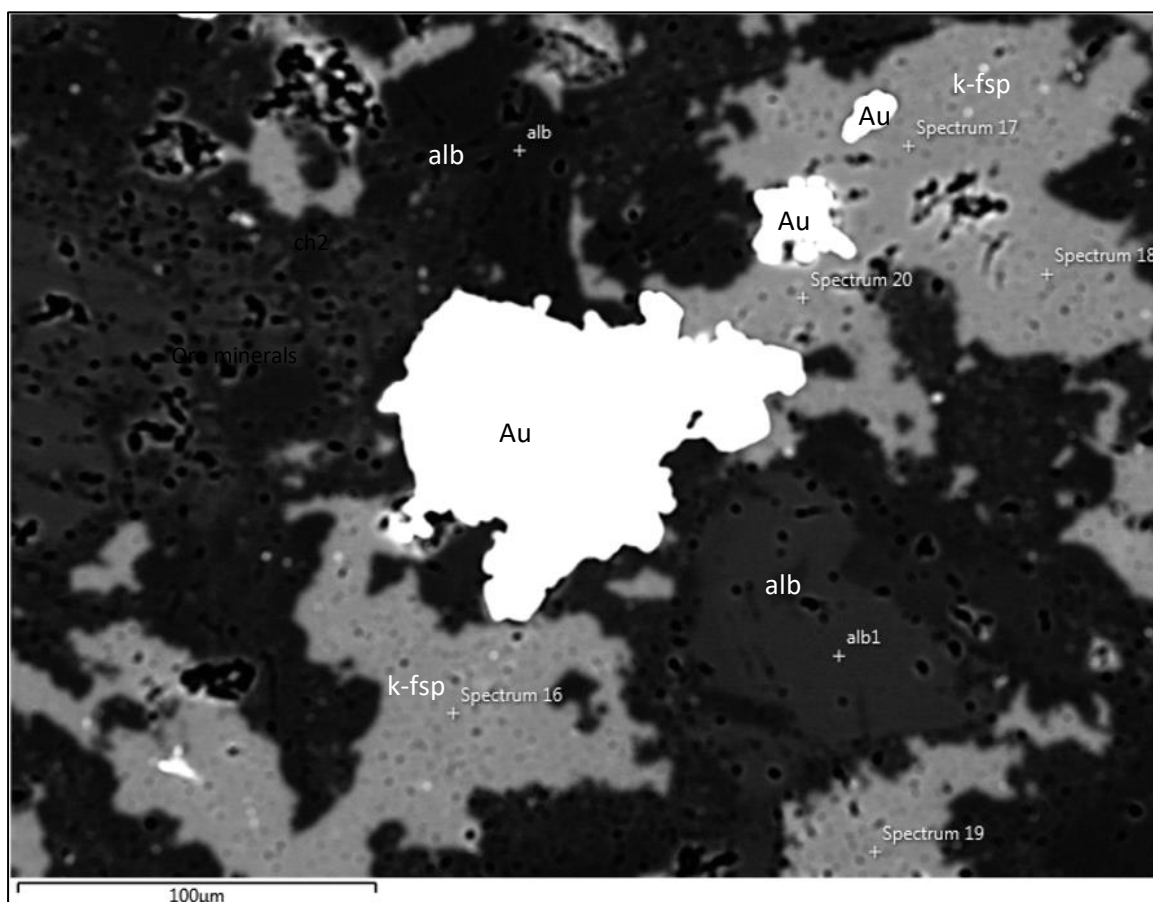
Figure 5.5. SEM images showing albite (alb) intergrown with K-feldspar (k-fsp) in quartz-feldspar mylonite (sample TH55) in which K-feldspar hosts Au inclusions.

5.3. Results

The chemistry for the major ore and silicate phases contained in each of the samples has been discussed below. The results of the analyses have been plotted in Figs.5.6-5.25 whilst the details of the analyses are presented in Appendix 6. The major ore minerals encountered in the altered quartz-feldspar mylonite will be described first, followed by compositional variations of the main silicate minerals hosted in different rock types (i.e. garnet, biotite, feldspar, amphibole, scapolite, clinopyroxene, chlorite, and epidote). Quartz appears in all samples.

5.3.1. Ore mineral composition

Au composition: A total of 69 analyses were taken from gold grains hosted in D_{1-2} metamorphic minerals from amphibole-rich calc-silicate, and D_3 (stages 2-4) mineralization in quartz-feldspar

mylonite and intensely silicified unit. All analyses for Au grains from calc-silicate and quartz-feldspar gneiss indicate that gold is pure, except for a single analysis of gold hosted in amphibole-rich, calc-silicate which contains minor Cu (~0.3%; Fig. 5.6). In contrast, 5 analyses for a ~50μm gold grain associated with quartz - albite - chlorite₂ - epidote alteration from stage 3 mineralization in the intensely silicified unit (sample TH 137), yield minor amounts of Cu (0.5-2%) and Ag (3.2-5.3%; Fig. 5.6).
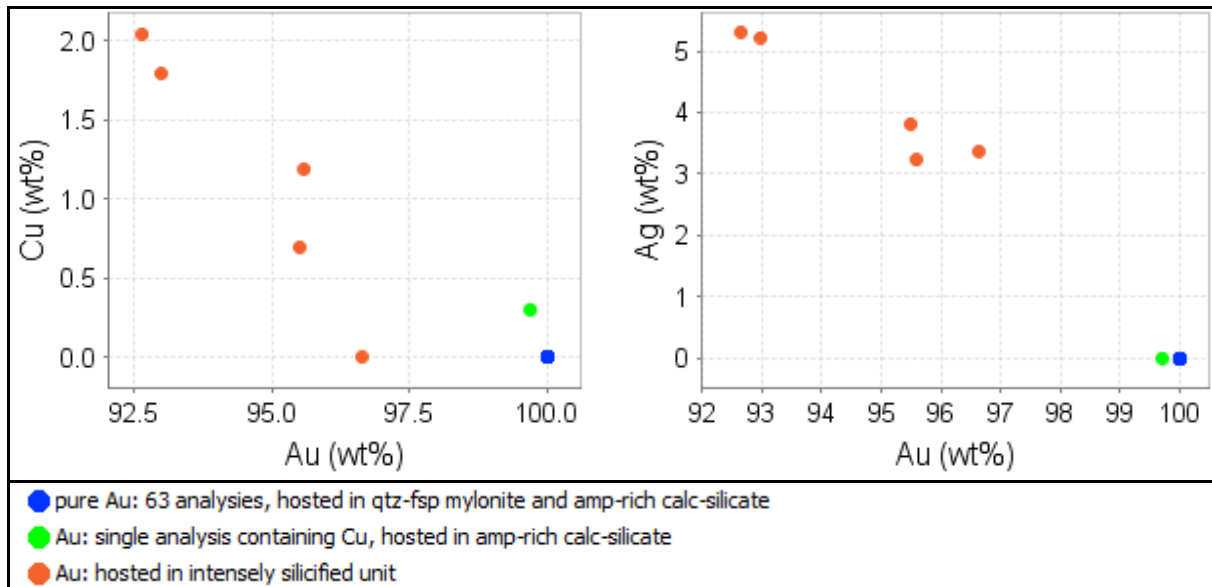
Figure 5.6. Gold composition from D₃ mineralization stages at Tick Hill, obtained with the SEM.

Various types of Bi-bearing *Selenides* commonly occur in association with gold in the quartz-feldspar mylonite unit. The most common selenide is guanajuatite (Bi_2Se_3), which locally contains minor Fe (0.4-1.2%) and Te (1.4-1.7%; Fig. 5.7). Other fine-grained selenides associated with gold in micro veins of calcite contain Pb, Cu and Bi consistent with the composition of Junoite - $Pb_3Cu_2Bi_8(S,Se)_{16}$, Cerromojonite - $CuPbBiSe_3$, and Clausthalite - PbSe or Molybdomenite - $PbSeO_3$.

Copper sulphides at Tick Hill include chalcopyrite and trace amounts of bornite and minerals with a composition close to (Fe-) Carrolite (Fig. 5.8). Most chalcopyrite and bornite grains are pure $CuFeS_2$ and Cu_5FeS_4 respectively and contain no other metals (Fig. 5.8). However, texturally late chalcopyrite grains associated with gold and bismuth selenide can contain minor amounts of selenium (0.5%; Fig. 5.8).

Small amounts of *Pyrrhotite* locally occurred in association with Au in the ore zone. Almost all pyrrhotite grains contain Se (commonly < 2%, which may be locally as high as 5.7%; Fig. 5.9).

There are at least two types of *Pyrite*, which formed during D₃ events at Tick Hill. The pyrite associated with D₃ events that was selected for this study include stage 2 and stage 3 pyrite. Stage 2 (pyrite₁) is commonly Ni-rich (0.02-2.9%) while stage 3 pyrite (pyrite₂) is commonly Se-rich (0.1-6.2%; Fig. 5.9, Appendix 6).
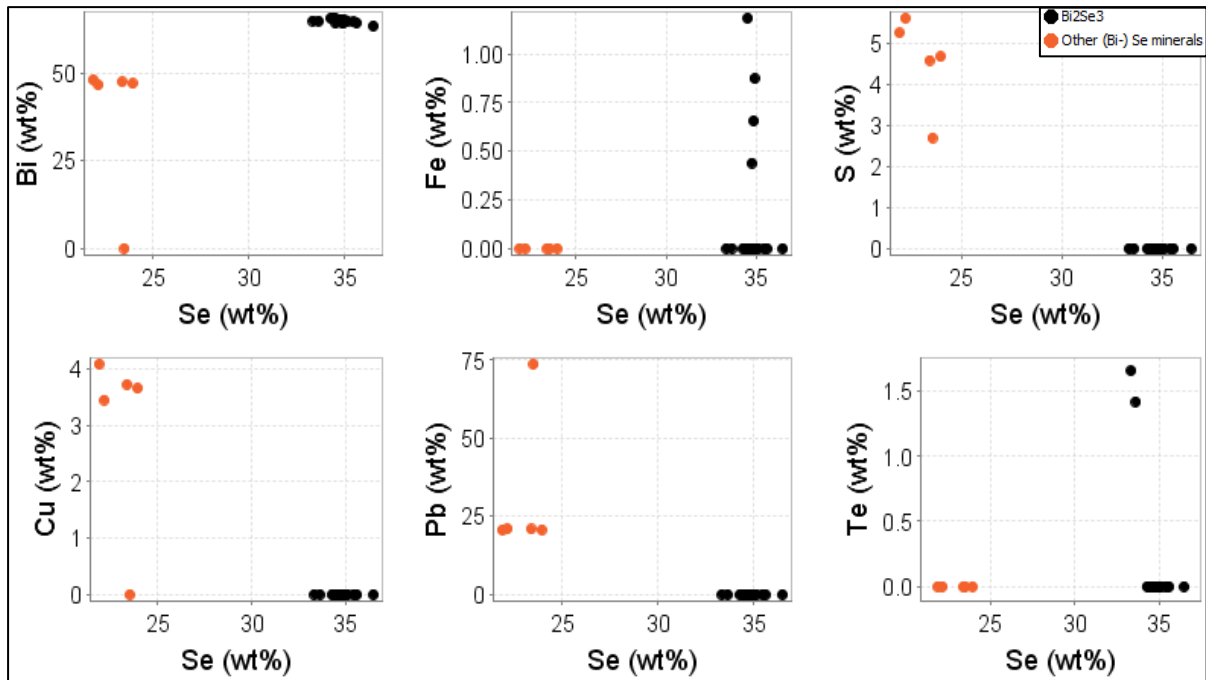
Figure 5.7. Composition of D₃ (bismuth-) selenide minerals hosted in quartz-feldspar mylonite at Tick Hill for samples TH55 and THM51C, measured with the SEM.
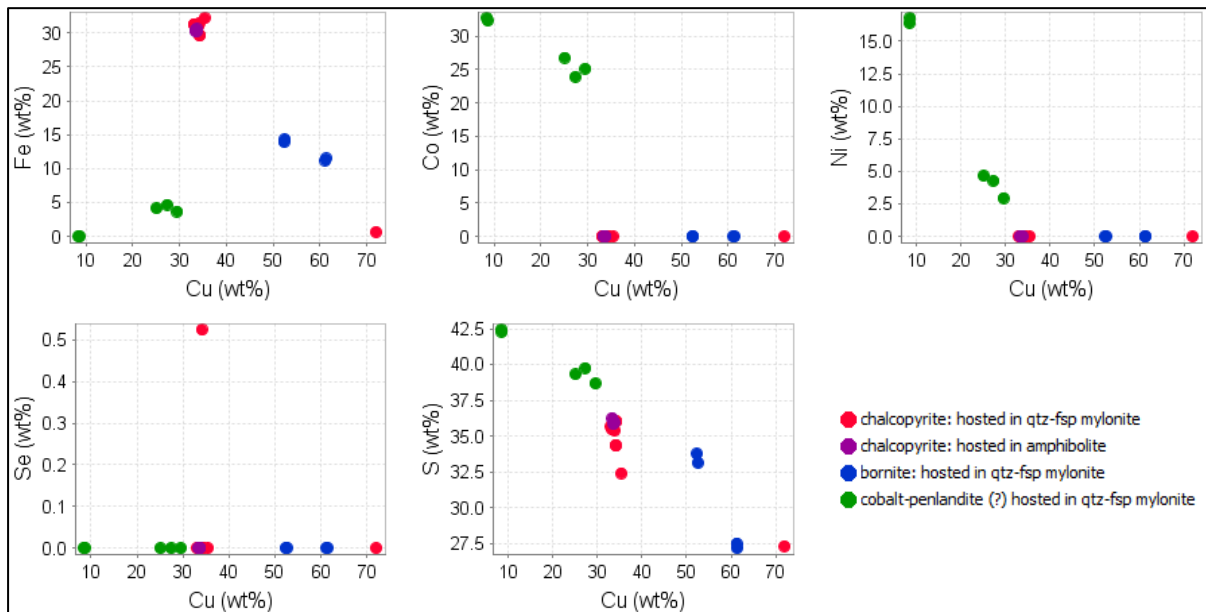
Figure 5.8. Composition of D₃ copper sulphides hosted in quartz-feldspar mylonite (samples THM22 and THM51C) and amphibolite (sample 99), measured with the SEM.

Hematite from the Au-rich quartz-feldspar-mylonite formed during D₃ events was selected for analysis. The hematite rarely occurs as pure hematite, but contains fine inclusions of leucoxene, Cu-sulphide, albite, K-feldspar and quartz, resulting in contamination with Ti (<1.2%), Cu (<0.5%), S (<0.6%), Al (<1.1%), Si (<5.1%), Na (<0.8%), K (<0.2%), and Ca (<4.5%; Fig. 5.10, Appendix 6).
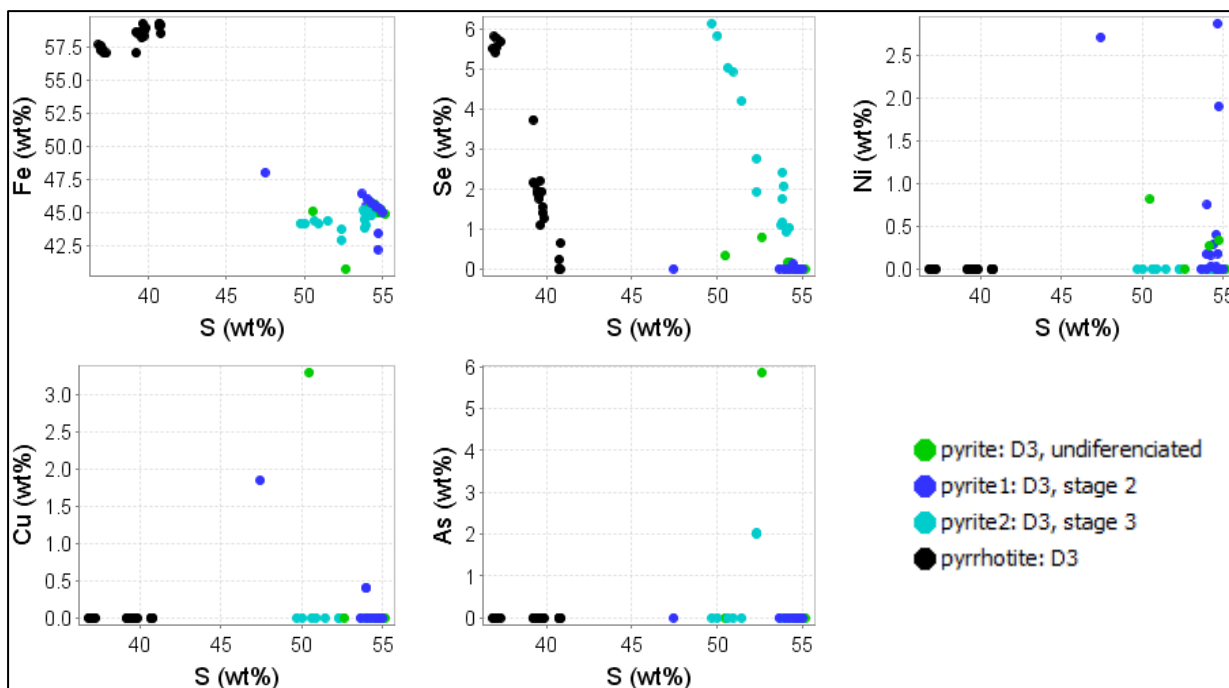
Figure 5.9. Pyrite and pyrrhotite composition from D₃ mineralization stages at Tick Hill, measured with the SEM.
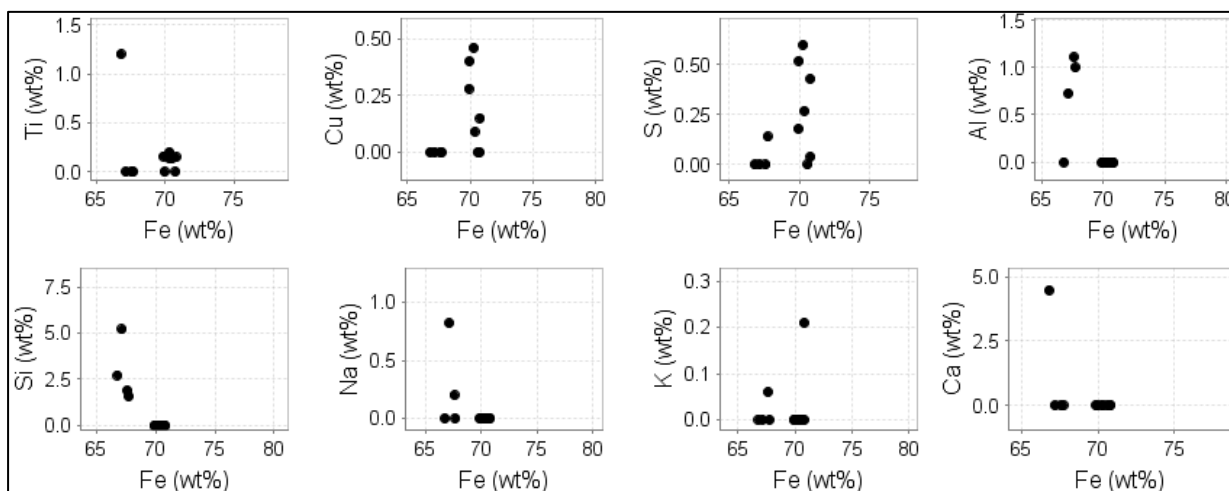
Figure 5.10. Compositional plots for D₃ hematite hosted in quartz-feldspar mylonite (samples THM22 and THM51C), measured on the SEM. The Si, Na, K, Al and Ca content is derived from small inclusions.

5.3.2. Mineral compositions for the garnet-bearing amphibolite unit (sample TH99)

The silicate minerals from the peak metamorphic amphibolite that were examined include garnet, biotite, plagioclase, amphibole, ilmenite and quartz. The composition of *Garnet* is plotted in Fig. 5.11a and the details of all analyses are shown in Appendix 6. According to the discrimination scheme from Geller (1967), this garnet has a composition of the almandine-pyrope group (Fig. 5.11b) with a mixture of almandine (~66-71%), pyrope (~11-18%) grossular (~11-14%), spessartine (~3-5%) and

andradite (<1%; Appendix 6). The garnet is relatively homogenous in composition with no discernable zoning, and contains 36.5-38.2% SiO_2, 19.8-22.1% Al_2O_3, 30.4-32.4% FeO_{total}, 2.7-4.3% MgO, 4.2-5% CaO, 1.4-2.3% MnO and minor TiO_2 (<0.42%; Fig.5.11). Results from SEM and EPMA analyses are similar, but the Al_2O_3 content measured by SEM is slightly higher (20.8-22%) compared to measurements taken with the EPMA (20-20.5%; Fig. 5.11a).

Syn-D_{1-2} *Biotite* occurs in the matrix aligned with S_{1-2} and as inclusions in garnet. The biotite composition is plotted in Fig. 5.12a and its details have been presented in Appendix 6. Biotite is homogenous in composition and it belongs to the Mg-biotite sub-group (Fig. 5.12; after Foster, 1960). In more detail, this Mg-biotite is relatively Ti-rich with 1.0-3.5% TiO_2, 10.5-12.4 % MgO, 19.8-25.3% FeO_{total}, 15.4-17.2% Al_2O_3, 33.4-36.3% SiO_2, 5.0-9.3% K_2O, and minor Cl (0.7-1.3%), CaO (<1.07%) and Na_2O (<0.51%; Appendix 6). Small compositional variability is due to localized (laminar) alteration to D3 $chlorite_1$ and muscovite. The SEM and EPMA data for biotite has been plotted in Figure 5.12a, and shows that the semi-quantitative SEM results are in close agreement with the quantitative EPMA data.

Syn-D_{1-2} *Feldspar* in TH99 consists of 56.5-58.4% SiO_2, 25.8-27.5% Al_2O_3, 7.8-9.1% CaO and 6.0-7.0% NaO with minor K_2O (<0.26%) and FeO_{total} (<0.6%; Fig. 5.13a) to reflect an andesine composition (Fig. 5.13b). The feldspar locally has trace amounts of TiO_2 (<0.01%, but locally up to 0.5%), MnO (<0.01%) and Cl (<0.02%; Fig. 5.13a, Appendix 6), probably reflecting fine inclusions of ilmenite or magnetite. Feldspar compositions for matrix grains and inclusions in garnet are similar. The composition obtained from the SEM and EPMA analyses for feldspar are similar (Fig. 5.13).

Syn-D_{1-2} *Amphibole* in sample TH99 consists of SiO_2 (37.5-40.4%), Al_2O_3 (13.8-16.4%), FeO_{total} (19.3-22.3%), MgO (5.0-7.8%), CaO (9.9-10.0%), Na_2O (1.4-2.0%), K_2O (0.8-1.3%), TiO_2 (mostly 0.7-1.2%), MnO (<1.0%) and Cl (~0.8-1.7%; Fig. 5.14a; Appendix 6). The amphibole has the composition of (Fe-)tschermakite (Fig. 5.14b, after Leake et al., 1997). The Fe-tschemakite in TH99 is homogenous in composition and shows no zoning or compositional variation between matrix amphibole and amphibole inclusions contained in garnet. Compositional measurements obtained with the SEM and EPMA are near-identical (Fig. 5.14).

Ilmenite selected from inclusions in garnet contain TiO_2 (48.7-52.0%), FeO (47.5-50.7%) and MnO (0.7%; Fig 5.15; Appendix 6).
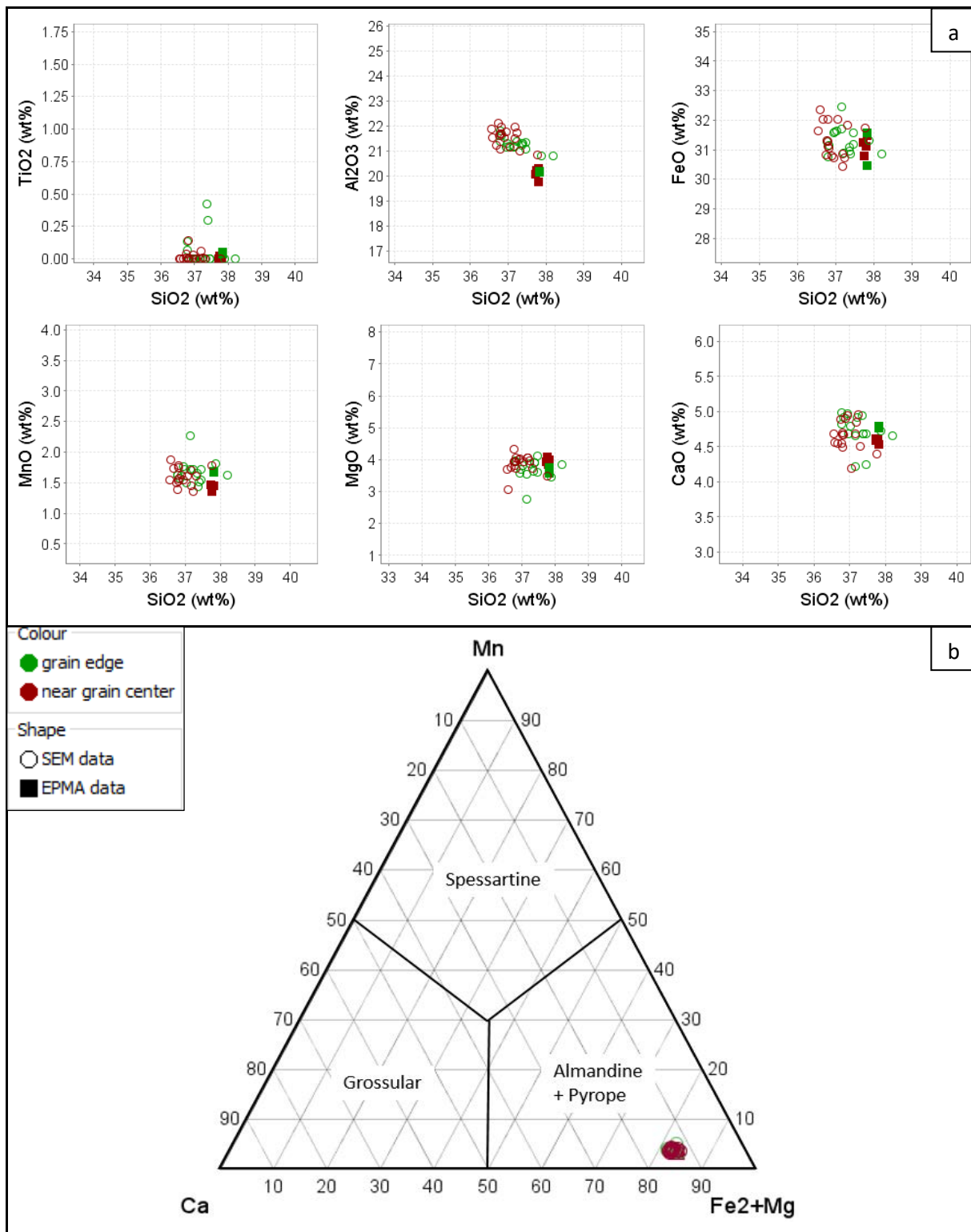
Figure 5.11. (a) Composition plots and (b) discrimination plot (after Geller, 1967) for garnet from peak metamorphic amphibolite in sample TH99. The coarse-grained, inclusion-rich garnet is homogenous in composition and displays no systematic zoning.
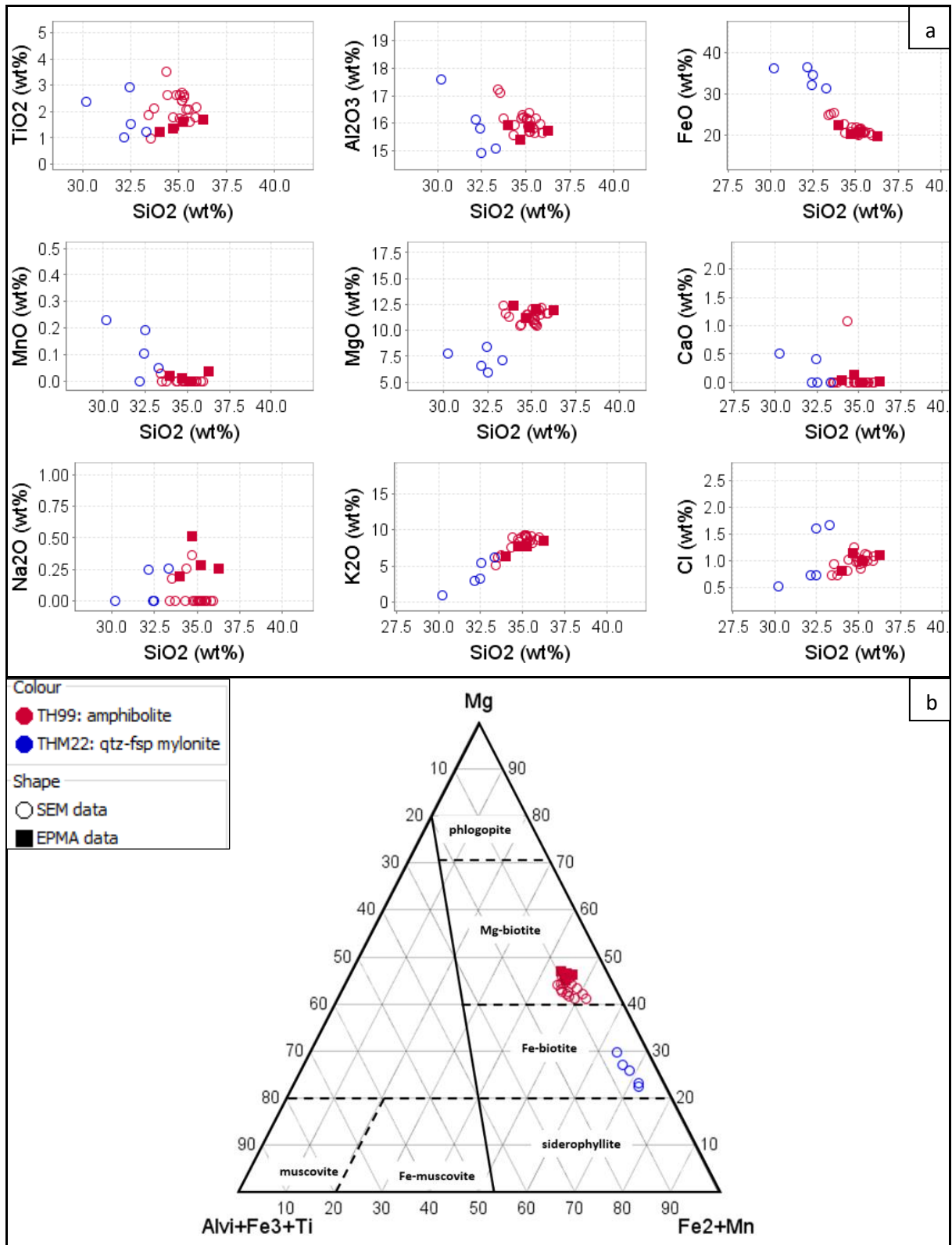
Figure 5.12. (a) Composition plots and (b) discrimination plot (after Foster, 1960) for biotite from amphibolite (sample TH99) and quartz-feldspar mylonite (sample THM22) at Tick Hill. The peak-metamorphic biotite in TH99 is homogenous.
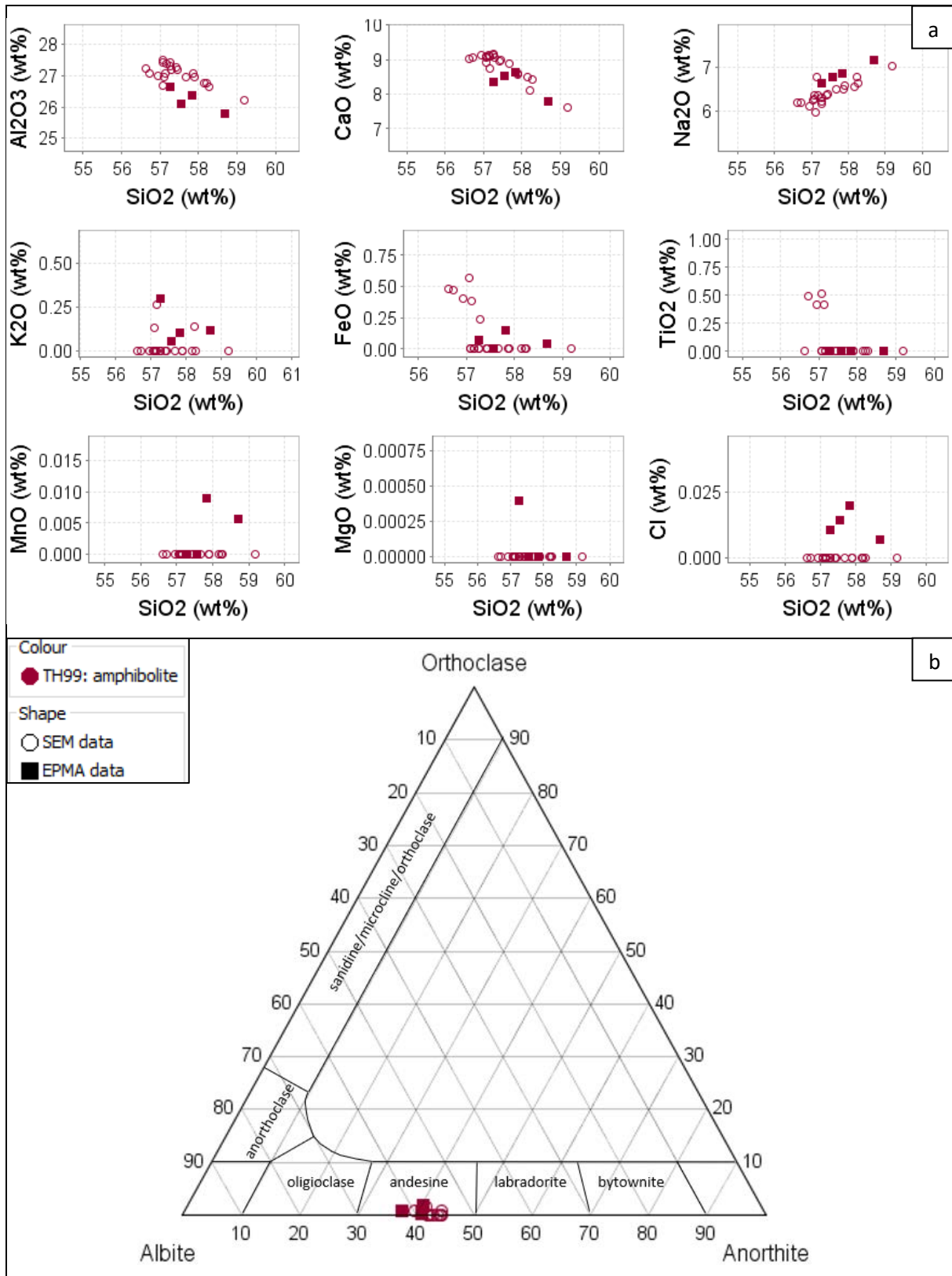
Figure 5.13. (a) Composition and (b) discrimination plots for feldspar from sample TH99. The peak-metamorphic feldspar in TH99 is andesine with no systematic variation in composition between matrix andesine and andesine inclusions in garnet.
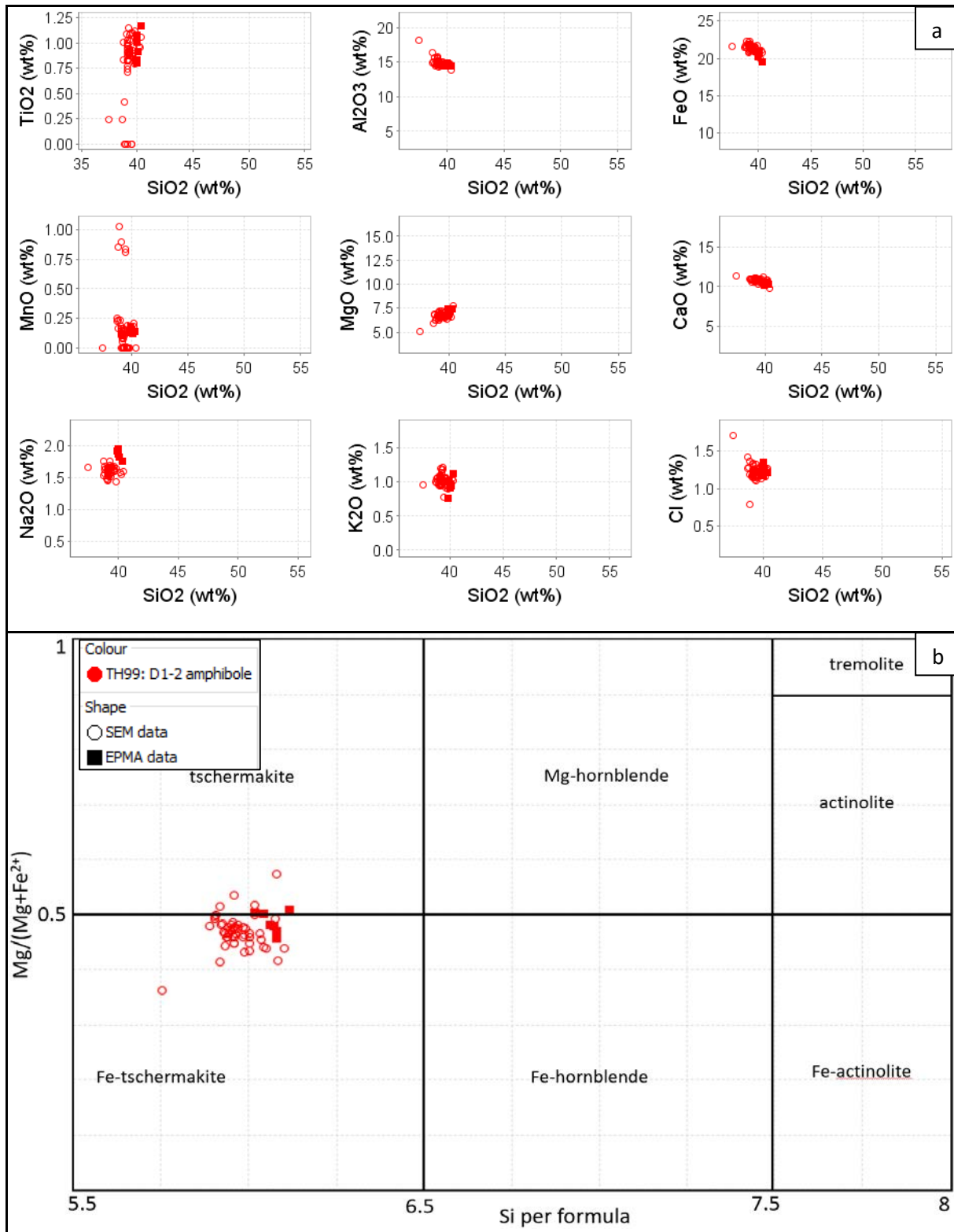
Figure 5.14 (a) composition plots and (b) discrimination diagram (after Leake et al., 1997) for amphibole from sample TH99. The peak-metamorphic amphibole is homogenous in composition with no systematic variation between matrix amphibole and amphibole inclusions in garnet. The amphiboles are not zoned.
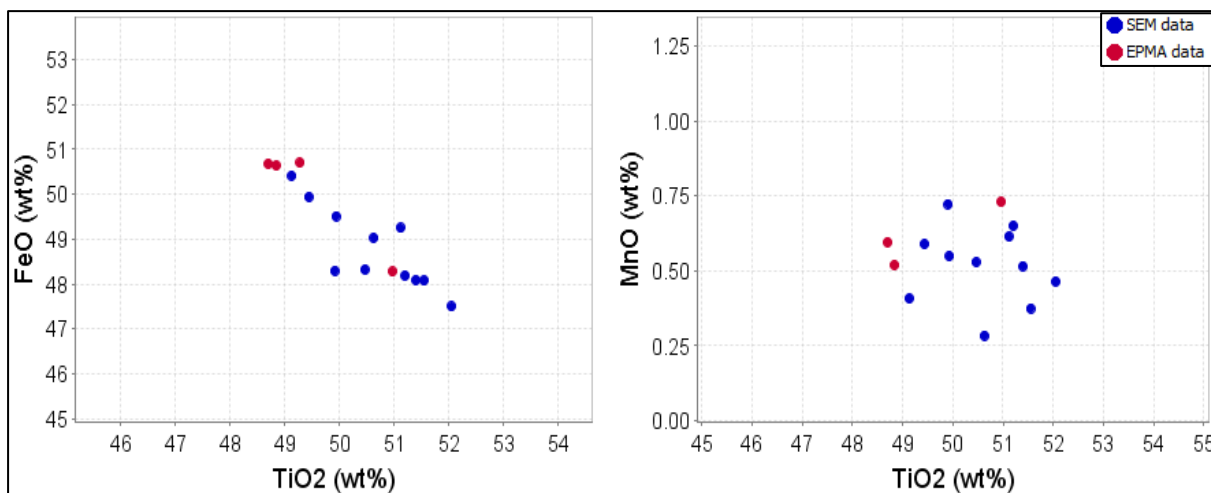
Figure 5.15. Composition of ilmenite inclusions within garnet from amphibolite, sample TH99.

5.3.3. Mineral composition of amphibole-rich calc-silicate unit (sample TH46)

The silicate minerals in the gold-bearing, amphibole-rich calc-silicate (sample TH46) selected for geochemical examination include D_{1-2} feldspar, clinopyroxene, amphibole and D_3 feldspar-actinolite-mica alteration. The compositions for these minerals are discussed as below.

Pyroxene composition is plotted in Figure 5.16a, and analytical details are presented in Appendix 6. The pyroxene's composition is homogenous and indicative of diopside (Fig. 5.16; after Morimoto, 1988). It consists of 53.3-54.4% SiO_2, 7.4-8.5% FeO, 12.8-14% MgO, 22.5-23.6% CaO with minor Al_2O_3 (<1%), MnO (<0.3%), Na_2O (<0.9%), TiO2 (<0.1%), Cr_2O_3 (<0.03%), K_2O (<0.03%) and Cl (<0.03%; Fig. 5.16a; Appendix 6). Individual diopside grains do not display zoning, and SEM and EPMA results are similar although EPMA results display a systematic increase in SiO_2 (Fig. 5.16a). Compositionally homogenous diopside locally contains fine inclusions of gold, with no evidence of microfractures.

The compositions of D_{1-2} *feldspar* aligned in the peak-metamorphic S_{1-2} fabric and D_3 feldspar formed during retrograde mineral reactions and overprints, have been plotted in the Figure 5.17, and details are presented in Appendix 6. D_{1-2} feldspar mainly consists of oligioclase, which locally contains andesine inclusions or is in contact with anorthite (Fig. 5.17b). D_{1-2} oligoclase contains 55.6-64.8% SiO_2, 22.5-23.7% Al_2O_3, 3.7-4.7% CaO (with an outlier of 7.4%) and 8.3-9.6% Na_2O with minor FeO (<0.25%), MnO (<0.05%) and Cl (<0.01%, Fig. 5.17a; Appendix 6). The single analysis of an andesine inclusion within oligioclase is characterized by 8.9% CaO and 5.3% Na_2O. The anorthite was strongly altered by D_3 fluids resulting in a complex framework and matrix texture. Two analyses for a relic anorthite grain are characterised by elevated CaO (27.4-28.4%) and Al_2O_3 (25.6-25.7%). The D_3 feldspar alteration includes albite and K-feldspar (Fig. 5.7b). The albite contains 9.8-11.3% Na_2O and 0-2.1% CaO while the K-felspar contains 15.5-16.3% K_2O and 0-0.8% BaO (Fig. 5.17a). Albite and K-

feldspar usually contain minor amounts of FeO (mostly <1.0%) as a result of hematite dust that formed with albite and K-feldspar during D₃ alteration. The SEM and EPMA results for feldspar are similar (Fig. 5.17).
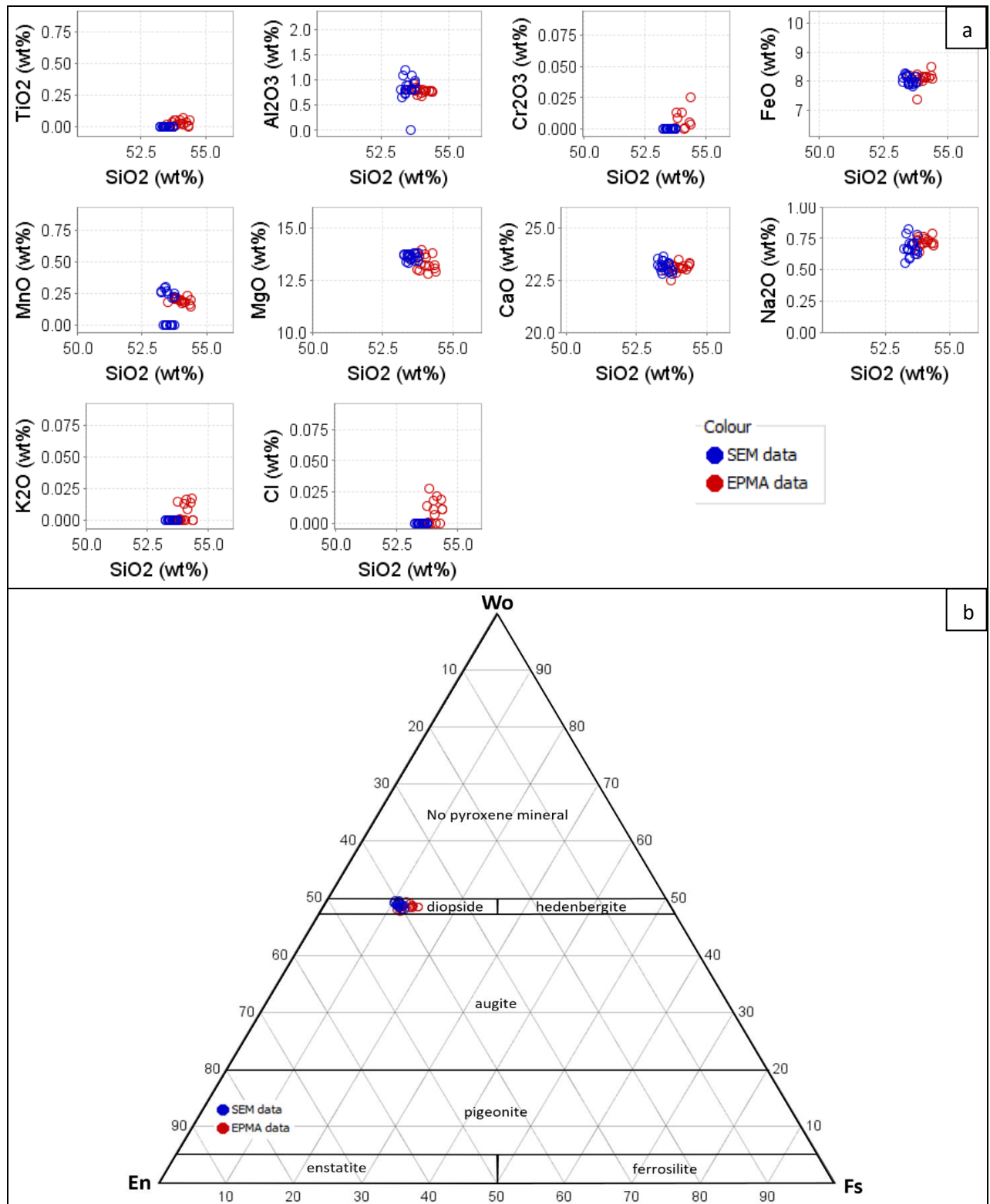
Figure 5.16. (a) Composition plots and (b) discrimination plot (after Morimoto, 1988) for pyroxene from amphibole-rich calc-silicate (sample TH46). The diopside is homogenous in composition and shows no zoning.
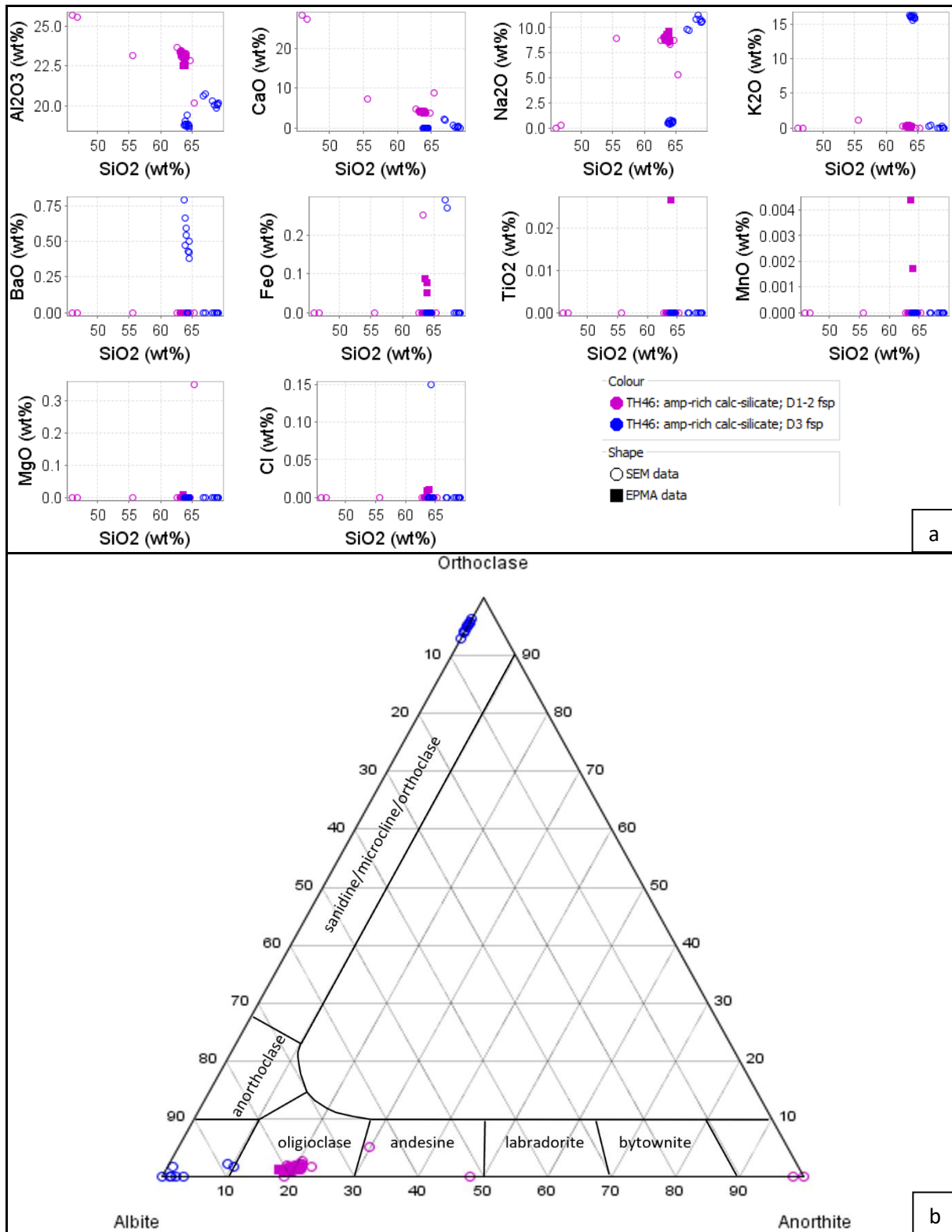
Figure 5.17. (a) Composition plots and (b) discrimination plot for D$_{1-3}$ feldspars from amphibole-rich calc-silicate (sample TH46).

The composition of *Amphibole* from TH46 is plotted in Fig. 5.18a, and its details are presented in Appendix 6. The amphibole grains are generally zoned and display a wide range of compositions that vary from Mg-hornblende to actinolite (Fig. 5.18b; after Leake et al., 1997). The Mg-hornblende is

variably composed of Al_2O_3 (4.85-8.0%), FeO_{total} (12.0-15.2%), MgO (12.5-15.3%), CaO (11.1-12.6%), Na_2O (0.8-1.7%) and minor K_2O (0.3-0.7%), Cl (0.2-0.6%), TiO_2 (<0.25%) and MnO (<0.25%; Fig 5.18a). The actinolite, compared to Mg-hornblende, has higher contents of SiO_2 (51.8-55.3%) and MgO (14.5-18.0%), but lower contents of Al_2O_3 (0.7-3.7%), FeO_{total} (7.5-13.5%), Na_2O (0.3-0.8%), K_2O (<0.3%) and Cl (<0.25%; Fig. 5.18a). The CaO and MnO contents in actinolite and Mg-hornblende are similar (Fig. 5.18a). The hornblende displays clear retrograde zoning towards the rims and near microfractures, with a gradual change in the contents of Al2O3, SiO2 (+FeO, MgO). The SEM and EPMA results are similar although EPMA results display a greater degree of variability (Fig. 5.18).

The composition of *Scapolite* is plotted in Fig. 5.19 and its details are presented in Appendix 6. The scapolite is sodium-rich (marialite) and contains 22.5-23.4% Al_2O_3, 8.7-9.7% Na_2O, 7.2-7.9% CaO, 0.7-1.1% K_2O, 2.9-3.3% Cl, and minor FeO (<0.3%), TiO_2 (<0.1%) and MnO (<0.03%; Fig. 5.19). The EPMA results compared to SEM data, display a slight enrichment in Na_2O, and depletion in Al_2O_3, CaO, Cl and FeO (Fig. 5.19).
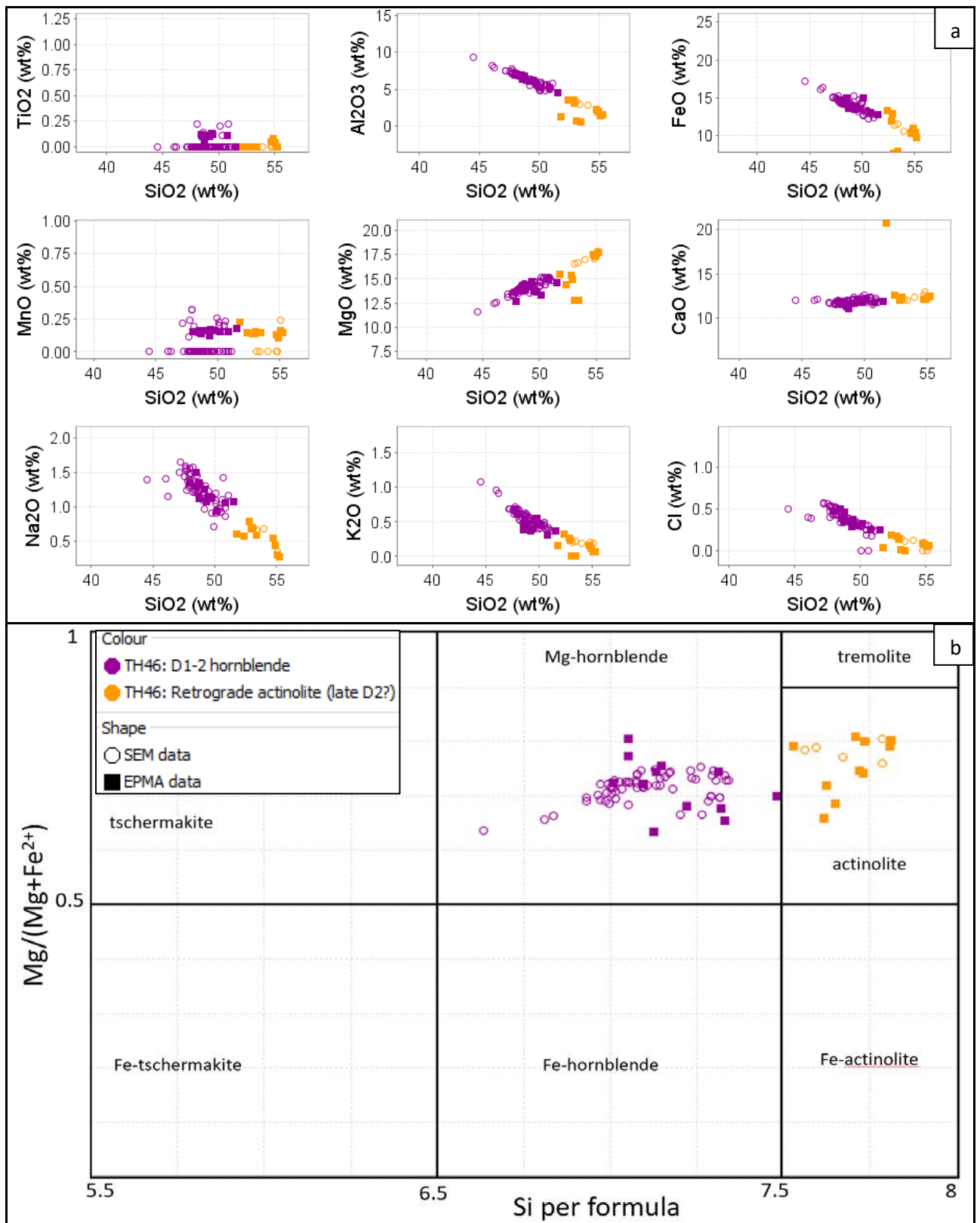
Figure 5.18. (a) Composition plots and (b) discrimination diagram (after Leake et al., 1997) for D$_{1-3}$ amphibole grains from amphibole-rich calc-silicate in sample TH46. The results show the clearly zoned nature of the D$_{1-2}$ amphibole, presumably as a result of the D$_3$ overprint.

127
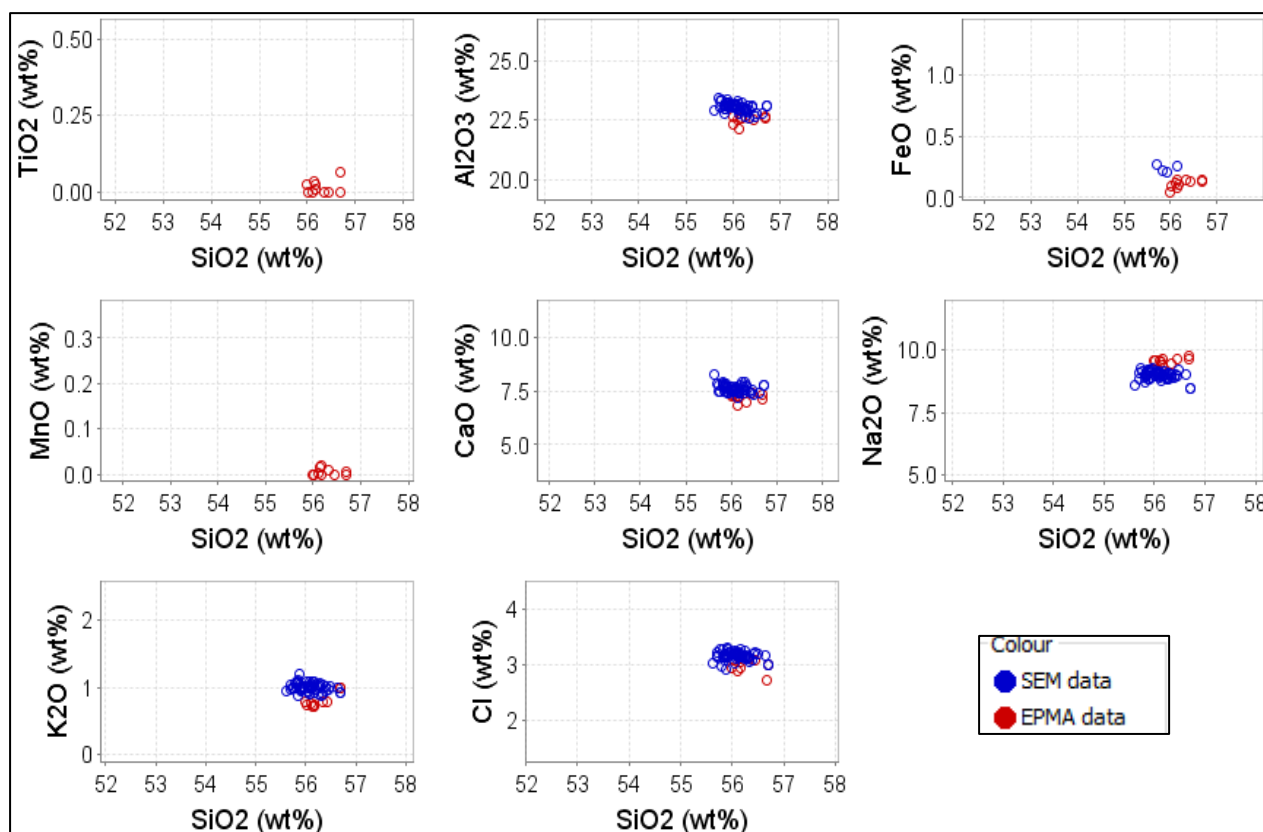
Figure 5.19. (a) Composition of scapolite aligned within the composite D₁₋₂ fabric in sample TH46. The scapolite is not zoned.

5.3.3. Composition of silicate minerals in quartz-feldspar mylonite

Silicate minerals in quartz-feldspar mylonite samples TH55, THM22 and THM51C were selected for the geochemical investigation including: biotite interpreted to have formed during D_{1-2}; various types of amphibole formed (and altered) during D_{1-3}; and feldspar, chlorite, and calcite formed during various stages in D_3. Their mineral composition is discussed as below.

Fine grained relict *Biotite* grains hosted in quartz-feldspar mylonite (sample TH55) were partly replaced by chlorite. This biotite consists of FeO_{total} (31-36.5%), MgO (6-8.4%) and K_2O (0.9-6.2%) with minor MnO (<0.2%), CaO (<0.5%), Na_2O (<0.3%; Fig. 5.12a; Appendix 6), and it belong to the Fe-biotite subgroup (Fig. 5.12b; after Foster, 1960). The small compositional variations observed in the biotite, probably resulted from partial retrograde replacement by fine chlorite.

Amphibole in samples TH55 and THM51C were selected for analysis and plotted in Figure 5.20. Relic D_{1-2} amphibole grains in sample TH55 consist of tschermakite (Fig. 5.20b; after Leake et al., 1997) that was overprinted by D_3 metasomatism (Chapter 2). The tschermakite consists of 41.2-42% SiO2, 10-10.7% Al_2O_3, 19.5-21.8% FeO_{total}, 8.1-10% MgO, 9.7-11.4% CaO, 1.4-1.8% Na_2O and 1.3-1.7% K_2O with minor TiO2 (<1.3%) and MnO (<0.3%; Fig. 5.20a). SEM and EPMA results for the tschermakite are similar (Fig. 5.20) except for MnO, which was not detected on the SEM.

The amphibole from sample THM51C includes Mg-hornblende interpreted as having formed during the early stages of D_3 (stage 1) alteration, and D_3 (stage 2) actinolite and rarely tremolite, which occurs as retrograde rims and along micro-fractures replacing the hornblende. Amphibole in this sample was analyzed with the SEM only. The Mg-hornblende displays zoning, in which the SiO_2 and MgO increase whilst FeO and Al_2O_3 gradually decreased as actinolite replaces hornblende. The Mg-hornblende is composed of SiO_2 (46.9-50.9%), Al_2O_3 (5.3-8%), FeO_{total} (13.4-17%), MgO (12.4-14.8%), CaO (11-12.2%) Na_2O (1-1.7 %) with minor K_2O (0.4-0.8%), Cl (0.2-0.6; Fig. 5.20a). The younger actinolite and a single analysis of tremolite are similar in composition, consists of SiO_2 (52.9-55.6%), Al_2O_3 (0.5-3.7%), FeO_{total} (11.6-13.8%), MgO (14.9-17%), CaO (9.9-12.7%), Na_2O (0.3-1%), K_2O (<0.4%) and Cl (<0.2%, Fig. 5.20a).

D_3 *Feldspar* in quartz-feldspar mylonite (samples THM22, THM51C and TH55) includes albite, K-feldspar and oligioclase with minor amounts of anorthoclase in retrograde reaction zones (Fig. 5.21). The albite mainly contains 8.3-11.9% Na_2O, 19.7-24.9% Al_2O_3 and 64-70.1% SiO2, with two outliers of depleted Al_2O_3 (13.2-15.9%) and elevated SiO_2 (75.7-79.1%). The K-feldspar contains 16.1-17.1% K_2O, 61.9-64.4% SiO_2 and 18.4-19.5% Al_2O_3, with two outliers of depleted K_2O (14.4-15.9%). The D_3 oligioclase in this sample contains 2.3-3.4% CaO, 9.2-10 % Na_2O, 63.8-65.9% SiO_2 and 22.2-23.2% Al_2O_3 (Fig. 5.21a; Appendix 6). Albite, oligioclase and K-feldspar are locally hematite-dusted as seen in minor values of FeO (commonly <1%, locally reaching 2.32%; Figure 5.21a). These feldspar minerals locally also contain minor contents of MgO (<0.4%) and Cl (<0.2%) and trace amounts of TiO_2 (<0.06%) and MnO (<0.05%). Anorthoclase is restricted to reaction rims and is characterized by 6.5-9.8% Na_2O, 1.7-5.2% K_2O, 57.8-67.6% SiO_2 and 16.7-24.9% Al_2O_3 (Fig. 5.21; Appendix 6). The SEM and EPMA results for feldspar are similar for major and minor elements (Fig. 5.21).
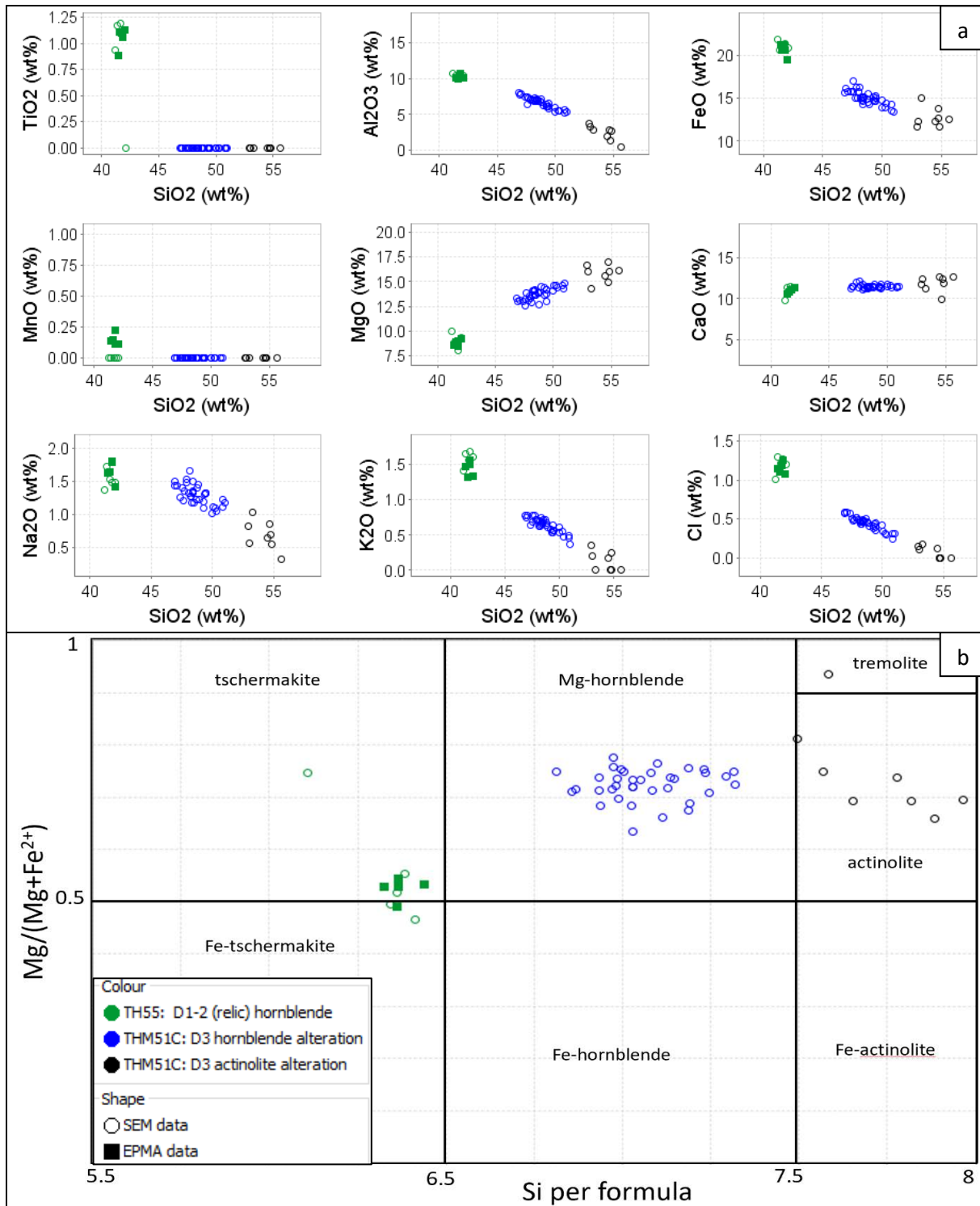
Figure 5.20. (a) Composition plots and (b) discrimination diagram (after Leake et al., 1997) for D_{1-3} amphibole from quartz-feldspar mylonite in samples TH55 and THM51C.
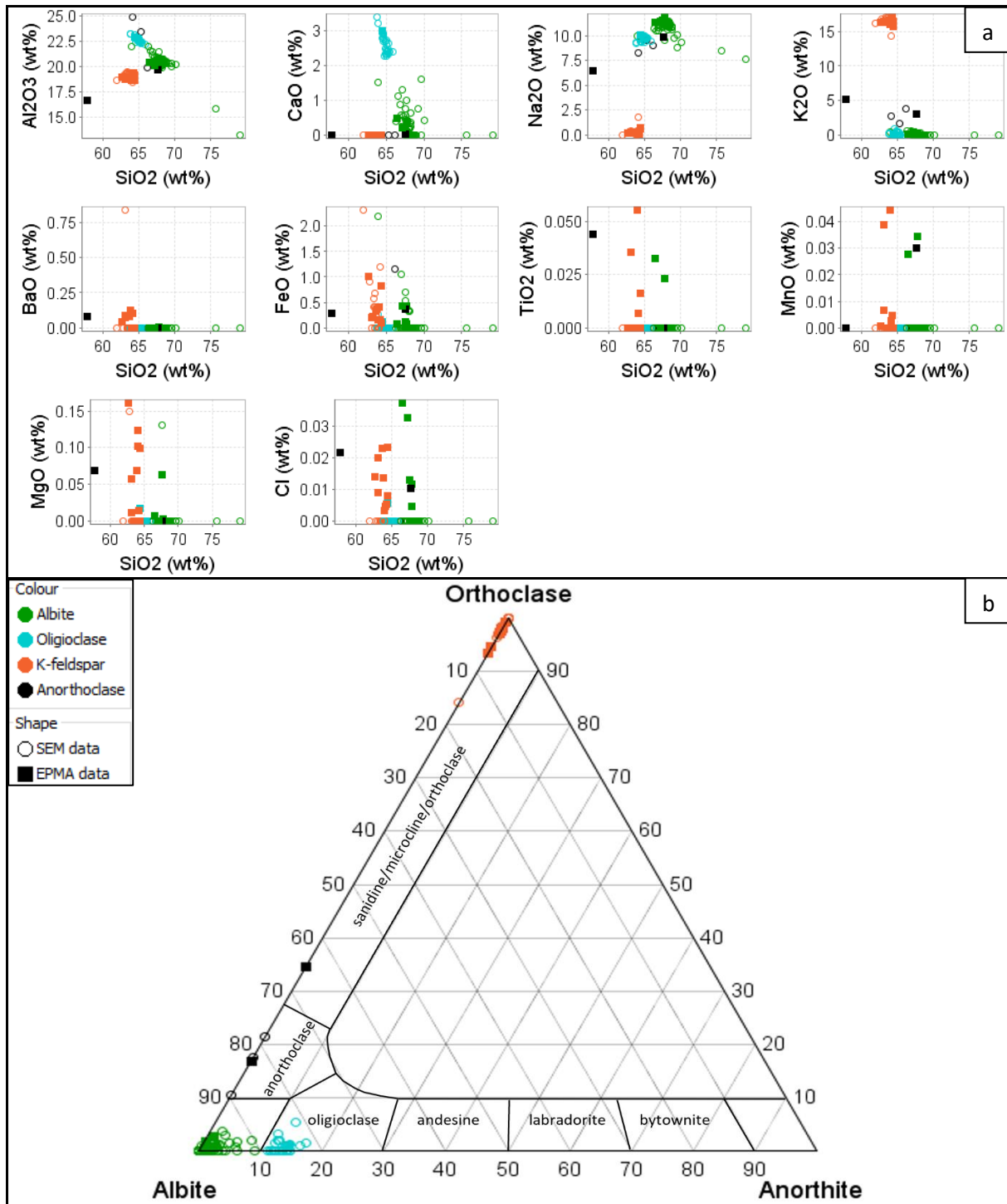
Figure 5.21. (a) Composition plots and (b) discrimination diagram for D_3 feldspar alteration from quartz-feldspar mylonite in samples TH55, THM22 and THM51C.

Based on composition and *Chlorite* morphology in thin sections, three types of *chlorite* have been recorded in the Tick Hill alteration halo, all of which formed during various alteration stages of D_3. The composition and classification of these chlorite types are plotted in Figure 5.22, and the details of all analyses are shown in Appendix 6. Chlorite$_1$ has elevated Al_2O_3 (15.0-21.7%, but mostly >17.4%), depleted SiO_2 (23.7-25.5%) and contains minor MnO (<1.9%), TiO_2 (<1.3%) and Cl (<0.2%). The FeO$_{total}$ and MgO content of chlorite$_1$ varies between 23.1-35.2% and 7.2-16.8% respectively, which

reflects localized, partial retrograde re-equilibration. All grains of chlorite$_1$ fall within the compositional fields of ripidolite, brunsvigite or picnochlorite (Fig. 5.22b; after Hey, 1954). Compared to chlorite$_1$, chlorite$_2$ generally contains less Al_2O_3 (13.2-17.7 %,) and FeO_{total} (21.2-36.8% but mostly < 31.8%) and is enriched in SiO_2 (25.7-32.8%) and MgO (8.3-19.3%; Fig. 5.22a, Appendix 6). Chlorite$_2$ also contains minor TiO_2 (<1.3%), MnO (<0.5%) and Cl (<0.3%). and mostly falls within the brunsvigite-diabantite compositional field reflecting transitional retrograde phases, with chlorite$_2$ 'proper' being diabantite (Fig. 5.22b; after Hey, 1954). Chlorite$_3$ has the lowest concentrations of Al_2O_3 (13-14% with an outlier of 14.8%) and FeO_{total} (10.4-16.3%), and is the most enriched in MgO (22.1-26.4%; Fig. 5.2, Appendix 6) that is consistent with a diabantite-penninite composition (Fig. 5.22b). Chlorite$_3$ contains minor TiO_2 (mainly <0.1%), MnO (<0.2%) and Cl (0.1-0.2%). All three types of chlorite locally contain some CaO (<1.3%), Na_2O (<0.6%) and K_2O (<1%; Fig. 5.22a, Appendix 6), which may reflect the presence of fine white mica or feldspar inclusions. The SEM and EPMA data for chlorite generally show a difference of 0.5-1% for major elements (Appendix 6).

Calcite formed late during D_3 events, (i.e. stage 4) as micro-veins in the alteration halo, and it is locally associated with Au, trace amounts of bismuth selenide, sulphide and chlorite$_3$. Most analyses are pure calcite with no Mg, Fe or Mn, although fine inclusions of albite occur (Fig 5.23, Appendix 6).
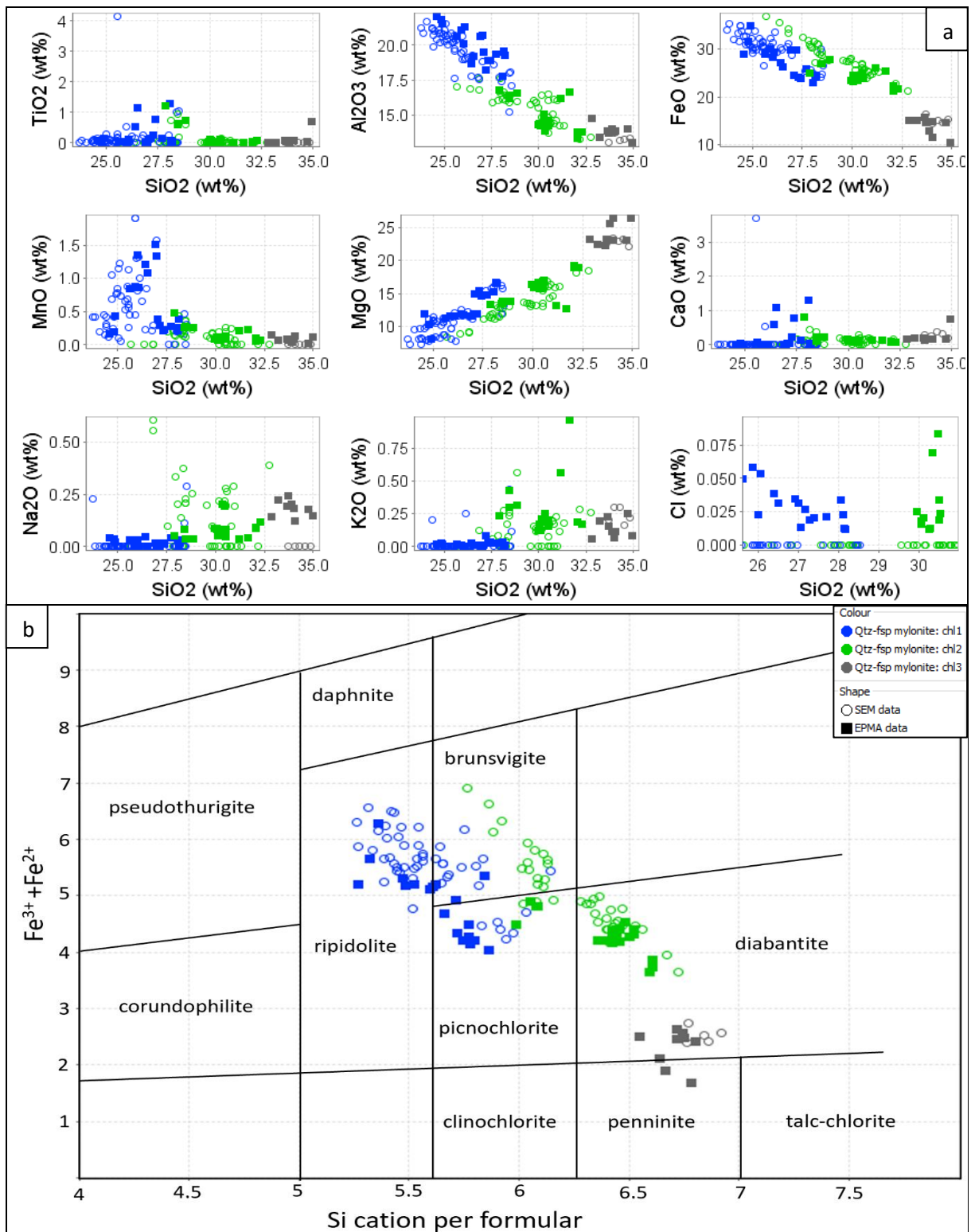
Figure 5.22. (a) Composition plots and (b) discrimination plot (after Hey, 1954) for D₃ chlorite (chl₁₋₃ refers to chlorite₁₋₃) from quartz-feldspar mylonite (samples TH55, THM22 and THM51C). Note that many of the chlorite grains are strongly zoned, reflecting continual retrograde re-equilibration as temperatures dropped.
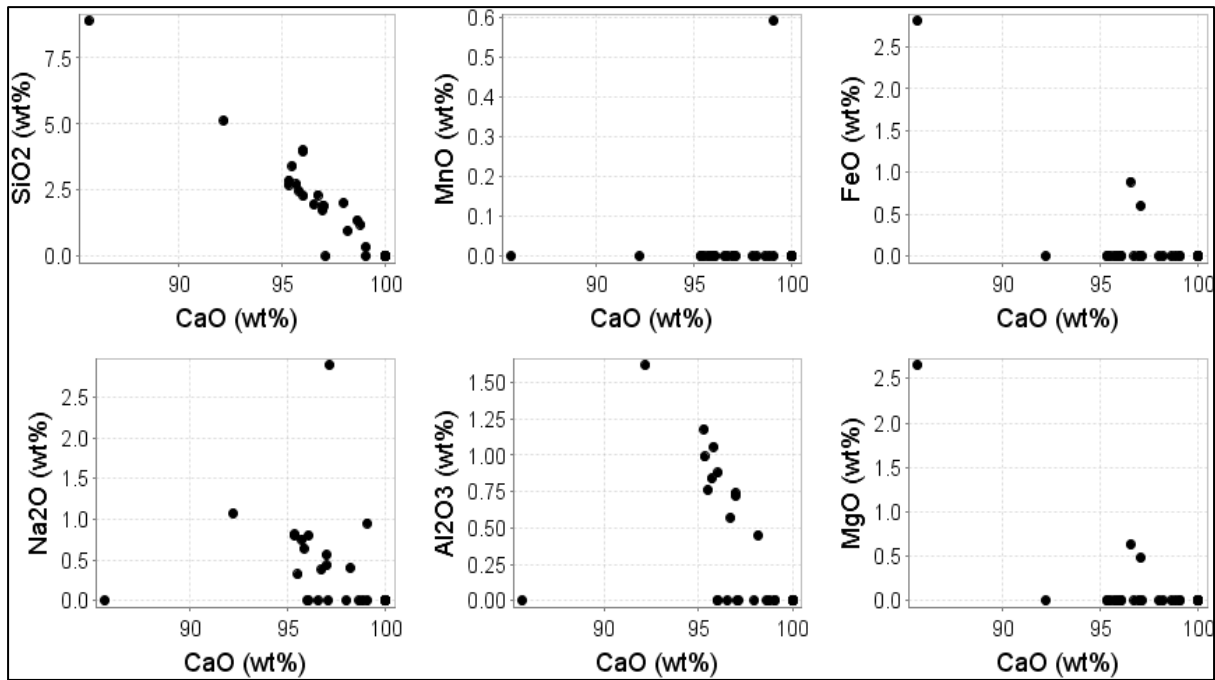
Figure 5.23. Composition plots for D_3 (stage 4) carbonates in quartz-feldspar mylonite (samples THM55 and THM51C) showing it mostly consists of pure calcite which locally contains small inclusions of albite (resulting in elevated Na_2O, SiO_2, Al_2O_3 values).

5.3.4. Composition of silicate minerals from the intensely silicified unit

The silicate minerals selected for geochemical analyses in the intensely silicified unit (the Hanging wall quartzite, sample TH137) include chlorite$_2$ and epidote that formed during D_3 - stage 2 hydrothermal events. Their mineral composition will be discussed below.

Chlorite$_2$ in sample TH137 mainly consists of picnochlorite, and contains 26.6-30.9% SiO_2, 16.7-19.1% Al_2O_3, 17.6-28.6% FeO_{total}, and 13.4-20.6% MgO. It locally contains minor Na_2O (<0.5%; Fig. 5.24, Appendix 6) which may reflect micro inclusions of albite.

The composition of *epidote* is relatively constant with a little variation in SiO_2 (36.8-40.2%), Al_2O_3 (21.2-25 %), Fe_2O_3 (12.2- 18.3 %) and CaO (20.4-23.4%; Fig. 5.25; Appendix 6). The least Fe-rich epidote in the analyzed group also contains 0.3% MnO. In addition, some analyses for epidote grains return minor K_2O (0.2-0.3%), Na_2O (0.2%) and MnO (0.3%; Fig. 5.25; Appendix 6), probably reflecting fine inclusions of mica and Mn-bearing minerals.
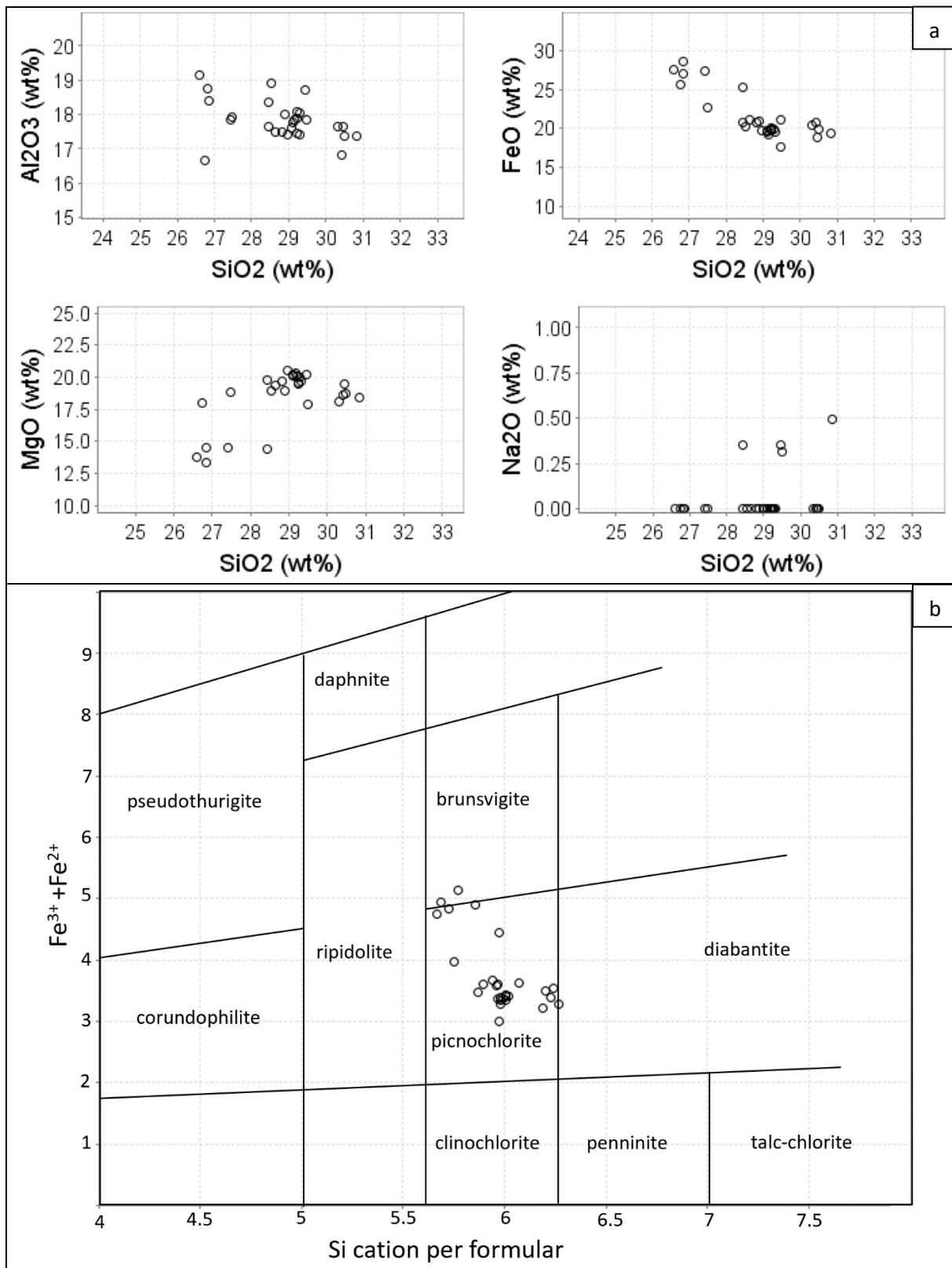
Figure 5.24. (a) Composition plots and (b) discrimination diagram (after Hey, 1954) for D₃ chlorites from intensely silicified unit (sample TH137).
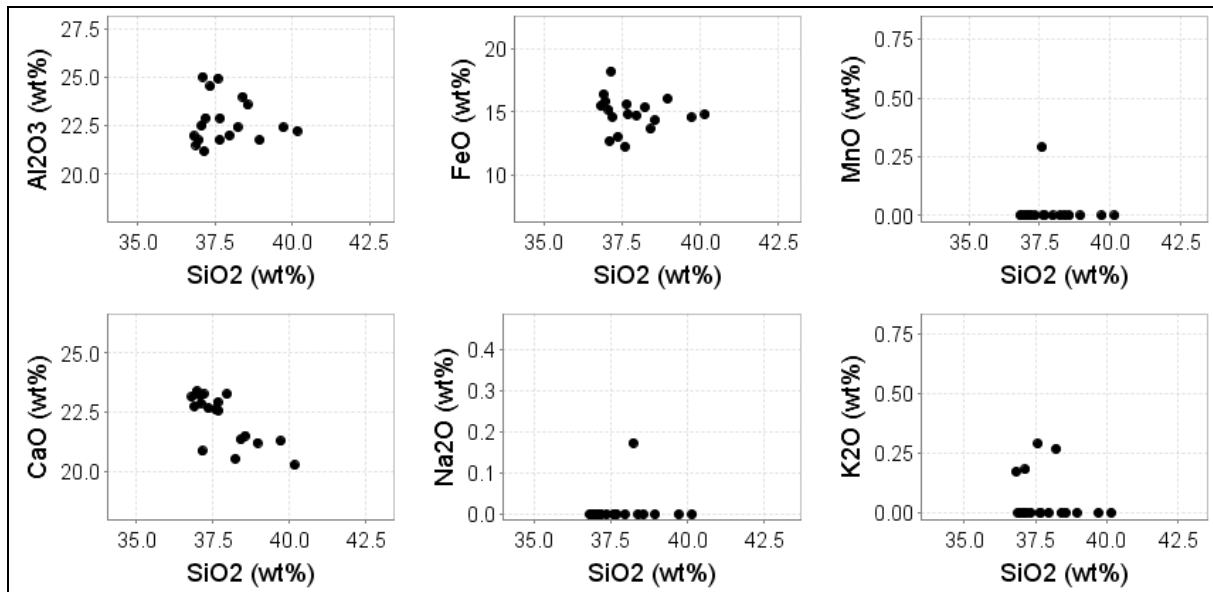
Figure 5.25. Composition plots for D₃ epidote from intensely silicified unit (sample TH137). The mineral is relatively constant in composition and consists of clinozoizite.

5.4. Geothermobarometry

Mineral geochemistry investigations in this study were mainly conducted using SEM techniques that do not have the same detection limit as EPMA. However, the data is adequate for identifying mineral types and textural variations. The EPMA technique was applied to limited number of analyses to examine the quantitative composition of mineral pairs selected for P-T estimates, and to check the precision of the SEM data. P-T estimates have been largely estimated based on the EPMA data only. However, considering the close similarity between EPMA and SEM results as shown above, semi-quantitative SEM data has been used to further constrain P-T estimates for non- or low-water-bearing minerals (i.e. garnet, feldspar, pyroxene and hornblende). Kohn and Spear (1999) have written a program named GTB which compiles calibrations for a wide range of classical geothermobarometers that can be applied to a range of bulk compositions. The latest version of GTB (provided in 2021) has been used for all P-T estimates in this study, except for T-estimates obtained from chlorite, for which calibrations presented by Cathelineau (1988) and Jowett (1991) were used.

5.4.1. Garnet-plagioclase-hornblende-quartz pressure estimates for sample TH99

The garnet-plagioclase-hornblende-quartz barometer was developed by Kohn and Spear (1989, 1990) and applied to metamorphic rocks including amphibolite. Kohn and Spear (1989) empirically calibrated barometers for this mineral assemblage involving parasite exchange reactions in amphibole. The uncertainty estimated for this calibration is 1-2 kbar, reflecting the variation in results from natural minerals that display minor compositional inhomogeneity (Kohn and Spear, 1990). Kohn and Spear (1990) generated additional calibrations using tschermakite (i.e. Fe-Mg) exchange reactions for the same

mineral assemblage in amphibole with an estimated uncertainty of 0.5-1 kbar (Kohn and Spear, 1990). The peak metamorphic amphibolite in sample TH99 has a near-identical composition and mineral assemblage, as those used for the P-estimates in both calibrations. Thus, the calibration of Kohn and Spear (1990) using the tschermakite exchange reaction was applied to estimate P for D_{1-2} peak metamorphic conditions in the Tick Hill area.

The composition of garnet-plagioclase-hornblende groups used for the barometric study is presented in the Table 5.2, and the result of the P-estimates are shown in Fig. 5.26a. The Mg-endmember model yielded P-estimates of 6-7 kbar that are largely independent from T, whilst the Fe-endmember model yielded temperature dependent P-estimates of 6-8 kbar in the temperature range of 600-800°C. Estimates based on SEM results are similar (Fig. 5.26).

Table 5.2. Composition of garnet, plagioclase and amphibole from amphibolite (sample TH99) used for pressure estimates

	Sample	TH99-P1	TH99-P2	TH99-P3	TH99-P4	TH99-P5	TH99-P6
	Data type	EPMA	EPMA	SEM	SEM	SEM	SEM
Garnet	SiO2	37.82	37.82	37.46	37.46	37.37	37.35
	Al2O3	20.19	20.18	21.07	21.36	21.25	21.32
	FeOtt	31.57	30.45	31.57	31.17	30.94	31.09
	MnO	1.69	1.67	1.54	1.72	1.43	1.65
	MgO	3.58	3.76	4.11	3.62	3.91	3.63
	CaO	4.80	4.77	4.25	4.68	4.68	4.95
	Sum	99.65	98.65	100.00	100.01	99.58	99.99
	Si	3.03	3.05	2.98	2.98	2.97	2.97
	Al	1.90	1.92	1.97	2.00	1.99	2.00
	Fe3+	0.04	0.00	0.07	0.04	0.02	0.06
	Fe2+	2.08	2.07	2.02	2.04	2.04	2.01
	Mn	0.11	0.11	0.10	0.12	0.10	0.11
	Mg	0.43	0.45	0.49	0.43	0.46	0.43
	Ca	0.41	0.41	0.36	0.40	0.40	0.42
	Almandine	68.53	67.96	68.01	68.32	68.01	67.57
	Spessartine	3.78	3.74	3.48	3.89	3.21	3.74
	Pyrope	14.10	14.80	16.36	14.41	15.47	14.49
	Grossular	13.33	13.65	11.72	13.14	13.18	13.78
Plagioclase	Ab	58.76	57.95	55.20	55.57	56.94	57.58
	An	40.91	40.34	44.05	44.43	43.06	40.97
	Or	0.32	1.71	0.75	0.00	0.00	1.45
Amphibole	SiO2	39.86	39.92	37.49	38.71	39.41	39.21
	TiO2	0.82	0.90	0.25	0.24	1.09	0.83
	Al2O3	14.67	14.65	18.17	16.37	14.71	14.83
	FeO	20.87	21.59	21.63	21.39	21.04	21.35
	MnO	0.14	0.14	0.00	0.23	0.00	0.00
	MgO	6.64	6.76	5.05	5.87	7.25	6.84
	CaO	10.50	10.55	11.30	11.01	10.28	10.88
	Na2O	1.91	1.92	1.65	1.74	1.66	1.61
	K2O	0.77	0.80	0.96	1.00	0.78	0.96
	Cl	1.18	1.16	1.71	1.42	1.33	1.24
	Sum	97.37	98.40	98.20	97.98	97.56	97.76
	Si	6.08	6.03	5.75	5.92	5.96	5.97
	Ti	0.09	0.10	0.03	0.03	0.12	0.10
	Al iv	1.92	1.97	2.25	2.08	2.04	2.03
	Al vi	0.72	0.63	1.04	0.87	0.58	0.63
	Fe3+	0.87	1.01	0.75	0.83	1.24	0.99
	Fe2+	1.79	1.72	2.02	1.90	1.42	1.73
	Mn	0.02	0.02	0.00	0.03	0.00	0.00
	Mg	1.51	1.52	1.16	1.34	1.63	1.55
	Ca	1.72	1.71	1.86	1.80	1.67	1.78
	Na	0.56	0.56	0.49	0.52	0.49	0.48
	K	0.15	0.15	0.19	0.19	0.15	0.19
	Cl	0.30	0.30	0.44	0.37	0.34	0.32
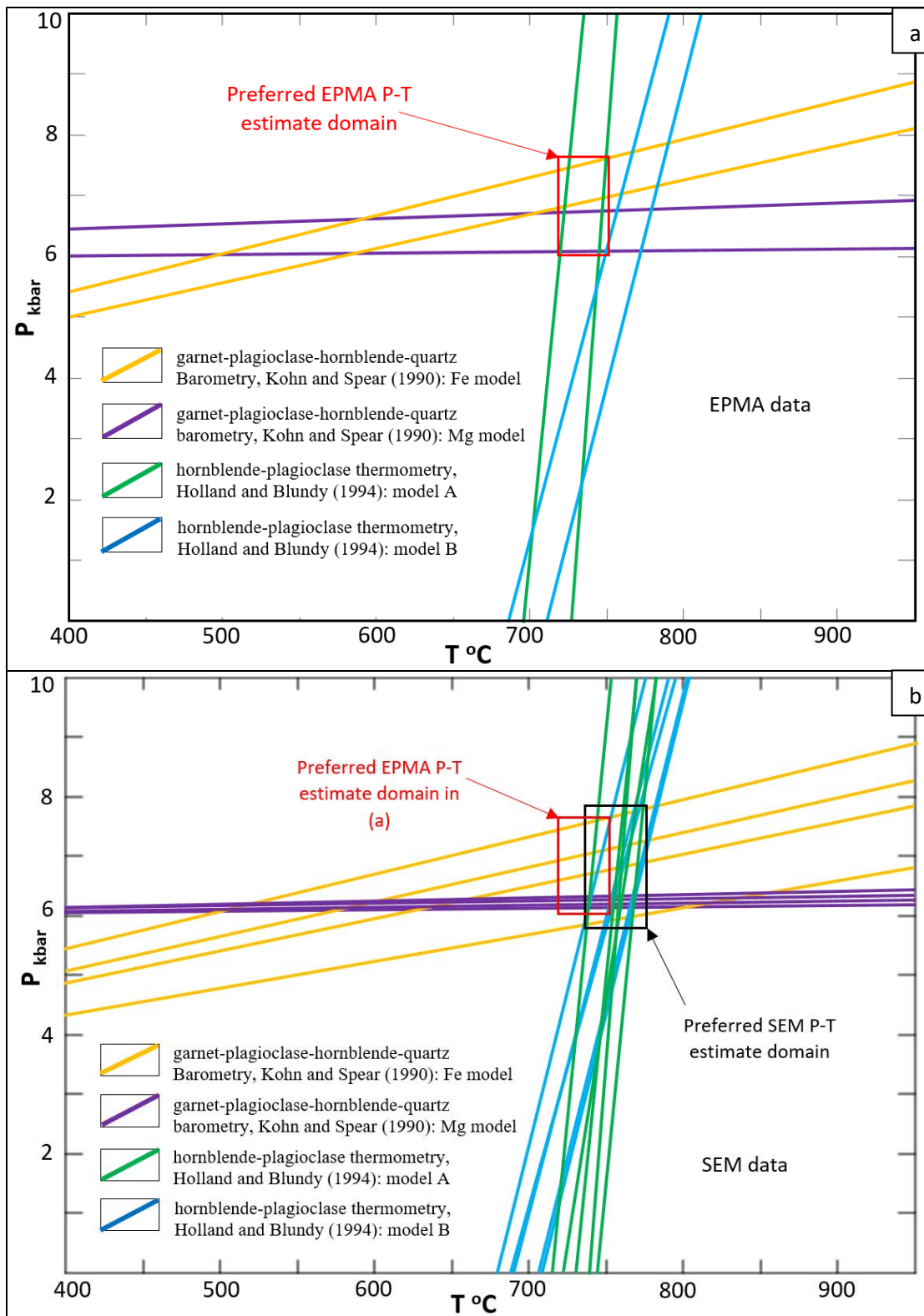
Figure 5.26. Garnet-plagioclase-hornblende-quartz P estimates (after Kohn and Spear, 1990) and hornblende-plagioclase T estimates (after Holland and Blundy, 1994) for peak metamorphic (D_{1-2}) assemblages in sample TH99. Figures (a) and (b) use composition estimates from EPMA and SEM data respectively. The preferred P-T estimates are 6.0-7.6 kbar at 720-750ºC based on EPMA data.

5.4.2. Hornblende-plagioclase geothermometry

The hornblende-plagioclase Fe-Mg exchange geothermometer was reviewed by Essene (1989), Spear (1993) and Anderson (1996). This thermometer was first developed by Spear (1980, 1981) based on hornblende-plagioclase pairs in metamorphic rocks. Blundy and Holland (1990), based on experimental and empirical data, formulated a calibration for the equilibrium reaction "edenite + 4 quartz = tremolite + albite" to account for non-ideal mixing in plagioclase, but this calibration was criticized by Poli and Schmidt (1992) for its imprecision. Holland and Blundy (1994) generated a revised calibration for the same equilibrium reaction (model A) and suggested that it should be applied to hornblende-plagioclase assemblages in quartz-bearing amphibolites. Holland and Blundy (1994) also formulated a new calibration for the equilibrium reaction "edenite + albite = richterite + anorthite" (model B) for hornblende-plagioclase assemblages in non-quartz bearing amphibolites. The model A calibration was used in study, because all samples from Tick Hill selected contain quartz. However, model B was tested to compare T-estimates with results generated using model A and other thermometry results, where available.

Hornblende-plagioclase T-estimates for sample TH99

The composition of hornblende-plagioclase pairs used for T-estimates is shown in Table 5.3. The result of EPMA and SEM T-estimates for hornblende-plagioclase pairs, using Holland and Blundy (1994) are shown in Fig. 5.26. T-estimates based on model A calibrations, yielded temperatures of 700-750°C over a wide range of pressures. In combination with the P-estimates discussed above, this results in a preferred T-P range (the intersection between the pressure estimate lines and temperature lines that were generated from EPMA data) of ~720-750°C and 6.0-7.6 kbar (Fig. 5.26a). The Holland and Blundy (1994) model B calibration is slightly more P-dependent and yields somewhat higher T-estimates in the same pressure range (Fig. 5.26a). Temperature estimates for EPMA and SEM results are similar (Fig. 5.26b).

Hornblende- plagioclase T-estimates for sample TH46

The composition of the hornblende-plagioclase pairs in this sample is shown in the Table 5.3 and the P-T estimates calculated using Holland and Blundy's (1994) models are shown in Fig. 5.27. Using the pressure estimates obtained from TH99, the preferred temperature range for EPMA data is 620-670°C. Estimates based on SEM results that include a wider range of retrograde amphibole compositions (Fig. 5.18), yield temperature estimates of 570-670°C (Fig. 5.27), which reflect peak conditions of ~670 °C and retrograde re-equilibration down to 570°C.
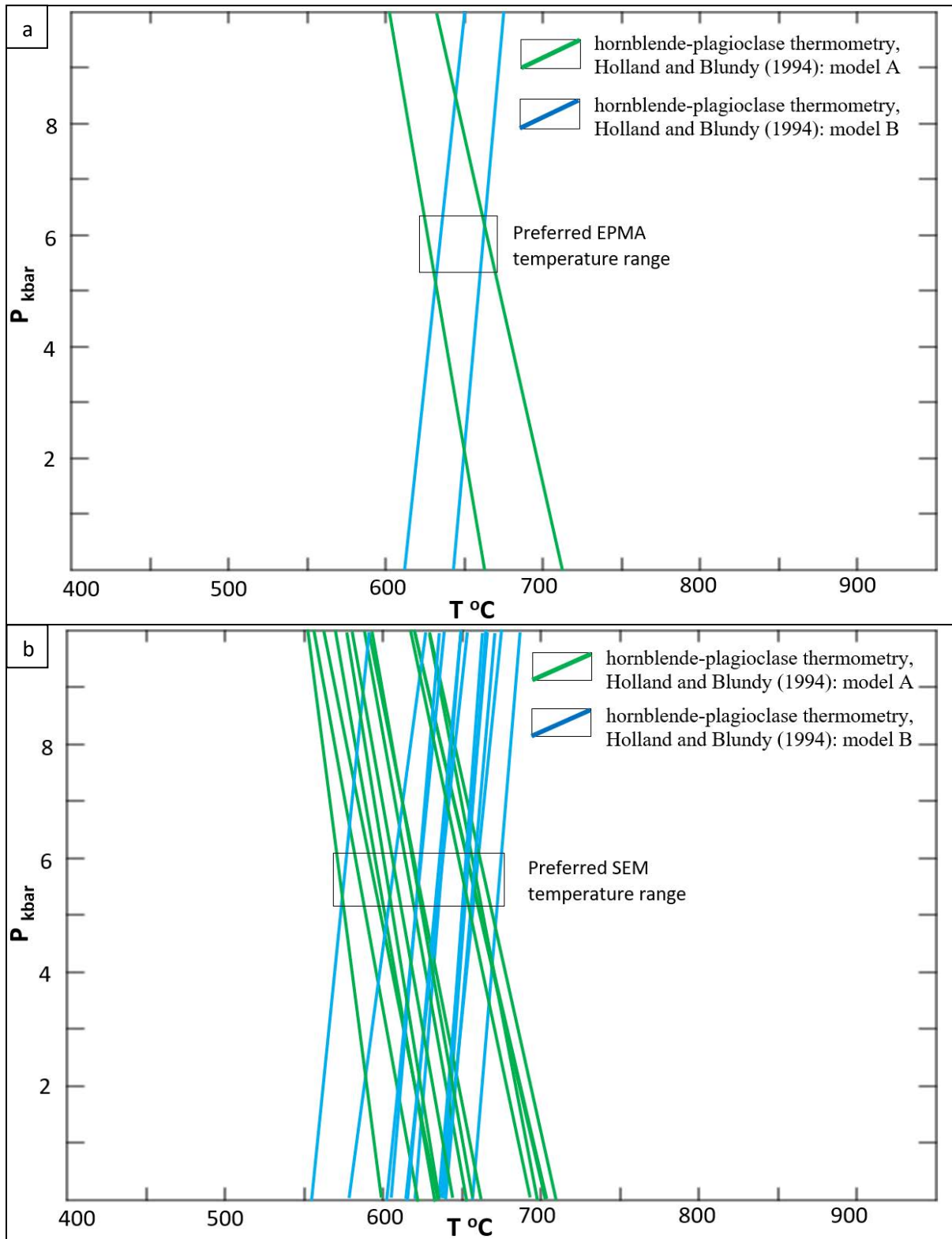
Figure 5.27. (a) EPMA-based and (b) SEM-based hornblende-plagioclase temperature estimates for the mineralized amphibole-rich calc-silicate unit (sample TH46) using Holland and Blundy's (1994) models A and B thermometers.

Table 5.3. Hornblende-plagioclase composition in amphibolite (sample TH99) and amphibole-rich calc-silicate (sample TH46) for temperature estimates

Sample	TH99-T1	TH99-T2	TH99-T3	TH99-T4	TH99-T5	TH99-T6	TH99-T7	TH46-T1	TH46-T2	TH46-T3	TH46-T4	TH46-T5
Data type	EPMA	EPMA	SEM	SEM	SEM	SEM	SEM	EPMA	EPMA	SEM	SEM	SEM
Amphibole												
SiO2	39.93	40.01	39.63	39.82	39.60	38.85	39.26	48.50	48.77	47.67	48.06	50.36
TiO2	0.80	1.01	0.89	0.79	0.87	0.41	0.88	0.12	0.11	0.00	0.00	0.11
Al2O3	14.62	14.44	14.67	14.45	14.51	15.67	14.83	6.93	6.84	7.42	6.99	5.45
FeO	20.87	20.88	21.56	21.73	21.57	21.51	21.52	14.97	13.88	14.84	14.32	12.93
MgO	6.71	6.90	6.47	6.36	6.65	6.24	6.47	13.79	13.87	13.28	13.87	15.00
MnO	0.18	0.16	0.00	0.00	0.00	0.23	0.00	0.15	0.16	0.12	0.20	0.16
CaO	10.21	10.32	10.75	11.28	10.87	10.99	10.95	11.59	11.57	11.68	11.58	11.86
Na2O	1.92	1.87	1.60	1.43	1.58	1.56	1.75	1.50	1.35	1.58	1.47	0.98
K2O	1.01	0.98	1.05	0.94	0.92	1.03	0.97	0.45	0.48	0.62	0.62	0.46
Cl	1.23	1.17	1.23	1.13	1.23	1.37	1.30	0.49	0.46	0.54	0.52	0.31
Sum	97.48	97.74	97.85	97.92	97.80	97.86	97.93	98.49	97.48	97.74	97.62	97.61
Si	6.08	6.07	6.04	6.08	6.04	5.93	6.00	7.01	7.10	6.98	7.01	7.26
Ti	0.09	0.12	0.10	0.09	0.10	0.05	0.10	0.01	0.01	0.00	0.00	0.01
Al iv	1.92	1.93	1.96	1.92	1.96	2.07	2.00	0.99	0.90	1.02	0.99	0.74
Al vi	0.70	0.65	0.68	0.69	0.64	0.75	0.67	0.19	0.27	0.27	0.21	0.19
Fe3+	0.94	0.95	0.89	0.75	0.93	0.96	0.83	0.68	0.53	0.52	0.63	0.51
Fe2+	1.72	1.70	1.86	2.03	1.82	1.79	1.92	1.13	1.16	1.30	1.12	1.05
Mn	0.02	0.02	0.00	0.00	0.00	0.03	0.00	0.02	0.02	0.01	0.02	0.02
Mg	1.52	1.56	1.47	1.45	1.51	1.42	1.48	2.97	3.01	2.90	3.02	3.22
Ca	1.67	1.68	1.76	1.85	1.77	1.80	1.79	1.79	1.80	1.83	1.81	1.83
Na	0.57	0.55	0.47	0.42	0.47	0.46	0.52	0.42	0.38	0.45	0.42	0.27
K	0.20	0.19	0.20	0.18	0.18	0.20	0.19	0.08	0.09	0.12	0.11	0.08
Cl	0.32	0.30	0.32	0.29	0.32	0.35	0.34	0.12	0.11	0.13	0.13	0.08
Plagioclase												
Ab	62.03	58.64	59.71	55.86	57.84	56.29	58.04	80.66	81.18	78.55	77.55	78.08
An	37.29	40.78	39.48	44.14	42.16	43.71	41.96	18.46	17.75	19.65	20.77	20.06
Or	0.67	0.59	0.81	0.00	0.00	0.00	0.00	0.88	1.07	1.80	1.69	1.86

5.4.3. Garnet-biotite geothermometry

Numerous calibrations for the garnet-biotite geothermometer exist that focus on the Fe-Mg exchange reaction between the two mineral phases (e.g. Thomson, 1976; Ferry and Spear, 1978; Hodges and Spear, 1982; Perchuk and Lavrent'eva, 1983; Berman, 1990). Many of these calibrations consider the concentration of not only Fe and Mg in garnet and texturally corresponding biotite, but also consider the influence of the concentration of Ca, Mn in garnet and Ti, Al^{vi} in biotite, which can affect the calibrations. The first experimental calibration was conducted by Ferry and Spear (1978) using the QFM buffer at 2.07 kbar in a simple KFMASH system with low Al in biotite. Hodges and Spear (1982) presented an alternative calibration by combining the solution models for garnet presented by Ganguly and Kennedy (1974) and Newton et al. (1977), and the revised Ferry and Spear (1978) calibration with the assumption of ideal mixing in biotite. This calibration was based on meta-pelitic rocks, and resulted in an estimated error range of ±15-25°C. Perchuk and Lavrent'eva (1983) generated a new experimental calibration using the Ni-NiO buffer at 6 kbar, natural garnet and high-Al biotite from metapelite but ignored the problem of non-ideal mixing in natural minerals. Berman (1990) developed a garnet-biotite thermometry that accounts for Ti and Al in biotite using a linear programing method, and he incorporated most of the available qualified experimental and natural data at time, excluding Perchuk and Lavrent'eva (1983).

Temperature-estimates for biotite-garnet pairs in TH99, are presented in Fig. 5.28, noting that most garnet-biotite calibrations are based on pelitic bulk compositions, and the garnet-biotite thermometer is susceptible to retrograde re-equilibration. Four calibration models (ie.: Ferry and Spear, 1978; Hodges and Spear, 1982; Perchuk and Lavrent'eva, 1983; and Berman,1990) were selected for the garnet-biotite T-calculations presented in this study. The composition of garnet-biotite pairs is presented in the Table. 5.4 and the T-estimates using the GTB program are shown in Fig. 5.29. All four calibrations are P insensitive. Assuming a preferred pressure range of 6-7.6 kb, the Perchuk and Lavrent'eva (1983) and Ferry and Spear (1978) calibration yield T-estimates of 625-655 °C and ~670-715 °C respectively, whilst Hodges and Spear (1982) and Berman (1990) calibrations provide T-estimates of ~717-760°C and ~725-770°C. The later estimates are consistent with hornblende-plagioclase temperature estimates (Fig. 5.26a).

Table 5.4. Garnet-biotite composition for amphibolite (sample TH99) obtained by the EPMA for temperature estimates.

Sample	Garnet				Biotite			
	TH99_T11	TH99_T12	TH99_T13	TH99_T14	TH99_T11	TH99_T12	TH99_T13	TH99_T14
SiO_2	37.75	37.75	37.75	37.80	36.25	33.99	35.21	34.68
TiO_2	0.02	0.02	0.02	0.00	1.68	1.2174	1.6107	1.3668
Al_2O_3	20.25	20.25	20.25	19.78	15.73	15.94	15.85	15.4
FeO	30.79	30.79	30.79	31.13	19.83	22.28	20.88	20.3
MnO	1.36	1.36	1.36	1.45	0.04	0.02	0.00	0.01
MgO	4.08	4.08	4.08	3.86	11.90	12.37	12.07	11.19
CaO	4.59	4.59	4.59	4.60	0.02	0.03	0.00	0.14
Na_2O	0.11	0.11	0.11	0.09	0.26	0.20	0.28	0.51
K_2O	0.03	0.03	0.03	0.02	8.49	6.27	7.72	7.79
Cl	0.01	0.01	0.01	0.01	1.10	0.81	0.98	1.14
Total	98.99	98.99	98.99	98.74	95.29	93.13	94.61	92.53
Si	3.03	3.03	3.03	3.05	5.52	5.35	5.43	5.50
Ti	0.00	0.00	0.00	0.00	0.19	0.14	0.19	0.16
Al iv	-	-	-	-	2.48	2.65	2.57	2.50
Al vi	-	-	-	-	0.34	0.31	0.31	0.38
Al	1.92	1.92	1.92	1.88	2.82	2.96	2.88	2.88
Fe^{3+}	0.01	0.01	0.01	0.01	-	-	-	-
Fe^{2+}	2.06	2.06	2.06	2.09	2.52	2.93	2.69	2.69
Mn	0.09	0.09	0.09	0.10	0.00	0.00	0.00	0.00
Mg	0.49	0.49	0.49	0.46	2.70	2.90	2.78	2.65
Ca	0.40	0.40	0.40	0.40	0.00	0.01	0.00	0.02
Na	-	-	-	-	0.08	0.06	0.08	0.16
K	0.00	0.00	0.00	0.00	1.65	1.26	1.52	1.58
Cl	0.00	0.00	0.00	0.00	0.28	0.22	0.26	0.31
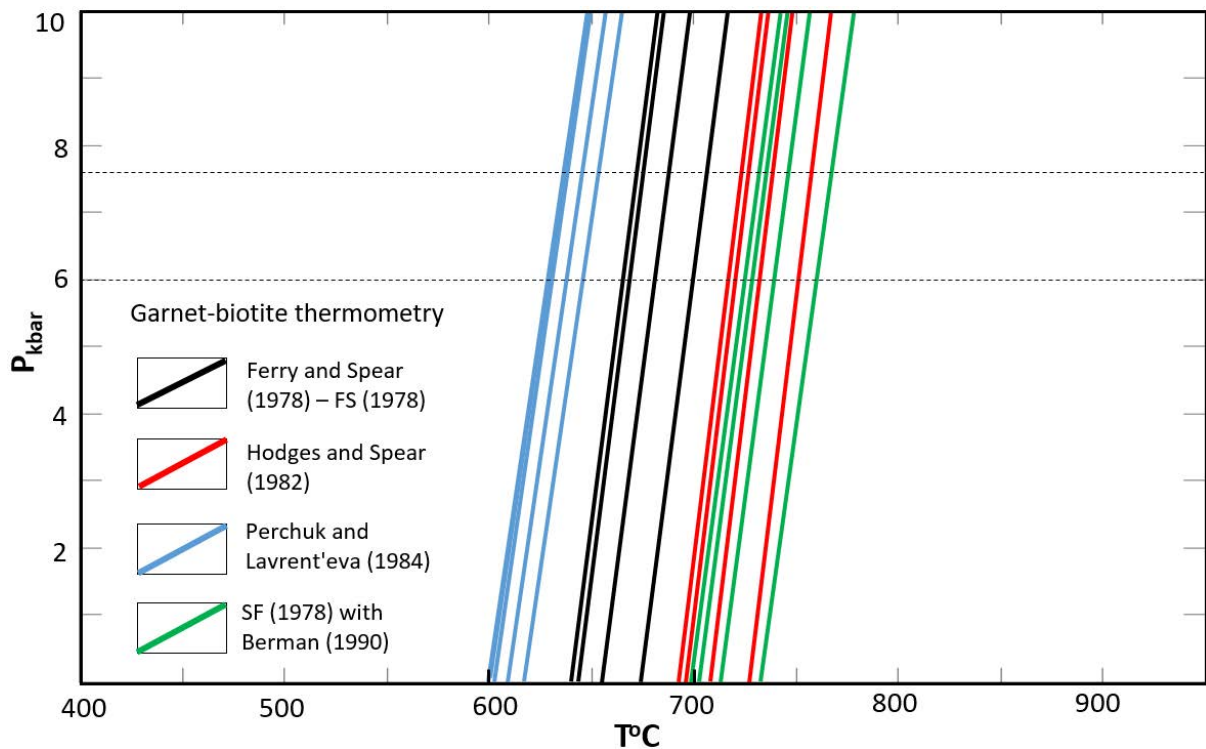
Figure 5.28. Temperature estimates based on the garnet-biotite [Fe-Mg]-exchange geothermometer using calibrations of Ferry and Spear (1978), Hodges and Spear (1982), Perchuk and Lavrent'eva (1983) and Berman (1990) for sample TH99 based on EPMA data.

5.4.4. Garnet-hornblende geothermometry

Garnet-hornblende Fe-Mg exchange geothermometers have been developed for over 40 years (e.g. Graham and Powell, 1984; Perchuk et al., 1985; Powell, 1985; Ravna, 2000). Among early calibrations, Graham and Powell's (1984) semi-empirical garnet-hornblende geothermometer using Fe-Mg exchange between garnet and hornblende from Ellis and Green (1979) is widely applied. This thermometer is applicable to hornblende-rich metamorphic rocks formed at low O_2 activity below 850°C and containing Mn-poor garnet, and can be applied to meta greywacke and mafic schist (Graham and Powell, 1984). Perchuk et al., (1985) presented the amphibole-garnet thermometry as a graph modifying the isotherm after Perchuk (1967, 1969 and 1970). More recently, Thomas and Rana (2020) applied three early models (i.e. Graham and Powell, 1984; Perchuk et al., 1985; Powell, 1985) and a later model developed by Ravna, (2000) to 79 samples collected from different metamorphic rocks and concluded that the calibration of Perchuk et al., (1985) is the most reliable for a wide range of metamorphic rocks, from greenschist to eclogite facies. Based on this test, the garnet-hornblende thermometry estimates for the peak metamorphic assemblage in sample TH99, has been calculated using the Perchuk et al. (1985) calibration, but the calibration from Graham and Powell (1984) was tested for comparison. As with other geotherbarometry estimates in this study, the calculation was completed using the updated 2021 version of Spear and Kohn's (1999) GTB program.

Three pairs of garnet-hornblende were selected for this thermometric estimate and their composition as determined by EPMA are presented in the Table. 5.5. The T estimates using Perchuk et al., (1985) calibration yielded a temperature range at ~590-615°C while T estimates using the Graham and Powell's (1984) calibration yielded a temperature range of ~565-585°C (Fig. 5.29). These temperature estimates are independent to the pressure and significantly lower compared to the T-estimates derived by hornblende-plagioclase and biotite-garnet thermometry (Fig. 5.26a).

Table 5.5. Garnet-amphibole composition from amphibolite (sample TH99) for temperature estimates.

	Garnet			Amphibole		
Sample	TH99_T8	TH99_T9	TH99_T10	TH99_T8	TH99_T9	TH99_T10
Data type	EPMA	EPMA	EPMA	EPMA	EPMA	EPMA
SiO2	37.81	37.73	37.80	39.94	40.32	39.99
TiO2	0.00	0.00	0.00	1.07	1.17	0.83
Al2O3	20.33	20.08	19.78	14.86	14.37	14.78
FeO	31.48	31.26	31.13	20.24	19.52	20.38
MnO	1.45	1.46	1.45	0.13	0.14	0.14
MgO	3.99	3.93	3.86	7.39	7.47	7.09
CaO	4.53	4.61	4.60	10.56	10.32	10.63
Na2O	0.05	0.15	0.09	1.95	1.75	1.93
K2O	0.03	0.04	0.02	1.01	1.13	0.91
Cl	0.00	0.01	0.01	1.27	1.22	1.35
Sum	99.68	99.26	98.74	98.42	97.40	98.04
Si	3.02	3.03	3.05	6.02	6.12	6.06
Ti	0.00	0.00	0.00	0.12	0.13	0.09
Al iv	-	-	-	1.98	1.88	1.94
Al vi	-	-	-	0.65	0.68	0.70
Al	1.91	1.90	1.88	2.64	2.57	2.64
Fe3+	0.04	0.04	0.01	0.92	0.85	0.85
Fe2+	2.06	2.06	2.09	1.63	1.63	1.73
Mn	0.10	0.10	0.10	0.02	0.02	0.02
Mg	0.48	0.47	0.46	1.66	1.69	1.60
Ca	0.39	0.40	0.40	1.70	1.68	1.73
Na	0.00	0.00	0.00	0.57	0.51	0.57
K	0.00	0.00	0.00	0.19	0.22	0.18
Cl	0.00	0.00	0.00	0.32	0.31	0.35
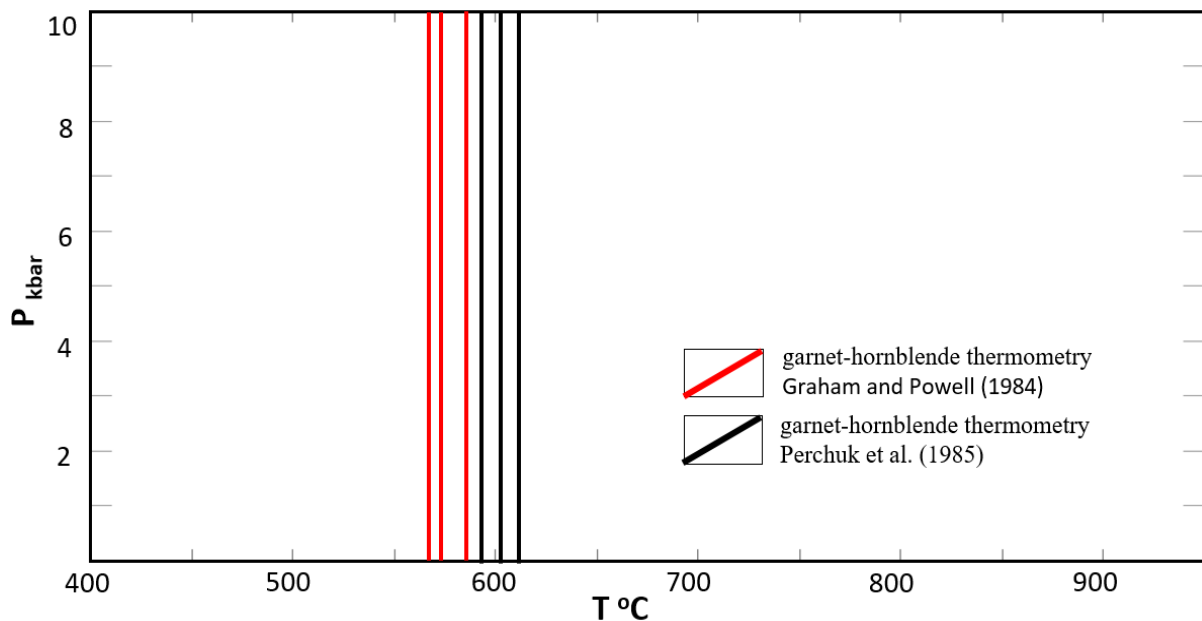
Figure 5.29 showing the garnet-hornblende thermometry results using calibrations from Graham and Powell (1984) and Perchuk et al. (1985) for sample TH99, based on compositional data obtained with the EPMA.

5.4.5. Chlorite thermometry

Chlorite thermometry has long been used in the study of alteration assemblages to constrain the temperature of mineralizing fluids, despite the lack of a buffering reaction (Essene, 2009). The chlorite empirical thermometer was firstly formulated by Cathelineau & Nieva (1985) and then revised by some researchers including Cathelineau (1988) and Jowett (1991). Details of chlorite thermometers have been presented in various reviews (e.g. Essene 2009; Inoue et al., 2009; Bourdelle & Cathelineau, 2015; Vidal et al., 2016). In general, Cathelineau and Nieva (1985) used the variation in Al^{IV} contents (based on 28 oxygen formula) in chlorite as a function of temperature, and Cathelineau (1988) revised this earlier calibration by reselecting chlorite samples for the experiment. Jowett (1991) used the Al^{IV} contents (based on 14 oxygen formula) of chlorite in combination with a Fe/(Fe+Mg) correction to reflect variations due to bulk composition and mineral reactions at changing conditions, and created a T-Al relationship as follows:

$$T°C= 318.5*(Al^{iv} +0.1Fe/(Fe+Mg)) - 68.7$$

The empirical chlorite thermometers are still widely used in ore deposit alteration studies in low-grade rocks (e.g. Laverne et al. 1995; Zang and Fyfe 1995; Gillis et al. 2001; Timpa et al. 2005; Moura et al. 2006; Esteban et al. 2007), despite being criticized for their reliability (e.g. Essene & Peacor,1995; Essene, 2009) or their applicability to metamorphic rocks (Vidal et al., 2006). In this study the chlorite thermometers of Cathelineau (1988) and Jowett (1991) have been applied to constrain the temperature ranges over which D_3 mineralization events took place.

The composition of chlorite based on EPMA and used for T estimates are shown in Table 5.6. Chlorite analyses and textural work identified three chlorite types ($chlorite_1$ to $chlorite_3$) with distinctive compositions (Fig. 5.21), of which $chlorite_1$ and $chlorite_3$ have the highest and lowest Al_2O_3 values respectively. The T estimates results using Cathelineau's (1988) and Jowett's (1991) calibration are plotted in Fig. 5.30. The estimated $T_{Jowett\,(1991)}$ is 280-385°C for $chlorite_1$, 160-270°C for $chlorite_2$ and 130-170°C for $chlorite_3$. The estimated $T_{Cathelineau\,(1988)}$ is 3-8°C lower than $T_{Jowett\,(1991)}$ for all three chlorite types. Collectively, the chlorite results show a near continuous temperature range of 130-380°C, reflecting retrograde re-equilibration as the various stages of D_3 alteration progressed.

Table 5.6. Composition of chlorite (chl) from quartz-feldspar mylonite obtained by the EPMA and chlorite thermometry estimates.

Oder	1	2	3	4	5	6	7	8	9	10	11	12	13	14	15	16
Sample	TH55	TH55	TH55	TH55	TH55	TH55	TH55	TH55	TH55	TH55	TH55	TH55	TH55	TH55	TH55	TH55
Analysis No	th55p-s1-7	th55p-s1-7b	th55p-s1-8	th55p-s1-9	th55p-s1-9b	th55p-s1-10	th55p-s5-ch1	th55p-s5-ch2	th55p-s5-ch3	th55p-s5-ch4	th55p-s5-ch6	th55p-s5-ch8	th55p-s5-ch9	th55p-s5-ch10	th55p-s5-ch13	th55p-s5-ch14
Chl type	chl1	chl1	chl1	chl1	chl1	chl1	chl1	chl1	chl1	chl1	chl1	chl1	chl1	chl1	chl1	chl1
SiO_2	25.88	26.08	28.19	28.13	28.14	27.01	26.92	27.07	26.02	26.52	25.62	26.40	27.30	27.41	28.06	27.70
TiO_2	0.05	0.10	0.03	0.07	0.00	0.03	0.00	0.12	0.00	1.16	0.04	0.53	0.25	0.77	1.28	0.16
Al_2O_3	21.09	21.32	19.27	19.57	19.53	20.72	20.63	19.52	20.08	19.20	20.66	18.71	18.93	18.91	17.77	19.33
FeO	30.08	29.45	24.43	24.62	24.13	29.74	29.73	24.61	28.39	26.29	28.88	27.15	24.17	23.89	23.12	25.81
MnO	0.88	0.87	0.26	0.26	0.39	1.34	1.52	0.38	1.36	1.09	0.85	1.21	0.21	0.23	0.21	0.28
MgO	11.54	11.64	16.50	16.75	16.47	11.90	11.52	14.97	11.59	11.82	11.21	11.88	15.38	14.61	15.32	14.82
CaO	0.00	0.00	0.02	0.01	0.03	0.03	0.01	0.05	0.03	1.10	0.06	0.59	0.22	0.77	1.31	0.15
Na_2O	0.00	0.00	0.02	0.00	0.00	0.00	0.02	0.00	0.03	0.00	0.03	0.05	0.02	0.01	0.03	0.04
K_2O	0.01	0.00	0.01	0.01	0.01	0.00	0.01	0.01	0.00	0.01	0.02	0.03	0.03	0.04	0.04	0.03
Cl	0.06	0.05	0.01	0.02	0.01	0.03	0.03	0.01	0.02	0.03	0.05	0.04	0.02	0.02	0.03	0.02
Sum	89.61	89.52	88.74	89.44	88.71	90.82	90.39	86.75	87.52	87.23	87.47	86.58	86.53	86.66	87.17	88.34
Cation per formula (28O)																
Si	5.47	5.49	5.80	5.75	5.78	5.61	5.62	5.72	5.60	5.66	5.52	5.71	5.77	5.77	5.86	5.77
Al iv	2.53	2.51	2.20	2.25	2.22	2.39	2.38	2.28	2.40	2.34	2.48	2.29	2.23	2.23	2.14	2.23
Al vi	2.73	2.79	2.48	2.47	2.52	2.69	2.71	2.59	2.70	2.52	2.78	2.51	2.50	2.49	2.26	2.53
Ti	0.01	0.02	0.01	0.01	0.00	0.00	0.00	0.02	0.00	0.19	0.01	0.09	0.04	0.12	0.20	0.02
Fe^{3+}	0.12	0.17	0.15	0.13	0.17	0.17	0.18	0.19	0.16	0.30	0.17	0.21	0.19	0.28	0.28	0.18
Fe^{2+}	5.20	5.01	4.05	4.08	3.98	4.99	5.01	4.16	4.95	4.39	5.04	4.71	4.09	3.93	3.76	4.31
Mn	0.16	0.15	0.04	0.04	0.07	0.24	0.27	0.07	0.25	0.20	0.16	0.22	0.04	0.04	0.04	0.05
Mg	3.63	3.65	5.06	5.10	5.04	3.68	3.58	4.71	3.72	3.76	3.60	3.83	4.84	4.59	4.77	4.60
Ca	0.00	0.00	0.00	0.00	0.01	0.01	0.00	0.01	0.01	0.25	0.01	0.14	0.05	0.17	0.29	0.03
Na	0.00	0.00	0.01	0.00	0.00	0.00	0.01	0.00	0.03	0.00	0.03	0.04	0.02	0.01	0.03	0.03
K	0.01	0.00	0.01	0.00	0.00	0.00	0.01	0.01	0.00	0.01	0.01	0.01	0.02	0.02	0.02	0.02
Total	19.85	19.79	19.81	19.84	19.79	19.79	19.78	19.76	19.81	19.62	19.80	19.76	19.77	19.66	19.65	19.79
T^{o}C_Ca.	346	343	293	301	296	323	321	306	325	315	337	306	297	296	282	297
Cation per formula (14O)_Jowett (1991)																
Fe+2	2.60	2.51	2.02	2.04	1.99	2.50	2.51	2.08	2.47	2.19	2.52	2.35	2.04	1.97	1.88	2.16
Mg	1.82	1.82	2.53	2.55	2.52	1.84	1.79	2.36	1.86	1.88	1.80	1.92	2.42	2.29	2.39	2.30
Al^{IV}	1.32	1.32	1.15	1.17	1.15	1.25	1.25	1.19	1.26	1.22	1.30	1.20	1.16	1.16	1.11	1.16
T^{o}C_Jo.	354	351	297	305	299	331	329	310	333	321	345	313	302	301	286	302

Table 5.6.*Composition of chlorite (chl) from quartz-feldspar mylonite obtained by the EPMA and chlorite thermometry estimates (cont.).*

Oder	17	18	19	20	21	22	23	24	25	26	27	28	29	30	31	32
Sample	THM22	THM22	THM22	THM22	THM22	THM22	TH55	TH55	TH55	TH55	TH55	TH55	TH55	TH55	TH55	TH55
Analysis No	thm22p-s8-ch2	thm22p-s10-sp84	thm22p-s10-sp86	thm22p-s10-sp89	thm22p-s9-sp54	thm22p-s9-sp55	th55p-s15-ch1	th55p-s15-ch2	th55p-s15-ch3	th55p-s15-ch4	th55p-s15-ch5	th55p-s16-sp193	th55p-s16-sp192	th55p-s16-sp191	th55p-s16-sp194	th55p-s18-sp200
Chl type	chl1	chl1	chl1	chl1	chl2	chl2	chl2	chl2	chl2	chl2	chl2	chl2	chl2	chl2	chl2	chl2
SiO_2	24.88	24.57	24.80	27.18	31.65	31.18	32.30	32.06	30.49	30.33	32.07	28.44	28.46	28.85	27.88	29.95
TiO_2	0.16	0.07	0.01	0.16	0.00	0.00	0.07	0.04	0.00	0.02	0.01	0.62	0.63	0.73	1.22	0.03
Al_2O_3	21.51	22.06	21.86	18.19	16.64	16.20	13.74	13.33	14.36	13.85	13.78	16.40	16.18	16.56	16.78	14.28
FeO	34.88	28.98	31.55	29.79	25.51	26.09	21.81	22.36	24.93	24.05	21.20	26.87	26.87	27.88	25.06	23.36
MnO	0.43	0.16	0.19	0.29	0.22	0.21	0.07	0.10	0.11	0.08	0.06	0.26	0.27	0.27	0.47	0.08
MgO	8.12	11.88	10.25	11.85	12.71	13.13	18.98	18.96	15.89	15.72	19.26	13.50	13.83	13.85	13.30	16.34
CaO	0.01	0.01	0.03	0.04	0.13	0.12	0.09	0.09	0.12	0.07	0.07	0.11	0.23	0.24	0.81	0.17
Na_2O	0.02	0.04	0.04	0.00	0.04	0.04	0.12	0.09	0.20	0.20	0.08	0.08	0.04	0.04	0.05	0.09
K_2O	0.02	0.02	0.02	0.08	0.97	0.56	0.17	0.18	0.19	0.25	0.19	0.43	0.30	0.32	0.24	0.13
Cl	0.07	0.14	0.10	0.03	0.00	0.01	0.03	0.03	0.08	0.07	0.03	0.19	0.15	0.11	0.30	0.02
Sum	90.12	87.95	88.84	87.62	87.87	87.55	87.38	87.3	86.37	84.68	86.75	86.91	86.96	88.86	86.17	84.45
Cation per formula (28O)																
Si	5.36	5.27	5.32	5.84	6.52	6.48	6.61	6.61	6.45	6.52	6.59	6.08	6.08	6.05	5.98	6.44
Al iv	2.64	2.73	2.68	2.16	1.48	1.52	1.39	1.39	1.55	1.48	1.41	1.92	1.92	1.95	2.02	1.56
Al vi	2.83	2.85	2.87	2.47	2.62	2.50	1.95	1.86	2.06	2.06	1.96	2.24	2.18	2.17	2.26	2.08
Ti	0.03	0.01	0.00	0.03	0.00	0.00	0.01	0.01	0.00	0.00	0.00	0.10	0.10	0.12	0.20	0.01
Fe^{3+}	0.13	0.07	0.10	0.20	0.52	0.48	0.29	0.23	0.23	0.27	0.28	0.22	0.22	0.21	0.32	0.26
Fe^{2+}	6.16	5.13	5.57	5.16	3.88	4.06	3.45	3.62	4.18	4.06	3.37	4.58	4.58	4.68	4.18	3.94
Mn	0.08	0.03	0.03	0.05	0.04	0.04	0.01	0.02	0.02	0.01	0.01	0.05	0.05	0.05	0.09	0.02
Mg	2.61	3.80	3.28	3.80	3.90	4.07	5.79	5.82	5.01	5.04	5.90	4.30	4.41	4.33	4.26	5.23
Ca	0.00	0.00	0.01	0.01	0.03	0.03	0.02	0.02	0.03	0.02	0.02	0.03	0.05	0.05	0.19	0.04
Na	0.02	0.03	0.03	0.00	0.04	0.03	0.10	0.07	0.16	0.17	0.07	0.07	0.03	0.03	0.04	0.07
K	0.01	0.01	0.01	0.04	0.51	0.30	0.09	0.10	0.10	0.14	0.10	0.24	0.16	0.17	0.13	0.07
Total	19.85	19.93	19.89	19.77	19.53	19.50	19.69	19.75	19.79	19.76	19.70	19.82	19.79	19.80	19.66	19.71
T°C_Ca.	364	378	369	285	176	182	162	162	187	176	164	247	247	252	263	190
Cation per formula (14O)_Jowett (1991)																
Fe^{+2}	3.08	2.56	2.78	2.58	1.94	2.03	1.72	1.81	2.09	2.03	1.68	2.29	2.29	2.34	2.09	1.97
Mg	1.30	1.90	1.64	1.90	1.95	2.04	2.89	2.91	2.51	2.52	2.95	2.15	2.20	2.17	2.13	2.62
Al^{IV}	1.39	1.42	1.40	1.14	0.79	0.81	0.73	0.73	0.82	0.78	0.74	1.01	1.01	1.03	1.06	0.82
T°C_Jo.	375	385	378	293	183	189	165	165	192	181	167	254	253	258	268	194

Table 5.6.Composition of chlorite (chl) from quartz-feldspar mylonite obtained by the EPMA and chlorite thermometry estimates (cont.).

Oder	33	34	35	36	37	38	39	40	41	42	43	44	45	46	47	48	49
Sample	TH55	TH55	TH55	TH55	TH55	TH55	TH55	TH55	TH55	TH55	TH55	TH55	TH55	TH55	TH55	TH55	TH55
Analysis No	th55p-s18-sp201	th55p-s18-sp202	th55p-s18-sp203	th55p-s18-sp204	th55p-s18-sp205	th55p-s17-ch1	th55p-s17-ch2	th55p-s17-ch3	th55p-s20-177	th55p-s20-178	th55p-s20-179	th55p-s20-180	th55p-s20-181	th55p-s20-182	th55p-s20-183	th55p-s20-184	th55p-s20-185
Chl type	chl2	chl2	chl2	chl2	chl2	chl2	chl2	chl2	chl3	chl3	chl3	chl3	chl3	chl3	chl3	chl3	chl3
SiO2	30.07	30.05	30.51	30.29	30.53	30.52	30.13	30.26	33.87	34.72	33.22	32.84	34.05	33.64	33.70	34.00	34.95
TiO2	0.09	0.12	0.10	0.00	0.03	0.08	0.00	0.05	0.01	0.04	0.02	0.01	0.07	0.10	0.05	0.09	0.69
Al2O3	14.24	14.38	14.60	14.68	14.47	14.23	14.32	15.03	13.99	13.99	13.38	14.77	13.85	13.88	13.73	13.76	12.99
FeO	24.55	23.27	23.95	23.45	23.99	23.99	24.44	23.96	12.97	14.73	15.08	15.01	14.92	15.76	14.72	11.55	10.42
MnO	0.12	0.10	0.12	0.10	0.14	0.09	0.07	0.10	0.05	0.03	0.07	0.14	0.13	0.09	0.07	0.09	0.12
MgO	16.11	15.97	16.93	16.49	16.94	15.92	15.96	16.68	25.60	23.10	22.41	23.29	23.08	22.31	23.27	26.41	26.36
CaO	0.09	0.10	0.10	0.09	0.09	0.11	0.13	0.10	0.18	0.16	0.19	0.15	0.16	0.19	0.14	0.18	0.75
Na2O	0.08	0.08	0.05	0.07	0.08	0.08	0.05	0.08	0.20	0.18	0.22	0.14	0.12	0.19	0.24	0.18	0.15
K2O	0.12	0.18	0.19	0.21	0.16	0.21	0.21	0.19	0.11	0.25	0.20	0.06	0.12	0.23	0.15	0.07	0.08
Cl	0.02	0.02	0.02	0.01	0.02	0.03	0.02	0.01	0.18	0.14	0.15	0.13	0.11	0.14	0.15	0.16	0.14
Sum	85.50	84.26	86.57	85.41	86.45	85.27	85.34	86.47	87.16	87.36	84.94	86.55	86.61	86.52	86.22	86.50	86.66
Cation per formula (28O)																	
Si	6.42	6.46	6.41	6.43	6.42	6.50	6.44	6.36	6.64	6.80	6.74	6.55	6.75	6.72	6.72	6.66	6.78
Al iv	1.58	1.54	1.59	1.57	1.58	1.50	1.56	1.64	1.36	1.20	1.26	1.45	1.25	1.28	1.28	1.34	1.22
Al vi	2.03	2.13	2.04	2.13	2.03	2.10	2.07	2.10	1.89	2.06	1.97	2.04	2.01	2.01	1.97	1.86	1.78
Ti	0.01	0.02	0.02	0.00	0.01	0.01	0.00	0.01	0.00	0.01	0.00	0.00	0.01	0.01	0.01	0.01	0.10
Fe3+	0.24	0.31	0.24	0.27	0.23	0.31	0.25	0.23	0.25	0.44	0.35	0.30	0.41	0.37	0.34	0.27	0.40
Fe2+	4.15	3.87	3.97	3.89	3.99	3.96	4.12	3.98	1.87	1.98	2.21	2.20	2.07	2.26	2.13	1.62	1.29
Mn	0.02	0.02	0.02	0.02	0.03	0.02	0.01	0.02	0.01	0.00	0.01	0.02	0.02	0.01	0.01	0.02	0.02
Mg	5.13	5.12	5.30	5.22	5.31	5.05	5.09	5.23	7.48	6.74	6.78	6.92	6.82	6.64	6.91	7.71	7.63
Ca	0.02	0.02	0.02	0.02	0.02	0.02	0.03	0.02	0.04	0.03	0.04	0.03	0.03	0.04	0.03	0.04	0.16
Na	0.07	0.07	0.04	0.06	0.06	0.07	0.04	0.07	0.15	0.14	0.18	0.11	0.10	0.15	0.19	0.14	0.11
K	0.07	0.10	0.10	0.12	0.09	0.11	0.12	0.10	0.06	0.13	0.10	0.03	0.06	0.12	0.08	0.04	0.04
Total	19.74	19.65	19.75	19.72	19.76	19.66	19.73	19.76	19.75	19.53	19.65	19.66	19.53	19.62	19.65	19.71	19.53
TᵒC_Ca.	192	186	195	191	192	180	189	202	158	131	140	172	140	145	145	153	134
Cation per formula (14O)_Jowett (1991)																	
Fe+2	2.07	1.93	1.98	1.95	2.00	1.98	2.06	1.99	0.94	0.99	1.11	1.10	1.03	1.13	1.06	0.81	0.65
Mg	2.56	2.56	2.65	2.61	2.66	2.53	2.54	2.61	3.74	3.37	3.39	3.46	3.41	3.32	3.46	3.86	3.81
Al^{IV}	0.83	0.81	0.84	0.83	0.83	0.79	0.82	0.86	0.70	0.62	0.65	0.75	0.65	0.67	0.66	0.69	0.62
TᵒC_Jo.	197	191	199	196	196	184	194	206	155	130	139	171	138	144	143	150	130
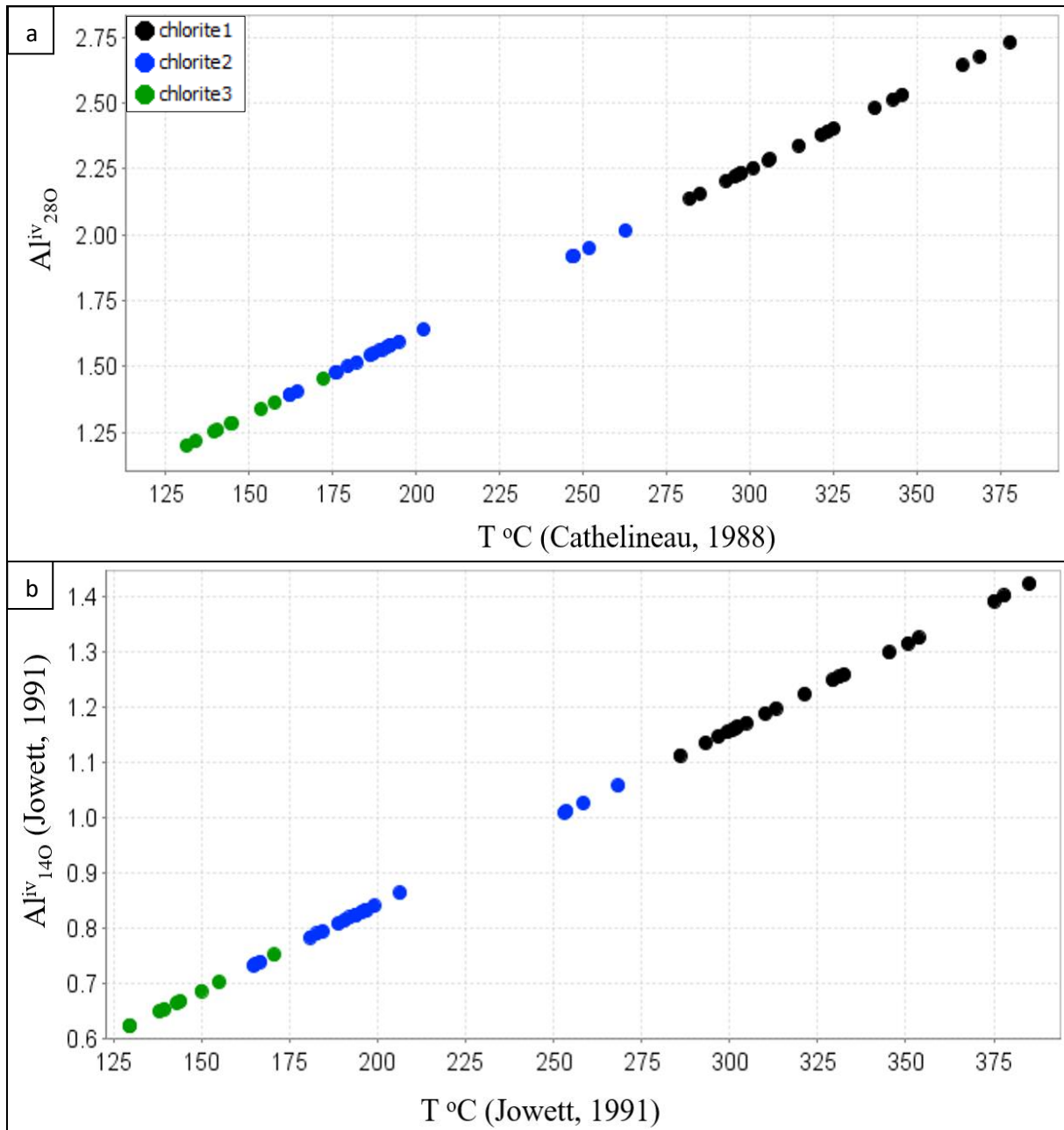
Figure 5.30. Temperature estimates for D3 based on chlorite geothermometry using calibrations of (a) Cathelineau (1988) and (b) Jowett (1991) for chlorite alteration hosted in quartz-feldspar mylonite at Tick Hill (samples TH55 and THM22).

5.5. Discussion

5.5.1. Mineralogy

Most gold grains measured are pure gold, except for a few, fine-grained gold grains that contain minor silver and copper. In most gold deposits, high Au/Ag ratios reflect medium- to high temperatures of mineralization (e.g. Huston et al.,1992). Gold is not associated with many other metals, based on the assay data set of the deposit, and this study. However other metals do occur in the deposit in association with sulphides and selenides, which mostly formed during the later stages of D_3. Selenides include

bismuth selenide and a range of fine-grained Bi-Pb-Cu selenide minerals with variable composition. Most sulphides (i.e. pyrite, pyrrhotite and chalcopyrite) that formed during the later D_3 mineralization stages also commonly contain minor amounts of Se. The role of selenide minerals has been discussed in Chapter 2 and possibly reflects a relatively low (<300°C) mineralization temperature, at low lithostatic pressures (<1 kbar). If the inference of high formation temperatures for pure Au and low formation temperatures for the Se-bearing minerals are both correct at Tick Hill, these compositional constraints may reflect the occurrence of two discrete mineralizing events (i.e. pre-D_1 and D_3 mineralization) as discussed in Chapter 2. It also means that despite being remobilized during D_3 events, the pre-D_1 pure Au grains were mostly not contaminated by other elements.

The EPMA/SEM study confirms the pervasive replacement of oligoclase and K-feldspar by albite during D_3 in quartz-feldspar mylonite and other lithologies. It also confirms the presence of micro-grains of hematite inside albite and K-feldspar to give the altered rocks their characteristic orange to red coloration. It indicates that albite - K-feldspar - hematite alteration at Tick Hill occurred under oxidized conditions.

5.5.2. P-T estimates for peak metamorphic amphibolite

The geothermobarometry study for peak metamorphic amphibolite is based on P estimates for the garnet-plagioclase-hornblende-quartz assemblage and T-estimates for hornblende-plagioclase, garnet-hornblende and garnet-biotite assemblages. The preferred P range is defined by the intersection between the pressure estimate lines and temperature lines that were generated from EPMA data. The peak metamorphic pressure (syn-D_1) based on the Kohn and Spear's (1990) calibrations for mineral assemblages that are nearly identical in composition to those encountered in sample TH99, is estimated at 6-7 kbar. Among the geothermometers applied to the mineral assemblages described, the results generated using the Holland and Blundy (1994) hornblende-plagioclase (model A) calibration is preferred, because it was based on mineral assemblages and compositions (garnet-tschermakite-plagioclase-quartz) that are similar to the metamorphic amphibolite in sample TH99 from Tick Hill. Thus, the preferred P-T range for rocks in the Tick Hill area during D_1 is 6-7.6 kbar and 720-750°C (Fig. 5.26a). This high temperature of formation is compatible with the observed migmatisation in the surrounding gneiss. The P-T results generated on the basis of EPMA data is similar to the estimates generated from semi-quantitative SEM data. The obtained temperature range from hornblende-plagioclase thermometry is comparable with results obtained from garnet-biotite pairs from using the calibrations of Hodges and Spear (1982) and Berman (1990). The garnet-hornblende temperature estimates based on Graham and Powell (1984) and Perchuk et al. (1985) are 100-150°C lower than other estimates (Fig. 5.28). Considering that sample TH99 is compositionally very well equilibrated with little compositional variation in any of the mineral phases, and no evidence for significant retrograde

alteration or re-equilibration it is concluded that the T-estimates based on coexisting garnet-hornblende pairs is unreliable.

The P-T estimates for the garnet-bearing amphibolite ~800m N of Tick Hill indicates that evidence for high-grade metamorphism is only locally preserved in the area. In most places in and around the Tick Hill pit peak metamorphic assemblages are largely re-equilibrated and destroyed during later retrograde overprints, including hydrothermal alteration events.

5.5.3. Temperature estimates for D_{1-2} amphibole-rich calc-silicate and the distribution of gold

The preferred temperature range for the gold-rich calc-silicate unit that contains the D_{1-2} assemblage diopside-hornblende-plagioclase with retrograde actinolite is 620-670°C (Fig. 5.27). This temperature estimate is a little lower, but comparable to that obtained from the garnet-bearing amphibolite in sample TH99, which occurs only 800m N of Tick Hill pit, but which displays limited evidence of retrograde replacement or hydrothermal overprint. Although the diopside-hornblende assemblage is aligned in the dominant gneissic fabric, which is a composite D_{1-2} fabric, the lower T-estimate suggests that this gold-bearing calc-silicate re-equilibrated during the later retrograde stages of the D_{1-2} events, or was affected by the early stages of the D_3 overprint. The fact that retrograde actinolite locally occurs as zonal replacement of hornblende suggests pervasive fluid infiltration during the retrograde stages. Gold within this sample occurs texturally in two distinct ways. It firstly occurs as inclusions within both diopside and hornblende that are aligned in the gneissic fabric, which is consistent with similar observations reported by Choy (1994) and Tedman-Jones (2001). This gold occurs in parts of the metamorphic minerals that are homogenous in composition and preserve intact crystal lattice structures that are not affected by visible micro-fracturing. It includes gold inclusions that are contained within small hornblende grains, which themselves are enclosed within diopside aligned within the gneissic fabric. A second type of gold inclusions in the same peak metamorphic minerals occurs along fine micro-fractures either as trails of fine equant or irregularly-shaped grains or as fracture fill. In other words, calc-silicate sample TH46 clearly illustrates that gold was presented during early high-T events, and that the gold was partly remobilized during later lower-T events that involved micro-fracturing, which presumably occurred during D_3.

5.5.3. Themormetry estimates for D_3 chlorite alteration

The chlorite thermometry results track the evolving T conditions during the later stages of D_3. Results as shown in Figs. 5.22 and 5.30 indicate that the chlorite composition (as expressed in Al, Fe and Mg and Si) re-equilibrated near continuously as temperatures dropped during syn-D_3 retrogression. The texturally earlier types of chlorite, i.e. chlorite$_1$ and chlorite$_2$, display the greatest compositional range (Fig. 5.22), suggesting continuous re-equilibration as retrograde conditions and fluid infiltration

progressed during D_3. During the early parts of D_3, stage 1 hornblende formed as non-oriented overgrowths in some of the quartz-feldspar mylonite units. This suggests that temperature conditions during the stage 1 of D_3 must have exceeded 500 °C. During stages 2-3 the T estimate range obtained from the compositionally variable grains of chlorite$_{1-2}$ varies between 160-380°C, which coincided with the wide-spread infiltration of oxidizing hydrothermal fluids (Chapters 2, 6). The grains of chlorite$_3$ are compositionally more homogenous (Fig. 5.22) resulting in a much narrower range of T estimates of 130-170°C, which may have prevailed during D_3, stage 4. This suggests that stage 4 assemblages may represent a product of a distinct hydrothermal alteration event, characterized by a separate suite of alteration minerals including calcite and some of the Pb-Cu-Bi selenides. The T-estimates obtained from chlorite are consistent with the observed assemblages that formed during each of these stages, e.g. the presence of Bi-selenides during stages 2-4.
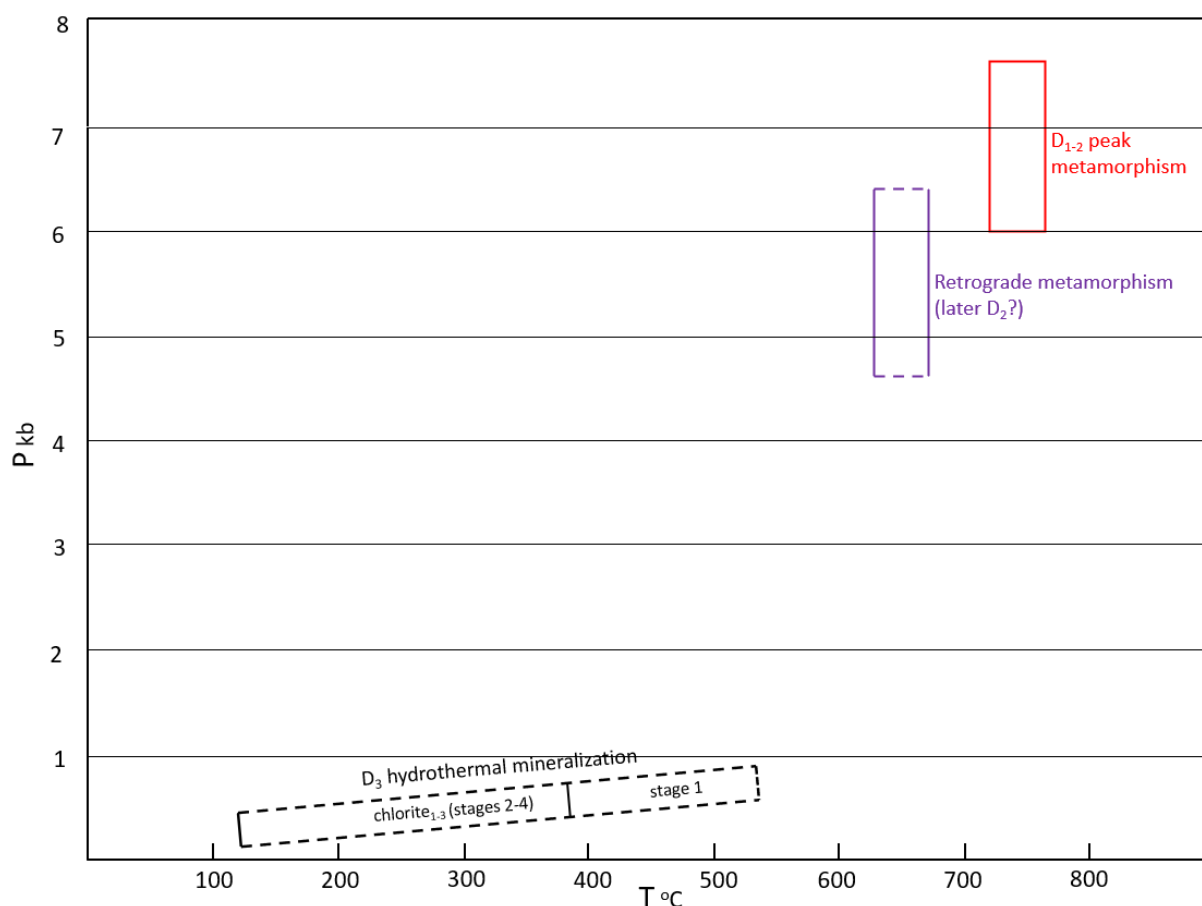
Figure. 5.31. P-T diagram for D_{1-3} metamorphism - hydrothermal events at Tick Hill Area. The pressure for retrograde metamorphism is unknown whilst the pressure for D_3 hydrothermal events is assumed based on the occurrences of bismuth selenide. The T estimates for D_3 events are based on the presence of hornblende during stage 1 and T estimates for chlorite$_{1-3}$ formed during stages 2-4.

Conditions during D_3 gold formation/remobilization can be tracked with chlorite thermometry in combination with P-T constraints imposed by mineral assemblages and the presence of Bi-selenides, as well as conditions obtained from oxygen isotope values in quartz (Chapter 6). Temperatures would

have peaked during stage 1 when hornblende-oligoclase-albite formed at temperatures of slightly over ~500ºC. During later D_3 alteration, temperatures would have gradually decreased from 380ºC to ~160ºC during stage 2 and stage 3, with a later low-temperature pulse during stage 4 when selenides precipitated with sulphides and calcite veins at conditions that may have been as low as ~130ºC. Thus, overall, the rocks track a clockwise P-T path travelling from the deep crust during early stages of D_1 deformation to the near surface towards the end of D_3, and their P-T estimates are summarized in the Fig. 5.31.

5.6. Conclusions

The chemical composition of mineral phases from Tick Hill help define the different mineral assemblages that formed during D_{1-3} events, and can be used in P-T estimates. Critical assemblages that were analyzed for P-T work include: (1) garnet (almandine+pyrope group)-plagioclase (andesine)-hornblende (tschermakite)-(Mg-) biotite-quartz-apatite-ilmenite in peak metamorphic amphibolite, which preserves D_{1-2} peak metamorphic conditions of ~720-750ºC, and ~6-7.6 kbar; (2) diopside-plagioclase (oligioclase)-scapolite - (Mg-) hornblende in amphibole-rich calc-silicate, which preserves peak metamorphism conditions of ~620-670ºC, and was affected by retrograde overprints; (3) relic D_{1-2} tschermakite hosted Au-rich quartz-feldspar mylonite; and (4) D_3 mineral assemblages for D_3 stages 2-4 mineralization and alteration events. The temperature estimates for the D_3 mineralization, based on chlorite thermometry, vary from 380ºC (stages 2) to 130ºC (stage 4). Metamorphic temperatures during D_3 stage 1, may have reached temperatures of >500ºC based on the presence of amphibole-oligoclase.

Geochemical analyses further confirm that: (1) all gold grains at Tick Hill, including D_{1-2} and D_3 gold, are pure (i.e. zero Ag) with the exception of rare D_3 gold grains containing minor Cu and Ag; (2) gold inclusions occur within D_{1-2} diopside, hornblende and scapolite; (3) D_3 albite-K-feldspar-oligoclase alteration minerals are hematite-dusted, which reflects the oxidized hydrothermal nature of the fluids that affected gold mineralization; and (4) many amphibole and chlorite grains are strongly zoned reflecting retrograde re-equilibration.

Chapter 6: An analysis of quartz oxygen isotope data from Tick Hill and surrounding rocks

Abstract

At Tick Hill, $\delta^{18}O_{quartz}$ results for host rocks to mineralization and surrounding lithologies are similar and fall within a narrow range of 10.5-13.7‰. The highly mineralized quartzo-feldspathic mylonite has $\delta^{18}O_{quartz}$ values of 11.3-13.6 ‰, which is similar to values for the surrounding rocks both locally and regionally. It means that the $\delta^{18}O_{quartz}$ by itself does not provide a useful exploration tool. These study results are similar to those from earlier $\delta^{18}O_{quartz}$ studies conducted at Tick Hill and the surrounding areas. The $\delta^{18}O_{quartz}$ results from the Tick Hill area most likely reflect fluid conditions at 1520-1525 Ma, during the late Isan hydrothermal overprint. The origin of the altering fluids is unclear, and the $\delta^{18}O_{quartz}$ values do not provide a conclusive answer, as they overlap with reported $\delta^{18}O$ values for both metamorphic and igneous fluids. When combining the $\delta^{18}O_{quartz}$ results with $\delta^{18}O_{calcite}$ results available from the literature, temperature estimates of 350-550ºC can be calculated-consistent with observed alteration assemblages that were associated with the mineralization.

6.1. Introduction

The Tick Hill deposit is a unique high-grade deposit with abundant free gold and only minor sulphide and carbonate alteration. The carbonate veins that occur in association with the ore body in the pit and drill core are texturally late, and not associated with the main stages of mineralization (see Chapters 2 and 3). Gold mineralization is concentrated along a highly strained shear zone between hangingwall and footwall quartzite units, and is characterized by partly annealed, D_{1-2}, blasto-mylonite that formed in quartz-feldspar and calcsilicate gneiss, and biotite-schist. The mineralized mylonites are associated with intense, D_3 silicification, which involved pervasive silica alteration as well as the emplacement of numerous, thin quartz veins both parallel and at high angles to the mylonitic layering. Apart from quartz veining, D_3 alteration was also associated with the emplacement of quartz-feldspar veins with extensive metasomatic haloes, and pegmatite veins (see Chapter 2 for details).

Gold at Tick Hill occurs towards the centre of a strongly silicified zone, and gold grains are commonly hosted inside quartz grains or intergrown with quartz that is distributed along the main mylonitic fabric. The paucity of sulphide and carbonate minerals in association with high-grade gold mineralization is a challenge to conduct a systematic S or C-O stable isotopic study of the Tick Hill deposit. Instead, we have focused on the collection of $\delta^{18}O$ data for quartz grains from rocks associated with the deposit, in line with earlier studies at Tick Hill (Choy, 1994; Hannan, 1994).

Oxygen isotope data for quartz can provide information on the source(s) of crustal fluids (Faure, 1986; Kleine et al., 2018). During the exploration stage, $\delta^{18}O_{quartz}$ studies at Tick Hill (Choy, 1994; Hannan, 1994) mostly focused on quartzite units and quartz veins that were linked to gold mineralization. These studies did not extensively sample the dominant lithologies in the Au-rich units (i.e. quartz-feldspar mylonite and intensely silicified units) and many of the common rock types in the area (e.g. syn- and post-tectonic intrusions, calc-silicate, amphibolite, late quartz veins). Quartzite ridges like the hanging wall quartzite were targeted, because they were interpreted as silicified D_1 shear zones that acted as conduit zones for mineralizing fluids, and it was hoped that quartz from these shears would provide a characteristic $\delta^{18}O$ isotope signature that could be used in exploration (e.g. Hannan, 1994). The $\delta^{18}O_{quartz}$ isotope data reported here includes quartz selected from Au-rich quartz-feldspar mylonite (the 'galahstone') and a variety of other rock types that occur in the immediate vicinity of the deposit. The study was aimed at obtaining $\delta^{18}O_{quartz}$ data to:

1. check and validate stable oxygen isotope data obtained during earlier studies;
2. determine if the highly mineralized zones are characterized by a specific $\delta^{18}O_{quartz}$ signature that is distinct from less altered distal host rocks;
3. ascertain whether significant differences exist between similar rock types of different ages (i.e. compare $\delta^{18}O_{quartz}$ results for early- syn- and late- tectonic rocks); and
4. determine a possible source for the $\delta^{18}O$ isotope signature in Au-bearing quartz.

6.2. Historical studies

In an MSc study of the Tick Hill deposit, Choy (1994) reports nine $\delta^{18}O_{quartz}$, six $\delta^{18}O_{whole\ rock}$, two $\delta^{18}O_{magnetite}$ and one $\delta^{18}O_{albite}$ values for samples from drill holes TH034 and TH076 (Table 6.1), with individual samples subdivided into peak-metamorphic, syn-D_1 samples and late-tectonic syn-D_3 samples. His sample descriptions are cursory, and he allocated samples to D_1 that are clearly affected by D_3 alteration, thus casting doubt on the validity of his D_1 - D_3 classification. He reported that the mineralized "galahstone" yielded a $\delta^{18}O_{whole\ rock}$ value of ~11.2‰. However, going through his data tables shows that samples for quartz that can be positively identified as being associated with mineralized galahstone returned an average $\delta^{18}O_{quartz}$ value of 12.3 ± 0.3 ‰ (n = 3), while quartz from altered calc-silicate rock in the immediate hanging wall of the deposit yield an average $\delta^{18}O_{quartz}$ value of 12.3 ± 0.7 ‰ (n = 6). Again, sample descriptions are poorly done and, in places, hard to interpret. He linked his results to a granite intrusion derived fluid that affected the galahstone but provided little evidence in support.

As part of an exploration targeting exercise, Hannan (1994) reports on data collected by Boda (1994). He focussed his study on the quartzite ridges and associated laminar quartz ribbons in the mineralised mylonite zones (Table 6.2). Hannan (1994) interpreted the quartz ridges as silicified D_1

decollement zones for which he expected a depleted $\delta^{18}O$ signature when compared to regional values. For 13 quartz samples he reported an average $\delta^{18}O_{quartz}$ value of 12.0 ± 0.6 ‰. He noted that there is little variation in average $\delta^{18}O_{quartz}$ values as a function of rock type or sample location (i.e. structural position). Hannan (1994) noted a reduced value of 10.3 ‰ for a gold-bearing quartz laminate sample interpreted as the main D_1 decollement zone, and suggested that this depleted value may indicate that the D_1 shear zones are generally characterized by slightly depleted $\delta^{18}O_{quartz}$ values, but hastened to add that more data is needed to confirm this result. He concluded that the narrow range of $\delta^{18}O_{quartz}$ values for quartz in the mine and the wider district indicates equilibration of the country rocks with a single fluid over a narrow temperature range, and attributed this to the homogenization of fluids at high metamorphic grades. The quartzites in the region do not possess a characteristic $\delta^{18}O$ signature that differentiates them from other rocks.

Table 6.1. $\delta^{18}O$ results for samples from Tick Hill reported by Choy (1994). Rock type descriptions and structural timing are based on Choy's (1994) original descriptions.

#	Sample ID	Rock type	Mineral	$\delta^{18}O$ (‰)	Timing	Description
1	76-150.15W	Quartz-feldspar mylonite	Whole rock	11.2	D_1	Whole rock (quartz-feldspar mylonite)
2	34-208.25	Quartz vein	Quartz	12.0	D_3	Vein quartz, 14m above Au zone
3	34-264.7Q	Quartz vein	Quartz	13.2	D_3	Quartz, from quartz vein, with sericitized plagioclase, chlorite and scapolite
4	76-176.2	Quartz vein	Quartz	11.7	D_3	From quartz in quartz vein in plagioclase-epidote
5	34-242.1	Quartz vein	Quartz	12.6	D_1	Clean quartz from quartz vein; with apatite and trace Au
6	34-234	Quartz vein	Quartz	12.4	D_1	Clean quartz from quartz vein; 7m above the ore zone
7	34-264.7B	Wall rock schist (calc-silicate ?)	Quartz	11.7	D_1	Quartz, from wall rock
8	76-148.7	Wall rock, schist	Quartz	12.3	D_1	Hand-picked quartz from wall rock in gold-bearing zone
9	76-150.32	Wall rock, schist (calc-silicate)	Quartz	12.9	D_1	Hand-picked quartz (plagioclase-amphibole-chlorite-epidote schist)
10	76-152.8W	Wall rock, (calc-silicate)	Whole rock	11.9	D_3	Whole rock (scapolite-amphibole schist, with sericitized scapolite and iron oxide stained amphibole
11	34-267.1W	Wall rock schist (calc-silicate)	Whole rock	9.3	D_1	Wall rock (scapolite-biotite-amphibole schist)
12	34-280W	Wall rock, schist (meta-pelite)	Whole rock	11.0	D_1	Whole rock (biotite-sillimanite-plagioclase-albite schist)
13	76--155W	Wall rock, schist (calc-silicate)	Whole rock	11.9	D_1	Whole rock; scapolite - amphibole - quartz rock
14	76-171W	Altered granite?	Whole rock	9	D_1	Whole rock, plagioclase-biotite-albite schist
15	34-221.55	Wall rock, schist	Magnetite	3.7	D_1	Hand pick magnetite in calc-silicate rocks above the ore zone
16	76-144.85	No information	Magnetite	11.6	D_1	Hand-picked magnetite
17	76-150.15Q	No information	Quartz	11.8	D_1	Quartz separate
18	34-220.7	No information	Albite	7.3	D_3	Albite separate

Table 6.2. $\delta^{18}O$ for samples from Tick Hill area as reported by Hanna (1994)

#	Sample ID	Rock type	Mineral	$\delta^{18}O$ (‰)	Description
1	MQ41066	Quartz-feldspar mylonite	Quartz	11.3	Ore-lode horizon with ribbon quartz, underground mining
2	MQ41072	Quartz-feldspar mylonite	Quartz	10.3	Underground mining, no info. of Au
3	MQ41061	Quartzite	Quartz	12.3	Foot wall quartzite, 100m N of open pit
4	MQ41063	Quartzite	Quartz	12.5	Hanging wall quartzite, 100m N of open pit
5	MQ41065	Quartzite	Quartz	12.2	Hanging wall quartzite, pit wall
6	MQ41064	Quartzite	Quartz	11.9	Hanging wall quartzite, 800m S of open pit
7	MQ41067	Quartzite	Quartz	11.7	At surveyor's Hill
8	MQ41068	Quartzite	Quartz	12.9	At Petticoat Ck, west ridge
9	MQ41070	Quartz ridge	Quartz	12.2	Quartz ridge, 2.5km S Tick Hill
10	MQ41071	Quartz ridge	Quartz	12.4	Quartz ridge, 2.5km S Tick Hill
11	MQ41065a	Wall rock	Quartz	12.1	Underground mine
12	MQ41062	Wall rock	Quartz	11.7	Amphibole-rich wall rock, 100m N of open cut
13	MQ41069	Granofels	Quartz	12.5	At Petticoat Ck, west ridge

Regional $\delta^{18}O_{calcite}$ values for the Mary Kathleen Domain (MKD) and interpretations of potential fluid sources were presented in Oliver et al. (1993, 1995). Oliver et al. (1993) provided a large dataset for $\delta^{13}C$ and $\delta^{18}O$ values from calcite pods and surrounding dolerite and calc-silicate rocks in the Corella Formation along the length of the MKD between Mt Godkin in the north and Trekalano mine in the south. The calcite pods are associated with albite-titanite-pargasite/actinolite- diopside (± chalcopyrite-pyrrhotite) alteration, and they were interpreted to be emplaced immediately after peak-metamorphism. This occurred during, or immediately after, D_2 during the formation of upright folds at metamorphic conditions of 530-570°C (calcite-dolomite geothermometry), which Oliver et al. (1993) interpreted as having occurred at ca. 1550 Ma. They calculated regional peak conditions at 530-630°C and 3-4 kbar for the area under investigation. Retrograde (syn-D_3) veins were also described. They were interpreted to form a continuum with D_2 veins, and occur in similar structural positions as the earlier veins, but are mineralized and associated with retrograde transitional greenschist-amphibolite facies assemblages. Oliver et al. (1993) also sampled late, D_4 quartz-calcite veins that occur in association with the large quartz veins and breccia zones along faults like the Fountain Range Fault in the central MKD. They found that the $\delta^{18}O_{calcite}$ values for the pods, and adjacent altered calc-silicate and meta-dolerite wall rock samples were similar along the length of the MKD and varied between 10.5-12.5 ‰ (with $\delta^{13}C_{calcite}$ ranging from -2 to -7 ‰). Away from the pods meta-dolerite wall rock samples yielded $\delta^{18}O_{whole-rock}$ values of 3.5-7.0 ‰, and unaltered calc-silicate and marble yielded heavier $\delta^{18}O_{calcite}$ values of 18-21 ‰ (with $\delta^{13}C_{calcite}$ ranging from -1.6 to -0.6 ‰), which they interpreted to be representative of $\delta^{18}O_{calcite}$ values for unaltered calc-silicate rock. The $\delta^{18}O_{calcite}$ results did not vary greatly as a function of host rock type, meaning that their isotope values probably did not result from the mixing of locally derived fluids, and they were not in isotopic equilibrium with the immediate host rocks. Rather, the homogenous $\delta^{18}O_{calcite}$ values were the result of infiltration of isotopically homogenous fluids that were not derived from the Corella formation exposed on surface today. The $\delta^{18}O_{calcite}$ values for D_4 veins were similar to

the values from the older veins. Oliver et al. (1993) and Oliver (1995) speculated that the ultimate source of the fluids could be crystallizing melts in the lower crust or upper mantle, with a minor component contributed by devolatilisation reactions in the calc-silicate and marble units to explain some of the local variations in isotopic compositions.

6.3. Methodology

A total of 39 quartz samples and one K-feldspar sample from different rock types at Tick Hill were selected for this $\delta^{18}O$ study (Fig. 6.1 and Table 6.3). The samples have been described in Table 6.3, and their sampling location is plotted in Figure 6.1. The samples reported here included 18 specimens of mineralized quartz-feldspar mylonite, with quartz obtained from either the mylonite fabric, or from thin quartz veins or lamellae that were emplaced parallel to the mylonitic fabric and locally resemble ribbon grains (e.g. Figs. 6.2a-f). Two samples of non-gold-bearing, D_3 quartz-feldspar veins that overprinted the intensely silicified units were taken to compare their oxygen isotopic values with those from the Au-bearing samples (e.g. Figs. 6.2g,h). An additional 5 quartz samples were taken from intensely silicified and locally mineralized amphibole-rich calc-silicate within the ore zone, or in the immediate hanging wall to the ore zone (e.g. Figs. 6.3a,b). A further footwall quartzite and two hanging wall quartzite samples were taken (e.g. Figs. 6.3c,d). Seven samples were collected from D_3 pegmatite veins or quartz-feldspar veins including one K-feldspar sample, and two samples were collected from post-mineralization, D_4 quartz and quartz-carbonate veins (e.g. Figs. 6.3e-g). Lastly, quartz from three D_2 leucogranite samples was collected for this study (e.g. Fig. 6.3h). Images of samples that are not presented here are shown in Appendix 8.

Samples were crushed into sand-sized grains before being panned, sieved and cleaned in distilled water. After drying, 30-40 g of quartz grains were hand-picked under the microscope using tweezers. For the Au-rich samples, Au-bearing quartz grains were preferentially selected. The samples were analyzed at the University of Cape Town (UCT), South Africa, using a laser fluorination method. Approximately 1-3 mg of quartz (1-5 grains) per sample was analyzed. Quartz grains were loaded into a highly polished Ni sample holder placed in the oven at 110°C for at least one hour before being transferred to the reaction chamber. After pumping for > 2 hours, the BrF_5 at 10 kPa was released into the reaction chamber for 30 seconds and left overnight to react with the oxygen. After the reaction was completed, excess BrF_5 and free Br were frozen into a cold finger, while the remained gas was passed to a KCl trap at ~200°C to remove any F_2. Then the gasses were expended into a double-U trap in liquid nitrogen, and the purified O_2 was collected in a molecular sieve set in glass bottles. A blank sample was run daily to clean the machine. The details of the technique have been described in Harris and Vogeli (2010).
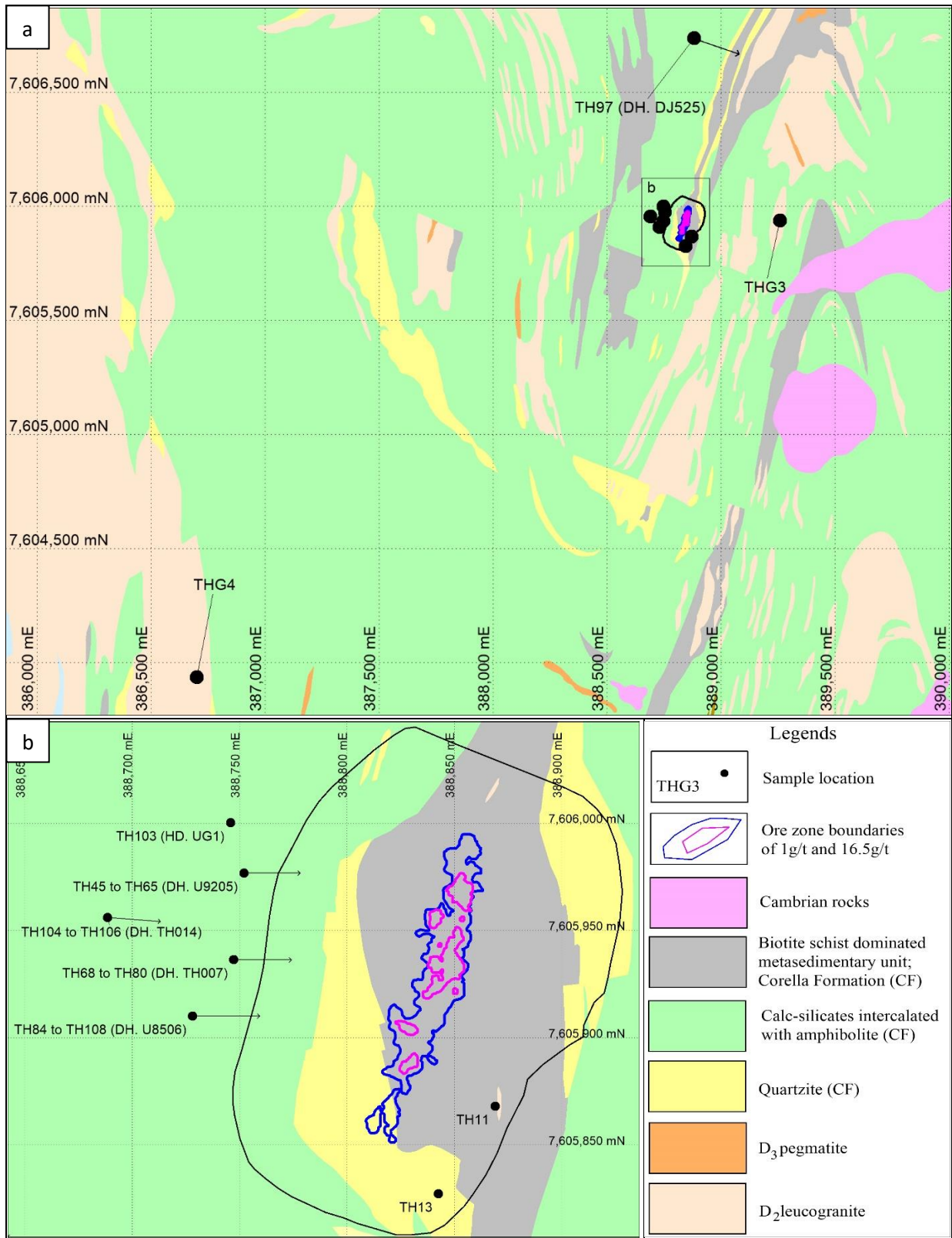
Figure 6.1. Locations of rock samples used in quartz oxygen isotope studies at Tick Hill in relation to (a) regional geological map. The black box is closed-up area as being shown in (b). The datum is Zone 54-GDA94.
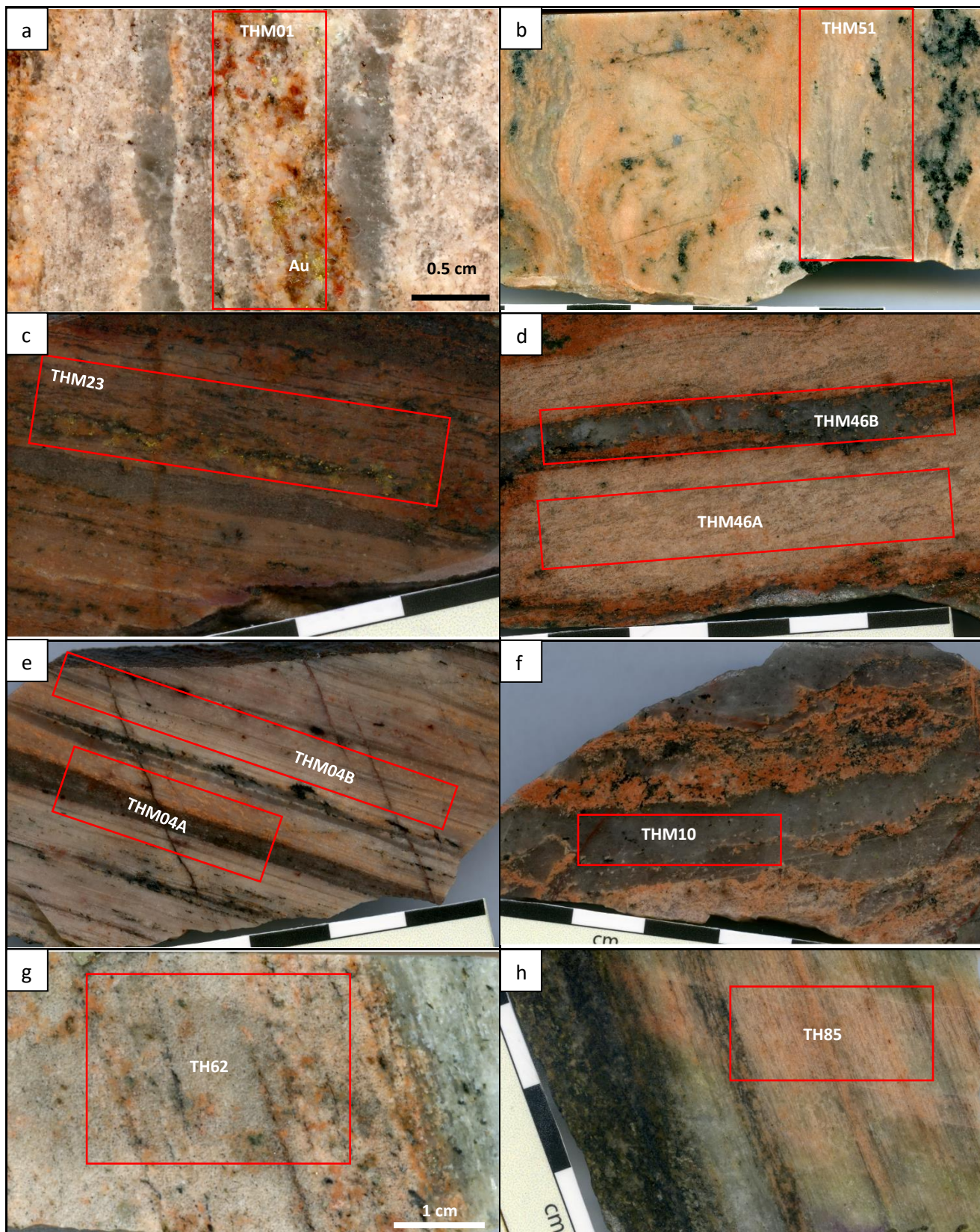
Figure 6.2. Images of sample locations of quartz used in the oxygen isotope study: (a-f) quartz feldspar alteration, including Au-rich quartz-feldspar laminae and laminated quartz veins; (g-h) non-Au-bearing quartz-feldspar alteration overprinting silicified units.

163
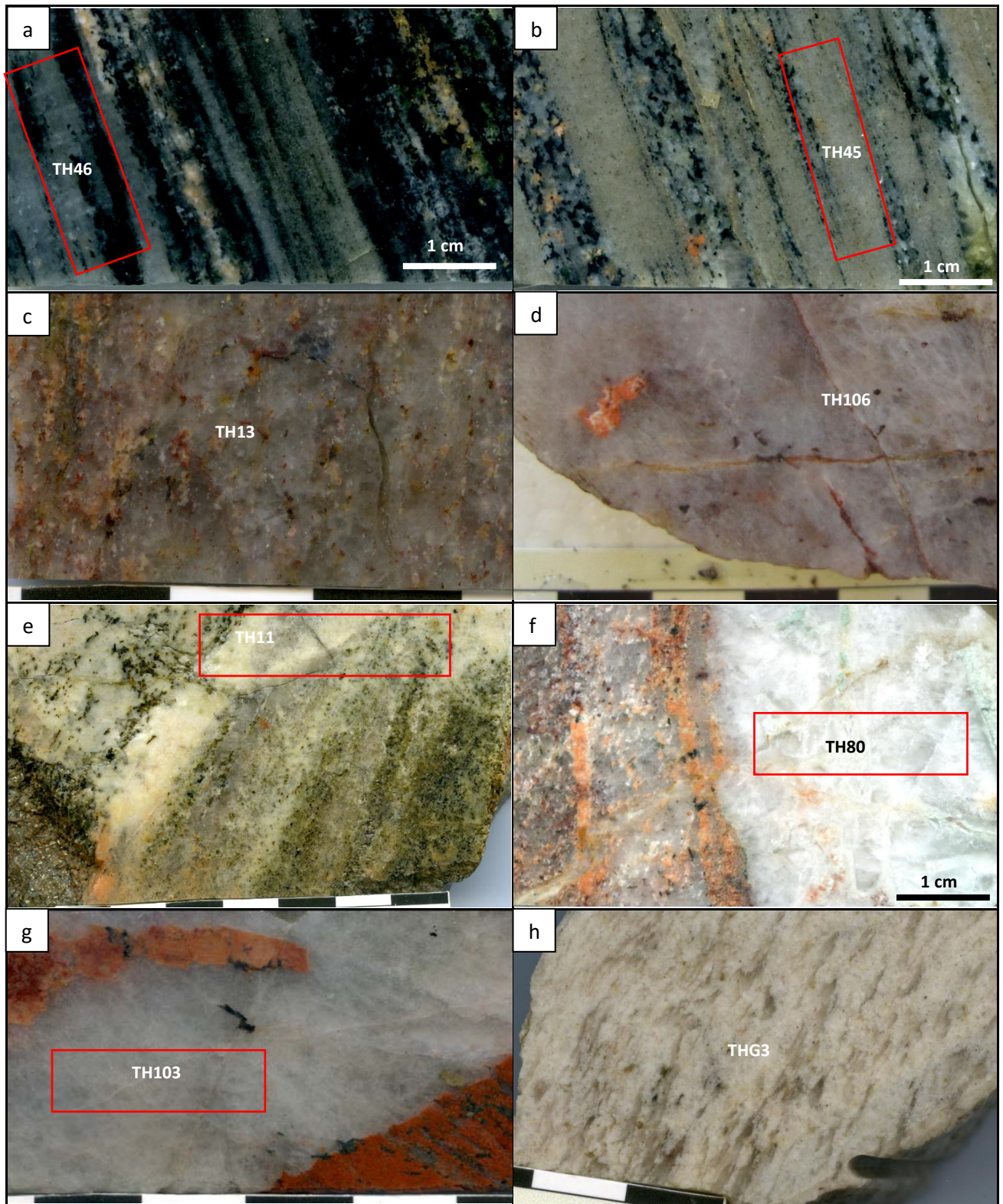
Figure 6.3. Images of different rock units selected for the quartz oxygen isotope study: (a) intensely silicified amphibole-rich calc-silicate; (b) intensely silicified calc-silicate; (c) quartz-feldspar metasomatosed hanging wall quartzite; (d) foot wall quartzite; (e) D₃ quartz feldspar veins; (f) D₄ quartz-calcite vein; (g) and quartz vein; (h) syn-D₂ leucogranite.

6.4. Results

The $\delta^{18}O$ values for the 40 samples are listed in Table 6.3. This data has been summarized and compared with $\delta^{18}O_{quartz}$ data from previous studies by Choy (1994), Hannan (1994) and Oliver (1993) in Table 6.4. Most (i.e. 34/39) of the $\delta^{18}O_{quartz}$ results from the different rock types are similar and fall within a relatively narrow range of 10.5-13.6‰. The $\delta^{18}O_{quartz}$ values for Au-rich, syn-tectonic (D_{1-2}), quartz-feldspar mylonite mainly varies between 11.3‰ and 13.6‰ (n=16; averaged at 12.4 ± 0.7‰) with two outliers of 14.9‰ and 15.3‰. Samples of D_3 quartz-feldspar veins overprinting the intensely silicified D_1 mylonitic texture yield similar $\delta^{18}O_{quartz}$ values of 11.9‰ and 12.8‰ (Table 6.3). The intensely silicified amphibolitic unit that occurs in close association with the mineralization has $\delta^{18}O_{quartz}$ values of 12.2‰ to 13.1‰ (n=4; averaged at 12.5 ± 0.4‰), with a distinct outlier of 19.4‰. The $\delta^{18}O_{quartz}$ results for syn-D_{1-2} leucogranites in the Tick Hill area (including THG3 and THG4, which were dated at 1778 ± 10 Ma and 1777 ± 10 Ma respectively; see Chapter 3 for details) are 11.17‰ and 11.78‰ respectively. These values are similar to $\delta^{18}O_{quartz}$ values from the mineralized quartz-feldspar mylonites in the pit, to which they are geochemically related (see Chapter 3 for details). The $\delta^{18}O_{quartz}$ values for the D_3 hydrothermal quartz-feldspar veins and D_3 pegmatites range from 10.5 ‰ to 12.5‰ (n=6; averaged at 12.0 ± 0.7‰). A single $\delta^{18}O_{k-spar}$ value for a pegmatite provides a result of 8.01‰. The $\delta^{18}O_{quartz}$ values for D_3 veins do not vary significantly with the composition of the host lithology (i.e. amphibolitic calc-silicate and quartz-feldspar mylonite).

The $\delta^{18}O_{quartz}$ values for hangingwall and footwall quartzite samples vary from 12.2‰ to 13.5‰ (n=3), with the footwall wall quartzite with sedimentary characteristics being slightly more positive than the values for the hanging wall quartzite, which has been interpreted as a silicified shear horizon (see Chapters 2 and 4 for details). The D_4 quartz-carbonate and quartz veins yield $\delta^{18}O_{quartz}$ results of 14.1‰ and 17.3‰ respectively, i.e. higher than the general $\delta^{18}O$ range.

Table 6.3. δ¹⁸O data obtained from quartz grains and a single K-feldspar grain from various rock types in and around the Tick Hill deposit.

Group	#	Sample ID	Rock Type	Zone 54-GDA94 DH./X (m)	Depth (m)/ Y (m)	Mineral	Description	Value δ18O (‰)
Au-bearing quartz-feldspar mylonite and laminated quartz veins	1	THM01	Quartz-feldspar mylonite	Ore zone, mining pit		Quartz	High-grade, Au-rich quartz - pink feldspar mylonite	12.55
	2	THM04A	Quartz-feldspar mylonite	Ore zone, mining pit		Quartz	Au-rich quartz-feldspar mylonite with thin laminated quartz veins	13.18
	3	THM04B	Quartz vein inside quartz-feldspar mylonite	Ore zone, mining pit		Quartz	Thin quartz vein (2-3mm wide), quartz grains are laminated	13.17
	4	THM10	Quartz vein inside quartz-feldspar alteration zone	Ore zone, mining pit		Quartz	Au-bearing thin quartz vein (1.2cm wide)	12.57
	5	THM23	Quartz-feldspar mylonite	Ore zone, mining pit		Quartz	1.5cm wide band of Au-rich quartz-red pink feldspar	12.43
	6	THM24	Quartz-feldspar mylonite	Ore zone, mining pit		Quartz	0.8cm wide band of Au-rich quartz- red pink feldspar	13.35
	7	THM26	Quartz-feldspar mylonite	Ore zone, mining pit		Quartz	1.3cm Au-rich quartz-red pink feldspar bands intercalated with laminar quartz veins	11.46
	8	THM40	Quartz-feldspar mylonite	Ore zone, mining pit		Quartz	Au-rich quartz - light pink feldspar mylonite	13.60
	9	THM46A	Quartz-feldspar mylonite	Ore zone, mining pit		Quartz	1cm wide band of Au-rich quartz-feldspar mylonite with thin laminated quartz veins	12.53
	10	THM46B	Quartz vein inside quartz-feldspar mylonite	Ore zone, mining pit		Quartz	Thin quartz vein intercalated with Au-bearing quartz- feldspar mylonite	11.72
	11	THM51	Quartz-feldspar mylonite	Ore zone, mining pit		Quartz	Au-rich quartz - light pink feldspar - amphibole mylonite	11.26
	12	THM56A	Quartz-feldspar mylonite	Ore zone, mining pit		Quartz	2.5cm wide band of Au-rich quartz - feldspar laminate	11.96
	13	THM56B	Quartz vein inside quartz-feldspar mylonite	Ore zone, mining pit		Quartz	0.8cm wide quartz veins next to Au-rich band	12.68
	14	TH48	Quartz-feldspar mylonite	DH. U9205	54.15	Quartz	Au-rich quartz - bright feldspar mylonite with	15.22
	15	TH51	Quartz-feldspar mylonite	DH. U9205	56.4	Quartz	Au-rich quartz - pale pink feldspar mylonite	12.26
	16	TH73	Quartz-feldspar mylonite	DH.TH007	102.3	Quartz	Au-rich quartz - pink feldspar mylonite with micro lenses of quartz, and laminated quartz veins (with ribbon like quartz grains)	12.37
	17	TH74	Quartz-feldspar mylonite	DH.TH007	106.2	Quartz	Au-rich quartz - pink feldspar mylonite with micro lenses of quartz. Some quartz grains are laminated.	12.5
	18	TH105	quartz-feldspar mylonite	DH. TH014	71.5	Quartz	Au-rich quartz -feldspar mylonite	14.86
Non-Au quartz- feldspar	19	TH62	Quartz-feldspar-altered mylonite	DH. U9205	76.8	Quartz	1 cm wide, D3-Stage 2 quartz-feldspar vein overprinted by D3- stage 3	11.9
	20	TH85	Quartz-feldspar-altered mylonite	DH. U8506	180.5	Quartz	D3 pale pink feldspar veins truncating mylonitic quartzite causing quartz-feldspar alteration haloes. Looks similar to the D1/2 quartz-feldspar mylonite	12.8
Intensely silicified	21	TH45	calc- silicate gneiss	DH. U9205	53.1	Quartz	Intensely silicified calc-silicate	19.36
	22	TH46	amphibole-rich calc-silicate gneiss	DH. U9205	54.05	Quartz	Intensely silicified Au-bearing amphibole-rich calc- silicate, most quartz grains are equant (annealed)	13.08

Table 6.3. δ¹⁸O data obtained from quartz grains and a single K-feldspar grain from various rock types in and around the Tick Hill deposit (cont.).

Group	#	Sample ID	Rock Type	Zone 54-GDA94 DH./X (m)	Depth (m)/ Y (m)	Mineral	Description	Value $\delta 18O$ (‰)
Intensely silicified units	23	TH56	Amphibole-rich calc- silicate gneiss	DH. U9205	59.85	Quartz	Intensely silicified amphibole-rich calc-silicate, most quartz grains are equant (annealed)	12.21
	24	TH60	Amphibole-rich calc- silicate gneiss	DH. U9205	62.8	Quartz	Silicified quartz-amphibolite, most of quartz grains are ribbon- like, with pyrite and chalcopyrite	12.27
	25	TH61	Amphibole-rich calc- silicate	DH. U9205	73.4	Quartz	Silicified coarse-grained quartz, overprinting an older fabric defined by amphiboles	12.25
D₃ pegmatite dykes and quartz feldspar veins	26	TH65	D₃ pegmatite dyke (1520-1525 Ma)	DH. U9205	144.75	Quartz	Coarse quartz grains, with undulose extinction	12.5
	27	TH68	D₃-Quartz-feldspar	DH.TH007	64.95	Quartz	D3-Stage 1 quartz-feldspar veins	10.5
	28	TH84	D₃ pegmatite dyke (1520-1525 Ma)	DH. U8506	141.5	Quartz	Pegmatite with coarse-grained biotite, coarse-grained quartz, and red pink feldspar	11.9
	29	TH87	D₃ pegmatite dyke (1520-1525 Ma)	DH. U8506	144.1	Quartz	Coarse quartz grains, with undulose extinction	12.3
	30	TH97	D₃-Quartz-feldspar vein into amphibolite	DH. DJ525	299	Quartz	Coarse grains of quartz-pink feldspar overprint amphibolite; pure quartz was picked	11.8
	31	TH108	D₃ pegmatite dyke (1520-1525 Ma)	DH. U8506	236.5	K-feldspar	Coarse feldspar grains	8.0
	32	TH11	D₃ pegmatite dyke (1520-1525 Ma)	388869	7605868	Quartz	Coarse quartz grains, with undulose extinction	12.2
D₄ veins	33	TH80	D₄ Quartz-carbonate vein	DH.TH007	137	Quartz	D4-Stage 6 vein - latest vein (quartz-carbonate-clay minerals)	14.08
	34	TH103	D₄ Quartz vein	DH. UG1	209.2	Quartz	D4 clean quartz vein	17.03
Quartzite	35	TH104	Hanging wall quartzite	DH. TH014	61	Quartz	Coarse-grained quartz, overprinting an older foliated fabric defined by scattered and altered feldspars that give the rock a speckled appearance	12.2
	36	TH106	Foot wall quartzite	DH. TH014	85.5	Quartz	Coarse-grained quartz; strongly recrystallized and annealed with few inclusions	13.49
	37	TH13	Hanging wall quartzite	388842	7605827	Quartz	Coarse-grained quartz, overprinting an older foliated fabric defined by scattered and altered feldspars	12.96
D₂ Leucogranite	38	THM32	D₂ Leucogranite	Tick Hill Area		Quartz	Quartz - white to pale pink feldspar mylonite without Au; contains laminated quartz grains	11.75
	39	THG3	D₂ leucogranite (ca. 1777 Ma)	389258	7605939	Quartz	Ribbon quartz in gneissic layering	11.17
	40	THG4	D₂ leucogranite (ca. 1777 Ma)	386702	7603938	Quartz	Ribbon quartz in gneissic layering	11.78

Table 6.4. Summary of reported $\delta^{18}O$ values inr the Tick Hill area for this study and for studies by Oliver et al. (1993), Choy (1994) and Hannan (1994). MKD = Mary Kathleen Domain

Rock type	Mineral	$\delta^{18}O$ (‰) in Tick Hill deposit		T. Hill/ regional	MKD
		This study	Choy (1994),	Hannan (1994)	Oliver et al. (1993)
Au-bearing quartz-feldspar mylonite including laminated quartz veins (D$_{1-2}$ mylonite overprinted by D$_3$ quartz-feldspar metasomatism/ alteration)	Quartz	11.3-13.6 (n=16) 14.9-15.2 (n=2)		10.3-11.3 (n=2, one in the ore zone)	
	Whole rock		11.2 (n=1)		
Non-Au-bearing D$_3$ quartz-feldspar alteration overprinting intensely silicified units	Quartz	11.9-12.8 (n=2)			
Intensely silicified units in mineralized zone	Quartz	12.2-13.1 (n=4) 19.4 (n=1)			
D3 pegmatite dykes and quartz feldspar veins (1520-1525 Ma)	Quartz	10.5-12.5 (n=6)			
	K-feldspar	8.0 (n=1)			
D$_4$ quartz-carbonate or quartz veins	Quartz	14.1-17 (n=2)			
Hanging and footwall quartzite (+ regional quartzite in Hannan, 1994)	Quartz	12.2-13.5 (n=3)		11.7-12.9 (n=8)	
D$_2$ leucogranite (ca. 1775 Ma, coeval with quartz-feldspar mylonite)	Quartz	11.2-11.8 (n=2; local) 11.8 (n=1; regional)			
D$_3$ quartz veins (D$_3$ in Choy, 1994)	Quartz		11.7-13.2 (n=3)		
D$_1$ quartz veins (D$_1$ in Choy, 1994)	Quartz		12.4-12.6 (n=2)		
Wall rock, schist (calc-silicate; including rock units near Tick Hill in Hannan, 1994)	Quartz		11.7-12.9 (n=3)	11.7-12.5 (n=3)	
Wall rock, schist (calc-silicate ?)	Whole rock		9-11.9 (n=4)		
Wall rock, granofels			11.9 (n=1)		
Wall rock, schist	Magnetite		3.7 (n=1)		
Syn- or late-D$_2$ calcite pods (D$_2$ in Oliver, 1993)	Calcite				10.5-12.5 (n=30)
Calcite-bearing altered wall rocks and veins (surrounding D$_2$ calcite pods; D$_2$ in Oliver, 1993)	Calcite				11.2-17.3 (n=42; average = 13.2)
Unaltered banded calc-silicate and marble wall rocks	Calcite				18-21 (n=7)
Metadolerite away from calcite pods	Whole rock				3.5-7 (n=10)

6.5. Discussion

6.5.1. How do our results compare to earlier studies ?

The $\delta^{18}O_{quartz}$ results presented here are generally identical within error to earlier results contained in Choy (1994) and Hannan (1994), thereby confirming the results from these earlier studies (Tables 6.2, 6.3). Results from the mineralized quartz-feldspar mylonite and associated quartz veinlets are relatively homogenous with average $\delta^{18}O_{quartz}$ values of 12.4 ± 0.7‰ (our study; n = 16), 10.3‰ (Hannan, 1994; n = 1) and 12.3‰ (Choy, 1994; n=3). The lower $\delta^{18}O_{quartz}$ value of 10.3 ‰ for quartzo-feldspathic mylonite mentioned by Hannan (1994), does not replicate in a systematic way in our study, and does not reflect systematic lowering of $\delta^{18}O_{quartz}$ values in the mineralized mylonite zones.

Results from altered, amphibole-bearing calc-silicate in the immediate hanging wall to the ore zone are also similar to earlier results with averages of 12.5 ± 0.4‰ (our study; n = 4) and 12.3 ± 0.7‰ (Choy, 1994; n=6), and they are near-identical to the values for the mineralized quartz-feldspar mylonite.

6.5.2. Are the highly mineralized zones characterized by a specific $\delta^{18}O_{quartz}$ signature

The $\delta^{18}O_{quartz}$ results (Tables 6.1-6.3) indicate that the highly mineralized and altered quartz-feldspar mylonites have $\delta^{18}O_{quartz}$ values that are indistinguishable from the highly altered hangingwall calc-silicate units, as well as the hanging wall quartzite. The $\delta^{18}O_{quartz}$ values for the mineralized mylonites also overlap with $\delta^{18}O_{quartz}$ results for leucogranites that occur 300 m east of Tick Hill (THG3) and 4.5km southwest of the pit (THG4). These leucogranites are geochemically similar to the mineralized quartz-feldspar mylonite samples (see Chapter 3 for geochemical details), and they are strongly albitized, although they are not as strongly altered as rocks in the pit.

The results indicate that $\delta^{18}O$ values for quartz from the mineralized zones cannot be distinguished from altered rocks that carry no mineralization. The $\delta^{18}O_{quartz}$ signature is similar for a range of different rock types, and it is widespread with little variation in values both within the pit and more regionally. This result is similar to the conclusion reached by Hannan (1994), and further confirms the observation of Oliver et al. (1993), that the Mary Kathleen Domain (MKD) was affected by a wide-spread and pervasive fluid alteration event. During this event most of the rocks in the MKD re-equilibrated in terms of oxygen isotopes with a voluminous fluid reservoir that infiltrated from depth. This narrow range of $\delta^{18}O_{VSMOW}$ values is also displayed in calcite deposited during IOCG mineralization and Na-(Ca) alteration in the Eastern Succession (Marshall and Oliver, 2008), reflecting the large regional extent of the altering fluids affecting the Mt Isa Inlier during D_3 events.

Some of the quartz-feldspar mylonite samples and one of the altered calc-silicate samples, as well as the footwall quartzite, yield elevated $\delta^{18}O_{quartz}$ results. These may represent analytical errors considering the homogenous nature of results from all other samples that are similar in composition, deformation style and alteration assemblage. Alternatively, it has been noted that regional background values in $\delta^{18}O$ may be elevated to around 17-21‰, within the calc-silicates of the Corella formation (e.g. Oliver et al., 1993, 1995). The elevated values obtained in this study could, therefore, reflect primary $\delta^{18}O$ isotope values that have been only partly re-equilibrated with a later fluid reservoir during regional alteration.

6.5.3. Do similar rock types of different age have different $\delta^{18}O_{quartz}$ signatures

Choy (1994) tried to sub-divide his isotope results into syn-D_1 (peak-metamorphic gneissic fabric) and syn-D_3 (later alteration overprint, including red rock alteration) values, but was unsuccessful in this, as both types of rocks yielded statistically indistinguishable results. We find the same in this study. Most $\delta^{18}O_{quartz}$ results fall within a narrow range (10.5-13.7‰) and there are no significant and systematic differences between different rock types or between mineralized and non-mineralised samples. Results from samples containing the pervasive D_{1-2} fabric, estimated to have formed around 1780 Ma (see Chapter 3) and affected by retrogression and younger alteration, are indistinguishable from samples obtained from later quartz-feldspar veins and pegmatites (with a $\delta^{18}O_{quartz}$ value of 12.0 ± 0.7‰) that were dated at 1525-1520 Ma (see Chapter 3).

Therefore, the $\delta^{18}O_{quartz}$ signatures of rocks that formed and were affected by deformation-metamorphism-alteration between D_1 and D_3 are indistinguishable from one another, which is consistent with observations made by Oliver et al. (1993). This either means that various fluid pulses affecting the rocks during D_1, D_2 and D_3 all had similar isotope values, or that the rocks were affected by a pervasive and penetrative alteration event during D_3, which largely reset the $\delta^{18}O_{quartz}$ isotopic values in all rock types throughout the Tick Hill region. We prefer the latter interpretation which is consistent with similar conclusions drawn in numerous previous studies (e.g. Oliver et al., 1993, 1995; Williams et al., 2005; Mark et al., 2006; Withnall & Hutton, 2013).

The two samples obtained from later, D_4 fault related quartz-calcite-clay veins yield elevated $\delta^{18}O_{quartz}$ values of 14.1‰ and 17.0‰, which are distinctly heavier than the older quartz, and may reflect a different fluid source that locally overprinted the pervasive alteration.

6.5.4. What is the possible fluid source for the $\delta^{18}O$ isotope signature in Au-bearing quartz

Based on near identical $\delta^{18}O_{calcite}$ results for calcite blows along the length of the MKD, Oliver et al. (1993, 1995) argued for a single homogenous, high-volume fluid reservoir that pervasively reset

variable oxygen isotope values in the host rocks. They discounted the involvement of locally derived metamorphic fluids, but instead invoked an intrusive source in either the lower crust or upper mantle. They assumed that this fluid event occurred during the Isan orogeny at ca. 1550 Ma.

Spence et al. (2020) remapped parts of the same general area from which Oliver et al. (1993) obtained their isotope data, and showed that upright folding and peak metamorphism was probably diachronous across the area, and occurred before 1715 Ma in the Mt Godkin area, and before 1735 Ma in the Mary Kathleen - Duchess area. This means that if the field relationships for the calcite pods described by Oliver et al. (1993) are correct, carbonate vein emplacement and associated chalcopyrite enrichment largely occurred before 1715 Ma. Spence et al. (2020) further noted that the timing of Isan Orogeny events appears to be largely constrained to networks of shear zones that reactivated earlier fabrics, with renewed amphibolite facies metamorphim and extensive alteration. Our field observations for several calcite pods described by Oliver et al. (1993) indicate that calcite grains in these veins are extremely coarse-grained and recrystallized, in spite of the strongly deformed nature of the pods, indicating post-deformational annealing. This could mean that the metamorphic conditions of emplacement (530-570°C) reported by Oliver et al. (1993) and based on calcite-dolomite geothermometry do not actually record peak-condition during upright folding at >1715 Ma, but rather record the elevated temperatures attained during recrystallization/annealing when a regionally pervasive hydrothermal fluid passed through the rocks, presumably during Isan Orogeny events.

The existence of a late Isan hydrothermal overprint is confirmed by abundant 1520-1525 Ma ages for hydrothermal titanite and high-U zircon overgrowths obtained from samples along the length of the Mary Kathleen Domain (e.g. Kositcin et al., 2019; Whitnall, 2019; Bodorkos et al., 2020). At Tick Hill this same event has been recorded in the emplacement of quartz-feldspar veins, pegmatite dykes, extensive alteration and gold mineralization. Thus, the $\delta^{18}O_{quartz}$ results from the Tick Hill area, reported here, most likely reflect fluid conditions at 1520-1525 Ma, during the late Isan hydrothermal overprint.

Given the well documented regional extent of the late Isan overprint across the Eastern Fold belt (e.g. Oliver et al., 2008), we can infer that the $\delta^{18}O_{calcite}$ values reported for the Mary Kathleen Domain by Oliver et al., (1993), and the $\delta^{18}O_{quartz}$ results reported here for Tick Hill reflect the isotopic effects of the same hydrothermal overprint. If we further assume that the $\delta^{18}O_{calcite}$ values that are similar along a 100 km stretch between Mt Godkin and Trekalano Mine, are most likely also going to be similar at Tick Hill, 18 km south of Trekalano Mine, then the reported average $\delta^{18}O_{calcite}$ and $\delta^{18}O_{quartz}$ values can be used as a geothermometer to estimate the temperature of the late Isan fluid reservoir with which the rock equilibrated. When making this comparison, it is noted that the $\delta^{18}O_{quartz}$ values from mineralized quartz-feldspar mylonite were obtained from annealed quartz grains associated with gold and D_3 alteration assemblages estimated to have formed at temperatures between 300-500 °C (see

Chapter 5). We realize that we did not measure $\delta^{18}O_{calcite}$ and $\delta^{18}O_{quartz}$ values in the same samples, but the exercise of calculating a fluid temperature is still informative.

Geothermometers based on the fractionation of oxygen isotopes in mineral pairs that co-precipitated from the same hydrothermal fluid, have the general form:

$$(\delta^{18}O_{phase1} - \delta^{18}O_{phase2}) = A*(10^6 T^{-2}) + B \qquad (1)$$

where T is the absolute temperature and A and B are calibration constants that have been determined experimentally (Friedmann & O'Neil, 1977; Matthews et al. 1983; Faure, 1986). Assuming an average value for $\delta^{18}O_{calcite}$ of 10.73 ± 0.39 ‰ (n = 10) based on samples from retrograde calcite pods reported in Oliver et al. (1993), and an average value for $\delta^{18}O_{quartz}$ of 12.43 ± 0.66 ‰ based on mineralized quartz-feldspar mylonite data presented here, and using the calibration constants tabulated in Faure (1986), a fluid temperature of 321 °C can be calculated, which increases to 366 °C, if we combine our data with the data reported in Choy (1994) and Hannan (1994) resulting in an average $\delta^{18}O_{quartz}$ of 12.2 ‰. Combining the average $\delta^{18}O_{quartz}$ value with the $\delta^{18}O_{calcite}$ value of 11.54 ± 0.67 ‰ (n = 20) for high temperature calcite pods reported in Oliver et al. (1993), provides a fluid temperature estimate of 548 °C. Whilst these temperature estimates are rough and obviously dependent on large assumptions they are consistent with the observed early stage, upper-greenschist facies D_3 alteration assemblages at Tick Hill (hornblende-albite-quartz-magnetite and actinolite-chlorite-epidote assemblages; Chapters 2 and 5). Thus, the reported $\delta^{18}O_{quartz}$ results for quartz in Tick Hill appear to reflect the earlier stages of fluid infiltration at 1520-1525 Ma, before and during the main-stage of gold mobilization. The precipitation of various Bi-selenites, during later stages of the gold mobilization events suggests that lithostatic pressures were probably below 1 Kbar (see Chapter 2 for details), i.e. the rocks were relatively close to surface during the late Isan hydrothermal events, and geothermal gradients would have been high across large areas.

The origin of the altering fluids is unclear, and the $\delta^{18}O_{quartz}$ values do not provide a conclusive answer, as they overlap with reported $\delta^{18}O$ values for both metamorphic and igneous fluids (e.g. Blatt, 1987; Rollinson, 1993; Harris and Vogeli, 2010). An igneous source is commonly invoked (e.g. Oliver et al., 2008), involving the laterally extensive upper- to mid-crustal granites of the Williams- Naraku Batholith (e.g. Page & Sun, 1998; Mark 2001; Oliver et al., 2008), in combination with a more CO_2 rich fluid component released from mafic rocks in the lower crust or mantle (Oliver et al. 2008). At Tick Hill there is no direct evidence for late-tectonic intrusions (or CO_2-rich fluids) other than the 1520-1525 Ma pegmatite veins.

6.6. Conclusions

At Tick Hill, the $\delta^{18}O_{quartz}$ values for Au-rich host units including quartz-feldspar mylonite and intensely silicified schist and quartzite vary from 11.3-13.6 ‰, and are similar to the $\delta^{18}O_{quartz}$ values obtained from surrounding rock types in the region. The results from this study are similar to those from earlier $\delta^{18}O_{quartz}$ studies conducted at Tick Hill and the surrounding areas, and they do not provide a useful exploration tool.

The $\delta^{18}O_{quartz}$ results from the Tick Hill area most likely reflect fluid conditions at 1520-1525 Ma, during the late Isan hydrothermal overprint. The origin of the altering fluids is unclear, and the $\delta^{18}O_{quartz}$ values do not provide a conclusive answer as they overlap with reported $\delta^{18}O$ values for both metamorphic and igneous fluids. When combining the $\delta^{18}O_{quartz}$ results with $\delta^{18}O_{calcite}$ results available from the literature, temperature estimates of 350-550°C can be calculated-consistent with observed alteration assemblages that were associated with Au mineralization during D_3. The D_4 quartz-calcite veins that postdate the 1520-1525 Ma D_3 deformation and mineralization events record higher $\delta^{18}O_{quartz}$ values that range from 14.08 to 17.03 ‰.

Chapter 7: Summary and conclusions

The aims of this project are to characterize the geological-structural setting of the Tick Hill gold deposit, determine the mineralization style for the deposit, and constrain the timing of mineralization. This study has improved the understanding of the Tick Hill deposit and will assist in future exploration in the area. The deposit was studied by means of field mapping, core logging, petrography, U-Pb zircon geochronology, whole-rock geochemistry, and oxygen stable isotope geochemistry.

This thesis includes an introduction chapter, five data chapters (Chapters 2-6) and a conclusion chapter (Chapter 7). **Chapter 2** documents the geological and structural-metamorphic setting and the mineralisation-alteration characteristic in Tick Hill. **Chapter 3** presents the geochronological data to constrain the timing of structural-metamorphic and hydrothermal events examined in Chapter 2. A geochemical investigation of the zircon (1780-1520 Ma) is presented in **Chapter 4. Chapter 5** presents the mineral geochemistry from the metamorphic and hydrothermal alteration minerals that have been described in Chapters 2 and 3. **Chapter 6** presents the results of an oxygen isotope study of the Au-rich rock units and surrounding rock types.

7.1. Geological setting

The Tick Hill gold deposit is hosted by gneissic amphibolite, calc-silicate, biotite schist, quartz-feldspar mylonite, and quartzite. This sequence was intruded by: (1) 1770-1790 Ma (syn D_{1-2}) granite, leucogranite and quartz-feldspar mylonite in the vicinity of Tick Hill and the surrounding area; and (2) 1520-1525 Ma (syn-D_3) pegmatite and associated hydrothermal activity that resulted in D_3 gold mobilization/mineralization. The maximum age estimate for the sequence, based on an age estimate for the youngest zircon population in the footwall quartzite is 1841±15 Ma. The new geochronological constraints suggest that the calc-silicate units hosting the tick Hill deposits do not belong to the Corella Formation, and were formed prior to the Argylla Formation, sometime between 1841 Ma and 1790 Ma. The youngest zircon age of ca. 1781 Ma from the hanging wall quartzite was derived from mostly prismatic, euhedral zircon and reflects the age of an original quartzo-feldspathic gneiss, that was silicified during D_1, presumably as a result of an early shearing and alteration event, associated with an early stage of gold mineralization. The pre-D_1 Kalkadoon Supersuite (1850-1855 Ma) granite is situated at 10 km west of Tick Hill but locally crops out at the Tick Hill area as a small inlier of remnant basement (4 km west of Tick Hill).

Chapter 4 presents the geochemistry of (1) zircons yielding ages ranging between 1780 and 1770 Ma from syn-D_{1-2} granite, leucogranite, quartz-feldspar mylonite and intensely silicified unit (hanging wall quartzite) and (2) zircons yielding ages ranging between 1600 and 1520 Ma from

pegmatite veins. The zircon geochemistry results show that the zircon aged 1770-1780 Ma has distinct trace element compositions compared to the younger zircon. The Th/U mass ratios for the older (1770-1780 Ma) and younger (1600-1520 Ma) zircon populations are > 0.2 and < 0.1 respectively. These Th/U mass ratios indicate that the older zircons are magmatic whereas the younger zircons are hydrothermal in origin. This result is consistent with the zircon morphology described in Chapter 3.

7.2. Structural-metamorphic setting

Four deformational events have been recorded at Tick Hill, including: (1) D_1 shearing that lead to the formation of high-strain textures (recrystallized mylonites, and regional gneiss fabric) at high-grade metamorphic conditions; (2) D_2 upright folding that formed the Tick Hill syncline, again at high-grade metamorphic conditions; (3) D_3 normal faulting with extensional quartz-feldspar veining and associated alteration, and (4) D_4 strike-slip faulting characterized by quartz-calcite alteration and the formation of cataclasite. The Tick Hill ore body occurs in strongly sheared (i.e. mylonitic) high-grade gneisses that were deformed at upper amphibolite facies during D_1 and D_2 (1790-1770 Ma) and overprinted at lower amphibolite to greenschist facies during D_3 (1600-1520 Ma). The D_3 events included a pervasive fluid-induced alteration event that resulted in regional albite-chlorite-hematite alteration and gold mobilization at 1520-1525 Ma. D_1 deformation events are characterized by the 100 m scale foliation truncation plane that resemble shear zones. The ore zone parallels one such D_1 foliation truncation plane, which was reactivated during D_3 as a sinistral normal fault. The ore zone is approximately parallel to the D_1 mineral extension lineation, and also parallels the intersection lineation between east- and north-northeast-trending D_3 faults and fracture/breccia zones. The high-grade ore zone transgresses lithological boundaries and most of the gold is hosted in D_3-altered, D_{1-2} quartz-feldspar mylonite.

7.3. P-T conditions of metamorphism

Peak-metamorphic mineral assemblages including garnet-hornblende-plagioclase-quartz-biotite-ilmenite from amphibolite, obtained from drill core 800 m north of the pit, record P-T conditions of 6.0-7.6 kbar and 720-750°C. Strongly mineralized, amphibole-rich calc-silicate gneiss from within the ore zone preserves mineral assemblages including diopside-hornblende-plagioclase-scapolite-quartz, that provide temperature estimates of 620-670°C, interpreted to reflect conditions during the later stages of D_1 or D_2. Gold is contained as inclusions within granoblastic diopside and hornblende grains that are aligned within the gneissic fabric. The P-T conditions during D_3 were more variable. Stage 1 (D_3) assemblages are characterized by hornblende-albite-oligoclase reflecting lower amphibolite to upper greenschist facies conditions (>500 °C). Chlorite geothermometry for stage 2 and stage 3 (D_3) chlorite associated with gold mineralization and chlorite-actinolite-albite-clinozoizite-bismuth selenide alteration, yields T estimates of 160-380°C. Stage 4 (D_3) chlorite in association with calcite-quartz-Bi-

Pb-Cu selenide alteration and yields T estimates of 130-170°C, reflecting the final stages of retrograde alteration. The strongly zoned nature of chlorite grains indicates that during D_3, when gold was mobile, alteration temperatures progressively decreased from ~380 (stage 2) to ~130°C (stage 4). These temperature estimates are consistent with presence of Bi-selenides (< ~300°C), which can only form at low P conditions (generally <1 kbar); i.e. towards the end of D_3 events, the rocks would have been close to surface.

7.4. Mineralisation and alteration characteristics

The gold at Tick Hill is mainly hosted within the quartz-feldspar mylonite unit. The gold is pure except for some rare grains associated with D_3 assemblages, which contain minor amounts of Cu and Ag. A characteristic feature of the Tick Hill deposit is the presence of Bi-selenides in the high-grade ore zone and the general paucity of sulphides. Available assay data for a restricted number of elements (Cu, Co, Ni, Pb, Zn, As, Fe, and Mn) from exploration drill holes indicate that, with few exceptions on a meter scale, gold values show no correlation with any of the other metals. Copper appears to be elevated in a shell (mainly the footwall) peripheral to the high-grade ore zone, and its concentration appears to be lithologically controlled (i.e., the presence of chalcopyrite correlates with more mafic lithologies). Early sulphides appear to have been partly resorbed during the earlier stages of D_3 (mostly stage 2) with some re-deposition (together with calcite, selenides, and re-mobilized gold) during a later D_3 stage (stage 4).

The alteration mineralogy associated with D_3 mineralization (stages 1 to 4) include hornblende, actinolite, albite, oligioclase, high-Al chlorite, K-feldspar, intermediate-Al chlorite, epidote, sericite, low-Al chlorite$_3$, quartz, hematite, calcite and clay minerals. The proximal mineralization coincided with D_3 brecciation and intense silicification, bounded by a strongly silicified zone and surrounded by a chlorite-epidote shell. However, the chlorite-epidote alteration also occurs in the proximal zone. The presence of bismuth selenide associated with gold and widespread hematite alteration in the ore zone indicates the involvement of a strongly oxidized, acidic, saline aqueous fluids. The $\delta^{18}O_{quartz}$ values for the Au-rich quartz-feldspar mylonite varies from 11.3-13.6 ‰, and is similar to the $\delta^{18}O_{quartz}$ values obtained from other surrounding rock types in the region.

7.5. Timing of mineralization

Geochronological and textural evidence indicate that gold at Tick Hill accumulated during two discrete geological events. An early gold mineralization event is recorded by the presence of coarse-grained gold hosted in D_{1-2} scapolite, hornblende, and diopside. The age of this mineralization event has been indirectly determined from syn-D_{1-2} intrusive units, which were dated at 1790-1770 Ma. Much of the gold occurs in close association with D_3 (stages 2 and 3) fractures and associated actinolite-chlorite-

epidote-hematite alteration. Gold also occurs in association with later D_3 fractures (stage 4) and carbonate veinlets, indicating further D_3 gold remobilization. A bi-modal grainsize distribution for gold is common in which coarse grains aligned in the main mylonitic fabric are surrounded by a 'halo' of finer grains suggestion localised remobilization. The age of D_3 gold remobilization has been determined from syn-D_3 pegmatite, which was dated at 1525-1520 Ma. Overall, gold mineralization was introduced prior to or during D_1 and was subsequently remobilized during D_3.

7.6. Deposit style

There is clear evidence that coarse-grained gold mineralization formed relatively early (pre- to syn-D_{1-2}) and that the gold was remobilized during D_3. The origin of the altering fluids is unknown as the $\delta^{18}O_{quartz}$ values overlap with $\delta^{18}O$ values for both metamorphic and igneous fluids. Earlier studies (Williams et al., 2005; Groves et al., 2010), have interpreted Tick Hill as a gold-rich end-member IOCG deposit. I have listed criteria for IOCG deposits that occur in Eastern Fold Belt of the Mt Isa Inlier (Williams et al., 2005, 2015; Foster et.al., 2007; Groves et al., 2010; Zhu 2016) in order to assess how Tick Hill fits these criteria (Table 7.1).

Oxygen isotope results and alteration assemblages indicate that during D_3, Tick Hill was overprinted by the same fluids that affected rocks throughout the Eastern Fold Belt, and which have been linked to IOCG deposits (e.g. Williams et al. 2005). Therefore, Tick Hill shares a number of characteristics with IOCG deposits, especially with regards to the alteration style. However, as mentioned previously, remobilized gold during D_3 was sourced from pre- or syn-D_{1-2} mineralization. The 1841-1790 Ma calc-silicate hosted Tick Hill deposit retains characteristics that are similar to the Au-Bi-Se rich, oxidized end-member type for ca. 1850 Ma ironstone-hosted Au-Cu-Bi deposits in the Tennant Creek Gold Field (e.g. Skirrow & Walshe, 2002). At Tick Hill, the host lithologies of the early gold mineralisation (pre- or syn- D_1) were repeatedly affected by deformational, metamorphic and metasomatic events. Thus, there are too many uncertainties (Table 7.1) to allow the Tick Hill deposit to be classified as an IOCG deposit.

Table 7.1 shows a comparison of mineralization characteristics between typical IOCG deposits (mainly in Mt Isa Inlier; Williams et al., 2005, 2015; Foster et.al., 2007; Groves et al., 2010; Zhu 2016) and the Tick Hill deposit.

Typical IOCG deposits	Tick Hill	Similarity
1. Cu with or without Au as an economic metal.	There is no major Cu mineralization at Tick Hill and the minor Cu enrichment that occurs is not directly associated with Au.	No
2. Au commonly contains Ag.	Almost all Au in Tick Hill is pure.	No
3. Hydrothermal vein, breccia, and/or replacement ore styles, characteristically in specific structural sites.	Tick Hill meets this characteristic.	Yes
4. Abundant magnetite and/or hematite	Tick Hill has abundant early magnetite overprinted by hematite	Yes
5. Fe oxides with Fe/Ti ratios greater than in most igneous rocks and bulk crust.	Tick Hill meets this characteristic.	Yes
6. No clear spatial associations with igneous intrusions as, for example, displayed by porphyry and skarn ore deposits.	Gold is largely hosted in ca. 1775Ma quartz-feldspar mylonite, interpreted as leucogranite. If Au was introduced then, it would have formed in association with the Tick Hill intrusive suite. If gold pre-dated D_1, then the relationship with intrusive rocks is not clear.	Unclear
7. Broad space-time association with batholitic granitoids.	The late D_3 fluid alteration stage dated at 1525 Ma coincides with the emplacement of the Williams-Naraku Batholith. But it is not clear if the gold was introduced during that stage. Gold is largely hosted in ca. 1775 Ma quartz-feldspar mylonite, interpreted as leucogranite. If Au was introduced then, it would have formed in association with the Tick Hill intrusive suite.	Unclear
8. In settings with pervasive alkali (Na) metasomatism.	Tick Hill meets this characteristic.	Yes
9. Late-stage carbonates are common	Tick Hill meets this characteristic.	Yes
10. Typically enriched in minor elements including F, P, Co, Ni, As, Mo, Ag, Ba, LREE, and U.	Tick Hill does not meet this characteristic. Instead, gold is pure, with high-grade zones showing a correlation with minor Ag, Bi, Pd and Pt.	No
11. Depth of formation 1-10 km.	Probably, but it depends on when gold was originally formed. During D_3, when Au was mobile, conditions were within this range.	Unclear
12. Widespread pre-sulphide, Na and Na-Ca alteration (albite) predates more proximal K-Fe alteration (sericite-chlorite) and mineralization.	Tick Hill meets this characteristic, but again there is the issue of when gold was actually introduced into the system, and there is little sulphide.	Unclear
13. Mineralizing fluids are complex brines, commonly with a carbonic component.	The fluids during D_3 were brines with no carbonic component.	Unclear
14. Brines may come from magma directly or indirectly, or could be derived from basinal/metamorphic fluids.	Oxygen isotope studies are inconclusive.	Unclear
15. Possible mixing of S-poor, metal-rich brines with S-bearing fluids at site of deposition.	Possibly.	Unclear
16. Tectonic setting uncertain, but possibly anorogenic and linked to underplating.	The rocks appear to have experienced a clockwise P-T path with significant exhumation following D_1. During D_3 alteration, the rocks appear to have been in an extensional environment.	Unclear

7.7. Exploration implications

The Tick Hill deposit is a unique deposit in the Mt Isa Inlier. Almost all major gold occurrences around the globe occur in association with other gold occurrences. The Tick Hill situation is highly anomalous in this regard. Based on historical exploration activities and characteristics of the Tick Hill deposit presented here, some exploration implications for similar mineralisation styles in the region are proposed as following:

- The volcano-sedimentary lithologies that host gold at Tick Hill were previously interpreted to be part of the Corella Formation. However, they are likely to be much older and (older than Argylla Formation). This means that the volcano-sedimentary sequences in the south Mary Kathleen domain could be prospective for gold. However the extent od this old sequence needs to be well constrained in the south MKD.

- The gold formed early and probably did not get introduced during pervasive fluid infiltration that resulted in the alteration assemblages that are visible in the pit (chlorite-epidote-actinolite-carbonate alteration). Instead, the gold is associated with an earlier alteration assemblage of silica-magnetite. Considering that Bi and Se probably represent localised remnants of an earlier alteration/mineralisation, exploration should focus on silica-magnetite alteration associated with elevated Bi-Se levels rather than typical IOCG style alteration/mineralisation.

- The D_3 deformation structures determine the current, local geometry of the orebody, but they may have been unrelated to deformation patterns at the time of gold introduction (i.e. this observation follows the syn-D_1 models that guided exploration in the early 1990s).

References

Aeon Metals Limited, 2017. Zambian Copperbelt-style geological model - a revised Walford Creek geological model, Exploration Report. https://www.aeonmetals.com.au/assets/uploads/2017/07/2017-Jul-28-Zambian-Copperbelt-Style-Geological-Model.pdf.

Alagna, K.E., Petrelli, M., Perugini, D., Poli, G., 2008. Micro-analytical zircon and monazite U-Pb isotope dating by laser ablation-inductively coupled plasma-quadrupole mass spectrometry. Geostandards and Geoanalytical Res., 32(1), 103-120.

Anderson, J. L., 1996. Status of thermobarometry in granitic batholiths. Transactions of the Royal Society of edinburgh 87(1-2): 125-138.

Babo, J., Spandler, C., Oliver, N.H., Brown, M., Rubenach, M.J., Creaser, R.A., 2017. The high-grade Mo-Re Merlin deposit, Cloncurry district, Australia: Paragenesis and geochronology of hydrothermal alteration and ore formation. Econ. Geol., 112(2), 397-422.

Berman, R. (1990). "Mixing properties of Ca-Mg-Fe-Mn garnets." American Mineralogist 75(3-4): 328-344.

Betts, P., Giles, D., Mark, G., Lister, G., Goleby, B., Ailleres, L., 2006. Synthesis of the Proterozoic evolution of the Mt Isa Inlier. Aust. J. Earth Sci., 53(1), 187-211.

Bhadra, S., Das, S., Bhattacharya, A., 2007. Shear zone-hosted migmatites (Eastern India): the role of dynamic melting in the generation of REE-depleted felsic melts, and implications for disequilibrium melting. J. of Petrology, 48(3), 435-457.

Blake, DH, 1980. The early geological history of the Proterozoic Mt Isa Inlier, northwestern Queensland: an alternative interpretation. BMR Journal of Austr. Geol. & Geophys., 5, 243-256.

Blake, D.H., Bultitude R.J., Donchak P.J.T., 1982. Dajarra, Queensland 1:100000 geological map commentary. BMR Geol. Geophys., 225, 83pp.

Blake, D.H., Bultitude, R.J., Donchak, P.J.T., 1984. Geology of the Duchess-Urandangi region, Mt Isa Inlier, Queensland. BMR Geol. Geophys. Aust. Bull., 219, 1-91.

Blake, D.H., 1987. Geology of the Mount Isa inlier and environs, Queensland and Northern Territory. BMR Geol. Geophys. Aust. Bull., 225, 1-83.

Blake, D., Steward, A., 1992. Stratigraphic and tectonic framework, Mount Isa. AGSO Bull., 243, 1-11.

Blatt, H., 1987. Perspectives; Oxygen isotopes and the origin of quartz. J. of Sedimentary Res., 57(2): 373-377.

Blenkinsop, T., Oliver, N., Dirks P.H.G.M., Nugus, M., Tripp, G., Sanislav I.V., 2020. Structural Geology applied to the evaluation of Hydrothermal Gold Deposits. SEG Reviews in Econ. Geol., 21, 1-23.

Blundy, J. D. and Holland T. J., 1990. Calcic amphibole equilibria and a new amphibole-plagioclase geothermometer. Contributions to Miner. and Petrology 104(2): 208-224.

Boda, S., 1994. Sample list, description, locations of samples for quartz isolation and $\delta^{18}O$ analysis: MIMEX Memorandum to K. Hannan 27 Jun 1994, file code TH5.2, 9pp, Mt Isa exploration office.

Bodorkos, S., Purdy, D.J., Bultitude, R.J., Lewis, C.J., Jones, S.L., Brown, D.D., Hoy, D., 2020. Summary of Results. Joint GSQ-GA Geochronology Project: Mary Kathleen Domain and Environs, Mt Isa Inlier, 2018-2020. Queensland Geological Record 2020/04.

Bourdelle, F. and Cathelineau, M., 2015. Low-temperature chlorite geothermometry: a graphical representation based on a T-R2+–Si diagram. European Journal of Miner., 27(5): 617-626.

Cabral A.R., Ließmann W., Jian W., Lehmann B. 2017. Selenides from St. Andreasberg, Germany: an oxidised fve-element style of mineralization and its relation to post-Variscan vein-type deposits of central Europe. Int. J. Earth Sci. (Geol Rundsch), 106, 2359–2369.

Carnaby Resources, 2021. Mount Isa Inlier Gold and Copper Projects. https://carnabyresources.com.au/projects/mount-isa-inlier-gold-and-copper-projects/ (accessed Apr 2021).

Carson, C., Hutton, L., Withnall, I., Perkins, W., Donchak, P., Parsons, A., Blake, P., Sweet, I., Neumann, N., Lambeck, A., 2011. Summary of results: Joint GSQ-GA geochronology project, Mount Isa region, 2009–2010. Queensland Geological Record 2011/03.

Chappell, B.W., White, A.J., 2001. Two contrasting granite types: 25 years later. Aust. J. Earth Sci., 48(4), 489-499.

Cathelineau, M. and Nieva, D., 1985. A chlorite solid solution geothermometer the Los Azufres (Mexico) geothermal system. Contributions to Miner. and Petrology, 91(3): 235-244.

Cathelineau, M., 1988. Cation site occupancy in chlorites and illites as a function of temperature. Clay Minerals, 23(4): 471-485.

Choy, D.K.W., 1992. The Tick Hill Gold Deposit in North-West Queensland Geology, Petrology, Mineralisation, Alteration and Structure. Report to MIM Exploration Pty Ltd., Misc.1992/089; Record No: 29966, Mt Isa exploration office.

Choy, D.K.W., 1994. The geology, structure, petrology, alteration and mineralization of Tick Hill, North-West Queensland. Master Thesis, Monash University, 220pp.

Colvine, A., Fyon, J., Heather, K., Marmont, S., Smith, P., Troop, D., 1988. Archean lode gold deposits in Ontario. Ontario Geological Survey, Miscellaneous Paper, 139, 136pp.

Compston, D.M., McDougall, I., 1994. 40Ar/39Ar and K-Ar age constraints on the Early Proterozoic Tennant Creek Block, northern Australia, and the age of its gold deposits. Aust. J. Earth Sci., 41, 609-616.

Cook N.J.; Ciobanu, C.L.; Spry P.G. , Voudouris P., 2009. Understanding gold-(silver)-telluride-(selenide) mineral deposits. Episodes 32(4), 249-263.

Corbett, G.J., Leach, T.M., 1998. Southwest Pacific Rim gold-copper systems: structure, alteration, and mineralization. Society of Economic Geologists, Special publication, 6, 237pp.

Corbett, G., 2002. Epithermal gold for explorationists. AIG News, 67, 1-8.

Corfu, F., Hanchar, J.M., Hoskin, P.W., Kinny, P., 2003. Atlas of zircon textures. Rev. in Miner. and Geochemistry, 53(1), 469-500.

Coughlin, T.J., 1993. Burke River; QLD; EPM 9083; Tick Hill Enclave 1:10000 Geological Mapping Programme. Internal MIMEX Report, Record No. 8548, Mt Isa exploration office.

Davidson, G., Large, R., Kary, G., Osborne, R., 1989. The BIF-hosted Starra and Trough Tank Au-Cu mineralization: A new stratiform association from the Proterozoic eastern succession of Mt. Isa, Australia. Econ. Geol., Monograph, 6, 135-150.

Davis, B., Pollard, P., Lally, J., McNaughton, N., Blake, K., Williams, P., 2001. Deformation history of the Naraku Batholith, Mt Isa Inlier, Australia: implications for pluton ages and geometries from structural study of the Dipvale Granodiorite and Levian Granite. Aust. J. Earth Sci., 48(1), 113-129.

Day, R., Whitaker, W., Murray, C., Wilson, I., Grimes, K., 1983. Queensland Geology: A companion volume to the 1: 2,500,000 scale geological map (1975). Publications of the Geological Survey of Queensland, 383.

Denaro, T.J., Randall, R.E., Smith, R.J., 2013. Chapter 10: Mineral and Energy Resources, in; Jell, P.A. (Eds): Geology of Queensland, Geological Survey of Queensland, Brisbane, pp 687-762.

De Jong, G.D., Williams, P.J., 1995. Giant metasomatic system formed during exhumation of mid-crustal Proterozoic rocks in the vicinity of the Cloncurry Fault, northwest Queensland. Aust. J. Earth Sci., 42(3), 281-290.

Derrick, G., Wilson, I., HIll, R., Glison, A., Mitchell, J., 1977. Geology of the Marry Kathleen 1:100 000 sheet area, north-west Queensland. BMR. Bull., 193, 114pp.

Dirks, P., Wilson, C., 1995. Crustal evolution of the East Antarctic mobile belt in Prydz Bay: continental collision at 500 Ma? Precambrian Res., 75(3-4), 189-207.

Dirks P.H.G.M., Charlesworth, E.G., Munyai, M.R., Wormald, R. 2013. Stress analysis, post-orogenic extension and 3.01Ga gold mineralization in the Barberton Greenstone Belt, South Africa; Precambrian Res., 226, 157-184.

Downs, R.C., 2000. Notes concerning thickness distributions of upper and lower quartzite horizons at Tick Hill and their control on gold mineralization. A down-plunge drill target. Internal report to MIM Exploration Pty Ltd , (B)CD.060, Record No. 20322, Mt Isa exploration office.

Duncan, R.J., Stein, H.J., Evans, K.A., Hitzman, M.W., Nelson, E.P., Kirwin, D.J., 2011. A new geochronological framework for mineralization and alteration in the selwyn-mount dore

corridor, eastern fold belt, mount isa inlier, australia: Genetic implications for iron oxide copper-gold deposits. Econ. Geol., 106(2), 169-192.

Duncan, R.J., Hitzman, M.W., Nelson, E.P., Togtokhbayar, O., 2014. Structural and lithological controls on iron oxide copper-gold deposits of the Southern Selwyn-Mount Dore Corridor, Eastern Fold Belt, Queensland, Australia. Econ. Geol., 109(2), 419-456.

Ellis, D.J. and Green, D.H., 1979. An experimental study of the effect of Ca upon garnet clinopyroxene Fe-Mg exchange equilibria. Contrib. Mineral. Petrol., v.71, pp.13-22.

England, R.N., 1993. Petrographic report for 35 samples from Tick Hill. Report to MIM Exploration Pty Ltd. ISAMISREP.018, Record No. 30874, Mt Isa exploration office.

England, R.N., 1995. The Tick Hill sedimentary exhalative gold deposit. Report to MIM Exploration Pty Ltd. ISAMISREP.023, Record No. 30881, Mt Isa exploration office.

Essene, E., 1989. The current status of thermobarometry in metamorphic rocks. Geological Society, London, Special Publications 43(1): 1-44.

Essene, E.J., 2009. Thermobarometry gone astray, Physics and Chemistry of the Earth's Interior. Springer, pp. 101-133.

Esteban, J., Cuevas, J., Tubía, J., Liati, A., Seward, D. and Gebauer, D., 2007. Timing and origin of zircon-bearing chlorite schists in the Ronda peridotites (Betic Cordilleras, Southern Spain). Lithos, 99(1-2): 121-135.

Etheridge, M., Rutland, R., Wyborn, L., 1987. Orogenesis and tectonic process in the Early to Middle Proterozoic of northern Australia. Proterozic Lithospheric Evolution, 17, 131-147.

Faure G., 1986. Principles of Isotope Geology. John Wiley & Sons, New York. 589pp.

Ferry, J.t. and Spear, F., 1978. Experimental calibration of the partitioning of Fe and Mg between biotite and garnet. Contributions to Miner. and Petrology, 66(2): 113-117.

Forrestal, P., Pearson, P., Coughlin, T., Schubert, C., 1998. Tick hill gold deposit. Geology of the mineral deposits of Australia and Papua New Guinea. Australian Institute of Mining and Metallurgy, Carlton South, VIC, Monograph 22, 699-706.

Foster, M.D., 1960. Interpretation of composition of trioctahedral micas. US Geological Survey, Prof. Pap. 354B, pp. 1-49.

Foster, A., Williams, P. and Ryan, C., 2007. Distribution of gold in hypogene ore at the Ernest Henry iron oxide copper-gold deposit, Cloncurry district, northwest Queensland. Exploration and Mining Geol., 16(3-4): 125-143.

Foster, D.R., Austin, J.R., 2008. The 1800-1610Ma stratigraphic and magmatic history of the Eastern Succession, Mount Isa Inlier, and correlations with adjacent Paleoproterozoic terranes. Precambrian Res., 163(1), 7-30.

Friedman I., O'Neil J.R., Fleisher M., Chap K.K., 1977. Compilation of stable isotope fractionation factors of geochemical interest. Data of geochemistry, v.440 6th edn, 1-12. US Geological Survey Professional Paper.

Fricker, M.B., Kutscher, D., Aeschlimann, B., Frommer, J., Dietiker, R., Bettmer, J., Günther, D., 2011. High spatial resolution trace element analysis by LA-ICP-MS using a novel ablation cell for multiple or large samples. International J. of Mass Spectrometry, 307(1-3), 39-45.

Ganguly, J. and G. C. Kennedy (1974). "The energetics of natural garnet solid solution." Contributions to Miner. and Petrology 48(2): 137-148.

Gazley, M., Sisson, M., Austin, J., Ben, P., leGras, M., Walshe, J., 2016. The Trekelano Cu-Au deposit: Integrated petrophysical and geochemical analyses. CSIRO, Australia, 21pp.

Geller, S. (1967). "Crystal chemistry of the garnets." Zeitschrift für Kristallographie-Crystalline Materials 125(1-6): 1-47

Gillis, K.M., Muehlenbachs, K., Stewart, M., Gleeson, T. and Karson, J., 2001. Fluid flow patterns in fast spreading East Pacific Rise crust exposed at Hess Deep. Journal of Geophysical Research: Solid Earth, 106(B11): 26311-26329.

Goldfarb, R.J., Baker, T., Dube, B., Groves, D.I., Hart, C.J., Gosselin, P., 2005. Distribution, character, and genesis of gold deposits in metamorphic terranes. Econ. Geol., 100th anniversary vol., 40, 407-450.

Goldfarb, R.J., Groves, D.I., 2015. Orogenic gold: Common or evolving fluid and metal sources through time. Lithos., 233, 2-26.

Graham, C.M. and Powell, R., 1984. A garnet–hornblende geothermometer: calibration, testing, and application to the Pelona Schist, Southern California. Jour. Metamorp. Geol., v.2(1), pp.13-31.

Hey, M. H., 1954. A new review of the chlorites. Mineralogical Magazine and Journal of the Mineralogical Society 30(224): 277-292.

Groves, D.I., Bierlein, F.P., Meinert, L.D., Hitzman, M.W., 2010. Iron oxide copper-gold (IOCG) deposits through Earth history: Implications for origin, lithospheric setting, and distinction from other epigenetic iron oxide deposits. Econ. Geol., 105(3), 641-654.

Geological Survey of Queensland, 2015. Hyperspectral data for drill hole TH007RD (71815), Tick Hill Deposit. Geological Survey of Queensland. https://minesonlinemaps.business.qld.gov.au/SilverlightViewer/Viewer.html?Viewer=momaps public (access 30 April 2018)

Hannan, K., 1994. Tick Hill District quartz oxygen isotope results. Report to MIM Exploration Pty Ltd, Memo.1996/024, Record No. 18742, Mt Isa exploration office.

Harris, C. and Vogeli, J., 2010. Oxygen isotope composition of garnet in the Peninsula Granite, Cape Granite Suite, South Africa: constraints on melting and emplacement mechanisms. South African J. of Geol., 113(4): 401-412.

Hart C.J.R., Goldfarb, R.J., 2005. Distinguishing intrusion-related from orogenic gold systems. New Zealand Minerals Conference Proceedings, 2005, 125-133

Heaman, L. M., Bowins, R. & Crocket, J. (1990). The chemical composition of igneous zircon suites: implications for geochemical tracer studies. Geochimica et Cosmochimica Acta 54, 1597–1607.

Hodges, K. and Spear F. S., 1982. Geothermometry, geobarometry and the Al2SiO5 triple point at Mt. Moosilauke, New Hampshire. American Mineralogist 67(11-12): 1118-1134.

Holcombe, R., Pearson, P., Oliver, N., 1991. Geometry of a middle Proterozoic extensional decollement in northeastern Australia. Tectonophysics, 191(3-4), 255-274.

Holland, T. and Blundy J., 1994. Non-ideal interactions in calcic amphiboles and their bearing on amphibole-plagioclase thermometry. Contributions to Miner. and Petrology 116(4): 433-447.

Hoskin, P. W. O. and Schaltegger, U., 2003. The composition of zircon and igneous and metamorphic petrogenesis. In: Hanchar, J. M. & Hoskin, P.W.O. (eds) Zircon. Reviews in Mineralogy and Geochemistry 53, 27-62.

Huston, D. L., Bottrill, R. S., Creelman, R. A., Zaw, K., Ramsden, T. R., Rand, S. W., Gemmell, J. B., Jablonski, W., Sie, S., and Large, R. R., 1992, Geologic and geochemical controls on the Miner. and grain size of gold-bearing phases, eastern Australian volcanic-hosted massive sulfide deposits: Econ. Geol., v. 87, p. 542-563.

Huston, D.L., Stevens, B., Southgate, P.N., Muhling, P. and Wyborn, L., 2006. Australian Zn-Pb-Ag ore-forming systems: a review and analysis. Econ. Geol., 101(6), 1117-1157.

Inoue, A., Meunier, A., Patrier-Mas, P., Rigault, C., Beaufort, D. and Vieillard, P., 2009. Application of chemical geothermometry to low-temperature trioctahedral chlorites. Clays and Clay Minerals, 57(3): 371-382.

Jackson, M., Scott, D., Rawlings, D., 2000. Stratigraphic framework for the Leichhardt and Calvert Superbasins: Review and correlations of the pre-1700 Ma successions between Mt Isa and McArthur River. Aust. J. Earth Sci., 47(3), 381-403.

Jackson, S.E., Pearson, N.J., Griffin, W.L., Belousova, E.A., 2004. The application of laser ablation-inductively coupled plasma-mass spectrometry to in situ U–Pb zircon geochronology. Chemical Geol., 211(1-2), 47-69.

Jercinovic, M.J., Williams, M.L. and Lane, E.D., 2008. In-situ trace element analysis of monazite and other fine-grained accessory minerals by EPMA. Chemical Geology, 254(3-4): 197-215.

Johnson, D., 2002. Tick Hill Abrief Review. Report to MIM Exploration Pty Ltd, ISAMISREP.208a, Record No. 31073, Mt Isa exploration office.

Jowett, E., 1991. Fitting iron and magnesium into the hydrothermal chlorite geothermometer–Geol. Assoc. Canada/Mineral. Assoc. Canada/Soc, Econ. Geol. Joint Annual Meeting, Toronto.

Kirkland, C., Smithies, R., Taylor, R., Evans, N. and McDonald, B., 2015. Zircon Th/U ratios in magmatic environs. Lithos, 212: 397-414

Kleine, B.I., Stefansson, A., Halldórsson, S.A., Whitehouse, M.J. and Jónasson, K., 2018a. Silicon and oxygen isotopes unravel quartz formation processes in the Icelandic crust. Geochemical Perspectives Letters, 7: 5-11.

Kohn, M. J. and Spear, F. S. 1989. Empirical calibration of geobarometers for the assemblage garnet + plagioclase + quartz. American Mineralogist 74(1-2): 77-84.

Kohn, M. J. and Spear, F. S. , 1990. Two new geobarometers for garnet amphibolites, with applications to southeastern Vermont. American Mineralogist 75(1-2): 89-96.

Kositcin, N., Bultitude, R.J., Purdy, D.J., 2019. Queensland Geological Record 2019/02. Summary of results. Joint GSQ-GA Geochronology Project: Mary Kathleen Domain, Mount Isa Inlier, 2018-2019. Queensland Geological Record 2019/02.

McLellan, J.G., Mustard, R., Blenkinsop, T., Oliver, N.H., McKeagney, C., 2010. Critical ingredients of IOCG mineralization in the Eastern Fold Belt of the Mount Isa Inlier: insights from combining spatial analysis with mechanical numerical modelling. PGC Publishing, pp. 233-255.

Laing, W.P., 1992. The metasomatic development of the quartz-feldspar laminate gold hostrock at Tick Hill, Illustrated. Report to MIM Exploration Pty Ltd., ISAMISREP.010; Record No. 30862, Mt Isa exploration office.

Laing, W.P., 1993. Geology of the Tick Hill region, Mount Isa, with implications for exploration. Report to MIM Exploration Pty Ltd., ISAMISREP.017; Record No. 30870, Mt Isa exploration office.

Large, R.R., 1975. Zonation of hydrothermal minerals at the Juno mine, Tennant Creek goldfield, central Australia. Econ. Geol., 70 (8), 1387-1413.

Laverne, C., Vanko, D.A., Tartarotti, P. and Alt, J.C., 1995. 15. Chemistry and geothermometry of secondary minerals from the deep sheeted dike complex, Hole 504B1, Proceedings of the ocean drilling program, Scientific results, pp. 140.

Le, T.X., Dirks, P.H.G.M., Sanislav I.V., Huizenga, J.M., Cocker, H., Manestar, G.N., 2021. Geological setting and mineralization characteristics of the Tick Hill Gold Deposit, Mt Isa Inlier, Queensland, Australia. Ore Geol. Rev. 137:104288.

Leake, B. E., Woolley, A. R., Arps, C. E., Birch, W. D., Gilbert, M. C., Grice, J. D., Krivovichev, V. G., 1997. Nomenclature of amphiboles; report of the Subcommittee on Amphiboles of the International Mineralogical Association Commission on new minerals and mineral names. Mineralogical Magazine 61(405): 295-310.

Ludwig, K.R., 2011. User's manual for Isoplot 4.15: A geochronological toolkit for Microsoft Excel. Berkeley Geochronology Center, Berkeley, California, U.S.A.

MacCready, T., Goleby, B., Goncharov, A., Drummond, B., Lister, G., 1998. A framework of overprinting orogens based on interpretation of the Mount Isa deep seismic transect. Econ. Geol., 93(8), 1422-1434.

Mark, G., 2001. Nd isotope and petrogenetic constraints for the origin of the Mount Angelay igneous complex: implications for the origin of intrusions in the Cloncurry district, NE Australia. Precambrian Res., 105(1): 17-35.

Mark, G., Tedman-Jones, C., 2001. Titanite U-Pb age dates for Tick Hill. Report to MIM Exploration Pty Ltd. Email form, Unnamed record, Mt Isa exploration office.

Mark, G., Oliver, N.H., Williams, P.J., 2006. Mineralogical and chemical evolution of the Ernest Henry Fe oxide–Cu–Au ore system, Cloncurry district, northwest Queensland, Australia. Mineralium Deposita, 40(8), 769-801.

Marshall, L. J. and N. H. Oliver (2008). "Constraints on hydrothermal fluid pathways within Mary Kathleen Group stratigraphy of the Cloncurry iron-oxide–copper–gold District, Australia." Precambrian Res., 163(1-2): 151-158.

Magee, C.W., Withnall, I.W., Hutton, L.J., Perkins, W.G., Donchak, P.J.T., Parsons, A., Blake, P.R., Sweet, I.P., Carson, C.J., 2012. Joint GSQ-GA geochronology project, Mount Isa Region, 2008-2009. Record 2012/07, Queensland Geological Survey, Brisbane.

Matthews, A., Goldsmith, J.R. and Clayton, R.N., 1983. Oxygen isotope fractionations involving pyroxenes: the calibration of mineral-pair geothermometers. Geochimica et Cosmochimica Acta, 47(3): 631-644.

McDonough, W.F., Sun, S.-S., 1995. The composition of the Earth. Chemical Geol., 120(3-4): 223-253.

Middlemost, E.A., 1994. Naming materials in the magma/igneous rock system. Earth-Sci. Rev., 37(3-4), 215-224.

MIM, 1993. Geological maps of underground mine levels at Tick Hill Mine. Mount Isa Mines, data repository, Mt Isa exploration office.

MIM, 2000. Assay data for exploration drill holes from Tick Hill. Mount Isa Mines, data repository, Mt Isa exploration office.

Morimoto, N., 1988. Nomenclature of pyroxenes. Mineralogical Magazine. 52: 535-550

Moura, M.R.A., Botelho, N.F., Olivo, G.R. and Kyser, T.K., 2006. Granite-related Paleoproterozoic, Serrinha gold deposit, Southern Amazonia, Brazil: hydrothermal alteration, fluid inclusion and stable isotope constraints on genesis and evolution. Econ. Geol., 101(3): 585-605.

Nano, S., 1999. Tick Hill geophysics, geology. Report to MIM Exploration Pty Ltd, Unnamed record, Mt Isa exploration office.

Nano, S., Croxford, B., Moloney, M., 2000. Poster of Tick Hill Petrology. Report to MIM Exploration Pty Ltd, Unnamed record, Mt Isa exploration office.

Neumann, N., Southgate, P., Gibson, G., McIntyre, A., 2006. New SHRIMP geochronology for the Western Fold Belt of the Mt Isa Inlier: developing a 1800-1650 Ma event framework. Aust. J. Earth Sci., 53(6), 1023-1039.

Neumann, N.L., Fraser, G.L., 2007. Geochronological synthesis and time-space plots for Proterozoic Australia. Geoscience Australia Record 2007/06.

Neumann, N., Gibson, G., Southgate, P., 2009. New SHRIMP age constraints on the timing and duration of magmatism and sedimentation in the Mary Kathleen Fold Belt, Mt Isa Inlier, Australia. Aust. J. Earth Sci., 56(7), 965-983.

Newton, R. C., Charlu, T. V., Kleppa, O. J., 1977. Thermochemistry of high pressure garnets and clinopyroxenes in the system CaO-MgO-Al2O3-SiO2. Geochimica et Cosmochimica acta 41(3): 369-377.

O'dea, M.G., Lister, G., MacCready, T., Betts, P., Oliver, N., Pound, K., Huang, W., Valenta, R., 1997. Geodynamic evolution of the Proterozoic Mt Isa terrain. Geological Society, London, Special Publications, 121(1), 99-122.

Oliver, N., Cartwright, I., Wall, V., Golding, S., 1993. The stable isotope signature of kilometer-scale fracture dominated metamorphic fluid pathways, Mary Kathleen, Australia. J. of Metamorphic Geol., 11(5): 705-720.

Oliver, N.H., Rawling, T.J., Cartwright, I., Pearson, P.J., 1994. High-temperature fluid-rock interaction and scapolitization in an extension-related hydrothermal system, Mary Kathleen, Australia. Journal of Petrology, 35(6), 1455-1491.

Oliver, N., 1995. Hydrothermal history of the Mary Kathleen Fold Belt, Mt Isa Block, Queensland. Australian Journal of Earth Sciences, 42(3), 267-279.

Oliver, N., 1998. Tick Hill - Altered and deformed granites and Corella metasediments. Report to MIM Exploration Pty Ltd. Email form, Unnamed record, Mt Isa exploration office.

Oliver, N., Pearson, P., Holcombe, R., Ord, A., 1999. Mary Kathleen metamorphic-hydrothermal uranium-rare-earth element deposit: Ore genesis and numerical model of coupled deformation and fluid flow. Aust. J. Earth Sci., 46(3), 467-484.

Oliver, N.H.S., Cleverley, J.S., Mark, G., Pollard, P.J., Fu, B., Marshall, L.J., Rubenach, M.J., Williams, P.J., Baker, T., 2004. Modeling the role of sodic alteration in the genesis of iron oxide-copper-gold deposits, Eastern Mount Isa Block, Australia. Econ. Geol., 99(6), 1145-1176.

Oliver, N.H.S., Butera, K.M., Rubenach, M.J., Marshall, L.J., Cleverley, J.S., Mark, G., Tullemans, F., Esser, D., 2008. The protracted hydrothermal evolution of the Mount Isa Eastern Succession: A review and tectonic implications. Precambrian Res., 163(1), 108-130.

Paces, J.B., Miller Jr, J.D., 1993. Precise U-Pb ages of Duluth complex and related mafic intrusions, northeastern Minnesota: Geochronological insights to physical, petrogenetic, paleomagnetic, and tectonomagmatic processes associated with the 1.1 Ga midcontinent rift system. J. of Geophysical Res.: Solid Earth, 98(B8), 13997-14013.

Page, R., 1978. Response of U-Pb Zircon and Rb-Sr total-rock and mineral systems to low-grade regional metamorphism in proterozoic igneous rocks, mount Isa, Australia. Journal of the Geological Society of Australia, 25(3-4), 141-164.

Page, R., 1983. Chronology of magmatism, skarn formation, and uranium mineralization, Mary Kathleen, Queensland, Australia. Econ. Geol., 78(5), 838-853.

Page, R., Sun, S.S., 1998. Aspects of geochronology and crustal evolution in the Eastern Fold Belt, Mt Isa Inlier. Aust. J. Earth Sci., 45(3), 343-361.

Passchier, C., 1986. Proterozoic deformation in the Duchess belt, Australia: A contribution to the BMR Mount Isa regional tectonic history program. Geologie en mijnbouw, 65, 47-56.

Passchier, C., Williams, P., 1989. Proterozoic extensional deformation in the Mount Isa inlier, Queensland, Australia. Geological Magazine, 126(1), 43-53.

Passchier, C., 1992. Geology of the Myubee area, Mt Isa Inlier, Queensland. Detailed studies of Mount Isa Inlier, pp. 199-208.

Passchier, C.W., Trouw, R.A., 2005. Microtectonics. Springer Science & Business Media, 366pp.

Paton, C., Hellstrom, J., Paul, B., Woodhead, J., Hergt, J., 2011. Iolite: Freeware for the visualisation and processing of mass spectrometric data. J. of Analytical Atomic Spectrometry, 26(12), 2508-2518.

Pearson, P., Holcombe, R., Page, R., 1992. Synkinematic emplacement of the Middle Proterozoic Wonga Batholith into a mid-crustal extensional shear zone, Mt Isa Inlier, Queensland, Australia. Detailed studies of the Mt Isa Inlier, 243, 289-328.

Perchuk, L., 1967. Analysis of thermodynamic conditions of mineral equilibria in amphibole-garnet rocks. Izvestiya Akademii Nauk SSSR, Seriya Geologicheskaya, 3: 57-83.

Perchuk, L., 1969. The effect of temperature and pressure on the equilibrium of natural iron-magnesium minerals. International Geol. Rev., 11(8): 875-901.

Perchuk, L.L., 1970. Equilibria OJ Rock-Forming Minerals, 301 'Nauka' Press, Moscow (in Russian)

Perchuk, L., Lavrent'Eva, I. , 1983. Experimental investigation of exchange equilibria in the system cordierite-garnet-biotite. Kinetics and equilibrium in mineral reactions, Springer: 199-239.

Perchuk, L.L., Aranovich, L.Y., Podlesskii, K.K., Lavrant'eva, I.V., Gerasimov, V.Y., Fed'Kin, V.V., Berdnikov, N.V., 1985. Precambrian granulites of the Aldan shield, eastern Siberia, USSR. Jour. Metamorp. Geol., v.3(3), pp.265-310.

Perkins, C., Wyborn, L., 1998. Age of Cu-Au mineralisation, Cloncurry district, eastern Mt Isa Inlier, Queensland, as determined by 40Ar/39Ar dating. Aust. J. Earth Sci., 45(2), 233-246.

Pettke, T., 2008. Analytical protocols for element concentration and isotope ratio measurements in fluid inclusions by LA-(MC)-ICP-MS. Laser Ablation ICP-MS in the Earth Sciences: Current Practices and Outstanding Issues. Mineralogical Association of Canada, Short Course Series, 40, 189-218.

Poli, S. and Schmidt M. W., 1992. A comment on "Calcic amphibole equilibria and a new amphibole-plagioclase geothermometer" by JD Blundy and TJB Holland. Contributions to Miner. and Petrology 111(2): 273-278.

Powell, R., 1985. Regression diagnostics and robust regression in geothermometer/geobarometer calibration: the garnet clinopyroxene geothermometer revisited. Jour. Metamorp. Geol., v.3(3), pp.231-243.

Spear, F. S., 1980. NaSi⇌ CaAl exchange equilibrium between plagioclase and amphibole. Contributions to Miner. and Petrology 72(1): 33-41.

Ravna, E.K., 2000. Distribution of Fe^{2+} and Mg between coexisting garnet and hornblende in synthetic and natural systems: an empirical calibration of the garnet–hornblende Fe–Mg geothermometer. Lithos, v.53(3-4), pp.265-277.

Richards, J., Cooper, J., Webb, A., 1963. Potassium-argon ages on micas from the Precambrian region of North-Western Queensland. J. Geol. Soc. Aust., 10(2), 299-312.

Robb, L.J., Robb, V.M., 1998. Gold in the Witwatersrand Basin, In: Wilson, M.G.C., Anheausser, C.R. (Eds.), The Mineral Resources of South Africa. Handbook, Council for Geoscience, 6, 294-349.

Rollinson, H., 1993. Using Geochemical Data: Evaluation, Presentation, Interpretation, Longman Group UK, Ltd, London, 352pp.

Rowe, R. , Zhou, X., 2007. Models and exploration methods for major gold deposit types. Proceedings of exploration, 7, 691-711.

Rubatto, D., 2002. Zircon trace element geochemistry: partitioning with garnet and the link between U–Pb ages and metamorphism. Chemical geology, 184(1-2): 123-138.

Rutherford, N.F., 1999. First annual joint venture report to 1st January 2000 for exploration permits for minerals 9083, 11012 & 11013, Burke River Region, Mt Isa-Cloncurry District, North West Queensland, Technical Report No: 1. https://qdexguest.dnrm.qld.gov.au/portal/site/qdex/search?REPORT_ID=30650 (access 12 Nov 2017)

Rutherford, N.F., 2000. Second annual joint venture report to 1st January 2000 for exploration permits for minerals 9083, 11012 & 11013, Burke River Region, Mt Isa-Cloncurry District, North West Queensland, Technical Report No: 2. https://qdexguest.dnrm.qld.gov.au/portal/site/qdex/search?REPORT_ID=31587 (access 12 Nov 2017).

Scott, D., Rawlings, D., Page, R., Tarlowski, C., Idnurm, M., Jackson, M., Southgate, P., 2000. Basement framework and geodynamic evolution of the Palaeoproterozoic superbasins of north-central Australia: an integrated review of geochemical, geochronological and geophysical data. Aust. J. Earth Sci., 47(3), 341-380.

Simon, G., Essene, E.J., 1996. Phase relations among selenides, sulfides, tellurides, and oxides; I, Thermodynamic properties and calculated equilibria. Econ. Geol., 91(7), 1183-1208.

Simon, G., Kesler, S.E., Essene, E.J., 1997. Phase relations among selenides, sulfides, tellurides, and oxides.II. Applications to selenide-bearing ore deposits. Econ. Geol., 92, 468–484.

Skirrow, R.G., 2000. Gold-Copper-Bismuth Deposits of the Tennant Creek District, Australia: A Reappraisal of Diverse High Grade Systems, in: Porter, T.M. (Eds.), Hydrothermal Iron Oxide Copper-Gold & Related Deposits: A Global Perspective. Austral. Min. Found. Adelaide, pp. 149-160.

Skirrow, R.G., Walshe, J.L., 2002. Reduced and oxidized Au-Cu-Bi iron oxide deposits of the Tennant Creek inlier, Australia: An integrated geologic and chemical model. Econ. Geol., 97 (6), 1167–1202.

Skirrow, R.G., Cross A.J., Lecomte A., Mercadier J., 2019. A shear-hosted Au-Cu-Bi metallogenic event at ca.1660 Ma in the Tennant Creek goldfield (northern Australia) defined by in-situ monazite U-Pb-Th dating. Precambrian Res. 332, 105402. DOI 10.1016/j.precamres.2019.105402.

Spear, F. S. , 1981. Amphibole-plagioclase equilibria: an empirical model for the relation albite+ tremolite= edenite+ 4 quartz. Contributions to Miner. and Petrology 77(4): 355-364.

Spear, F. S., 1993. Metamorphic Phase Equilibria and Pressure-temperature-time Paths, Mineralogical Society of America.

Spence, J., Sanislav, I. and Dirks, P., 2020. 1750-1710 Ma deformation along the eastern margin of the North Australia Craton. Precambrian Res., 353, 106019.

Solar, G.S., Brown, M., 2001. Petrogenesis of migmatites in Maine, USA: possible source of peraluminous leucogranite in plutons? J. of Petrology, 42(4), 789-823.

Southgate, P., Neumann, N., Gibson, G., 2013. Depositional systems in the Mt Isa Inlier from 1800 Ma to 1640 Ma: Implications for Zn–Pb–Ag mineralisation. Aust. J. Earth Sci., 60(2), 157-173.

Spooner, E.T.C., 1993. Magmatic sulphide-volatile interaction as a mechanism for producing chalcophile element enriched, Archean Au-quartz, epithermal Au-Ag and Au skarn hydrothermal ore fluids. Geol. Rev., 7, 359–379.

Tedman, C.J., 1993. Gold dispersion and geochemistry at the Tick Hill gold deposit and implications for exploration, Mt Isa Inlier, northwest Queensland. Master of Science, James Cook University, 122pp.

Tedman-Jones, C., 2001. Tick Hill core relogging review. Internal report to MIM Exploration Pty Ltd. Misc.2001/010, Record No. 30764, Mt Isa exploration office.

Thompson, A. B., 1976. Mineral reactions in pelitic rocks; II, Calculation of some PTX (Fe-Mg) phase relations. American J. Sci. 276(4): 425-454.

Thompson, J., Sillitoe, R., Baker, T., Lang, J., Mortensen, J., 1999. Intrusion-related gold deposits associated with tungsten-tin provinces. Mineralium Deposita, 34(4), 323-334.

Timpa, S., Gillis, K.M. and Canil, D., 2005. Accretion-related metamorphism of the Metchosin igneous complex, southern Vancouver Island, British Columbia. Canadian J. Earth Sci., 42(8): 1467-1479.

Tucker, R.F., Viljoen R.P., Viljoen M.J. 2016. A review of the Witwatersrand Basin - The world's greatest goldfield. Episodes, 39(2), 105-133.

Vidal, O., Lanari, P., Munoz, M., Bourdelle, F. and De Andrade, V., 2016. Deciphering temperature, pressure and oxygen-activity conditions of chlorite formation. Clay Minerals, 51(4): 615-633.

Whalen, J. B., Currie, K. L. and Chappell, B. W., 1987. A-type granites: geochemical characteristics, discrimination and petrogenesis. Contributions to Mineralogy and Petrology, 95(4), 407-419.

Walters, S., Bailey, A., 1998. Geology and mineralization of the Cannington Ag-Pb-Zn deposit; an example of Broken Hill-type mineralization in the eastern succession, Mount Isa Inlier, Australia. Econ. Geol, 93(8), 1307-1329.

Watkins, R., 1993. Deformation, felsic magmatism and alteration associated with the Tick Hill Gold Deposit, northwest Queensland, B.Sc. Hons. Thesis, Monash University.

Wedekind, M.R., Large, R.R., Williams, B.T., 1989. Controls on high-grade gold mineralization at Tennant Creek, Northern Territory, Australia. Econ. Geol., Monograph 6, 168-179.

Wiedenbeck, M., Alle, P., Corfu, F., Griffin, W., Meier, M., Oberli, F., Quadt, A.v., Roddick, J., Spiegel, W., 1995. Three natural zircon standards for U-Th-Pb, Lu-Hf, trace element and REE analyses. Geostandards Newsletter, 19(1), 1-23.

Williams, P., 1998. Metalliferous economic geology of the Mt Isa eastern succession, Queensland. Aust. J. Earth Sci., 45(3), 329-341.

Williams, P.J., Pollard, P.J., 2001. Australian Proterozoic iron oxide-Cu-Au deposits: An overview with new metallogenic and exploration data from the Cloncurry district, northwest Queensland. Exploration and Mining Geology, 10(3), 191-213.

Williams, P.J., Dong, G., Ryan, C.G., Pollard, P.J., Rotherham, J.F., Mernagh, T.P., Chapman, L.H., 2001. Geochemistry of hypersaline fluid inclusions from the Starra (Fe oxide)-Au-Cu deposit, Cloncurry District, Queensland. Econ. Geol., 96(4), 875-883.

Williams, P.J., Barton, M.D., Johnson, D.A., Fontboté, L., De Haller, A., Mark, G., Oliver, N.H., Marschik, R., 2005. Iron oxide copper-gold deposits: Geology, space-time distribution, and possible modes of origin. Econ. Geol., 371-405.

Williams, M.R., Holwell, D.A., Lilly, R.M., Case, G.N. and McDonald, I., 2015. Mineralogical and fluid characteristics of the fluorite-rich Monakoff and E1 Cu–Au deposits, Cloncurry region, Queensland, Australia: Implications for regional F–Ba-rich IOCG mineralisation. Ore Geol. Rev., 64: 103-127.

Withnall, I., Hutton, L., 2013. Chapter 2: North Australian Craton, In: Jell, P.A. (Ed.), Geology of Queensland. Geology of Queensland, Geological Survey of Queensland, Brisbane, pp 23-112.

Withnall, I.W., 2019. Review of SHRIMP zircon ages for the Eastern Succession of the Mt Isa Province and magmatic events in its provenance. Queensland Minerals and Energy Review Series, Department of Natural Resources, Mines and Energy, Queensland.

Wyborn, L., Page, R., 1983. The Proterozoic Kalkadoon and Ewen batholiths, Mt Isa Inlier, Queensland-source, chemistry, age and metamorphism, BMR J. Aust. Geol. Geophys., 8(1), 53-69.

Wyborn, L., Page, R., McCulloch, M., 1988. Petrology, geochronology and isotope geochemistry of the post-1820 Ma granites of the Mount Isa Inlier: mechanisms for the generation of Proterozoic anorogenic granites. Precambrian Res., 40, 509-541.

Wyborn, L., A.I., 1997. Dajarra 1:100,000 digital geology, part of Mt Isa geological digital dataset. Geoscience Australia, http://pid.geoscience.gov.au/dataset/ga/30923 (access 10 Aug 2020).

Xu, G., 1996. Structural geology of the Dugald River Zn-Pb-Ag deposit, Mount Isa Inlier, Australia. Ore Geol. Rev., 11(6), 339-361.

Yakymchuk, C., Kirkland, C.L. and Clark, C., 2018. Th/U ratios in metamorphic zircon. Journal of Metamorphic Geology, 36(6): 715-737.

Zang, W. and Fyfe, W., 1995. Chloritization of the hydrothermally altered bedrock at the Igarapé Bahia gold deposit, Carajás, Brazil. Mineralium Deposita, 30(1): 30-38.

Zhu, Z., 2016. Gold in iron oxide copper–gold deposits. Ore Geol. Rev., 72: 37-42.

Appendices: Attached file